



Electromechanical control of surface domain walls

Grégoire Magagnin

► To cite this version:

Grégoire Magagnin. Electromechanical control of surface domain walls. Materials Science [cond-mat.mtrl-sci]. Université Paris-Saclay, 2023. English. NNT : 2023UPASP043 . tel-04155512

HAL Id: tel-04155512

<https://theses.hal.science/tel-04155512>

Submitted on 7 Jul 2023

HAL is a multi-disciplinary open access archive for the deposit and dissemination of scientific research documents, whether they are published or not. The documents may come from teaching and research institutions in France or abroad, or from public or private research centers.

L'archive ouverte pluridisciplinaire **HAL**, est destinée au dépôt et à la diffusion de documents scientifiques de niveau recherche, publiés ou non, émanant des établissements d'enseignement et de recherche français ou étrangers, des laboratoires publics ou privés.

Electromechanical control of surface domain walls

*Contrôle électromécanique des parois de domaines en
surface*

Thèse de doctorat de l'université Paris-Saclay

École doctorale n° 564 Physique en Île-de-France (ED-PIF)

Spécialité de doctorat: Physique

Graduate School : Physique, Référent : Faculté des sciences d'Orsay

Thèse préparée dans l'unité de recherche SPEC (Université Paris-Saclay, CEA, CNRS), sous la direction de Nicholas Barrett, directeur de recherche

Thèse soutenue à Paris-Saclay, le 18 Avril 2023, par

Grégoire MAGAGNIN

Composition du jury

Pierre-Eymeric JANOLIN

Professeur des universités, CentraleSupélec

Président

Gustau CATALAN

Directeur de recherche, Institut Català de
Nanociència i Nanotecnologia

Rapporteur & Examineur

Frédéric LEROY

Professeur des universités, Université Aix-
Marseille

Rapporteur & Examineur

Mojca OTONICAR

Docteur, Jožef Stefan Institute

Examinatrice

Titre: Contrôle électromécanique des parois de domaines en surface

Mots clés: ferroélastique, paroi de domaines, CaTiO_3 , LEEM, PEEM, déformation

Résumé:

Le travail de thèse porte sur le contrôle électromécanique des parois de domaines ferroïques dans les céramiques titanate de baryum et titanate de calcium. La première partie est consacrée à l'observation et quantification in-situ de l'ordonnement ferroélastique dans le titanate de calcium par des techniques de microscopie à photoémission. Nous utilisons l'imagerie par microscopie de photoémission d'électrons (PEEM), au seuil de photoémission, pour étudier la topographie physique de la surface ferroélastique avec sa structure caractéristique en forme de toit d'usine de type vallée/crête et pour quantifier les angles de macle. Par des considérations de symétrie, à partir des angles de macle, on peut déduire les directions des déformations ferroélastiques dans les domaines. Les résultats concordent avec la mesure indépendante des angles par microscopie à force atomique (AFM). Avec cette méthode, il serait possible de mesurer avec précision la topographie physique sur n'importe quelle surface ferroélastique et de quantifier les états de contrainte dans les domaines jacents.

De plus, nous identifions directement l'orientation du paramètre d'ordre ferroélastique dans les domaines, la déformation spontanée, par la spectroscopie d'absorption des rayons X dans un microscope d'électrons en photoémission (XAS-PEEM). La grandeur de l'interaction de la lumière polarisée avec les orbitales 3d du titane dans le titanate de calcium dépend de l'orientation de la déformation des domaines. Ainsi, un contraste correspondant aux différents états de déformation spontanée est visible par dichroïsme linéaire des rayons X (XLD), qui est la différence entre les images avec des polarisations de la lumière transverse orthogonales. La détermination in-situ des angles de topographie physique et de l'orientation de la déformation par PEEM ouvre des perspec-

tives pour une analyse complète de la réponse électromécanique des parois ferroélastiques.

Dans une deuxième partie, nous avons étudié un rétrécissement de la bande interdite au niveau des parois de domaine dans le titanate de calcium. La bande interdite est mesurée par spectroscopie des pertes d'énergie électronique (EELS) dans un microscope électronique à basse énergie (LEEM) en mode dispersif. Un diaphragme dans un plan image est centré sur les domaines ou sur les parois. Dans chaque cas nous mesurons l'écart en énergie entre le pic élastique et le début du pic des pertes. Le rétrécissement aux parois est compris entre 0.01 et 0.33 eV, avec une réduction plus importante pour les parois de domaine polarisées vers le haut que pour celles polarisées vers le bas. Le rétrécissement de la bande interdite est suggéré comme un effet extrinsèque de l'interaction entre les lacunes d'oxygène et les parois, générant des états dans la bande interdite. Une modulation du rétrécissement de la bande interdite en fonction de la concentration des lacunes d'oxygène est également observée.

Dans la dernière partie, nous étudions la mobilité des parois de domaine ferroélastiques du titanate de baryum sous l'effet d'un fluage. Le mouvement des parois ferroélastiques de domaine ferroélectrique est un processus non linéaire où la propagation continue des parois se superpose souvent à des sauts soudains. L'accumulation de plusieurs sauts forme une avalanche. Nous profitons de la résolution spatiale du PEEM pour observer les parois de domaines sur une longue plage de temps en s'aidant de la modulation de la polarisation des domaines ferroélectriques. Nous avons constaté que la distribution en énergie du mouvement brusque des parois ferroélastiques suit une loi de puissance avec un exposant de 1.37, ce qui confirme la dépendance du mouvement d'avalanches indépendante de l'échelle.

Title: Electromechanical control of surface domain walls

Keywords: ferroelastic, domain wall, CaTiO_3 , LEEM, PEEM, strain

Abstract:

In this thesis, we investigate the electromechanical control of the domain walls in ferroelastic calcium titanate and ferroelectric barium titanate single crystals. We first observe and quantify in situ the ferroelastic ordering in calcium titanate by photoemission electron microscopy (PEEM). We use threshold PEEM to study and quantify the physical topography of the ferroelastic surface with its characteristic valley/ridge factory roof-like structure and quantify the surface twin angles. From symmetry considerations, we deduce the ferroelastic strain ordering. The results agree well with the independent measurement of the tilt angles using atomic force microscopy (AFM). This method allows measurement of the physical topography of any ferroelastic surface by PEEM and identification of the strain states in the adjacent domains.

We directly identify the orientation of the ferroelastic order parameter by X-ray absorption spectroscopy photoemission electron microscopy (XAS-PEEM). The polarized light interaction with the titanium 3d orbitals is not equivalent between ferroelastic domains with different strain orientations. Contrast related to the different spontaneous strain orientations is visible in X-ray linear dichroism (XLD), which is the difference between images acquired by transverse vertical and horizontal polarization light. In-situ twin angle and strain determination by PEEM open perspectives to complete analysis of the domain wall electromechanical response.

In the second part of the thesis, we measure the band gap narrowing at the calcium titanate domain walls. The gap is determined by electron energy loss spectroscopy (EELS) in a low-energy electron microscope (LEEM) operating in dispersive mode. A field aperture in an image plane is centered on domains and on domain walls. In each case, the gap is given by the separation of the elastic and the onset of the loss peak. The reduction at the domain walls is between 0.01 and 0.33 eV, with higher values for upward polarized domain walls. The narrowing is suggested to be an extrinsic effect stemming from the interaction between oxygen vacancy defects and the domain walls, generating gap states. A possible tuning of the band gap energy with the oxygen vacancy concentration is also observed.

Finally, we investigate ferroelastic domain wall creep in barium titanate. Dynamical domain wall behavior is at the core of ferroelastic/ferroelectric switching. The motion of ferroelectric domain walls is a nonlinear process where continuous propagation often superimposes with sudden jumps called jerks. We take advantage of the PEEM spatial resolution to observe domain walls over a long time range from the surface potential modulation of the ferroelectric domain polarizations. A residual stress from the sample mounting provides a driving force for domain wall fluctuating movement. We found that the domain's wall creep follows a power law with an exponent of 1.37 from the jerk energy distribution, providing striking confirmation of a scale-independent motion.

Remerciements

Je souhaite commencer par remercier chaleureusement mon directeur de thèse Nick Barrett pour l'opportunité de travailler sur ce sujet de thèse. Son investissement et encadrement au quotidien dans mon travail de thèse m'a beaucoup aidé pour mener à bien ce travail de recherche exploratoire. J'ai beaucoup appris à ses côtés, au travers de longues discussions, opportunités d'aller en conférences et runs synchrotrons. Je souhaite d'ailleurs aussi le remercier pour tout le temps passé à relire et corriger mes présentations, abstracts et manuscrits, notamment ce manuscrit de thèse !

Je remercie les membres du jury qui ont évalué mon travail de thèse Gustau Catalan, Frédéric Leroy, Pierre-Eymeric Janolin et Mojca Otonicar. Je suis particulièrement reconnaissant envers les rapporteurs Gustau Catalan et Frédéric Leroy pour leurs commentaires sur mon manuscrit de thèse.

Cette thèse n'aurait pu être menée à son terme sans le soutien des membres du laboratoire au CEA. Je tiens à remercier tout particulièrement Christophe Lubin pour son soutien indéfectible et pour le maintien du PEEM en bon état. Ce n'est pas sans raison que les parois extérieures du PEEM brillent autant ! Je pense aussi à Dominique Martinotti qui m'a beaucoup aidé sur l'utilisation du PEEM et avec qui j'avais plaisir à discuter des observations LEEM. Ludovic Douillard a aussi été très présent et m'a apporté beaucoup de soutien sur le LEEM, notamment une solide base plus théorique sur le fonctionnement du LEEM. Un grand merci à Ludovic Tortech pour les mesures AFM et aussi pour sa présence très rafraichissante dans le laboratoire et les pauses café. J'ai aussi eu la chance de travailler en salle blanche au C2N et je tiens à remercier Thomas Maroutian pour l'opportunité d'utiliser la PLD et son encadrement. Je pense aussi aux doctorants et post-docs avec qui j'ai partagé beaucoup de moments dans le laboratoire et qui m'ont apporté beaucoup de soutien : Wassim, Myriam, Santiago, Tom, Natalya, Sergei, Anthony, Omar, Paul, Anas, Bihn, Maikane, Anyssa.

Je tiens aussi à remercier les collaborateurs avec qui j'ai pu travailler sur différents sujets liés à ma thèse. Je pense tout particulièrement à Ekhard Salje avec qui j'ai pu avoir une première discussion au début de ma thèse pour définir la marche à suivre sur tout mon travail de thèse étant donné sa grande expertise dans les ferroélastiques, et toutes celles qui ont suivi ! Je remercie aussi les collaborateurs avec qui j'ai eu la chance de travailler : Francesco Maccherozzi, Brice Sarpi, Blai Casals, Matthias Escher, Nils Weber, Mael Guennou, Charles Paillard, Gregory Geneste et Guillaume Nataf.

Je veux ensuite remercier le personnel scientifique et administratif du SPEC sans qui ma thèse ne serait pas déroulé sans accros ! Je pense à mon tuteur au SPEC Simon Vassant, au chargé des thésards François Ladiou et au chef de service Patrice Roche. Nathalie Royer et Carole Becquet ont aussi été très présents et d'une grande aide pour les tâches administratives.

Je n'oublie pas de remercier très chaleureusement l'encadrement que j'ai reçu à Centrale Lyon de la part de Bertrand Vilquin et pendant mon stage de fin d'étude à GeorgiaTech de Nazanin Bassiri-Gharb. J'ai beaucoup appris scientifiquement et aussi sur le métier de chercheur à leur côtés et je ne serais certainement pas arrivé jusqu'au doctorat sans leur aide.

Et bien évidemment je souhaite terminer ces remerciements avec une pensée pour ma famille, qui m'ont grandement soutenu pendant ces 3 années de thèse. Ce soutien a été proportionnel à la quantité de gâteaux préparés pour ma soutenance de thèse (énormément !!!).

Contents

I	Ferroelectric and ferroelastic domain and domain wall	13
A	Ferroelectric and ferroelastic properties	13
A.1	Perovskites	13
A.2	Ferroelectricity	14
A.2.1	Ferroelectric phase transition	14
A.2.2	Order parameter: spontaneous polarization	15
A.2.3	Ferroelectric domain	18
A.2.4	Ferroelectric domain walls	20
A.3	Ferroelasticity	21
A.3.1	Ferroelastic phase transition	22
A.3.2	Order parameter: spontaneous strain	22
A.3.3	Ferroelastic domain	23
A.3.4	Ferroelastic domain wall	24
B	CaTiO ₃ and BaTiO ₃	27
B.1	Calcium titanate CaTiO ₃	27
B.1.1	Structure	27
B.1.2	Polar domain walls	28
B.1.3	CTO twin angle	30
B.2	Barium titanate BaTiO ₃	32
C	Domain wall engineering	35
C.1	Definition	35
C.2	Domain wall conductivity	35
C.3	Domain wall dynamics	37
II	Experimental methods	41
A	Photoemission techniques	41
A.1	Photoemission process	42
A.1.1	Photoelectric effect	42
A.1.2	Three steps model	42
A.1.3	Detection	45
A.2	X-ray Photoemission Spectroscopy (XPS)	45
A.3	Photoemission Electron Microscopy (PEEM)	46
A.3.1	Generalities	46
A.3.2	NanoESCA experimental setup	48
A.3.3	Photoemission threshold	51
A.3.4	Non-isochromaticity	52
A.3.5	X-Ray Absorption Spectroscopy PhotoEmission Electron Microscopy (XAS-PEEM)	53

B	Low Energy Electron Microscopy (LEEM)	56
B.1	SPELEEM experimental setup	56
B.2	Surface potential: MEM-LEEM transition	57
B.3	Electrical topography	59
B.4	Physical topography	60
B.5	Low Energy Electron Diffraction (LEED)	61
B.6	Electron Energy Loss Spectroscopy (EELS)	62
C	Thin film deposition: Pulsed Laser Deposition (PLD)	63
D	Thin film characterization techniques	64
D.1	Atomic Force Microscopy (AFM)	65
D.2	X-ray Diffraction (XRD)	65
D.3	X-ray Reflectivity (XRR)	66
E	Raman spectroscopy	66
E.1	Technique description	66
E.2	Principal Component Analysis (PCA)	67
III	Surface domain ordering in CaTiO_3 (001)	71
A	CaTiO_3 strain states	71
A.1	Spontaneous strain tensor	71
A.2	Domain wall orientation	73
B	Surface topography quantification of CaTiO_3 (001) ferroelastic twin angles	74
B.1	CaTiO_3 surface topography	74
B.2	Experiment conditions	75
B.3	Angular sensitivity of the contrast aperture	76
B.4	Photoemission threshold shift	77
B.5	PEEM surface tilt angle	79
B.5.1	Model	80
B.5.2	Tilt angle map	81
B.5.3	Twin angles	84
B.6	Twin angles of another CTO ferroelastic ordering	85
B.7	Conclusion	86
C	Ferroelastic domains spontaneous strain observation and quantification by X-ray Linear Dichroism	88
C.1	Polarization in X-ray Linear dichroism	88
C.2	XLD contrast in ferroelastic CaTiO_3	89
C.2.1	Experimental conditions	90
C.2.2	MEM imaging	90
C.2.3	XAS of the analyzed area	91
C.2.4	XAS in another area	94
C.3	Absorption spectra calculation	94
C.4	Domain identification	96
C.5	Conclusion	97

IV	Surface band gap narrowing in CaTiO_3 domain walls	99
A	Experimental conditions	99
B	Domain wall polarity	101
C	Band gap estimation by EELS	102
D	Band gap narrowing at the domain walls	105
E	Tunable domain wall surface band gap	108
F	Conclusion	110
V	Surface domain wall creep in BaTiO_3	111
A	Domain-wall dynamics and avalanches	111
B	Experimental conditions	112
C	Averaged image analysis	113
D	Pixel-by-pixel image analysis	115
E	Drift correction and noise	118
F	Discussion and conclusion	121
VI	Conclusion and perspectives	123
A	Conclusion	123
B	Perspectives	125
	Appendices	127
A	Domain wall orientation table	127
B	Simulated XAS spectra	129
C	PEEM shear stress sample holder for creep experiments	130
C.1	Shear stress sample holder	130
C.2	BaTiO_3 domain wall shear stress test	132
D	Domain walls engineering in CaTiO_3 epitaxial thin films	134
D.1	Epitaxial strain in CaTiO_3 thin films	134
D.1.1	Substrate choice	134
D.1.2	CaTiO_3 thin film epitaxial deposition	134
D.2	Domain walls topography in CaTiO_3 thin films	137
D.3	Domain walls polarity in CaTiO_3 thin films	138
D.4	Vibrational states of $\text{LaAlO}_3/\text{LaSrMnO}_3/\text{CaTiO}_3$	139
VII	French summary	159

Introduction

In ferroic materials, domains of uniform order parameters, whether magnetization, electrical polarization, or mechanical strain, form to minimize the free energy of the material. Domain walls are transition regions between domains. Their formation is a trade-off between the energy cost of the wall and the gain associated with domain formation. Domain wall structure, symmetry, and even chemistry can differ from adjacent parent domains, potentially giving rise to unique physical properties. In the case of ferroelectric and ferroelastic materials, they minimize the electrostatic and mechanical free energy, respectively [1].

Furthermore, walls are intrinsically nano-sized 2D objects with a thickness of only a few unit cells [2]. As such, they have the potential to become a new paradigm for nanoelectronics where the wall is the active element of the device. This concept of “the material is the machine” [3] offers perspectives in terms of information density, (multi-)functionality, and low power consumption.

Domain walls are interfaces that can influence material properties. For example, up to 40% (33%) of the piezoelectric coefficient d_{33} in $BaTiO_3$ ($PbZrTiO_3$) is reported to originate from the domain wall motion. Understanding and engineering the ferroelectric domain structure may enhance the material properties. Moreover, domain walls may also have distinct properties, including conductivity [4], superconductivity [5], and polarity [6]. The research topic into these properties is labeled “domain boundary engineering” [7] or “domain walls nanoelectronics” [8]. Such domain walls are expected to carry information given their functional properties and could act as memory devices with potentially high density (low wall thickness) [9].

We extensively studied the ferroelastic ordering in $CaTiO_3$, a simple ferroelastic perovskite that exhibits polar domain walls. At the twin walls, one of the octahedral tilts goes to zero allowing the emergence of polarity by off-centering of the Ti cation. The polarity could be augmented and controlled electromechanically, adding functionality to the system. For example, the polar character could be used for memory devices [10]. The thesis aims to study the functional properties of ferroelastic domain walls at the surface.

The first step is to characterize the ferroelastic ordering, i.e., the surface strains in the domains and the polarity at the walls, with high spatial resolution techniques. Observations are performed with a sub-micrometric lateral resolution by photoemission electron microscopy (PEEM) and low-energy electron microscopy (LEEM). These techniques analyze the surface interface, which can have different properties from the bulk. It provides valuable information for technological applications where the interaction with the material is at the surface.

The manuscript is organized as follows: In **Chapter I**, the physics behind ferroelectric and ferroelastic domain and domain walls are presented, along with

the studied materials $CaTiO_3$ and $BaTiO_3$. A focus is made on the engineering of functional properties in domain walls. The experimental methods used for domain wall observation are presented in **Chapter II**. In **Chapter III**, we investigate the $CaTiO_3$ ferroelastic surface ordering with photoemission microscopy. We first describe the ferroelastic strain tensor and the possible strain orientations in the domain walls from the symmetry breaking, then quantify the twin angles *in-situ* by photoemission electron microscopy (PEEM). We also observe the surface strain by x-ray absorption spectroscopy (XAS) in PEEM. We can describe the strain ordering at the surface from the twin angle determination and strain observation. In **Chapter IV**, we analyze the surface potential modulation and band gap narrowing of domain walls at the $CaTiO_3$ (001) surface. The surface potential contrast shows the presence of both outwards (P_{up}) and inwards (P_{down}) pointing polarity. Electron energy loss spectroscopy (EELS) on selected twin walls measures the band gap. In **Chapter V**, the creep movement of $BaTiO_3$ ferroelastic domain walls is studied under residual strain. The movement is composed of jerks forming avalanches and is scale independent, determined by an analysis of the jerk energy power law distribution.

I - Ferroelectric and ferroelastic domain and domain wall

Ferroelectric and ferroelastic materials are characterized by an order parameter, which is electric polarization for ferroelectrics and mechanical strain for ferroelastics, that can point in two or more symmetry-related directions and are switchable by the application of an external field [8]. The order parameter appears at the phase transition. In the ordered phase, ferroics spontaneously organize in domains of homogeneous order parameter directions separated by domain walls. The latter can have significantly different properties from the domains. Ferroelectric domain walls are being actively explored to develop agile, low-energy electronics for applications in memory, logic, and brain-inspired neuromorphic computing [11]. The perspective of the thesis is to investigate the possibility of electromechanical control of ferroic domain walls, more specifically ferroelectric and ferroelastic domain walls, through first a study of the ferroelastic domain walls at the surface. In the thesis framework, we focused our study on CaTiO_3 and BaTiO_3 perovskites which show interesting ferroelectric/ferroelastic domain and domain wall properties. This chapter will introduce perovskites and ferroelectric and ferroelastic properties, the specific studied materials in the thesis, and domain wall functional properties engineering.

A . Ferroelectric and ferroelastic properties

A.1 . Perovskites

Perovskite materials have an ABO_3 chemical formula. Initially, the structure owes its name to Gustave Rose, who discovered calcium titanate CaTiO_3 in 1839 and named it after the Russian nobleman and mineralogist Count Lev Alekseyevich von Perovski [12]. It started to be used as a general term for the crystal structure in 1926 by Victor Goldschmidt. Figure I.1a represents the perovskite cubic cell structure. The A anions sit at the cube corners, B cations at the cube center, and O at the face-centered positions form an octahedron. Perovskite oxides exhibit many interesting ferroic properties such as ferroelectricity, for example, in BaTiO_3 , PbTiO_3 , ferroelasticity in CaTiO_3 , LaAlO_3 or even multiferroicity with at least two ferroic orders co-existing in the same phase BiFeO_3 , EuTiO_3 . We focused our thesis on ferroelectric and ferroelastic BaTiO_3 and ferroelastic CaTiO_3 .

In ferroelectric perovskite materials, the B or A atoms and the O atoms are displaced along the polar axis, as represented in the case of a B cation displacement along the long axis on figure I.1b. The off-centering of the A or B atoms with respect to the oxygen octahedron induces polarization. In ferroelastics, the ferroic transition induces a unit-cell volume change. The spontaneous strain can be

because of a cooperative rotation of the oxygen octahedra (in the case of CaTiO_3) or a lattice direction reorganization (in the case of BaTiO_3). A distorted cell with a rotated oxygen octahedron is represented in figure I.1c [13].

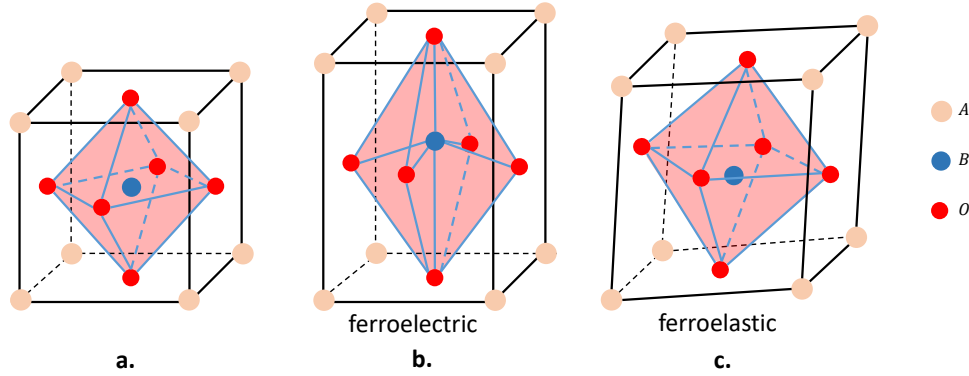


Figure I.1: a. Centrosymmetric perovskite structure ABO_3 . b. Off-centering of the B atom with respect to the oxygen octahedron. c. Rotation of the oxygen octahedron

The perovskite structure stability can be evaluated by the Goldschmidt factor t , expressed with the radius of the A , B , and O atoms respectively defined as r_A , r_B , and r_O :

$$t = \frac{r_A + r_O}{\sqrt{2}(r_B + r_O)} \quad (1)$$

The perovskite structure is energetically favorable when $t \approx 1$. In the case of CaTiO_3 , A is small ($t < 1$), so rotation and tilting of the oxygen octahedra will be favored to minimize the total energy at the origin of its ferroelastic properties. On the other hand, for BaTiO_3 , the B atom is small ($t > 1$), and the structure will develop a ferroelectric distortion [12].

The ferroelectric properties and domain ordering are first presented in the following subsection A.2, followed by the ferroelastic domain ordering in subsection A.3.

A.2 . Ferroelectricity

Hysteretic behavior of the electric polarization under an electric field was first observed on Rochelle salt ($\text{C}_4\text{H}_4\text{KNaO}_6 \cdot 4\text{H}_2\text{O}$) in 1920 by J. Valasek [14], represented on figure I.2. This class of materials is called ferroelectrics, by analogy with ferromagnetism, where such hysteretic behavior of the permanent magnetic moment is observed with an application of a sufficiently strong magnetic field. For ferroelectrics, the order parameter is spontaneous electrical polarization, which can be switched by an electric field.

A.2.1 . Ferroelectric phase transition

The ferroelectric phase transition is distortive, meaning that the chemical bonds are kept but are distorted, and some cations/anions are displaced. The crystal

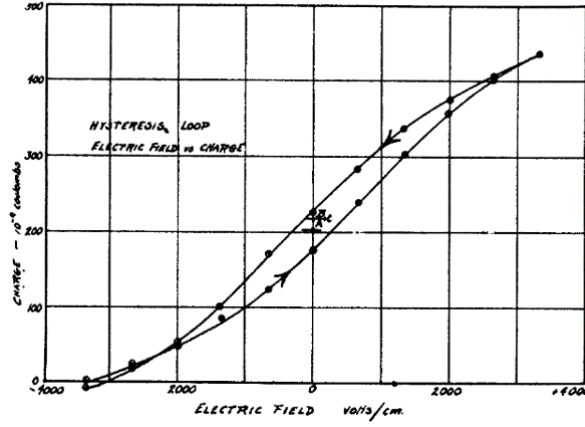


Figure 1.2: First electric hysteresis loop measured on Rochelle salt by J. Valasek [14]

symmetry changes from a higher to a lower phase symmetry. A phase transition is ferroelectric when a non-centrosymmetric lower symmetry phase exists with a spontaneous polarization P_S whose direction can be reoriented by an applied electric field.

Experimentally, there is no direct electrical measurement of the polarization vector itself. A more rigorous definition of the ferroelectric phase transition is based on a change of polarization with respect to another physical variable rather than with the polarization itself [1]. One definition is based on the pyroelectric effect. The pyroelectric coefficient vector \vec{p} is defined as:

$$p_i = \left(\frac{\partial P_i}{\partial T} \right) \quad (2)$$

with \vec{P} the electric polarization and T the temperature. The pyroelectric coefficient is non-zero only in polar crystals. Then we can define a ferroelectric phase transition: a phase transition is called ferroelectric if it results in a lower symmetry phase in which the vector of pyroelectric coefficients acquires new components which were zero, by symmetry, in the high-symmetry phase [1]. The electric polarization is the order parameter of a ferroelectric material.

A.2.2 . Order parameter: spontaneous polarization

Definition

We can first write the electric dipole moment \vec{p} between two charges $\pm q$ separated by a distance vector \vec{d} :

$$\vec{p} = q \vec{d} \quad (3)$$

The polarization \vec{P} can be expressed as the sum of the dipole moments per unit of volume V :

$$\vec{P} = \sum_i \frac{d\vec{p}_i}{dV_i} \quad (4)$$

In any insulating material, when an electric field is applied, the material will be polarized from the displacement of the bound charges. We can write the dielectric polarization response P_d as:

$$\vec{P}_d(\vec{E}) = \epsilon_0 \chi \vec{E} \quad (5)$$

with ϵ_0 the vacuum permittivity and χ the electric susceptibility. In a ferroelectric, a spontaneous polarization P_s exists in the material from the material symmetry breaking at the phase transition, even without an applied electric field. This polarization is switchable with an electric field.

As a first approximation, polarization is defined as the integrated contribution of individual local permanent dipoles. However, in finite crystalline solids, the charge distribution is periodic, and the polarization cannot be unambiguously partitioned into localized contributions. Then the dipole moment cannot be unambiguously introduced as a bulk property of the system [15, 16]. From this observation, Resta [17], King-Smith and Vanderbilt [18] built a theory to address polarization on the microscopic scale by calculating the polarization difference with the time-integrated adiabatic current when a crystal structure is modified (for example, an atomic displacement).

The polarization difference is between two states of the crystal in an adiabatic process (no heat transfer). A parameter λ is introduced as a dimensionless adiabatic time from zero (initial system, centrosymmetric) to one (final system: non-centrosymmetric ferroelectric structure). The spontaneous polarization P_s can then be written [19]:

$$\Delta \vec{P} = \int_0^1 d\lambda \frac{d\vec{P}}{d\lambda} \quad (6)$$

with $\frac{d\vec{P}}{d\lambda}$ is the transient current vector carried by electrons and nuclei. For this definition in the theory, the quantum nature of electrons needs to be considered, whereas the nuclei can be considered classical point charges. Within a quantum-mechanical description, the current is related to the phase of the electron Bloch wave function [19, 20].

As a corollary, we can also express the dynamical charge of an atom as the rate of change in the polarization with respect to atomic displacement. However, static charges cannot rigorously define polarization in a crystalline material because the covalent character of bonding orbitals prevents the unambiguous attribution of electronic charge to an atom. Then, it would be more relevant to consider a dynamic charge. Z^* is a measure, in a linear approximation, of the polarization change in the α direction in a unit cell, induced by a sublattice displacement u_s of atoms in the β direction [19]:

$$Z_{s,\alpha\beta}^* = \frac{\Omega}{e} \frac{\partial P_\alpha}{\partial u_{s,\beta}} \quad (7)$$

with P_α the polarization in the α direction by atomic displacement $u_{s,\beta}$ in the β direction, at zero electric field and Ω the unit cell volume. In $BaTiO_3$, dynamical charges are +7.25 for Ti^{4+} , +2.77 for Ba^{2+} and -2.15 or -5.71 for O^{2-} depending of its chemical environment in the lattice [21], higher than the static charge in an ionic approximation. This dynamical charge gives insight into the absolute ionic contributions to spontaneous polarization.

Ferroelectric hysteresis

Under an applied electric field, randomly oriented ferroelectric domains reorient their polarization as close as possible to the electric field in directions the crystal symmetry structure allows. The hysteresis gives information about the positive and negative remnant polarization P_R , i.e., the polarization at zero electric fields, the saturation polarization P_S , and the coercive field E_C , the field to switch the polarization. The polarization reversal with an electric field describes a hysteresis loop and is the signature of a ferroelectric material. An example is shown in figure I.3b [22].

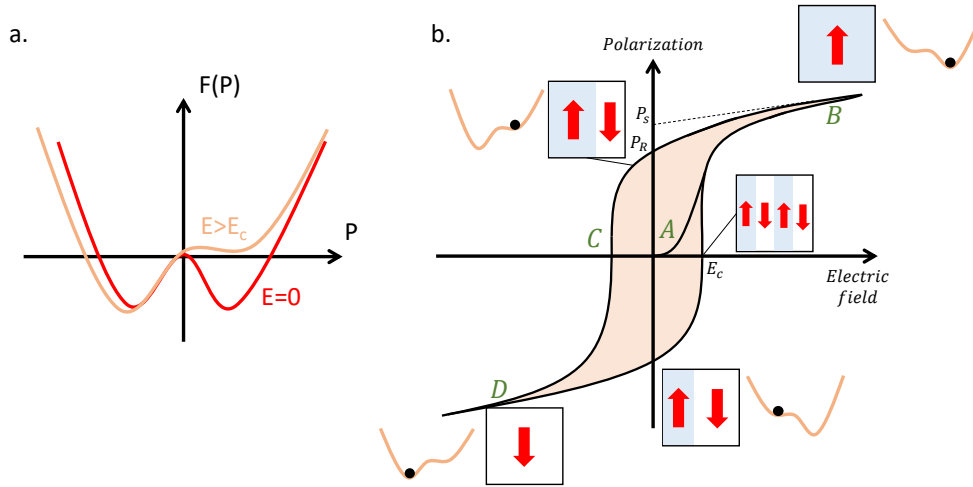


Figure I.3: a. Free energy F as a function of the polarization P for a system with two minima. b. Ferroelectric hysteresis loop. Blue and white regions are ferroelectric domains with two polarization directions. Adapted from [22]

We can thermodynamically define a ferroelectric by a double potential well of the system free energy from the Landau-Devonshire theory [23], as shown in figure I.3a. The two minima of the free energy correspond to different orientations of the spontaneous polarization. After the ferroelectric transition, naturally formed domains have their polarization oriented randomly with an average macroscopic polarization equal to zero (at point A in figure I.3b). When we apply an electric field higher than E_C along one of the polar axes, the polarization will be switched

from one ground state to the other (at points B and D). It corresponds to the maximum polarization P_S and could correspond to a monodomain state except if there is strong domain pinning. When a maximum number of domains are aligned, the ferroelectric has a saturated dielectric behavior with an increasing electric field. When the field is decreased, domains start to back-switch to the other polarization ground state.

Typical coercive field values are between 0.1-10 MV/m; in most materials, remnant polarization values are between 0.001 to 1 C/m² [24]. For $BaTiO_3$ single crystals, a typical coercive field is ≈ 1 kV/cm at room temperature [25].

A.2.3 . Ferroelectric domain

Domain formation and size at a fixed temperature depend on the material boundary conditions and defects. In thin films, the polar discontinuity at the surface from the polarization gives rise to a surface charge density. This charge induces an electric field, called depolarizing field E_d , of the opposite sign to the polarization field, represented in figure I.4:

$$E_d = -\frac{\vec{P}_s \cdot \vec{n}}{\epsilon_0 \epsilon_r} \quad (8)$$

with \vec{n} the surface normal, ϵ_0 the vacuum dielectric permittivity and ϵ_r the material dielectric constant (permittivity). For a typical ferroelectric, $P = 10 \mu C/cm^2$ and $\epsilon_r = 100 - 1000$, we have $E_d = 10 - 100$ kV/cm, well above typical ferroelectric coercive fields. It means that the polarization would be destabilized by the depolarizing field [8]. Then, the depolarizing field or the surface charges need to be screened to maintain the ferroelectric polarization.

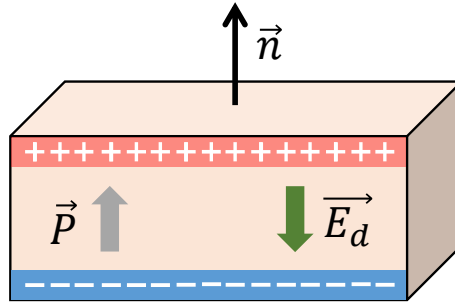
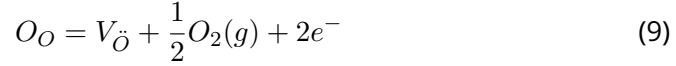


Figure I.4: Schematic of the depolarizing field E_d induced by unscreened polarization charges.

Screening mechanisms

The screening can be extrinsic, by the surface adsorption of molecules such as water or carbon [26], which will partially or entirely screen surface charges [27] or by charges from electrodes [28]. Moreover, it can also be intrinsic, with a charge compensation from free charges migrating to the surface by material defects

such as vacancies and dopants. For example, in perovskite oxides, annealing under vacuum above $\approx 300^\circ\text{C}$ will generate free charges following the formation of oxygen vacancy 9: two free electrons e^- and one double positively charged oxygen vacancy $V_{\ddot{O}}$ [29]. Neutral and +1 charged oxygen vacancies are also possible but have a lower probability of formation. The primary source of oxygen vacancies is double ionized oxygen vacancies in perovskites [30].



The third screening mechanism is domain organization, where domains rearrange themselves to minimize the system's energy. For tetragonal ferroelectric perovskites such as $BaTiO_3$, 1.5 shows two possible domain configurations at room temperature in its tetragonal phase. Figure 1.5a is stripe domains with an alternating antiparallel polarization, usually called 180° domains because the angle between the adjacent polarizations is 180° . The stray field from one domain screens the depolarizing field in the adjacent domain and so on, making it a very stable domain configuration. 180° domain walls are not necessarily or even usually straight, but 90° walls are straight. It will be discussed with the electrical and mechanical compatibility equations between domains.

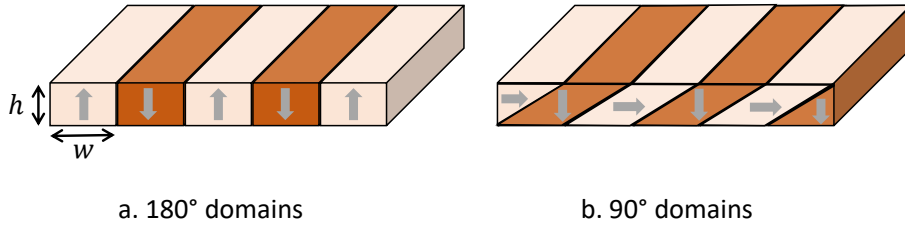


Figure 1.5: Schematic of ferroelectric domain configurations. a. 180° domains with out-of-plane polarity and b. 90° domains with polarization orthogonal to each other.

Another possible domain configuration is 90° domains with polarizations orthogonal to each other, which minimize strain via the formation of twin walls (ferroelastic and ferroelectric domain walls). Twin walls are discussed in the ferroelastics section. Another ferroelastic domain geometries which leads to a macroscopic neutral charge are closure domains (Landau-Lifshitz domains).

Domain size

A model to express the domain size was proposed by Kittel in 1946 [31, 32]: domain size can be determined by the competition between the energy of the domains, proportional to the domain size w and the energy of the domain walls. With U the volume energy density of the domain, the energy density of the domain can be written as $E = Uw$. The energy cost of domain walls increases linearly with the number of domain walls, so the number of domain walls is inversely proportional to the domain size, i.e., $n = \frac{1}{w}$. The energy of each domain wall is proportional to its area. For n the number of domain walls and σ the energy density per unit

area, the energy density of the domain wall is $E = \frac{\sigma h}{w}$. When the cost of forming the walls is equal to the bulk energy of domains, we obtain 10:

$$w = \sqrt{\frac{\sigma}{U}} h \quad (10)$$

Kittel's law was first derived from ferromagnetic systems but it applies also to ferroelectrics and ferroelastics in thick crystals [33] to thin films [8]. The universality of the Kittel law is the square root dependence of the domain width on the material thickness.

A.2.4 . Ferroelectric domain walls

The order parameter changes at the domain wall to match the following domain's orientation. The order parameter switch at the domain wall can be of different types, represented in figure 1.6. When the polarization changes its magnitude and orientation across the wall in the same plane, the domain wall is called Ising wall. Alternatively, the magnitude of the spontaneous polarization can rigidly rotate within the domain wall plane (Néel wall) or perpendicularity to the plane (Bloch wall).

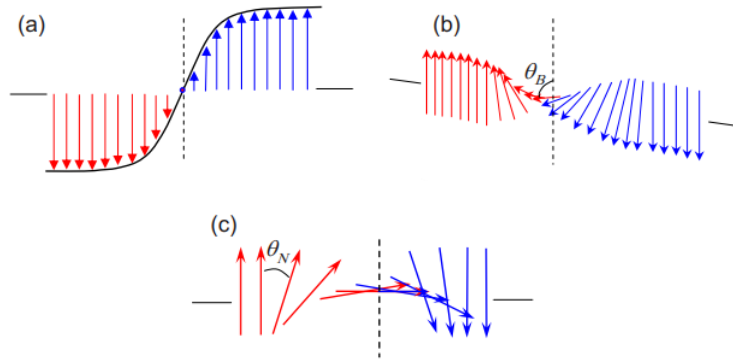


Figure 1.6: Different types of domain walls: a. Ising type, b. Bloch type and c. Néel type with arrows representing the polarization, θ_N , and θ_B the maximum angle of polarization rotation in the plane. From [34]

For 180° ferroelectric domain walls, rotating the polarization in another plane than the symmetry-allowed direction would be energetically costly because of the coupling between polarization and strain. Moreover, it would also induce a high electrostatic cost as a polarization change perpendicular to the wall will generate an accumulation of charges at the wall. The charge density at the wall ρ_b can be written as 11 [1]:

$$\rho_b = -\text{div}(\vec{P}) \quad (11)$$

Then a domain wall between P_{up} and P_{down} domain polarizations is considered an Ising wall. Other types of domain walls (Néel, Bloch, or mixed Ising/Néel

or Bloch types) are also observed [34, 35]. The elastic component in the wall in multiferroic materials (ferroelectric and ferroelastic) can also induce a mixed Ising/Néel, or Bloch types of domain wall [36].

From equation 11, we can also deduce the electrical compatibility of ferroelectric domain walls, which gives their orientation. The energetically preferable orientation of the wall corresponds to its electrically neutral state (especially if there are few free carriers to compensate for the charges at the wall). Then we want $\rho = 0$ for a wall with a normal vector \vec{n} separating two domains with polarizations \vec{P}_1 in the first and \vec{P}_2 in the second domain, giving the condition 12:

$$(\vec{P}_1 - \vec{P}_2) \cdot \vec{n} = 0 \quad (12)$$

This electrical neutrality condition plays a significant role in ferroelectric domain wall orientation. An ideal 180° domain wall is charge neutral, but other configurations can be stabilized in a material. For example, a tail-to-tail polarization configuration would give a maximum negative fixed charge at the domain wall [1] and a head-to-head polarization a net positive fixed charge. Charged domain walls can be stabilized in $BaTiO_3$ single crystals with a (110) surface.

Domain wall thickness

Experimentally, most studies measure domain wall thickness by Transmission Electron Microscopy (TEM) [37]. Piezoelectric Force Microscopy (PFM) or optical methods can also be used. However, it tends to overestimate the domain wall width due to their limited resolution compared to domain walls of a few nanometers [38]. From phenomenological Landau-Ginzburg theory, the profile of the polarization across a domain wall can be expressed as [39]:

$$P(x) = P_0 \cdot \tanh\left(\frac{x}{\delta}\right) \quad (13)$$

with P the polarisation order parameter, P_0 the polarization far from the wall, x the spatial coordinate perpendicular to the wall, and δ the domain wall thickness. Generally, this profile is used to calculate the wall thickness from experimental measurements. For ferroelectric non-ferroelastic domain walls, the thickness of 180° stripes domain wall is of the order of one unit-cell [37], i.e., $\approx 1\text{-}4$ nm.

This tanh relation is also used for the mechanical strain evolution across a wall, the ferroelastic order parameter.

A.3 . Ferroelasticity

Ferroelasticity plays a major role in the mineralogical behavior of the earth's crust and mantle, and it is the most common nonlinear effect in natural materials [40]. They are characterized by an elastic hysteresis behavior under mechanical stress related to the switching between at least two possible strain orientation states of the crystal. An hysteresis example from ferroelastic $Pb_3(PO_4)_2$ is shown on figure 1.7. The macroscopic hysteresis is related to the switching of atomic positions. In this case, the Pb-O chemical bonds are not equivalent. The Pb atom

shifts towards one of the three pairs of oxygen in the ferroic phase. This anisotropy shears the lattice, and the different orientations of the short bonds correspond to the different strain orientations, which can be switched by external mechanical stress.

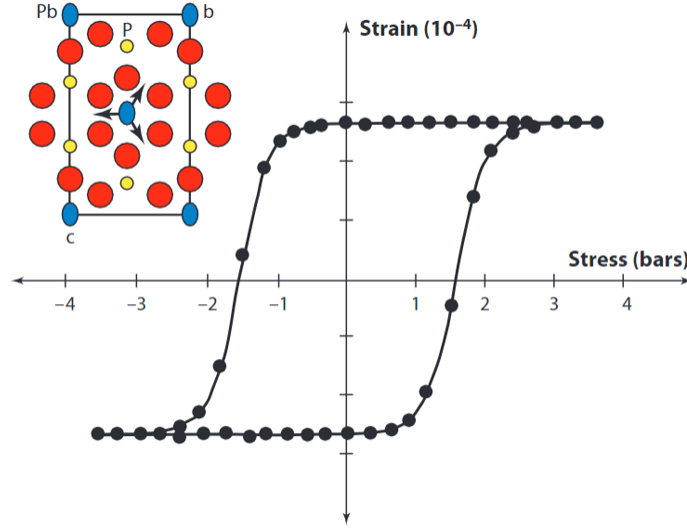


Figure I.7: Ferroelastic hysteresis in $Pb_3(PO_4)_2$ [40, 41].

A.3.1 . Ferroelastic phase transition

If the temperature of a crystal is changed, the resulting deformation may be specified by the strain tensor $\bar{\epsilon}$. When a small temperature change ΔT takes place uniformly throughout the crystal, the deformation is homogeneous, and it is found that all the components of the thermal expansion tensor $\bar{\alpha}$ are proportional to ΔT ; thus [42]:

$$\epsilon_{ij} = \alpha_{ij} \Delta T \quad (14)$$

where α_{ij} are coefficients of thermal expansion. Since $\bar{\epsilon}$ is a tensor, so also is the thermal expansion tensor $\bar{\alpha}$, and, moreover, since $\bar{\epsilon}$ is symmetrical so also is $\bar{\alpha}$ [42]. A transition is called ferroelastic if it results in a low-symmetry phase in which the thermal expansion tensor changes the number of its independent components with respect to those in the high-symmetry phase [1].

A.3.2 . Order parameter: spontaneous strain

At a ferroelastic phase transition, the shape and size of the unit cell change. We can express this unit cell change as a spontaneous strain, which is the ferroelastic order parameter [43]. From the thermal dilatation tensor components α_{ij} , we can express the spontaneous strain components ϵ_{ij} for a given temperature T_f in the ferroelastic phase:

$$\epsilon_{ij}(T_f) = \int_{T_p}^{T_f} (\alpha_{ij}(T) - \alpha_{ij}(T_p)) dT \quad (15)$$

with T_p a temperature in the parent (non-ferroelastic) phase. The diagonal spontaneous strain coefficients are an expansion (if $\alpha_{ii} > 0$) or a contraction in the three lattice directions. Off-diagonal terms are shear stress between two lattice directions. A simple representation of two possible spontaneous strains between a parent cubic phase and an orthorhombic ferroelastic phase is represented in figure I.8.

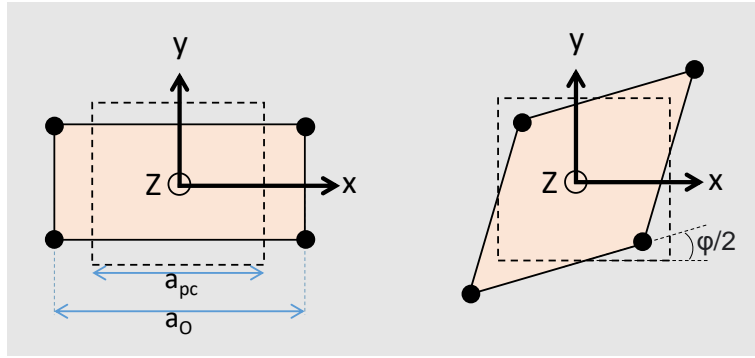


Figure I.8: Two possible transitions between a cubic and an orthorhombic ferroelastic phase for a. a diagonal spontaneous strain term ϵ_{11} and b. an off-diagonal term ϵ_{12} . (x,y,z) are respectively along the cubic phase directions [001], [010], and [001].

A.3.3 . Ferroelastic domain

At a ferroelastic transition, domains form to lower the free energy of the material. From the phase symmetry, two or more strain orientations can coexist with the same probability, often called spontaneous strain states. A simple example of a domain configuration, with two equivalent orientations of the spontaneous strain, is given in figure I.9.

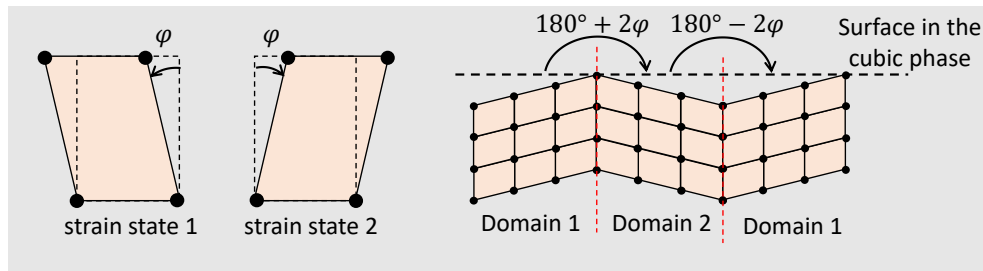


Figure I.9: Simple illustration of ferroelastic strain states and one possible domain configuration and the twin angle between domains.

The spontaneous strain tensor is a second-rank tensor that does not break inversion symmetry. Thus ferroelastic materials can't have 180° domains. Typical

ferroelastic domains, also called twins, minimize the elastic energy cost of the wall. The plane separating the domains is the twin wall. From symmetry considerations, the number of possible spontaneous strain orientations and the symmetry relationship between them can be precisely formulated, knowing the symmetries of the parent and ferroelastic structures [1].

Twin angle

The spontaneous deformation in domains will induce a surface topography. Figure 1.9 shows the deformation of domains around a ferroelastic domain wall. In order to keep the domains in physical contact, each of them has to be rotated by an angle φ , defined in figure 1.8 and related to the spontaneous deformation in the domains. This angle varies between materials depending on the "degree of ferroelasticity" up to a few degrees (for example 3.5° in $PbTiO_3$) [1]. The twin angle is then $180^\circ \pm 2\varphi$.

A.3.4 . Ferroelastic domain wall

Experimentally, most studies measure the ferroelastic domain wall thickness by Transmission Electron Microscopy (TEM) or X-Ray Diffraction (XRD). As for ferroelastic walls, the profile of the strain across a domain wall can be expressed as [40]:

$$Q(x) = Q_0 \cdot \tanh\left(\frac{x}{\delta}\right) \quad (16)$$

with Q the strain order parameter, Q_0 the strain far from the wall, x the spatial coordinate perpendicular to the wall, and δ the domain wall thickness. Generally, this profile is used to calculate the wall thickness from experimental measurements. The order parameter profile has been verified experimentally by TEM and XRD on several materials [44, 45, 46, 47]. Domain wall thickness for ferroelastics is in the range of 2 to 10 unit cells [45].

Domain wall orientation

Twin walls have a specific orientation in the material to minimize the wall energy cost, given by the mechanical compatibility relation 17 between two adjacent domains S_1 and S_2 [48, 49]. Domain walls following the equation 17 are stress-free walls, adding no additional elastic strain to the system. Moreover, this equation defines a plane so the domain wall trace at the material surface is always a straight line.

$$(\epsilon_{ij}(S_1) - \epsilon_{ij}(S_2)) \cdot x_i x_j = 0 \quad (17)$$

with $\epsilon_{ij}(S_1) - \epsilon_{ij}(S_2)$ a symmetric strain tensor and x_i, x_j the components of a vector in the wall. The equation can be solved from possible strain tensors to give the permissible domain wall planes for all ferroelastic transitions. Then we can distinguish two types of twin walls called W and W' planes. W planes are crystallographically prominent planes of fixed indices (mirror planes) and W' planes are determined by the relative magnitude of the components of the second-rank

tensor representing the spontaneous strain. For the latter, the plane orientation can change with temperature [48].

Polarity at the domain wall

The Landau theory of the strain hyperbolic tangent profile across the domain walls, as shown in figure I.10a, is usually sufficient to understand experimental observations. Domain walls in ferroelastics have a gradient of one component of the spontaneous strain tensor I.10b. A second-order parameter, polarization, in a centrosymmetric material, can emerge at the center of the domain wall, where the primary order parameter goes to zero, as shown in figure I.10c. This domain wall state is bistable so that the wall can split spontaneously into two possible variants of upward and downward polarization [50, 36].

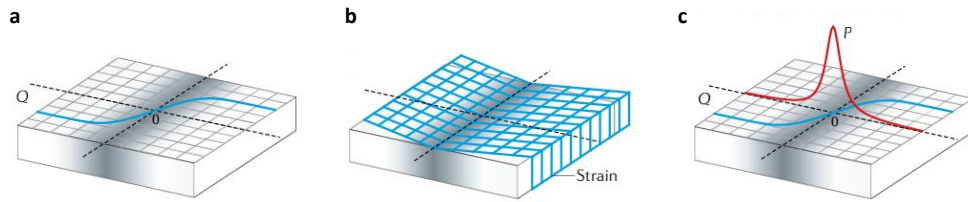


Figure I.10: Mechanisms leading to polar domain walls. a. Schematic of an elementary domain wall with strain order parameter Q , and tanh profile. b. Ferroelastic wall, with a discontinuity (or gradient) in spontaneous strain. c. Phase transition in a domain wall, with the emergence of an additional instability, a polarization component P . From [51].

Two mechanisms can explain polarization in a wall. First, the strain gradient over the wall width of a few unit cells can induce polarization by flexoelectric effect [52]. The strain breaks inversion symmetry, so the polarization vector has a specific direction. All strain-compatible domain walls are polar through a flexoelectric effect [53]. In CaTiO_3 (and SrTiO_3), the octahedral distortions block the tendency of the material to off-center its cations/anions. However, at the wall, one of the octahedra rotations goes to zero, allowing off-centering and so polarity [54]. Materials with this repulsive coupling between polarization and antiferrodistortive tilts of the oxygen octahedral network can induce polarization at the wall interface [55].

For the rotation of the oxygen octahedra in perovskite structures [56] inducing a polar domain wall by off-centering the Ti cation in the wall, Goncalves-Ferreira et al. [57] explored the idea that all TiO_6 -based perovskite structures tend to possess polar walls even when the bulk of the material is non-polar. Furthermore, it was experimentally observed for SrTiO_3 [58] and for CaTiO_3 , which will be presented in the next section.

We still need to study polarity at the domain wall with regard to the potential use of ferroelectric wall polarization as a functional element. Therefore, this thesis

is oriented toward studying the ferroelectric domain walls at the surface, particularly in CaTiO_3 .

B . CaTiO_3 and BaTiO_3

B.1 . Calcium titanate CaTiO_3

B.1.1 . Structure

Calcium titanate (CTO) has a phase transition from cubic (space group $Pm\bar{3}m$) to tetragonal ($I4/mcm$) at $T_{C1} = 1523K$ and then another transition to an orthorhombic ($Pnma$) structure at $T_{C2} = 1373K - 1423K$ [59]. The $Pm\bar{3}m$ to $Pnma$ transition induces a change of crystal family so the transition is ferroelastic [1] but the space group $Pnma$ is centrosymmetric so CTO is not polar in its orthorhombic phase. Ferroelastic domains are formed in the orthorhombic phase, observable on a monocrystal by the eye or under an optical microscope, as shown in image I.11 thanks to birefringence.



Figure I.11: Optical microscope image of a CTO single crystal. Parallel domains are visible by birefringence.

In the ferroelastic phase, the oxygen octahedral tilts along the three directions of the unit cell are defined by $a^-a^-c^+$ in Glazer's notation [60]. It means successive out-of-phase octahedra tilts in the $[100]$ and $[010]$ directions and successive in-phase tilts in the $[001]$ direction. At room temperature, the orthorhombic lattice parameters are $a = 5.38 \text{ \AA}$, $b = 5.44 \text{ \AA}$, $c = 7.64 \text{ \AA}$ [61]. The orthorhombic and pseudo-cubic lattice is represented in figure I.12. The pseudo-cubic lattice parameter is $a_{pc} \approx \frac{a_{or}}{\sqrt{2}} \approx \frac{b_{or}}{\sqrt{2}} \approx \frac{a_{or}}{2} = 3.82 \text{ \AA}$.

Two ferroelastic domains are represented in figure I.13, separated by a W-type domain wall in the $[\bar{1}\bar{1}0]_{pc}$ direction. The first order parameter is the spontaneous strain given by the octahedra tilts, represented in red on the graph on I.13, and at the domain wall, the tilt in one of the directions goes to zero. This relaxation allows

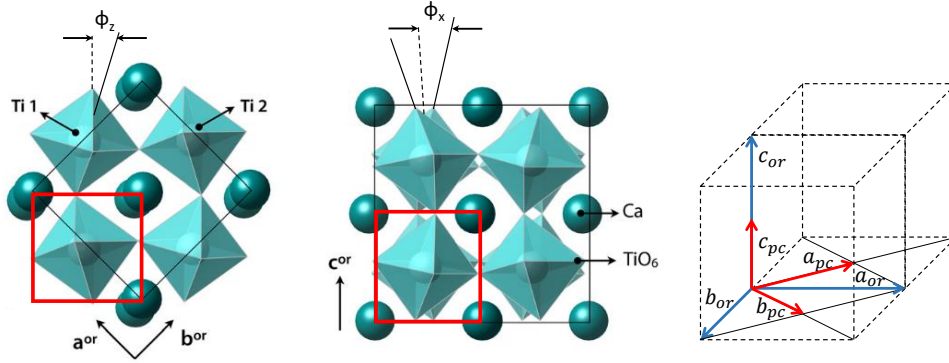


Figure I.12: Schematic views of bulk CaTiO_3 unit cell and the tilt angles along the $[100]$ and $[001]$ directions: Φ_x is the tilt angle along $[100]$ and Φ_z along $[001]$. Black rectangles show the orthorhombic unit cell and red squares the pseudo-cubic unit cell. Adapted from [62].

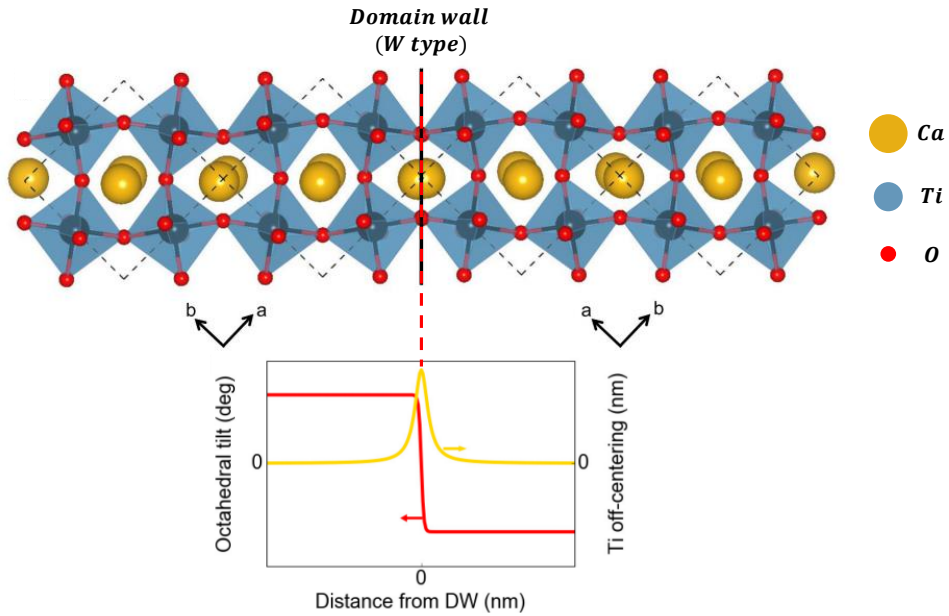


Figure I.13: Ferroelastic domain structure of CTO. a. Stick-and-ball model of two ferroelastic domains and a W-type domain wall (mirror $[1\bar{1}0]_{pc}$ plane). The octahedral tilt (red) and Ti off-centering (yellow) as a function of the distance from the DW are plotted below, illustrating schematically the emergence of cation displacement at a domain wall. Adapted from [63].

the Ti cation to off-center along the domain wall plane, giving rise to polarity as a second-order parameter in the wall [63].

B.1.2 . Polar domain walls

Polar domain walls in CTO are predicted from atomic-scale numerical simulations with empirically defined forces between atoms. Goncalves-Ferreira et al. [57]

simulated two consecutive ferroelastic domain walls. The hyperbolic tangent profile of the octahedra rotation in one of the directions, on figure I.14a was observed, with the dashed lines corresponding to the domain wall positions. In the other two directions, the rotation shows slight anomalies [60]. A domain wall thickness of 10.9 Å was extracted from this hyperbolic tangent. The Ti off-centering component from the center of charge of the corresponding oxygen octahedron, as shown in figure I.14b is within the wall and corresponds to a net displacement of 0.6 pm per Ti atom [57].

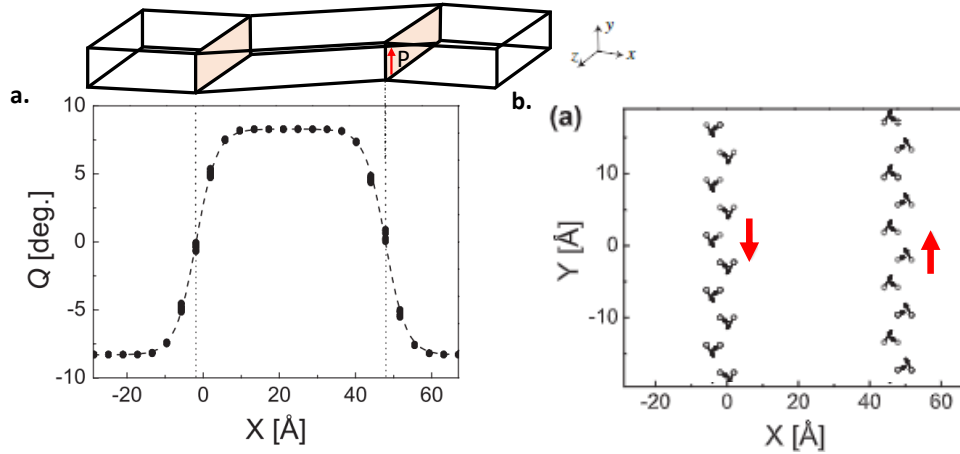


Figure I.14: a. Octahedra rotation as a function of the position perpendicular to the domain wall. The vertical dashed lines are the domain walls positions and the curved dashed line is the expected hyperbolic tangent fit. b. Ti displacement as projected onto the xy plane. The arrows indicate the Ti displacement from the center of the corresponding O octahedron. The red arrows indicate the direction of the net polarization. From [57].

Theoretical calculations of the Born effective charge of CaTiO_3 atoms report $Z_{\text{Ca}}^* = 2.58$, $Z_{\text{Ti}}^* = 7.08$ and $Z_{\text{O}}^* = -5.65/-2$ depending on the oxygen displacement direction [64]. Given the high value of the Born effective charge of the Ti cation, close to the Ti dynamical charge in BaTiO_3 , the calculated Ti atom displacement would give rise to a significant polarization in the twin wall.

The first experimental evidence of polar domain walls in CaTiO_3 was obtained by aberration-corrected Transmission Electron Microscopy (TEM) [6]. It was found that the $\text{Ca} - \text{Ca}$ interatomic distance stays constant, however the $\text{Ti} - \text{Ti}$ distance changes near the wall. Then, off-centering of the Ti atoms with respect to the center of charge of the corresponding oxygen octahedron was extracted by averaging in planes perpendicular to the domain wall above and below the domain wall. The displacements are shown in figure I.15a. In the perpendicular direction to the domain wall, Ti atoms are shifted by 3.1 pm in the second closest layer of Ti atoms from the wall (I.15b), and a larger displacement of 6.1 pm was extracted in the parallel direction of the domain wall in the adjacent Ti layer (I.15c). The

latter displacement, depending on the chosen model, corresponds to spontaneous polarization of 0.04 to 0.2 C/m^2 . If we calculate with the Ti Born effective charge on the pseudo-cubic lattice, we obtain 0.13 C/m^2 . This polarization is comparable with the bulk polarization (domain polarization) of barium titanate (0.26 C/m^2) [6].

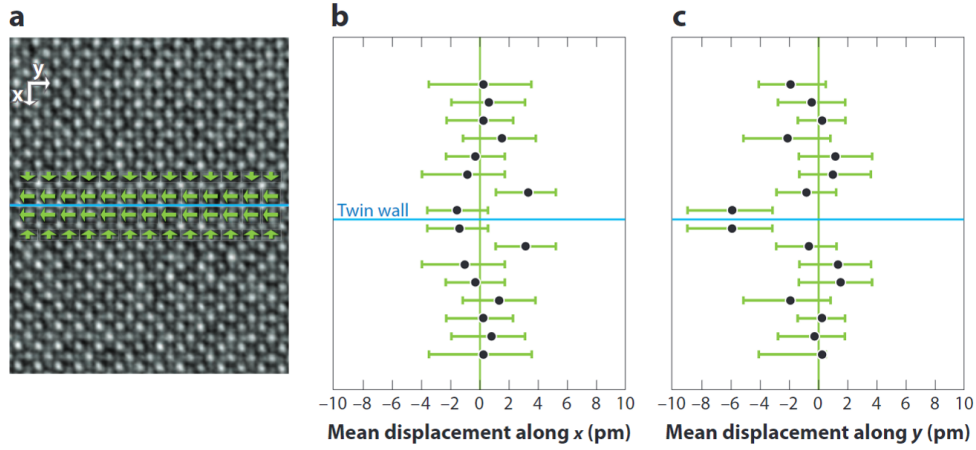


Figure I.15: a. High-resolution electron microscopic image of $CaTiO_3$ near a (110) twin boundary. The location of the center of the twin boundary is shown as a horizontal blue line (left). The Ti atoms are displaced near the twin boundary with two rows of atoms inside the twin boundary shifted horizontally to the left and two further rows shifted vertically towards the twin boundary. No shifts are seen for Ca. Displacements of Ti atomic columns in the x (b.) and y (c.) directions averaged along and in mirror operation with respect to the twin wall. From [6].

Polar domain walls were also observed using Second Harmonic Generation (SHG) [65]. An SHG signal can occur only if the second-order electrical susceptibility is non-zero, which implies a non-centrosymmetric structure i.e. polarity. CTO is centrosymmetric but not at the domain wall where the centrosymmetry is broken. Then SHG is sensitive to the polar domain wall. Contrary to the TEM observation, SHG can observe domain walls in volume by focusing the light at different depths of the sample. A CTO single crystal sample with several ferroelastic domain walls, shown in figure I.16a, was analyzed by confocal SHG with a scanning step of 1 μm parallel to the surface. Three depths are shown in figure I.16(b-d) and the domain wall was reconstructed in 3D from this SHG experiment [65]. We can see that these domain wall planes are inclined (and not perpendicular) from the surface. Domain walls appear as bright lines on the image with dark domains, as expected for non-polar areas. SHG confirmed the non-centrosymmetric symmetry of strain-compatible ferroelastic walls.

B.1.3 . CTO twin angle

The twin angle can be measured by Atomic Force Microscopy (AFM), by scanning the height variation across a domain wall at the surface. It can also be

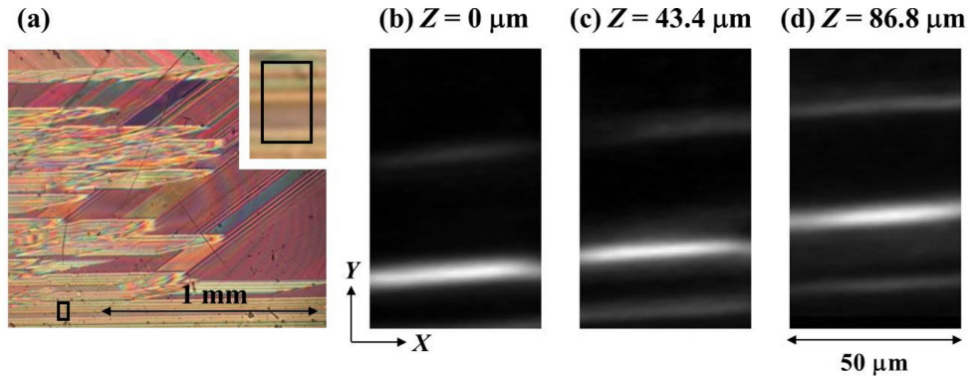


Figure I.16: a. Polarization microscope image of CTO in the crossed Nicols configuration. (b-d) SHG section images at different depths (Z) from the surface. The observed area is the enclosed square in a. A zoom-in picture of the enclosed region is also shown in an inserted figure. From [65].

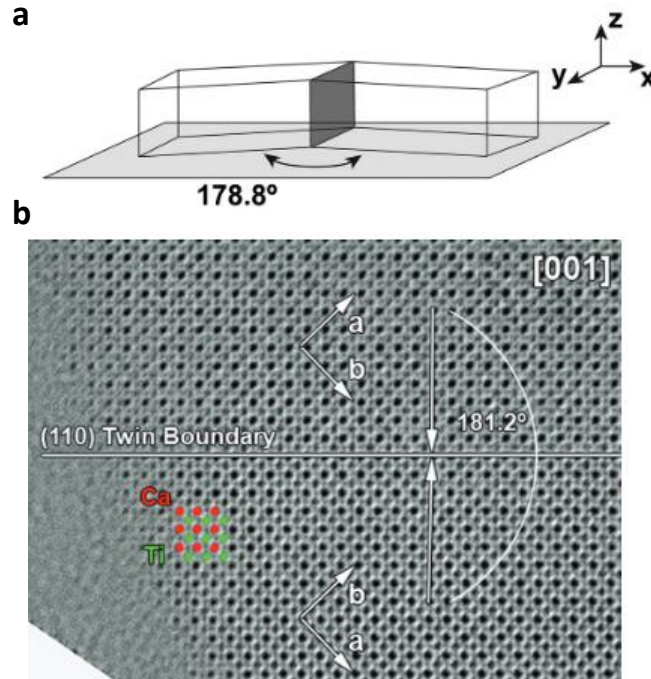


Figure I.17: a. Single twin wall indicated as standing dark grey plane. b. TEM amplitude of a CaTiO_3 crystal along the $[001]$ axis orientation, the (110) twin boundary is indicated by the horizontal white line. From [6].

deduced from the TEM angle between the atom rows across a twin boundary. For CaTiO_3 , an angle of 181.2° (respectively 178.8°) for a (110) twin wall was found, as shown in figure I.17. The surface in the case of only two possible domain states has a factory roof like structure with polarity pointing either up or down at the domain walls.

B.2 . Barium titanate BaTiO₃

In $BaTiO_3$ (BTO), decreasing the temperature leads to a structural phase transition from the high-symmetry cubic phase (paraelectric) to lower-symmetry ferroelectric phases due to the off-centering of the Ti cation in the oxygen octahedron along polar axes depending on the phase structure. $BaTiO_3$ exhibits three ferroelectric phases: tetragonal (278K to 393K), orthorhombic (183 K to 278 K), and rhombohedral phase (up to 183K) [66]. In each case, the Ti is off-centered, following the $\langle 001 \rangle$, $\langle 011 \rangle$, and $\langle 111 \rangle$ directions respectively, giving the polar vector directions, as shown in figure I.18.

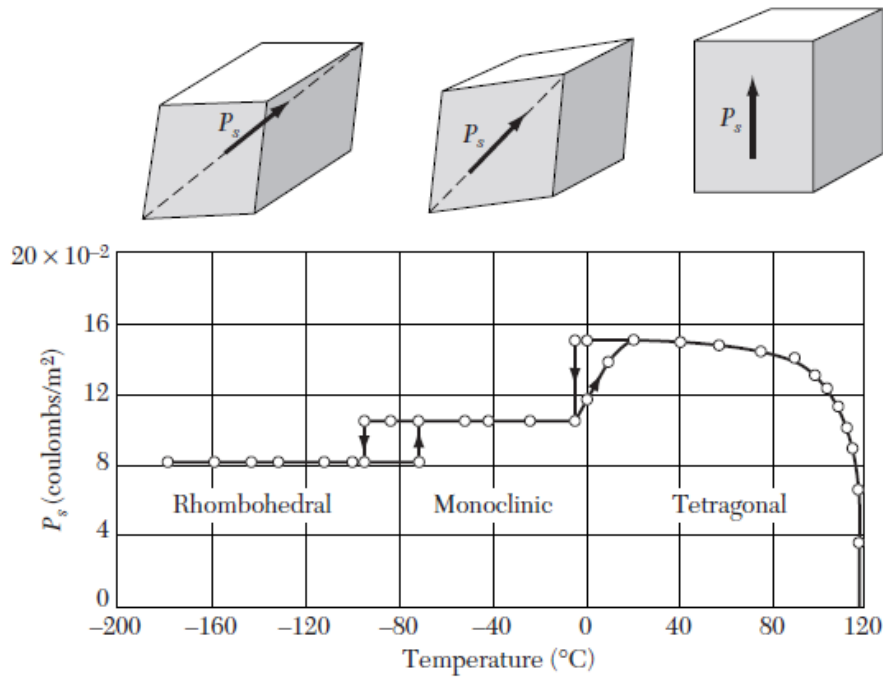


Figure I.18: $BaTiO_3$ phases transitions and polarization vector directions.

In the tetragonal phase, the Ti cation is off-centered with respect to the equatorial oxygens, along the lattice long axis, as shown in figure I.19, which is the polar axis of this phase. The asymmetric charge distribution induces a local dipole moment, which is the microscopic origin of the ferroelectricity in $BaTiO_3$.

The material exhibits either 90° ferroelectric/ferroelastic domain walls between domains with out-of-plane/in-plane polarization (P_{\uparrow} or P_{\downarrow}/P_{in}), which minimize the strain and 180° purely ferroelectric domain walls between P_{\uparrow} and P_{\downarrow} domains to minimize electric energy of the sample. An example of BTO in-plane and out-of-plane polarized domains by Piezoresponse force microscopy (PFM), sensitive to the polarization in the ferroelectric domains, are shown in figure I.20.

The ferroelectric order was observed at the surface of $BaTiO_3$ above the Curie temperature of 393 K [68]. The persistence of the tetragonal phase and its domain

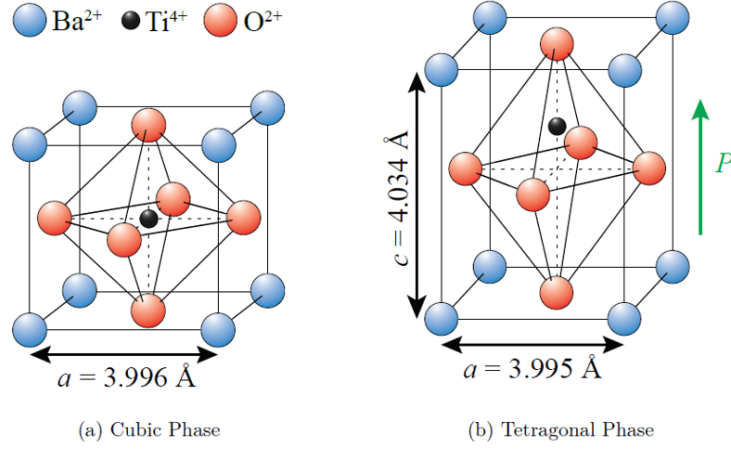


Figure I.19: $BaTiO_3$ perovskite structure in the paraelectric and ferroelectric/ferroelastic phase, showing the polarization direction along the $\langle 001 \rangle$ direction in the tetragonal phase.

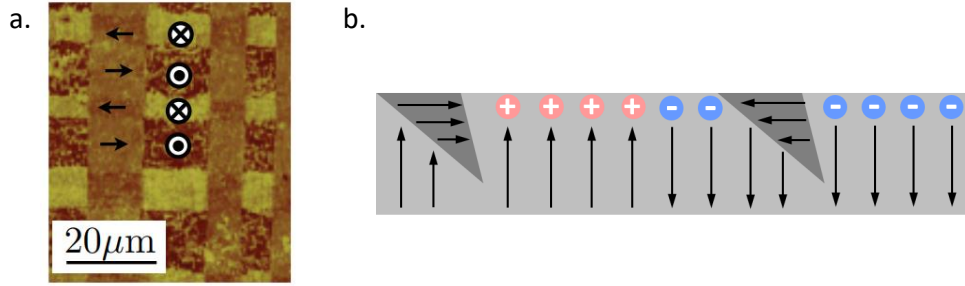


Figure I.20: a. PFM images of $BaTiO_3$ domains with in-plane and out-of-plane polarizations [67], and b. schematic of the domain ordering.

ordering above T_c was observed by threshold Photoemission electron Microscopy (PEEM) [69]. As shown in figure I.21, work function contrast, corresponding to domain polarization states, is visible and persists above T_c . Wide vertical 90° stripe domains have a downward polarization P_\downarrow (dark) for the thinner stripes and broader stripes have an in-plane polarization P_{in} (gray) and fine-scale tweed, the crossed domain patterns in the PEEM images, with inward polarization P_\uparrow . After quenching from 550K, above the Curie temperature, the surface conserves the initial ferroelastic ordering but after annealing at 975K and quenching back in the tetragonal phase, the surface domain pattern changed. Stripes are narrower and not at the same position, highlighting that the surface's initial domain configuration was erased.

This surface effect is related to the electrostatic and elastic boundary conditions modification at the surface [70]. The bulk material is in the cubic symmetry while the surface layer remains tetragonal at 550K and conserves the ferroelectric

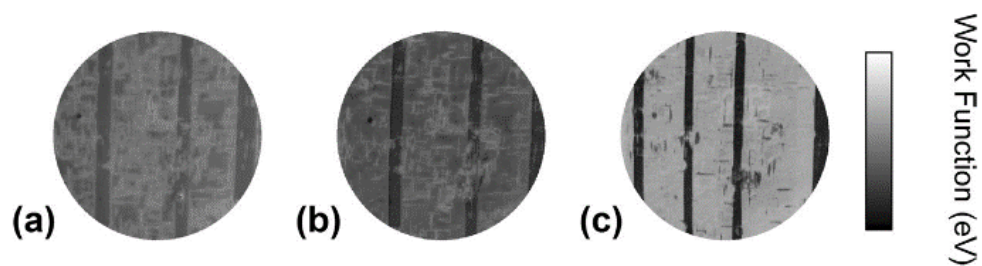


Figure I.21: Surface potential maps of a. initial surface, b. after heating at 550 K, and c. after heating at 975 K. The maps are generated from image series recorded as a function of electron kinetic energy at room temperature. The field of view is $67\ \mu\text{m}$ in diameter and in each case, the work function variation spans 0.5 eV. From [69].

ordering similar to that in the bulk tetragonal phase.

C . Domain wall engineering

C.1 . Definition

It is possible to generate properties inside twin walls that do not exist anywhere else in the structure. A well-known example is the apparition of superconductivity at ferroelastic domain walls in tungsten oxide WO_3 [5]. It opens perspectives for new types of memory devices [9] and electronic logic circuits can be reproduced with domain walls [71]. The challenge of "domain walls nanoelectronics" [8] or "domain boundary engineering" [7] is in generating and controlling reliably domain walls for reliable devices with higher storage density and low power consumption.

There are different approaches in domain wall engineering. In the first approach, the chemical composition of the twin wall is modified by local doping. Local modification is possible because the chemical potential of the wall can be drastically different from the bulk value. Dopants or defects can be attracted or repelled by the walls [72]. It can generate a higher conductivity in the wall. Another approach is directly related to the structure at the domain wall which can induce atom off-centering movements and then local polarity.

C.2 . Domain wall conductivity

Domain walls can be more conductive than the neighboring domains, for example in $BiFeO_3$ [73] or more insulating as in $YMnO_3$ [74]. It was also observed that selective doping at the domain walls of WO_3 induces superconductive domain walls [5]. Doping twin walls in WO_3 is an example in which Na, Li, or oxygen vacancies migrate to the wall [75], which increases the carrier concentration inside the wall and generates high electron conductivity. A phase transition at 3 K between conducting walls and superconducting walls in WO_3 occurs without any structural changes of the bulk [5]. Local conductivity modification was also observed in La-doped twin walls in $BiFeO_3$ [76]. The experimental control of the domain wall electronic properties with doping is an example of domain wall engineering to possibly tailor electronic devices.

One interesting example of conductive domain walls is $BiFeO_3$ at domain walls. In thin films, the material display 3 types of ferroelectric domain walls with polarization angles of 71° , 109° , and 180° between adjacent domains, as shown in image I.22 [77].

$BiFeO_3$ is an insulator but some domain walls are conductive. On image I.23 [4], the conductivity is checked by c-AFM (conductive Atomic Force Microscopy). 109° and 180° domain walls are conductive and we can also see the absence of conduction at 71° domain walls.

Distinct mechanisms can operate individually or together to enhance conductivity in domain walls. It can be an extrinsic effect coming from the presence of charge defects near the domain wall [78, 76] and/or an intrinsic contribution leading to the reduction of the band gap, because the atomic and associated electronic configurations are locally distinct from the bulk. For the latter, detailed electronic

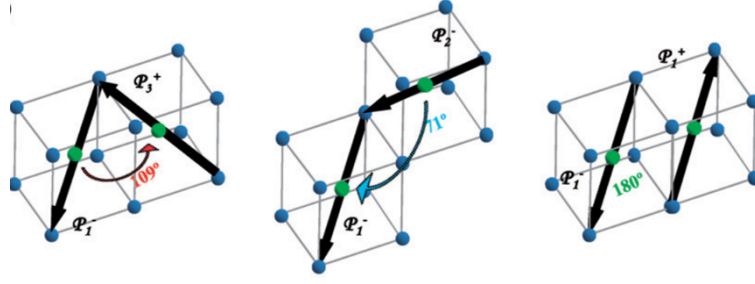


Figure I.22: The three different types of domain walls in rhombohedral bismuth ferrite. 109° domain wall in red, 71° in blue and 180° in green. Arrows indicate polarization directions in adjacent domains [77].

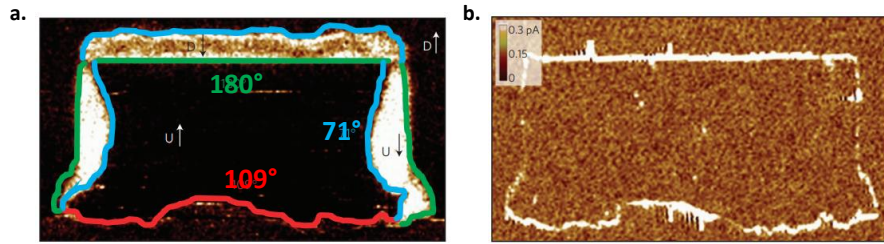


Figure I.23: a. In-plane PFM image of a written domain pattern in a monodomain $BiFeO_3$ (110) thin film with the three types of domain walls. 180° domain walls are in green, 71° in blue and 109° in red. b. Conduction atomic force microscopy (c-AFM) image showing conduction at both 109° and 180° domain walls and no conduction at the 71° domain walls [4]. The current color bar scale is ranging from 0 to 0.3 pA.

properties of domain walls in bismuth ferrite have been investigated by Lubk et al. [79]. Using density functional theory, the layer-by-layer densities of states were calculated. It was found that the domain walls have a significantly reduced band gap compared to the domains for all types of domain walls, up to 0.2 eV of reduction for 180° domain walls, as shown in figure I.24. However, the local density approximation to the exchange-correlation energy functional underestimates the band gap energy. Moreover, the intrinsic origin of the band gap narrowing at the $BiFeO_3$ domain walls is debated, other studies show that the conductivity at 109° domain walls is likely due to free electrons originating from oxygen vacancies [76], with the current at the domain wall dependent on the concentration of oxygen vacancies.

Both intrinsic and extrinsic contributions can explain the different transport properties at the domain walls [78]. One extrinsic contribution example is 180° domain wall conductivity in $Pb(Zr,Ti)O_3$, originating from oxygen vacancies at or near the domain walls [80]. Another conduction mechanism, associated with head-to-head/tail-to-tail charged domain walls will shift the electronic band structure at the domain wall. Then the conduction band can be shifted below the Fermi level or valence bands above it, enhancing conductive properties [51].

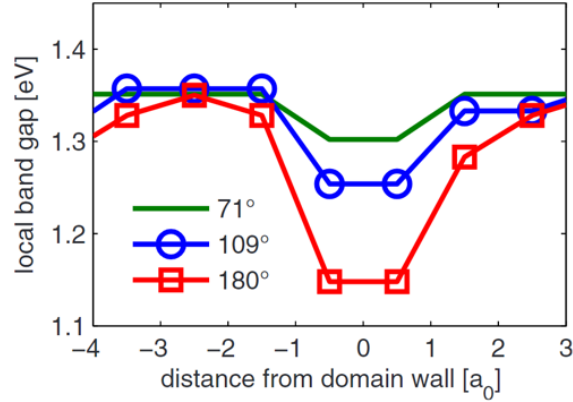


Figure I.24: Local band gap extracted from the layer-by-layer densities of states in the three types of $BiFeO_3$ domain walls [79]. Each point is on consecutive FeO_2 planes.

The control of the electronic structure at walls by doping (atoms, defects) in ferroelectric and ferroelastic oxides opens a way to effectively engineer nanoscale functionality, like tunable conductivity in the walls.

C.3 . Domain wall dynamics

Domain wall dynamics are intensively studied for ferroelectric and ferroelastic switching. In ferroelectrics, polarization switching can proceed by nucleation or domain wall movement [81]. In the former mechanism, nucleation of the opposite polarization direction under an electric field happens at a defect site, then the formed domain grows parallel to the applied field and spreads sideways until filling the space [82]. For surfaces with domain walls, another switching mechanism is the movement of domain walls. The relative contribution of nucleation and domain wall motion into polarization reversal depends on the material, defects, and geometry. In all cases, the domain wall velocity represents a speed limit to switching [83, 84].

The motion of domain walls is a nonlinear dynamic process where ballistic propagation is often superimposed by sudden jumps called jerks. Such jerks are initiated when walls are pinned and depinned on defects in a stop-and-go mechanism. Jerk is less likely to appear for small forces and low frequencies [40]. The theoretical wall speed limit is the maximum phonon velocity, which is the velocity of sound in the material ($\approx 10^3$ m/s). But ferroelectric thin film walls reach a maximum speed of the order of 10 m/s [85]. The objective is then to understand the underlying mechanisms of the jerk propagation, to engineer faster switching dynamics [40].

One approach is to directly study individual domain wall movement. A unified kinetic approach to the domain structure evolution in the electric field was for-

mulated [86, 87] and analyzed by optical microscopy [88] and piezoresponse force microscopy (PFM) [89]. The challenge is the observation of the movement with a sufficient time resolution.

Another approach relies on the fact that ballistic propagation of domain walls is often superimposed by an ensemble of jerky or spiky movements (discrete impulsive jumps) that make up an avalanche. Given the large number of discrete movements required for an observable, a statistical approach is used to understand the collective movement of the domain walls. One example is the study of $BaTiO_3$ 90° domain wall movement during ferroelectric switching [90]. In the experiment, piezoelectric sensors are used to detect acoustic signals related to the domain wall jumps (jerks). Strain relaxation from the pinning/depinning of domain walls generates an acoustic wave that is detected by a piezoelectric transducer. Pinning follows not only from extrinsic defects but also from jamming by intersecting domain walls [91]. Statistical analysis has shown that the energy distribution $P(E)$ of the jerky movement follows a scale-independent power-law dependence:

$$P(E) \sim E^{-\epsilon} \quad (18)$$

with ϵ the energy exponent. This domain wall “crackling noise” follows scale invariant avalanche dynamics: the avalanche energy and amplitude probability distribution functions follow power laws with exponents $\epsilon = 1.65$. Other ferroelastic materials show a similar exponent, in the range of 1.3 to 2 [92, 93] with a statistical approach on collective domain walls observed by optical microscopy.

Systems, from earthquakes to domain walls, can exhibit crackling when responding to changing external conditions. Because the response is scale independent, their behavior is independent of microscopic and macroscopic details, and interpretation can be made by the use of simple models [94]. For example, the plastic deformation of a material (or a domain wall) can be described as a simple discrete mean-field model, based on a local failure threshold: when the stress locally exceeds the threshold, it slips by a certain distance, resulting in a stress reduction. The released stress is redistributed to other sites in the system. This mean field theory (MFT) predicts for crystals the energy distribution of the slip avalanches i.e. jerks. If the energy is defined as proportional to the time integral of the slip velocity squared, the MFT power law exponents for the jerk energy are 1.33 when looking at jerks over a small stress range and 1.67 for the integral over the entire stress range.

Jerk dynamics are present in other systems besides domain wall motion. The earth responds to the slow shear strains imposed by the continental drift through a series of violent impulses, earthquakes, spanning over many orders of magnitude, from barely noticeable to catastrophic. Peaks of the related jerk energies are shown in figure I.25a. The distribution of the seismic energy follows a power law [95] $P(E) \approx E^{-\epsilon}$ with $\epsilon = 1.7$, shown on figure I.25b [96]. From the MFT, the jerks accumulate to a few avalanches. Fracturing systems (cracks) also display

such dynamics, so-called crackling noise, with seemingly random sudden energy release spanning over a broad energy scale, reminiscent of earthquakes [96, 97].

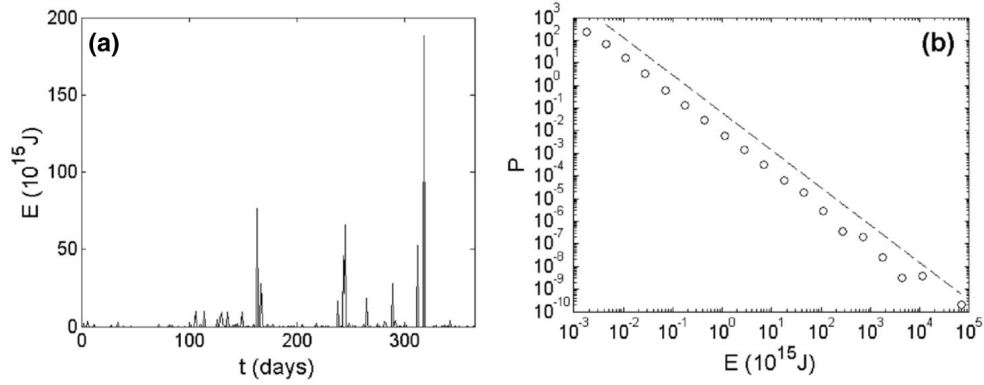


Figure I.25: (a) Energy radiated by earthquakes of magnitude $M \geq 3$ for each day of the year 2005, in a region of California spanning 32°N – 37°N latitude and 114°W – 122°W longitude. (b) Distribution in energy of earthquakes having occurred in this region from 1987 to the present. The axes are logarithmic. The dashed line is the power law with $\epsilon = 1.7$. From [96].

II - Experimental methods

The main experimental techniques are based on surface-sensitive spectroscopy and microscopy. X-Ray Photoemission Spectroscopy is used to determine the surface chemistry and contamination, and Photoemission Electron Microscopy to observe the surface topography of ferroelastic domains and X-ray absorption PEEM, with synchrotron light to image the ferroelastic domains strains. Low Energy Electron Microscopy investigates the domain walls' polarity at the surface.

Commercial and laboratory-grown single-crystal samples were used. Thin films of ferroelastic CaTiO_3 were grown by Pulsed Laser Deposition, characterized by Atomic Force Microscopy for the surface topography. X-Ray Diffraction was used to determine the orientation, epitaxial strain, and X-Ray Reflectivity for the film thickness. Raman Spectroscopy further investigated the vibrational signature of the thin film domain walls. First results on the preparation and investigation of CaTiO_3 thin film domain walls functional properties are presented in the [Appendix D](#).

A . Photoemission techniques

PhotoEmission Spectroscopy (PES) is widely used in surface science to determine a material's surface electronic and chemical properties. The technique uses the photoelectric effect, which is the emission of electrons (called photoelectrons) from core and valence energy levels on the interaction of electromagnetic radiation with a material. Photoelectrons are then analyzed as a function of kinetic energy, wave vector, position, and emission angle with a variety of photoemission-based techniques: X-Ray PhotoEmission Spectroscopy (XPS), PhotoEmission Electron Microscopy (PEEM), Angle-Resolved X-ray PhotoEmission Spectroscopy (ARPES), X-ray Photoemission Diffraction (XPD). PES allows access to a wide range of information on materials' chemistry and electronic structure.

The photoelectric effect was discovered by Frank and Hertz in 1887 [98], where they observed electrons ejected from a metal when illuminated by electromagnetic radiation. A theoretical explanation was then given by Einstein in 1905 [99] in one of his three famous papers published that year, and for which he was awarded the Nobel prize in 1921. The PES technique was first developed by Siegbahn et al. in 1957 [100]. The technique was called Electron Spectroscopy for Chemical Analysis (ESCA), later called X-Ray Photoemission Spectroscopy (XPS). Siegbahn received the Nobel prize in 1981 for his contribution to developing high-resolution electron spectroscopy [101, 102].

A.1 . Photoemission process

A.1.1 . Photoelectric effect

When illuminated by a photon beam, the absorption with a given probability of an incident photon by an atom leads to the emission of an electron, called a photoelectron. The initial state is an atom with N electrons of total energy $E(N)$. In the final state, one photoelectron is emitted so there are $(N - 1)$ electrons and a total energy $E^*(N - 1)$ at an excited state and one electron in a vacuum with kinetic energy E_k . Energy is conserved in this process, we can write the equation 1.

$$h\nu + E(N) = E^*(N - 1) + E_k \quad (1)$$

Where h is Plank's constant and ν is the photon frequency. The binding energy E_B can be written as shown in equation 2. For E_k measured with respect to the Fermi level, we can deduce the famous Einstein relation which links the binding and kinetic energy of the photoelectron, in equation 3.

$$E_B = E^*(N - 1) - E(N) \quad (2)$$

$$h\nu = E_k + E_B \quad (3)$$

An electron needs energy (given by the photon, $h\nu$) higher than E_B plus the work function Φ_s of the sample to reach the vacuum level E_{vac} and be emitted. So in the case of a metal, Φ_s is the minimal energy at which a photoelectron can be emitted. We can write the complete Einstein equation with the work function 4.

$$h\nu = E_k + E_B + \Phi_s \quad (4)$$

The photoemission process in solids can be semi-classically described by a three-step model which separates the photoemission of a single electron into three main steps: photo-ionization, the path through the material to the surface, and the last transmission of the photoelectron from the solid to the vacuum.

A.1.2 . Three steps model

An accurate description based on a quantum description of the photoemission process has been developed by Ref. [103, 104]. The three steps model presented here, less accurate, offers a clear illustration of the phenomena involved in a photoemission spectrum.

1. Photo-ionization

The emission of an electron under the light of energy $h\nu$ happens with a probability called photo-ionization cross-section. An electron in an atomic subshell nl excited by a photon, the absorption probability σ_{nl} (where n and l are the principal and orbital quantum numbers respectively) depends on the atom, the considered

core level electron, and the incident photon energy. σ_{nl} can be approximated for the solid angle and the atomic subshell nl with the relation 5 [105, 106, 107].

$$\frac{d\sigma_{nl}}{d\Omega} = \frac{\sigma_{nl}}{4\pi} \left(1 + \frac{\beta_{nl}}{2} (3\cos^2\gamma - 1)\right) \quad (5)$$

With σ_{nl} the photo-ionization cross-section of the atomic subshell nl . γ is the angle between the direction of ejected electrons and the polarization of the incident light. β_{nl} is an energy dependent asymmetry parameter of the atomic subshell nl . The photoemission probability is proportional to the photo-ionization cross-section of the atom at the considered energy level for a given incident energy [108].

2. The path through the material to the surface

Photoelectrons travel from the bulk to the surface of the material. Photoelectrons in the bulk can lose energy through inelastic collisions. Electrons losing energy through those events make up the continuous secondary electron background whereas electrons without energy loss will compose the elastic peak(s) [109].

As a result, the deeper from the surface a photoionized atom is, the more electrons are likely to have lost energy via inelastic scattering. The attenuation of the elastic peak intensity is described by the inelastic mean free path, which is the mean distance traveled by an electron without undergoing an inelastic collision, following a Beer-Lambert type law:

$$I(d) = I_0 \cdot \exp\left(-\frac{d}{\lambda(E)}\right) \quad (6)$$

with d the probing depth, I_0 the intensity without attenuation and λ the inelastic mean free path. The inelastic mean free path depends on the electron kinetic energy, as shown in figure II.1. From equation 6, for a normal emission, 95% of the total intensity is coming from up to 3λ from the surface, giving the probing depth of the photoemission techniques [110].

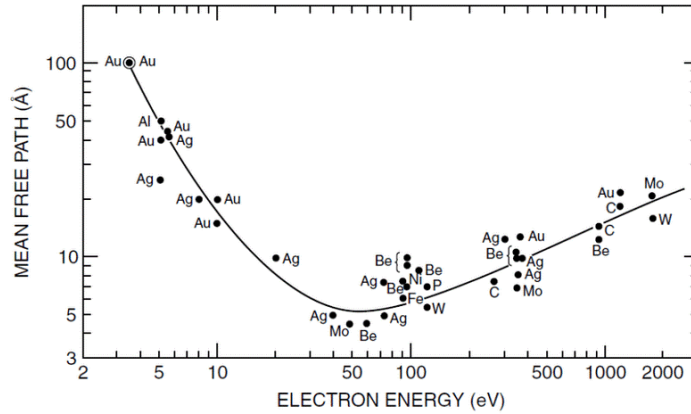


Figure II.1: Inelastic mean free path of electrons in solids [111]. The universal curve has a probing depth minimum of 5 Å at kinetic energies of 50-100 eV.

Moreover, by selecting the take-off angle of the photoelectrons, we can also reach a higher surface sensitivity (smaller probing depth), usually by rotating the sample. Mathematically, the equation 6 should be corrected by having $\lambda \sin \theta$, with θ the take-off angle instead of λ . Photoemission experiments are conducted in ultra-high vacuum (UHV) for the detection of photoelectrons. Emitted photoelectrons are not scattered in the vacuum chamber if the pressure is at $\approx 10^{-10}$ mbar.

3. Surface emission

The photoelectron has to cross a barrier potential called work function Φ_s to exit the material. The definition of the work function of a surface is the smallest energy needed at 0 K to extract an electron from the solid into the vacuum. The kinetic energy of an electron outside the material follows Einstein's equation 4. The Fermi level is the reference for the binding and kinetic energies in this equation. The equation is illustrated in figure II.2.

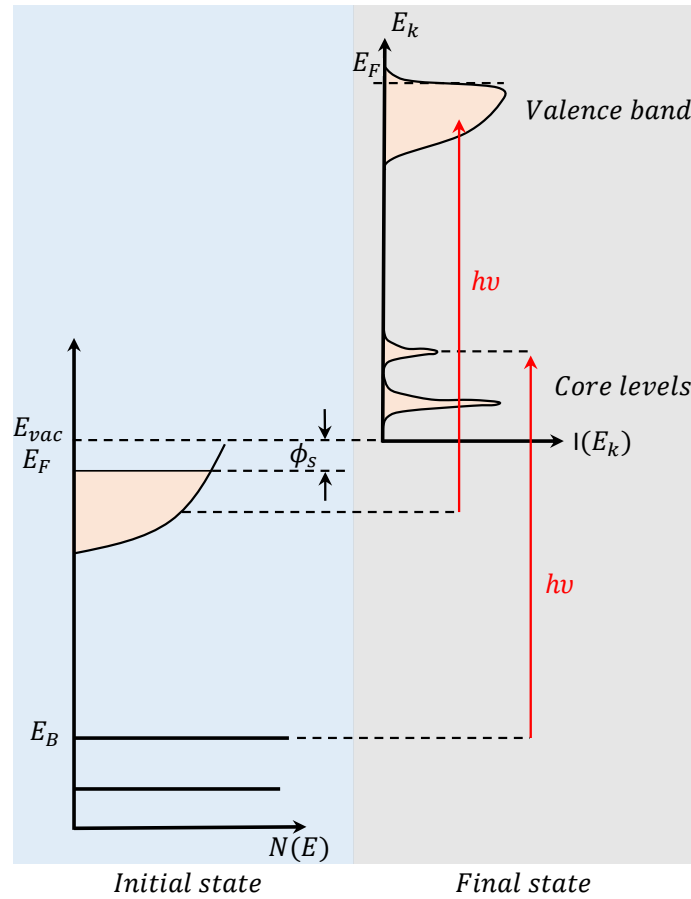


Figure II.2: Schematic of the photoemission process, adapted from [112]. The binding energy E_B is referred to the Fermi level E_F . The kinetic energy of the photoelectron is given by $E_k = h\nu - E_b - \Phi_s$

A.1.3 . Detection

Emitted photoelectrons are going through the vacuum to reach the electron analyzer. A specific method is used to determine the binding energy of the electron, shown in schematic II.3. The spectrometer Fermi level is aligned with the sample one through an ohmic contact and the measured kinetic energy noted E'_k is referenced with respect to the work function of the spectrometer ϕ_{sp} . This can be determined by measuring the Fermi level with a metallic reference sample.

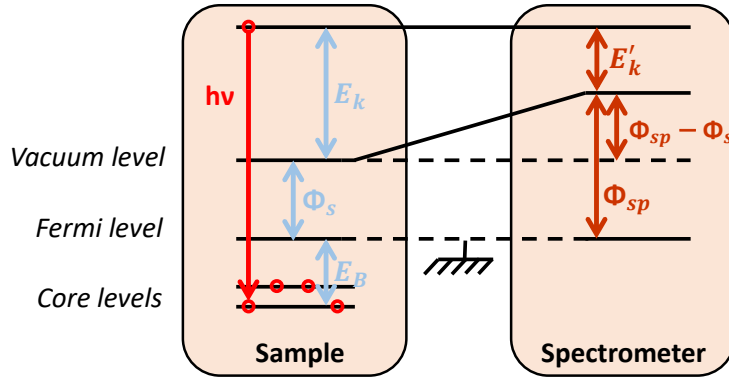


Figure II.3: Energy alignment of a sample connected to the spectrometer

The photoelectron kinetic energy E_k can then be written as in equation 7, with E'_k the measured kinetic energy, ϕ_{sp} the spectrometer work function and ϕ_s the sample work function. And we can deduce E_B as shown in equation 8.

$$E_k = E'_k + (\Phi_{sp} - \Phi_s) \quad (7)$$

$$E_B = h\nu - (E'_k + \Phi_{sp}) \quad (8)$$

A.2 . X-ray Photoemission Spectroscopy (XPS)

XPS is used in the thesis to identify surface contamination by carbon or organics on the analyzed sample. Spectra are made before and after sample cleaning processes to check the surface contamination. Figure II.4 shows a schematic of an XPS spectrum with the contribution of several types of photoelectrons.

Secondary electrons (SE) have lost energy by inelastic scattering(s). SE are present at all kinetic energies, forming the photoemission background, with a peak at low kinetic energies. The photoemission threshold, annotated in the figure, corresponds to the minimum energy at which the electrons are emitted into the vacuum. For metals, it corresponds to the work function.

Primary electrons give information about the chemical elements present in the sample for core levels electrons (sharp peaks) and the electronic structure for valance band electrons (more dispersed) [113]. For the latter electrons, the band

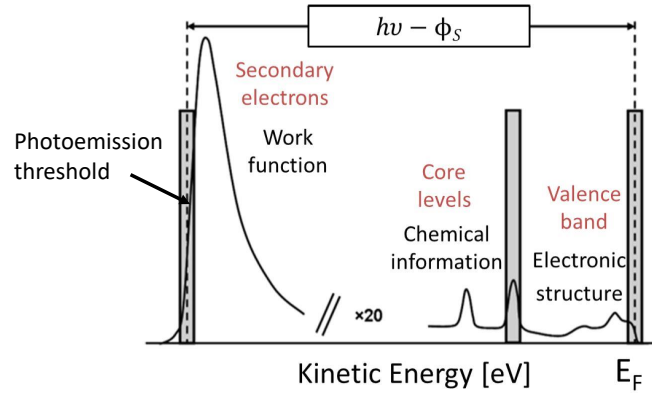


Figure II.4: Typical photoemission spectrum showing the contribution of three types of electrons: secondary electrons and electrons coming from core and valance bands.

structure of the material can be deduced from their angle of emission. Techniques using this method are Angle-resolved photoemission spectroscopy (ARPES) and Reciprocal space PhotoEmission Electron Microscopy (k-PEEM). Each core level of a given atom present in the material will give a peak intensity that is proportional to the cross-section of this level at the incident photon energy.

A.3 . Photoemission Electron Microscopy (PEEM)

A.3.1 . Generalities

PEEM is a photoemission non-invasive surface technique with lateral resolution. The material is excited by photons and creates a spectral distribution of emitted photoelectrons $I(E_k)$ in front of the surface, which may vary between neighboring points $I(E_k, x, y)$ due to surface chemical and topography differences. These differences give contrast to the observed image. There are two existing options to map the electron distribution at the surface. One method is scanning imagery, i.e., $I(E_k, x_i, y_i)$ with a focused photon beam scanning the surface [114, 115]. Another method is parallel imaging; the lateral distribution is imaged energy by energy, i.e., $I(E_{ki}, x, y)$, by a dedicated electron-optical column which transfers the lateral distribution onto a 2-dimensional detector [116]. This approach provides a higher data acquisition rate and the possibility to take energy-filtered images at selected XPS lines and in real-time [117]. In electron emission microscopy, we can obtain a 3D data stack of microscopic and spectroscopic information to perform spatially resolved surface chemical and electronic structure analysis.

Several technical approaches exist to perform the energy-filtering of the photoelectrons. Three existing electron optical systems from different concepts of energy-filtered PEEM instruments are represented in figure II.5 [118]. Widely used in conventional XPS, hemispherical analyzers are also integrated into PEEM. Both simple and double hemispherical analyzers exist, as shown in figure II.5a and c. The spectral resolution of a hemispherical analyzer is defined by the size of the analyzer

slit widths and the pass energy, and it can reach 300 meV [119]. Another energy filter, shown in figure II.5b, uses the energy dispersion in a magnetic prism which is also used to separate the primary and secondary electron beam in Low Energy Electron Microscopy (LEEM) [120, 121]. The best energy resolution attainable in this system is about 150 meV [120] for low kinetic energies of the electrons. The setups in figure II.5a and c were used in this thesis and will be discussed in detail in this section.

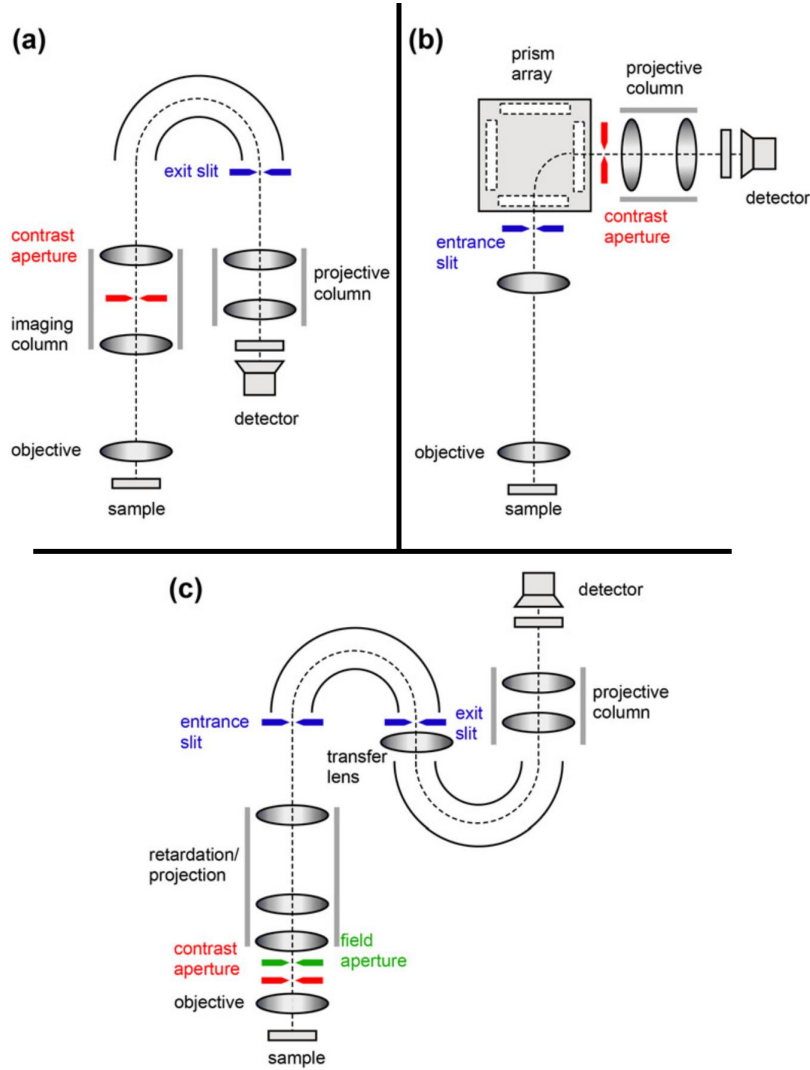


Figure II.5: Major blocks of the electron optical systems from different concepts of energy-filtered PEEM instruments: (a) hemispherical energy analyzer (SPELEEM design); (b) magnetic prism (Tromp design); double-hemispherical analyzer (NanoESCA design). From [118].

In the three presented configurations, the objective lens is designed to accept large solid angles to obtain a high magnification. An immersion objective lens

realizes this, also called a cathode lens, because the sample is the source of the electrons, whether they are emitted or reflected. A high electric field is applied between the sample and the first electrode (extractor) to accelerate the electrons into the objective lens [116]. The distance between the sample and the objective lens is 2-3 nm [122]. This method of collecting electrons, where the sample is the cathode of the electric field, is also used in other emission electron microscopy techniques, including LEEM [123]. It was first introduced by Brüche in 1933 [124]. The pioneered work of Brüche was followed by theoretical considerations of Recknagel in 1941 [125], and improvement by Rempfer et al. [126], and Bauer [127]. The first emission electron microscope was built in the 60s (Balzers 'Metioskop') [128] but very limited in applications because of the vacuum quality (10^{-7} mbar at the time).

In PEEM experiments, photoelectrons are usually excited by UV/VUV lamps (Hg 4.9 eV or $He - I_{\alpha}$ 21.2 eV) or monochromatized synchrotron radiation. We will present more specifically the ScientaOmicron NanoESCA design (PEEM) and later the Elmitec SPELEEM design (PEEM and LEEM) in the LEEM section, both used in this thesis.

A.3.2 . NanoESCA experimental setup

A schematic of the NanoESCA PEEM principal optics elements, present in our laboratory, is shown in figure II.6. Photons of energy $h\nu$ are generated by UV/VUV lamps (Hg 4.9 eV or $He - I_{\alpha}$ 21.2 eV) towards the sample. Photoelectrons are generated and travel in the microscope through the lenses following an optical path represented by the red line.

The sample is close to the ground potential, and electrons are extracted by the high potential of 12-20 kV of the electrostatic objective lens, placed at around 2.5 mm from the sample. Photoelectrons emitted with a large angle with respect to the normal of the sample are collected. The first part of the electronic microscope is composed of an imaging column, where imaging optics are used to keep the spatial provenance of the photoelectrons [118]. The objective lens is mounted with an octopole stigmator to compensate for axial astigmatism from the eventual sample tilt from the normal direction in the NanoESCA design.

After passing through the objective lens, electrons are decelerated to 2 keV. Then the entrance lens collects, focuses, and further retard the electrons to the pass energy E_{pass} of the energy filter before entering at the entrance slit of the hemispherical analyzer [129]. A hemispherical analyzer consists of a hemispherical deflector composed of two concentric hemispherical electrodes (of radius R_1 and R_2 , mean radius R_0), which are at a different potential, creating an electric field. The passage energy E_{pass} selects the electron energy going through the analyzer. Electrons with higher or lower energies will hit the hemispherical electrodes (narrow band pass energy filter) as portrayed in image II.6 on the first analyzer with the green and brown electron line paths. To scan the kinetic energy, E_{pass} stays fixed, and the sample potential is swept. So the effective kinetic energy of the electrons

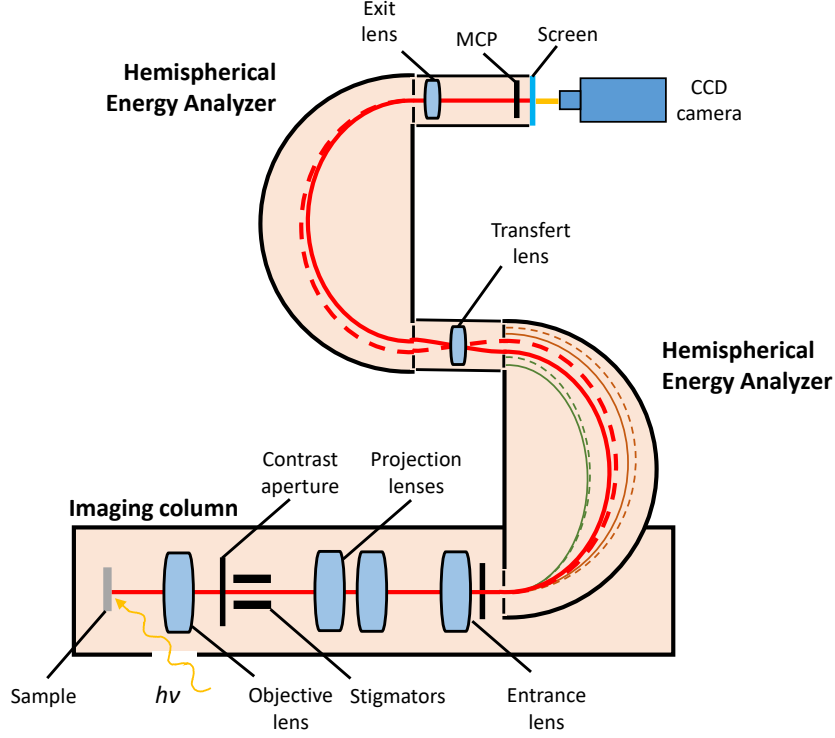


Figure II.6: Optics of the NanoESCA PEEM.

going through the analyzer is also swept. As a result, the energy resolution of the analyzer dE is given by equation 9 [129, 130].

$$dE = E_{pass} \left(\frac{W_1 + W_2}{2R_0} + \alpha^2 \right) \quad (9)$$

with W_1 and W_2 , respectively, the entrance and exit slit width and α the maximum angle of electrons with respect to the optical axis (at the entrance slit). α^2 represents the spherical aberration of the analyzer's dispersion. For the NanoESCA experiments, the slits of the first hemispherical analyzer are smaller than the second. Thus, the slits of the first analyzer determine $W_1 + W_2$. Usually, $E_{pass} = 50 \text{ eV}$, the width of the apertures are $W_1 = 1 \text{ mm}$, $W_2 = 8 \text{ mm}$, $R_0 = 125 \text{ mm}$.

Another energy filtering stage is added in the NanoESCA design to form a double-hemispherical energy analyzer [117] and keep a high electron transmission. The electron circular trajectory becomes a complete revolution with the second hemispherical analyzer, so electrons exit the analyzer at the same spacial position they entered. The second analyzer compensates for the dispersion of the first analyzer, so the energy filtering stage does not limit the lateral resolution. The α^2 -term of the spherical aberration of the analyzer is eliminated due to the antisymmetry of the tandem configuration of two identical analyzers [117].

After the analyzing stage, electrons are magnified by projective lenses to the multichannel plates to multiply the electron signal, imaged by a CCD camera on a fluorescent screen. The projection can be adjusted over an extensive range between 5 to 650 μm field of view. Furthermore, from the additional transfer lens after the contrast aperture, the angular distribution of the photoelectrons can also be imaged in a mode called reciprocal space PEEM (k-PEEM) [131].

The lateral resolution limit of the PEEM is impacted by the energy filtering stage in the NanoESCA design, as shown in the image II.7 representing the final resolution of a PEEM with single (HSA) and double hemispherical analyzer (IDEA). For small pass energies, the hemispherical analyzer aberrations contributions dominate the resolution whereas the double hemispherical analyzer maintains its imaging properties for all the pass energy range. The final lateral resolution is then fixed by the electron optical aberrations of the other lenses. Primary aberrations are then chromatic (not all wavelengths are focused on the same point) and then spherical aberrations (off-centered electrons are not focused on the same point) from the instrument lenses. The ultimate limit is the diffraction limit of the electrons through the lenses (Airy disk), fixed by the electron wavelength.

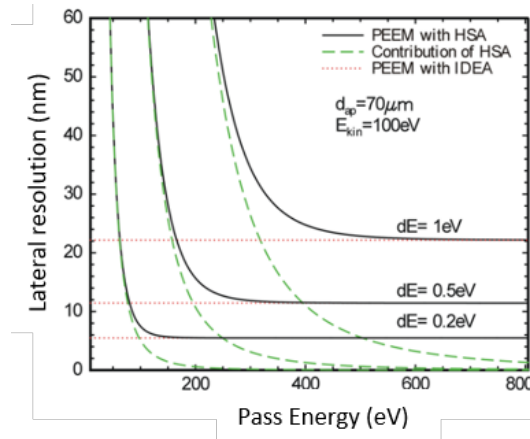


Figure II.7: Calculated ultimate resolution of the NanoESCA using the double hemispherical analyzer (IDEA), compared to a version with a single hemispherical analyzer (HSA). Calculations with a 70 μm contrast aperture and $E_k = 100\text{eV}$ [117].

A theoretical lower boundary for the spatial resolution in the NanoESCA is 10-20 nm [129], mainly because of lens chromatic aberrations. Above the chromatic and spherical aberration, the main limiting factor is the signal-over-noise ratio which can limit the attainable resolution [132]. Energy-filtered UV-PEEM images allow reaching a lateral resolution of 40 nm [133] and $\approx 100\text{nm}$ for core levels [134] and the best energy resolution in threshold PEEM, measured at low temperature (35 K), is 28 meV [135].

A.3.3 . Photoemission threshold

The NanoESCA used in the laboratory with UV/VUV lamps (Hg 4.9 eV and $He - I_{\alpha}$ 21.2 eV) is mainly used to perform threshold PEEM. Photoelectrons have a broad energy distribution, from elastic photoelectrons to low-energy secondary electrons. The photoemission threshold is the minimum energy at which an electron is ejected from the surface. It corresponds to the rising edge energy of the secondary electron peak. Kinetic energies are referenced with respect to the Fermi level in PEEM ($E - E_F$), so the photoemission threshold corresponds to the work function Φ_s in the case of metals.

Contrast in an image can be defined as a variation of intensity $I(x, y)$ across the image. Local perpendicular distortion of the electric field can deviate photoemitted electrons, causing accumulation (high intensity) or depletion (low intensity) of electrons. It can originate from surface topography [136] or surface charges induced by polar/ferroelectric domains or domain walls. Contrast can also result from a work function difference as its origin because of a different chemical state and a crystallographic orientation at the surface. For example, polarization differences between different $PbZr_{0.2}Ti_{0.8}O_3$ patterned ferroelectric domains, as shown in figure II.8. Ferroelectric domains with different polarizations have a different surface charge, which shifts the electronic levels, including the vacuum level, and hence the photoemission threshold of the emitted electrons, of 0.24 eV to 0.44 eV in the example.

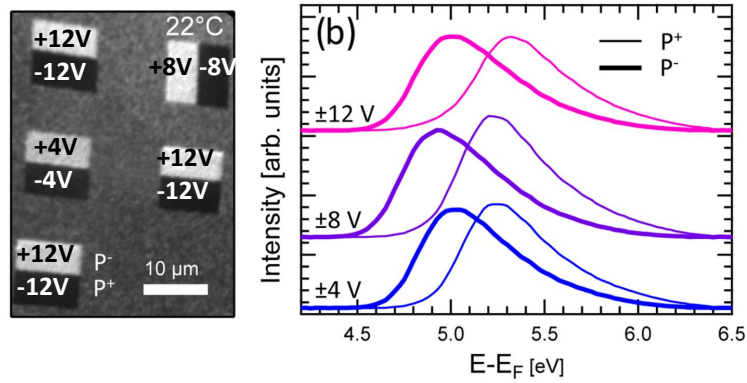


Figure II.8: a. PZT threshold PEEM image at $E - E_F = 4.9$ eV. b. Threshold spectra extracted from the P+ and P- domains written with different DC voltage amplitudes [137].

It is possible to reconstruct a map of the photoemission threshold values at each pixel. For this, images are taken at energies $E_i - E_F$ with an intensity distribution $I(E_i - E_F, x, y)$ so each pixel (x_i, y_i) is a photoemission energy threshold spectrum. Then, the photoemission threshold can be extracted pixel-by-pixel on the rising edge of the threshold spectra secondary electron peak with an error function, which corresponds to the integral of a Gaussian function, described in equation 10 [138, 139].

$$I(E - E_F) = 1 - \operatorname{erf}\left(\frac{E_{tr} - (E - E_F)}{\sqrt{2}\sigma}\right) \quad (10)$$

with E_{tr} the photoemission threshold, σ the standard deviation of the Gaussian (corresponding to the analyzer's energy broadening, $\sigma = 200 \text{ meV}$), and $\operatorname{erf}(x) = \frac{2}{\sqrt{\pi}} \int_0^x e^{-t^2} dt$.

A.3.4 . Non-isochromaticity

The energy resolution on a PEEM single image can also be impacted by the non-isochromaticity of the energy filtering stage. Ideally, an image would have a constant energy across the field of view (FoV), i.e. isochromatic. Hemispherical analyzers introduce an energy dispersion in one direction of the field-of-view because off-optical axis electrons on the sample at the same take-off angle as electrons on the optical axis are transferred to higher angles (chromatic aberration) and fall shorter in the hemispherical analyzer. So for a high analyzer bandwidth, these electrons are transmitted generating a spectral dispersion in the vertical direction, increasing far from the optical axis. The dispersion is reduced when reducing the pass energy. So it depends on the pass energy, the analyzer slits, and the FoV [129].

This non-isochromaticity can reach 1 or more eV per 10 μm [120]. The dispersion has a simple quadratic dependence on position [140]. For a point on the sample at a distance x_0 from the optical axis in the dispersive direction of the energy filter, the non-isochromaticity energy shift ΔE can be written as [129]:

$$\Delta E = E_{pass} \left(\frac{M_1 x_0}{f} \right)^2 \quad (11)$$

with $M_1 = 35$, the first lateral magnification of the microscope at the first image plane, and $f = 29 \text{ mm}$ the focal length of the objective lens, making ΔE dependent on the energy pass of the filtering stage and the field of view imaged. The bigger the field of view, x_0 can take higher values, and the bigger the non-isochromaticity. In the NanoESCA setup, for a typical field of view of 70 μm with a pass energy of $E_{pass} = 50 \text{ eV}$, the energy shift between the center of the image and the border in the energy dispersion direction is $\Delta E \approx 0.1 \text{ eV}$. Usually, the optical axis is off-centered, making the energy dispersion on one of the vertical borders of the image more important (asymmetry).

For precise determination of the photoemission threshold on every image pixel, we must correct this non-isochromaticity effect. In the NanoESCA PEEM images, the non-isochromaticity is in the vertical direction, as shown in figure II.9a, with an intensity gradient on a homogeneous surface because of the non-isochromaticity. For threshold PEEM images $I(E - E_f, x, y)$, a custom python program is written based on an anterior correction algorithm [140] to correct the vertical dispersion.

The vertical dispersion is extracted from an image 3D stack by plotting the threshold energy for each y line mean value. Then, the best dispersion fit is

obtained using a parabolic function, as predicted by the equation 11. An energy dispersion example and the fit are shown in II.9b. The vertical slices of the 3D stack are then readjusted accordingly to the dispersion.

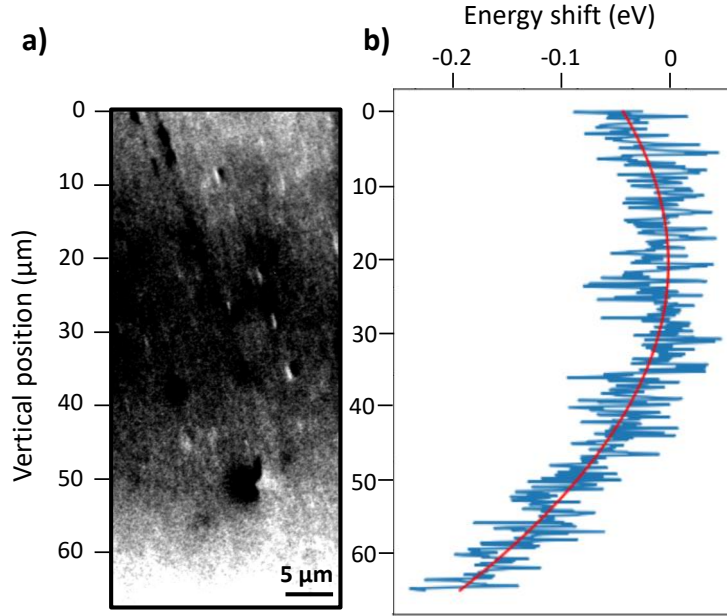


Figure II.9: PEEM non-isochromaticity. a) PEEM threshold image showing an intensity gradient between the center and the vertical borders in a homogeneous surface, corresponding to an energy dispersion. b) Non-isochromaticity measurement by a parabolic fit (in red) to the energy dispersion of each horizontal line of a PEEM threshold 3D stack on the area shown in a). The maximum measured energy shift is $\Delta E = 0.19 \text{ eV}$. The image field of view is $67 \mu\text{m}$ and the optical axis is off-centered, at $20 \mu\text{m}$ from the top. The equation 11 estimates $\Delta E = 0.16 \text{ eV}$ with $x_0 = 67 - 21 = 46 \mu\text{m}$, close to the experimental value.

A.3.5 . X-Ray Absorption Spectroscopy PhotoEmission Electron Microscopy (XAS-PEEM)

Synchrotron radiation can be used in PEEM to reach core state information. In XPEEM (X-Ray PhotoEmission Electron Microscopy), the PEEM detects the kinetic energy of the electrons up to the atomic core levels to probe the chemical state of the emitting atoms by measuring their binding energies and the surface valence band structure. In this case, $h\nu$ is generally fixed, and the energy filtering stage analyzes the photoelectron kinetic energies. In XAS-PEEM (X-ray Absorption Spectroscopy-PEEM), the PEEM image the total yield of the secondary photoelectron emission as a function of varying $h\nu$. The measured secondary electron intensity is proportional to the absorbed electrons. In principle, no energy filter is needed in XAS-PEEM, but it improves the lateral resolution [119].

The XAS principle is detailed in schematic II.10. An incident photon excites a core electron into an unoccupied valence state above the Fermi level. There is

photon absorption when the photon energy matches the ionization energy of the core electron. Afterward, the inner shell hole can be filled by an electron of higher energy to trigger fluorescence or the ejection of an electron from a higher energy state (Auger Electron). Auger electrons lead to multiple inelastic collisions giving rise to secondary electrons (SE). SE have a small escape depth so XAS-PEEM is sensitive to the surface $\approx 1\text{-}10\text{ nm}$ [141].

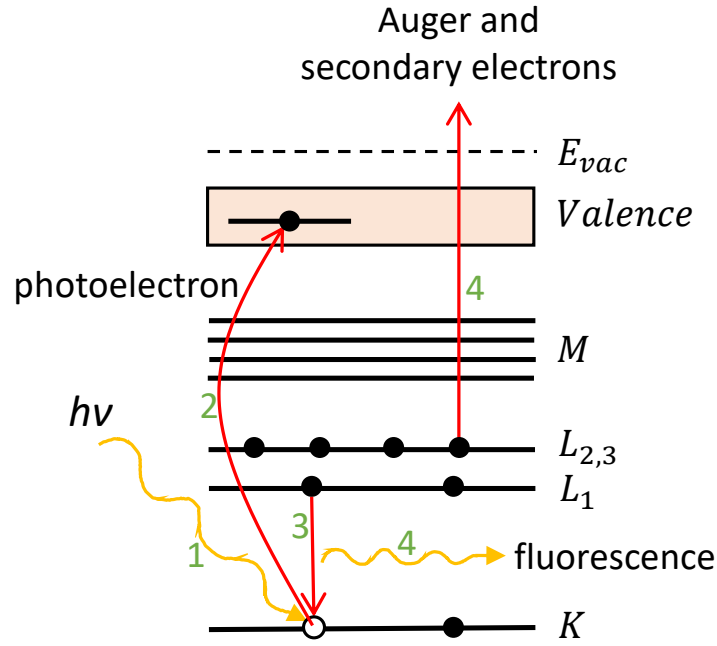


Figure II.10: Schematic of the X-ray absorption process and emission of secondary electrons.

By scanning incident photon energy and detecting the transmitted radiation, XAS reflects the absorption intensity corresponding to a transition between the core to valence band specific to an element. From Fermi's Golden Rule, the transition probability of an electron from the initial core level to an unoccupied state depends on the density of states.

In the thesis, we are interested in the x-ray absorption near edge structure (XANES) of an absorption spectrum at the Ti $L_{2,3}$ edge to probe the ferroelastic strain at the surface. The Ti $L_{2,3}$ edge corresponds to the excitation of Ti $2p$ core levels into the Ti $3d$ band.

Generally, x-ray absorption depends on the orientation of the electromagnetic wave electric field with respect to the sample. This makes two possible XAS imagery modes: X-ray Magnetic Circular Dichroism (XMCD) and Linear Dichroism (XLD). XMCD is used to probe the magnetic state of ferromagnetic 3d transition compounds. The XMCD image is the subtraction of two XAS images with opposite circular polarization (c_+/c_-): $I_{XMCD} = (I(c_-) - I(c_+))$ [142]. Ferromagnetic

domains with an opposite orientation along the photon beam will appear as bright and dark regions on the XMCD image.

XLD follows the same principle as XMCD, but the photon polarizations are linear: l_h horizontal polarization and l_v vertical polarization: $I_{XLD} = (I(P_h) - I(P_v))$. XLD can be sensitive to electric polarization [143]. Moreover, ferroelastic domains have different spontaneous strain directions, which could be probed by the polarized light interaction on the directional 3d orbitals for the L-edge. As shown in figure II.11, linearly polarized light is sensitive to the 3d orbital direction. For example, in the figure configuration, there will be a significant absorption between the l_v polarized light and the d_{z^2} orbital and no absorption with d_{xy} . XLD-PEEM images can then highlight the ferroelastic strain distortions on the Ti 3d orbitals.

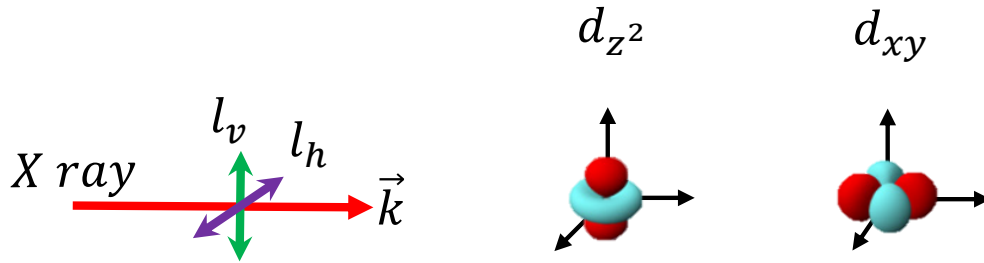


Figure II.11: Schematic of the linearly polarized X-ray probing of the empty 3d orbitals.

B . Low Energy Electron Microscopy (LEEM)

In 1933, Brüche showed that a surface can be imaged by using photoelectric emission [124] and the same year, Zworykin showed that a surface can be imaged with bombarding electrons [144]. Low Energy Electron Microscopy (LEEM) is an electron-in, electron-out technique which improved with the development of electron optics and UHV chambers. LEEM images were shown by Teliëps and Bauer in 1985 with a resolution of 20 nm [145, 146] thanks to new UHV chamber design. The general principles of electron emission microscopy were discussed in section A.3. We will directly focus here the presentation on the Elmitec Spectroscopic Photoemission and Low Energy Electron Microscopy (SPELEEM) specificities.

B.1 . SPELEEM experimental setup

Thesis LEEM experiments and synchrotron PEEM were performed with a SPELEEM represented in figure II.12. The microscope can perform LEEM and PEEM experiments by switching between an electron gun and a photon source. The imaging column is common to both.

The electron gun has a potential of -15 to -20 kV. Magnetic condenser lenses in the illumination column shape and center the electron beam on the sample. The electron source and the electron optics of the illumination column are chosen to produce in the back focal plane of the objective lens (diffraction plane) a sharp cross-over point with high current density to obtain a parallel illumination on the sample. A LaB_6 thermionic emitter, a high brightness and angular range electron gun is used.

As in the NanoESCA PEEM, the sample is part of the electron optics, in which the incident electron beam with an energy of 15-20 keV is decelerated in the retarding field over the last 2 mm in front of the sample to interact with the sample at a low energy of -5 to 50 eV. Electrons are backscattered or reflected by the sample depending on their kinetic energy. Then electrons are reaccelerated into the objective lens. The prism behind the objective lens bends the incident electrons towards the sample to have a normal electron emission and the emitted/reflected electrons of the sample to the imaging column. The sample holder is at a potential of -15 to -20 kV \pm , a low voltage called the start voltage, so that effectively the electrons have incident energy equal to the start voltage (STV) with respect to the sample [146].

In the magnetic prism, an aperture on an incident electron side or on the reflected side can be used to select a smaller area on the surface for local spectroscopy EELS (Electron Energy Loss Spectroscopy) or micro-LEED (Low Energy Electron Diffraction). The intermediate lens in the imaging column is used to switch between imaging an image plane for real space imaging and the diffraction plane for LEED.

The hemispherical analyzer is an energy-filtering stage for spectroscopic imaging. As in the NanoESCA setup, to scan the photoelectron kinetic energy, E_{pass}

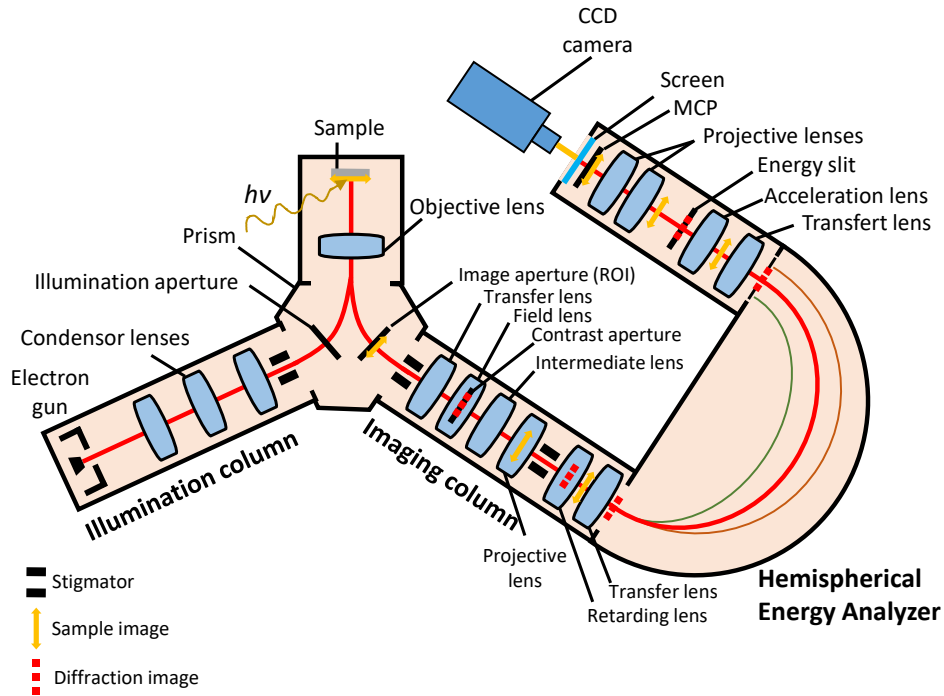


Figure II.12: Schematic of the Elmitec SPELEEM. The electron path is shown by the red dashed lines.

stays fixed, and the sample potential (STV) is swept.

A contrast aperture in a diffraction plane is also present to cut high-angle electrons to improve the spatial resolution for real space imagery. The typical spatial resolution in the LEEM is 20 nm [134]. A slit after the analyzer can be used to remove secondary electrons which form a continuous background on the image and to improve the energy resolution.

B.2 . Surface potential: MEM-LEEM transition

As explained above, the sample start voltage is the kinetic energy of the incident electrons with respect to the sample surface. If incident electrons have a lower kinetic energy than the surface potential of the sample, they are repelled by the surface potential, weakly interacting with the surface. At these energies, the observation is called Mirror Electron Microscopy (MEM) reflection. For higher kinetic energies, electrons have a stronger interaction with the surface and penetrate the sample. Then they are elastically or inelastically scattered and backscattered electrons are detected. This is called Low Energy Electron Microscopy (LEEM). At low start voltage, the reflected intensity is high (mirror mode) and when the energy of the electrons becomes high enough to overcome the surface potential barrier, the electrons penetrate the surface, and the reflectivity intensity decreases suddenly. The transition between the MEM and LEEM is the surface potential, corresponding to the energy when electrons start to penetrate the sample. An

example of MEM and LEEM images of upwards (P_{up}) and downwards (P_{down}) polarized domains and intensity curves in function of the start voltage $I(STV)$ of polar domains are shown on image II.13 [147]. The MEM-LEEM transition shift between the two domains gives the surface potential difference due to the polarization difference. Contrast at the MEM-LEEM transition is therefore an ideal tool to probe, for example, charge differences in calcium titanate domain walls intersecting the surface with a polarization component perpendicular to the surface, pointing either inwards or outwards.

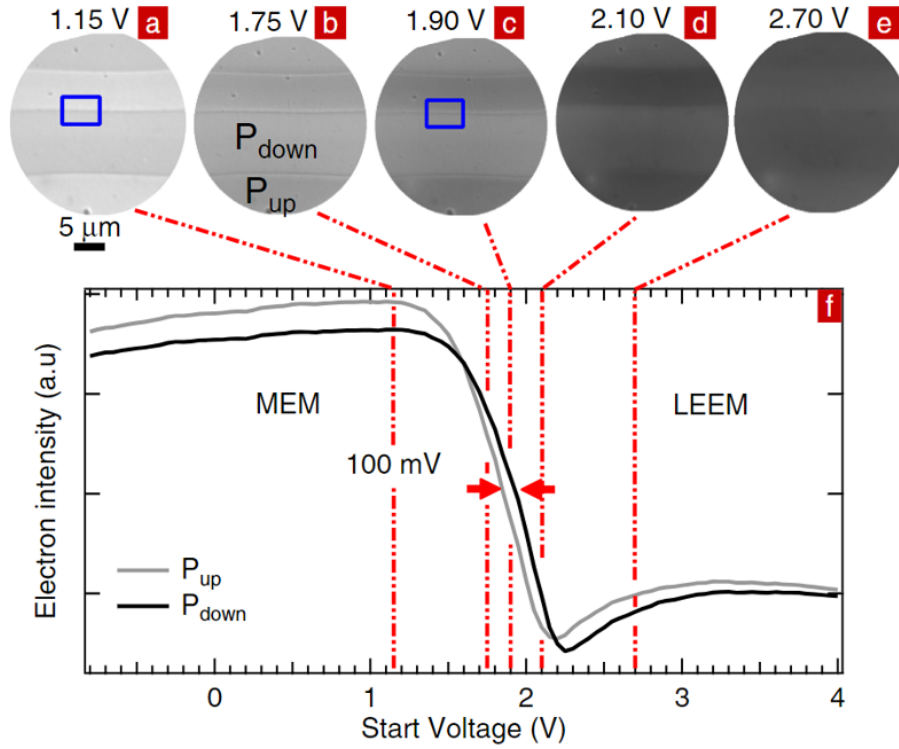


Figure II.13: (a)-(e) MEM and LEEM images at different start voltages of a $Mg : LiNbO_3$ surface. (f) Electron intensity curves extracted from P_{up} and P_{down} domains [147].

The $I(E_{STV})$ curves can be fitted by a complementary error function described in equation 12 to accurately extract the energy of the MEM-LEEM transition i.e. the surface potential energy [148].

$$I(E_{STV}) = I_0 + A \cdot \text{erfc}\left(\frac{E_{SP} - E_{STV}}{\sqrt{2}\sigma}\right) \quad (12)$$

with E_{STV} the start voltage i.e. the incident energy, E_{SP} the surface potential energy, A the amplitude of the error function, σ the standard deviation of the Gaussian and $\text{erfc}(x) = 1 - \text{erf}(x)$ so $\text{erfc}(x) = \frac{2}{\sqrt{\pi}} \int_x^\infty e^{-t^2} dt$. With a series of images as a function of start voltage i.e., $I(E_{STV}, x, y)$ images, we can extract

at each pixel (x, y) the surface potential by using the function in an automated procedure and generate a map of the surface potential.

B.3 . Electrical topography

Domain or domain wall surface polarity can be seen in LEEM because it gives rise to a surface charge density that locally modulates the electrostatic potential. For example, domain walls of CaTiO_3 are polar and can be seen in LEEM because of this effect, as polar domains in BaTiO_3 . As a first approximation, if the converging lenses are not taken into account, incident electrons interact with the charged area (for example, a domain wall in CTO) such that positively charged areas sweep the electrons inwards, as shown in image II.14 [149], so give rise to a bright contrast in MEM. On the other hand, negatively charged areas sweep the electrons outwards and give a dark contrast. In the SPELEEM, the imaging column is made of 5 lenses, an odd number, which inverts the resulting contrast on the detector: a positively charged area will give rise to dark contrast, and a negatively charged area bright contrast in MEM.

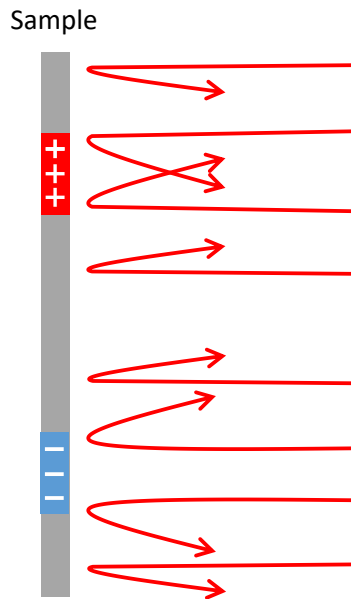


Figure II.14: Distortion of electron trajectories by positively and negatively charged areas on the surface in MEM. Adapted from [149]

Over or under-focusing the surface can enhance the domain wall contrast. The focus is modulated by the objective lens current. In the setup, lowering the current by 100 mA is equivalent to decreasing the sample-lens distance by 1 mm. The focus behavior is the same as in optical microscopy: going away from the focus value has an incidence on the visualized object size, as shown in the example on image II.15 [147].

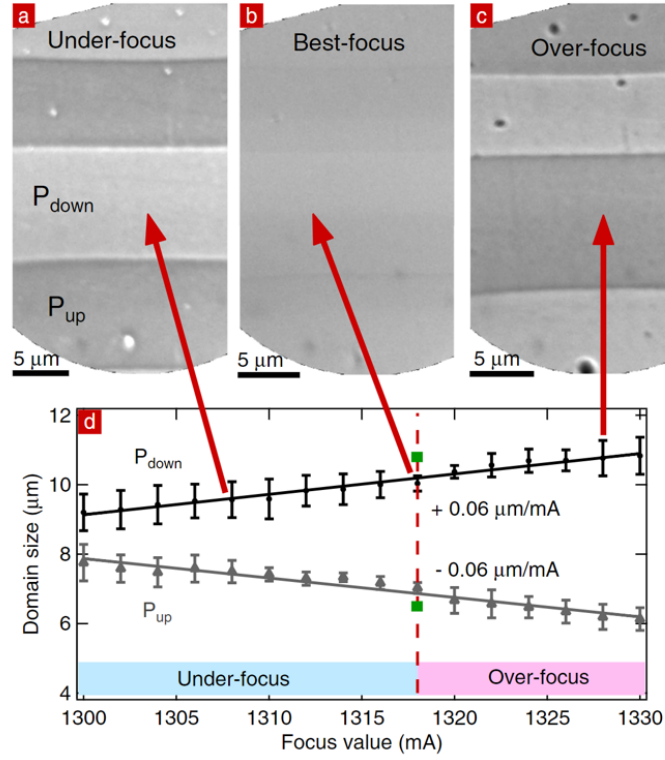


Figure II.15: Domains and domain walls of magnesium-doped lithium niobate in the same area in (a) Under-focus (b) best-focus and (c) over-focus. (d) Evolution of the domain sizes with focus values expressed in coil current (mA): under-focus indicated by the light blue bar, best-focus indicated by the fuchsia dashed line, and over-focus images indicated by the light pink bar. Green squares indicate the domain size as measured by Piezoresponse Force Microscopy (PFM). [147]

In our MEM observations for CaTiO_3 , in under-focus, domain walls with a darker contrast have a polarization pointing upwards (P_{up}) and domain walls with a brighter contrast have a polarization pointing downwards (P_{down}). The contrast is inverted in over-focus. MEM images shown in the thesis are taken slightly under-focus.

B.4 . Physical topography

Physical topography also influences local electric fields. Theoretical studies on the effect of topography were done by Nepijko et al. [149, 150, 151]. For example, a step on the analyzed surface of a sample will give contrast in MEM. Figure II.16 shows the current density j on the LEEM screen relative to the current without the topographical feature j_0 and without a contrast aperture and converging lenses between the sample and the image. At the modeled surface step, a dark area (current ratio below 1.0) appears on the image, and further away, a more defined bright area appears because of the topography. Other geometrical reliefs would

also locally modify the surface electric field and then show a contrast in MEM.

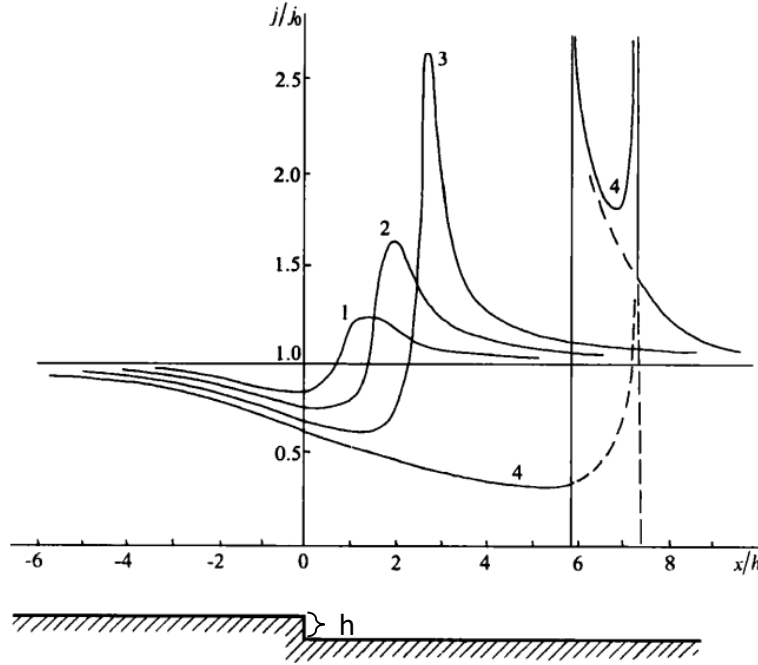


Figure II.16: Current density distribution j/j_0 on the screen in MEM mode for a geometrical step of different heights: $h = 7.2$ (1), 14.3 (2), 23 (3), and 72 Å (4) [149].

B.5 . Low Energy Electron Diffraction (LEED)

Low Energy Electron Diffraction (LEED) is used to check the crystallinity of the first few surface atomic layers. LEED uses electrons with a wavelength comparable to the inter-atomic distances to produce a diffraction pattern in reflection.

Shortly, this technique consists of an electron gun emitting electrons normal to the surface, which are elastically diffracted by the surface lattice periodicity. because of the atoms' crystalline arrangement at the surface. Angular-specific diffraction beams form a diffraction pattern (LEED spots) on a fluorescent screen, showing the reciprocal lattice of the surface of the sample. Electrons have energies from 30 to 200 eV and penetrate up to 1 nm on the surface. The technique is very surface sensitive, excellent to assess the surface crystalline quality from the spot pattern. If a sample is significantly contaminated by organics and/or carbon at the surface, the LEED spots would be more diffuse and extinguished for highly contaminated surfaces.

LEED can be done area averaged on a sample in our UHV preparation chamber to assess the surface quality before PEEM/LEEM experiments. In the LEEM, we can perform more specifically μ -LEED, where we select emission from an area with an aperture of varying size placed in an image plane and perform LEED in diffraction mode (project a diffraction plane on the CCD camera) with electrons coming

specifically from the selected area. In this technique, incident electron energies can vary between 10-100 eV. It enables us to locally access the crystal quality and relative orientation, useful for ferroelastic materials where domain surface angles and lattice orientation can be seen. Figure II.17 shows diffraction patterns from the CTO surface at (b) and far from (c) a domain wall. The fourfold splitting of the spots in figure II.17b is due to the four ferroelastic domain twinning in the selected area by the aperture. Four domains with different angles between each other mean four diffraction patterns slightly shifted in the reciprocal space. Moreover, the LEED pattern on both images shows the orthorhombic lattice of CTO with the distance between the specular (0,0) and peripheral (1,0) diffraction spots slightly different (lattice parameters $a \neq b$). Green spots in between are long-range surface reconstructions, possibly oxygen vacancies. The shorter range periodicity highlighted by the blue spots corresponds to the pseudo-cubic periodicity, rotated by 45° from the orthorhombic axes with $a_{pc} = \frac{\sqrt{2}}{2}a_O$, as already shown with the lattice orthorhombic to pseudo-cubic correspondence in figure I.12.

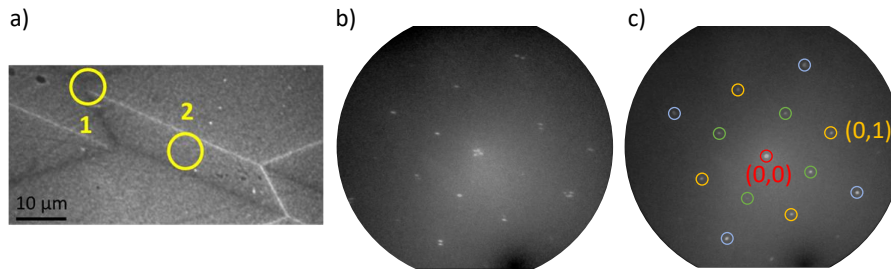


Figure II.17: Micro-Low Energy Electron Diffraction: μ -LEED on CTO ferroelastic domain and domain walls at 30 eV. a. MEM image of CTO surface showing the μ -LEED area of interest. b. μ -LEED on several domain walls of area 1. c. μ -LEED on a domain of area 2 (outside a domain wall).

B.6 . Electron Energy Loss Spectroscopy (EELS)

Electron Energy Loss Spectroscopy (EELS) is performed in the LEEM setup using dispersive mode. In this mode, the hemispherical analyzer disperses the electrons according to their energy after the imaging column. We then register on the detector an intensity trace representing the loss intensity as a function of energy. A typical dispersive trace is shown in figure II.18. We use an image aperture in the sector field (see figure II.12) to irradiate a small area on the surface. Typically the aperture has a diameter of $3 \mu\text{m}$ on the surface.

We fix the incident electron energy and look at the detected electron spectrum. We have on the dispersive image two spots corresponding to the elastically backscattered electrons: the elastic peak and the loss peak, corresponding to the inelastically backscattered electrons. The possibility to perform loss spectroscopy on specific features on the surface, thanks to the MEM imagery's good spatial

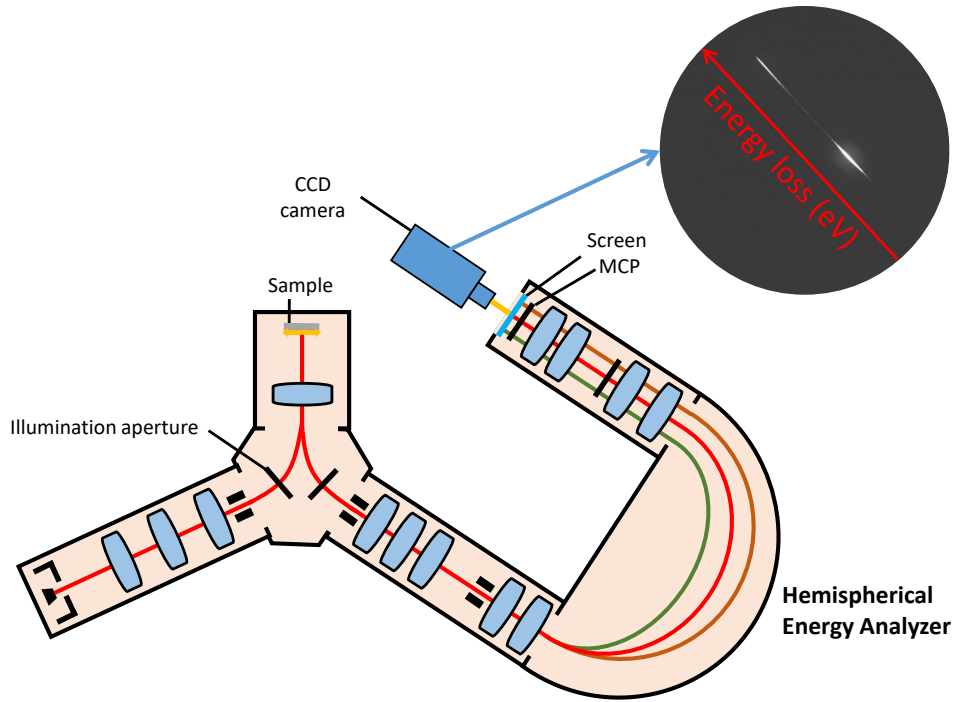


Figure II.18: LEEM setup in dispersive mode. The illumination aperture and the electron path in the analyzer are shown. An image of the typical energy loss dispersion is also shown. The brighter central peak is the elastic electrons followed by the secondary electrons loss peak.

resolution, opens the perspective to study the electronic properties of CTO ferroelastic domains and domain walls. Domain walls are small features in width at the surface, but the technique is sensitive enough to show loss spectroscopy variation between domains and domain walls.

C . Thin film deposition: Pulsed Laser Deposition (PLD)

Several chemical and physical deposition techniques can be used for oxide deposition. To grow (001) oriented CaTiO_3 thin films, we considered Pulsed Laser Deposition (PLD), which has many advantages. It allows epitaxial growth, which constrains the orientation of the film in the same direction as the substrate, and a fast deposition speed (up to 10 nm/min). For complex material deposition, it permits also a good stoichiometric transfer from the target to the thin film for non-volatile elements.

Pulsed laser deposition is a high vacuum technique. A laser is guided with mirrors and its size is fixed by a mask to ablate a rotating target, made of the desired material for the thin film, with the desired stoichiometry. The substrate is at a high temperature, in front of the target. The laser photons' interaction with the target ablates material from to the substrate in the form of a plume made of

the target ionized atoms [152]. Partial pressure of oxygen is present in the chamber to stabilize the oxygen content in the substrate and film oxides. A schematic of the technique is represented in figure II.19.

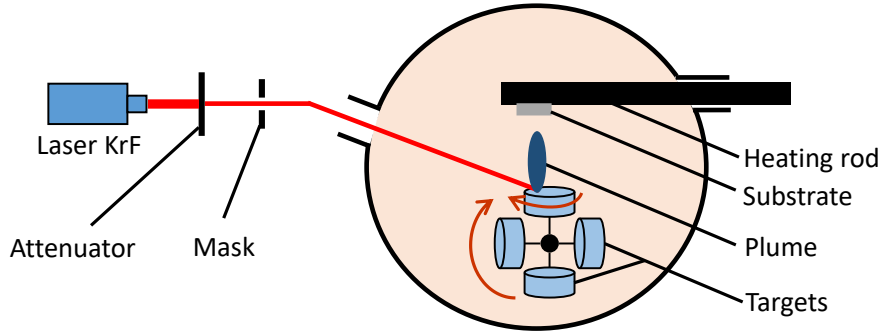


Figure II.19: Schematic of the pulsed laser deposition growth.

The deposition chamber is under vacuum by a turbomolecular pump coupled with a primary pump. Typical pressure in the chamber before the deposition is 2.10^{-6} mbar . The oxide substrate is heated with a partial pressure of oxygen to avoid oxygen desorption. Several targets can be mounted in the chamber, shown in image II.19, to allow in-situ deposition of several thin film layers of materials without breaking the vacuum or temperature, for example, to grow an electrode layer followed by a CaTiO_3 layer. The laser is focused on the edge of the target which rotates in-plane, with an angle of 45° from the surface, to maximize the use of the target (bigger effective surface) than if the target was focused in the center. A mask is used to control the size of the laser spot on the target i.e. the amount of ablated material per pulse. The substrate is fixed on the heating rod with silver paste for a good thermal transfer, at a distance of 5 cm from the target. Before deposition, the targets are cleaned by the laser at high fluence and with a bigger mask than the one used for deposition.

After the deposition, samples are structurally characterized by means of Atomic Force Microscopy (AFM), to check the surface roughness, X-ray diffraction (XRD) for the orientation and epitaxial conditions, and X-ray reflectivity (XRR) for the thickness of the films. Deposition parameters for thin film CaTiO_3 are discussed in Appendix D.

D . Thin film characterization techniques

In order to characterize our films, several techniques are used. Atomic Force Microscopy (AFM) is a surface topography technique from which we analyze the surface roughness of the thin film samples and observe the ferroelastic domain topography. X-Ray Diffraction (XRD) and X-Ray Reflectivity (XRR) techniques are used to analyze the structural properties and thickness of our deposited thin films.

D.1 . Atomic Force Microscopy (AFM)

Atomic force microscopy is a technique used to measure the surface topography of substrates and film. We can also calculate the surface roughness. Most of the topography images shown in the thesis are done in contact mode. The surface is scanned with a tip on top of a cantilever and its deflection by the surface topography is measured by a laser. The laser reflection hit a quadrant detector which will reconstruct a surface topography map from the laser position. From the surface height $z(x, y)$ on a map of area S , we can estimate the quadratic roughness R_{RMS} with equation 13.

$$R_{RMS} = \sqrt{\frac{1}{S} \sum_0^S (z(x, y) - z_{moy})^2} \quad (13)$$

D.2 . X-ray Diffraction (XRD)

The growth of the films by PLD is epitaxial: the out-of-plane orientation of $CaTiO_3$ follows the orientation of the substrate. Deposition parameters are tuned to enable good epitaxial growth and so a good orientation of the film. Film orientation is an important step to engineer the desired electromechanical parameters in the film. XRD is a characterization technique that can indicate the lattice parameters of our films. The measurement was realized at C2N, in collaboration with Thomas Maroutian, with a PANalytical diffractometer.

X-rays with wavelength λ are diffracted from the atomic planes of the analyzed crystal, separated by a distance $d_{h,k,l}$. The reflected waves' constructive interferences are occurring for specific angles θ between the incident beam and a family of planes (h, k, l) . The interference pattern follows Bragg's law 14.

$$2d_{h,k,l} \sin(\theta) = n\lambda \quad (14)$$

For a simple cubic structure with a lattice parameter a , we have 15:

$$d_{h,k,l} = \frac{a}{\sqrt{h^2 + k^2 + l^2}} \quad (15)$$

To determine the interatomic plane spacing, we realize $\theta - 2\theta$ scans. The detector and the X-ray source are moving together to scan 2θ , the angle between the transmitted beam and the reflected beam. The family of planes (h,k,l) present in the sample will satisfy the Bragg condition for given angles θ of the X-ray source with the surface, and from the resulting intensity will be detected and form a peak in the spectra. We extract from the measurements the out-of-plane lattice parameter of $CaTiO_3$ in a pseudo-cubic approximation on the (002) peak. We will then use $d_{001} = \frac{a}{2}$ and $a = \frac{\lambda}{\sin(\theta)}$ to calculate the lattice pseudo-cubic parameter. The X-ray wavelength is $\lambda = 1.54058 \text{ \AA}$ from a copper anti-cathode X-ray emission with a monochromator.

D.3 . X-ray Reflectivity (XRR)

This technique is used to estimate the thickness of thin films (up to approximately 100 nm). The beam penetrates the film and is reflected by the internal interfaces between different layers and the film/substrate interface. The electronic density and the film thicknesses can be deduced because of the difference in refractive index between materials and the interferences fringes. When $\theta > \theta_c$, the critical angle when the beam penetrates in the sample, interference fringes appear as shown in image II.20. The sample is an $LaSrMnO_3$ electrode film on $LaSrAlTaO_3$ substrate.

The fringe spacing $\delta\theta$ is related to the film thickness d_{film} following equation 16. By averaging the spacing on several fringes, we measure a thickness of 27 nm.

$$\delta\theta = \frac{\lambda}{2d_{film}} \quad (16)$$

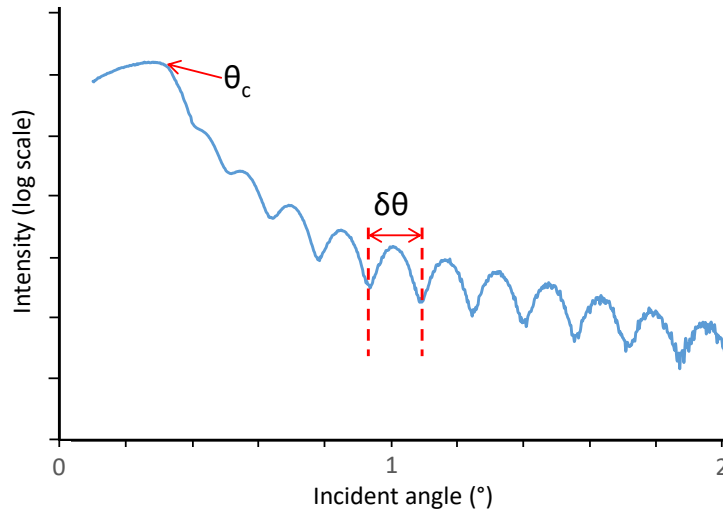


Figure II.20: X-ray reflectivity scan in log scale. Experimental data in blue shows the fringes from the beam reflections at the interfaces of a thin film sample.

E . Raman spectroscopy

E.1 . Technique description

Raman spectroscopy is a non-destructive, non-contact technique used to study the domains and walls in thin film samples and their accommodation with the substrate. The Raman-active modes correspond to the structure vibrational states, related to the material symmetries. With a polarized incident light, it is possible to excite different Raman-active modes depending on the ferroelastic ordering [153] and observe small Raman peak variations at the walls [154].

This technique is used to better understand the relation between the ferroelastic domain walls of the $LaAlO_3$ substrate and the PLD-grown thin film. The probing depth of this technique is a few microns, corresponding to the IR wavelength, excellent to detect simultaneously signals from the $CaTiO_3$ thin film and from the $LaAlO_3$ substrate.

Experiments were performed on a Renishaw inVia confocal Raman microscope. Monochromatic laser with defined polarization interacts with the material vibrational states. Backscattered light after the interaction is going through the optical setup again and then is spectrally dispersed by a diffraction grating on a CCD camera. Several lasers with wavelengths of 442 nm, 532 nm, and 633 nm are available. The spectral resolution depends on the laser and diffraction grating used. The spatial resolution is fixed by the Rayleigh equation (diffraction limit).

Experiments in this thesis were performed with the 442 nm laser (red) which gives the best spectral resolution of the available lasers ($\approx 1\text{ cm}^{-1}$). The excitation of a vibrational state gives rise to a peak at a wavenumber related to the vibration frequency, its intensity is proportional to the square of the symmetric second-rank Raman tensor mode. At this wavelength, the theoretical spot size, which gives the spatial resolution, is $d = 635\text{ nm}$. Pixel-by-pixel mappings, across ferroelastic domain walls, have a pixel size of $0.1\text{ }\mu\text{m}$. We present in the [Appendix D](#) pixel-by-pixel scans of the Raman modes in LAO/LSMO/CTO. The generated 3D stack of data is analyzed by Principal Component Analysis (PCA).

E.2 . Principal Component Analysis (PCA)

The experimental data in Raman spectroscopy consists of one Raman spectrum at each pixel of a selected area. One example of a Raman spectrum on a CTO single crystal is given in figure [II.21a](#). We are interested in mapping the Raman modes across the pixels to see variations. One method can simply be to map one peak intensity, as in image [II.21b](#), or a ratio between two peaks for each pixel. We can see that different ferroelastic domains can be mapped depending on the polarization conditions and the peak choice.

In our case, in order to know which peaks would give different Raman mode strengths between ferroelastic domains, we perform a PCA. In addition to the data analysis, PCA is also useful to extract weak signals from the noise, relevant for the CTO thin film Raman peaks that are less intense compared to substrate peaks. PCA extracts similarities and differences across all the pixels. Characteristic signatures from a Raman spectrum and also spectral features hidden in the noise can be identified.

The basis of PCA is that each spectrum S can be written as a linear combination of a reduced number of components PC_i , as in equation [17](#) [[155](#)]. We can then plot the component score k_i at each pixel on a map to see the component strength, giving one map per component.

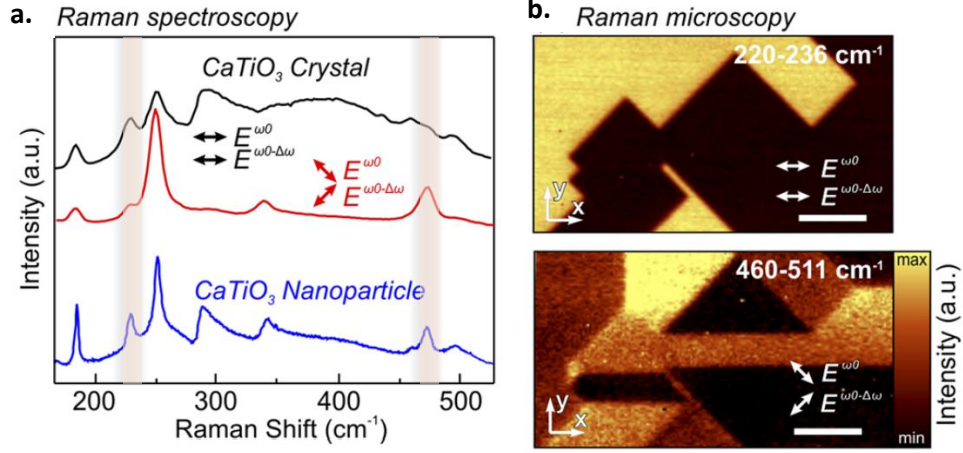


Figure II.21: a. Raman spectroscopy of CaTiO_3 bulk single crystal with different polarization conditions. For comparison, the spectrum for CaTiO_3 nano-particles (blue) is shown at the bottom. b. Raman mapping of a (110) CaTiO_3 bulk single crystal surface, with the white bar being $8\ \mu\text{m}$ [153].

$$S = S_{mean} + \sum_i k_i \cdot PC_i \quad (17)$$

with k_i the component PC_i score, a scalar, of the analyzed pixel and S_{mean} the mean of all spectra. Having the right number of total components is important, for not missing some information because there were not enough components calculated or having components that show only noise from the data. The key is to select the minimal number of components that explain the total variance of the data. The proportion P of the variance V for a parameter is written as in equation 18. The graph in figure II.22 shows the variance for each component on a dataset from one CTO thin film Raman measurement. We can see that the first 2 components are enough to explain most of the variance of the system, the 3 others are very close to zero, likely to be only noise.

$$P(PC_i) = \frac{V(PC_i)}{\sum_i V(S)} \quad (18)$$

For the Raman 2D maps in this thesis, shown in the CTO thin film domain wall engineering Appendix D, we would typically have components each representing ferroelastic domains. The crystallographic axes between domains are rotated, which induces a variation in the intensity of some of the Raman peaks that can be imaged on PCA component score maps.

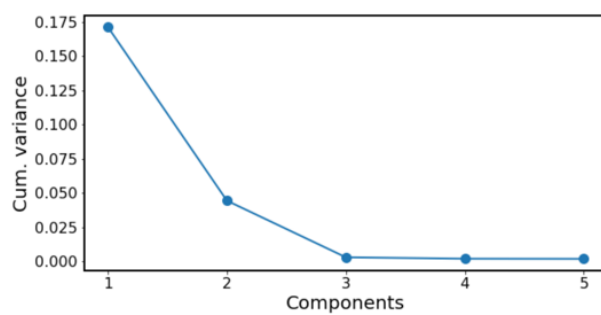


Figure II.22: Variance of a PCA analysis of the first five components for a thin film CaTiO_3 Raman spectroscopy 2D map.

III - Surface domain ordering in CaTiO_3 (001)

Ferroelastic domain walls are oriented so as to satisfy strain compatibility between two adjacent ferroelastic domains, and therefore minimize stress and elastic energy. Identification of the ferroelastic domain state, as the strain direction and/or a surface twin angle, is necessary to understand the electromechanical response of the material.

In this chapter, we will first present the theoretical domain states in CaTiO_3 from symmetry and strain considerations. Then, the quantitative identification of the surface topography related to the surface twin angle will be addressed in section III.B. Lastly, in section III.C, the observation of the surface strain state in CTO ferroelastic domains using X-ray linear dichroism.

For the ferroelastic surface topography and domain strain identification, we use a surface-sensitive electronic microscopy technique, PEEM, in both photoemission and absorption modes, which combine a spatial resolution of several orders smaller than the typical domain width and high sensitivity to the surface topography and strain.

A . CaTiO_3 strain states

The condition of strain compatibility between two adjacent ferroelastic domains allows us to derive equations for possible domain walls and hence the possible domain spontaneous strains and the possible domain walls. For each pair of ferroelastic domains, we then deduce the possible twin wall plane orientation and surface topography angle.

A.1 . Spontaneous strain tensor

The CaTiO_3 second rank symmetric spontaneous strain tensor S_1 is given by the cubic $Pm\bar{3}m$ to orthorhombic $Pnma$ ferroelastic transition [48], in the pseudo-cubic approximation:

$$S_1 : \begin{pmatrix} \epsilon_{11} & \epsilon_{12} & 0 \\ \epsilon_{12} & \epsilon_{11} & 0 \\ 0 & 0 & -2\epsilon_{11} \end{pmatrix} \quad (1)$$

The spontaneous strains ϵ_{11} and ϵ_{12} are referred to the pseudocubic lattice directions and are calculated from the lattice constants in the cubic and orthorhombic phase, determined by XRD measurements [156, 59]. The tensor strain coefficients are [156]:

$$\begin{aligned}
\epsilon_{11} = \epsilon_{22} &= \frac{1}{2} \left(\frac{\frac{a_o}{\sqrt{2}} - a_c}{a_c} + \frac{\frac{b_o}{\sqrt{2}} - a_c}{a_c} \right) \\
\epsilon_{33} &= \frac{\frac{c_o}{\sqrt{2}} - a_c}{a_c} = 2\epsilon_{11} \\
\epsilon_{12} &= \frac{1}{2} \left| \frac{\frac{a_o}{\sqrt{2}} - a_c}{a_c} - \frac{\frac{b_o}{\sqrt{2}} - a_c}{a_c} \right| \\
\epsilon_{13} = \epsilon_{23} &= 0
\end{aligned} \tag{2}$$

with a_o , b_o and c_o the orthorhombic lattice constants and a_c the lattice constant of the high symmetry phase. Strain coefficients represent the lattice deformation from the high to low symmetry phase, with a 45° rotation of the $[100]$ and $[010]$ directions between the two phases (lattice structure details in [B.1.1](#)). We have at room temperature: $\epsilon_{11} = 5.7 \times 10^{-4}$ and $\epsilon_{12} = 5.5 \times 10^{-3}$ [65]. Moreover, the second-rank strain state S_1 in the lattice is linked to the second-rank mechanical stress tensor σ_1 by a generalized Hooke's law: $\sigma_1 = c \cdot S_1$, with c the fourth order stiffness tensor.

Then six possible strain states S_i exist in $CaTiO_3$ in its orthorhombic phase, from the material lost symmetry operations between the cubic and orthorhombic phase. They correspond to six possible strain orientations, i.e. six possible ferroelastic domains. They differ by their spontaneous strain tensor direction in the lattice:

$$\begin{aligned}
S_1 &: \begin{pmatrix} 0.00057 & 0.0055 & 0 \\ 0.0055 & 0.00057 & 0 \\ 0 & 0 & -0.00114 \end{pmatrix} \\
S_2 &: \begin{pmatrix} 0.00057 & -0.0055 & 0 \\ -0.0055 & 0.00057 & 0 \\ 0 & 0 & -0.00114 \end{pmatrix} \\
S_3 &: \begin{pmatrix} 0.00057 & 0 & -0.0055 \\ 0 & -0.00114 & 0 \\ -0.0055 & 0 & 0.00057 \end{pmatrix} \\
S_4 &: \begin{pmatrix} -0.00114 & 0 & 0 \\ 0 & 0.00057 & 0.0055 \\ 0 & 0.0055 & 0.00057 \end{pmatrix} \\
S_5 &: \begin{pmatrix} 0.00057 & 0 & 0.0055 \\ 0 & -0.00114 & 0 \\ 0.0055 & 0 & 0.00057 \end{pmatrix} \\
S_6 &: \begin{pmatrix} -0.00114 & 0 & 0 \\ 0 & 0.00057 & -0.0055 \\ 0 & -0.0055 & 0.00057 \end{pmatrix}
\end{aligned} \tag{3}$$

A.2 . Domain wall orientation

From the possible spontaneous strain directions, we can deduce the possible domain pairs (S_i, S_j) and calculate the difference in their spontaneous strain tensors $\Delta\epsilon = \epsilon_i - \epsilon_j$. For each pair, the equations of the two possible compatible domain walls, one for each compatible orientation, are calculated from the mechanical compatibility equation $\Delta\epsilon_{ij}x_ix_j = 0$. The equations of the possible domain walls are [48, 65]:

$$\begin{aligned} x = 0 \quad or \quad y = 0 \quad or \quad z = 0 \\ y = \pm z \quad or \quad z = \pm x \quad or \quad x = \pm y \\ 3\epsilon_{11}(x \pm y) \pm 2\epsilon_{12}z = 0 \\ 3\epsilon_{11}(z \pm x) \pm 2\epsilon_{12}y = 0 \\ 3\epsilon_{11}(y \pm z) \pm 2\epsilon_{12}x = 0 \end{aligned} \tag{4}$$

with x,y, and z as the pseudocubic axes. Two wall types are obtained: nine W mirror planes, whose orientation is fixed by symmetry, and twelve W' planes, whose orientation depends on the coefficients of the spontaneous strain tensor describing the orthorhombic distortion [63]. From the equations of the plane of the domain walls, we can also deduce the inclination angle with respect to the surface and the twin angle of the ridge/valley. The full possible ferroelastic domain pairs and the domain wall plane equations are given in the annexed table 1. A short table highlighting the equivalent domain wall is given here in table III.1.

Pairs	Wall equation	Azimuthal angle/[100]	Wall inclination angle/(001)	Twin angle
S_1/S_2	$x = 0$	90°	90°	180°
S_1/S_4	$z = x$	90°	135°	180°
S_2/S_5	$y = -z$	180°	45°	180°
S_3/S_4	$x = -y$	135°	90°	180.9°
S_3/S_5	$x = 0$	90°	90°	181.3°
S_3/S_6	$x = y$	45°	90°	180.9°
S_4/S_6	$y = 0$	180°	90°	178.7°
S_5/S_6	$x = -y$	135°	90°	179.1°

Table III.1: Domain walls plane equations for some non-equivalent W walls, wall surface trace angle with respect to the $[100]_{pc}$ direction, inclination angles from the (001) surface, and twin angles. The complete table is the appendices table 1.

Each domain pair are ordered, i.e. (S_i/S_j) is different from (S_j/S_i) . For example, three consecutive domains with the consecutive strain states $S_1/S_2/S_1$ will form two walls with opposite P_{up} and P_{down} polarity. So for one possible wall, two supplementary twin angles are possible depending on the wall polarity, but only one is displayed in the table.

B . Surface topography quantification of CaTiO_3 (001) ferroelastic twin angles

The ferroelastic domain ordering gives rise, at the surface, to a factory roof like topography with valleys and ridges. The topography is intimately connected to a particular strain state in the ferroelastic domains and determines the orientation and polarity of domain walls.

We have studied the physical topography resulting from the factory roof-like surface. This has been done by exploring the angular space in PEEM, specifically by using an aperture in the microscope's back focal plane to select photoelectron take-off angles and reveal and quantify the twin angles. Surface topography is usually observed by AFM techniques. We propose full-field imagery of several twins for direct in-situ analysis of the ferroelastic ordering. In the PEEM, angles are usually observed in reciprocal space [118, 157] but the spatial resolution is limited by the region-of-interest aperture size. We implemented a method to quantify surface topography angles in real-space PEEM imaging, to have a better spatial resolution and image several domains at the same time (FoV in the order of $10\ \mu\text{m}$) in order to directly analyze several twins.

B.1 . CaTiO_3 surface topography

The ferroelastic topography at the surface has been observed by atomic force microscopy (AFM). On a CaTiO_3 single crystal sample, surface topography forming valleys and ridges are visible, shown in figure III.1a. The schematic shows the typical factory roof like surface topography. From the height measurements, twin angles can be calculated, as shown in figure III.1b. This twin wall has an angle of 178.8° , close to the theoretical twin angle value between S_3 and S_5 domains of table III.1.

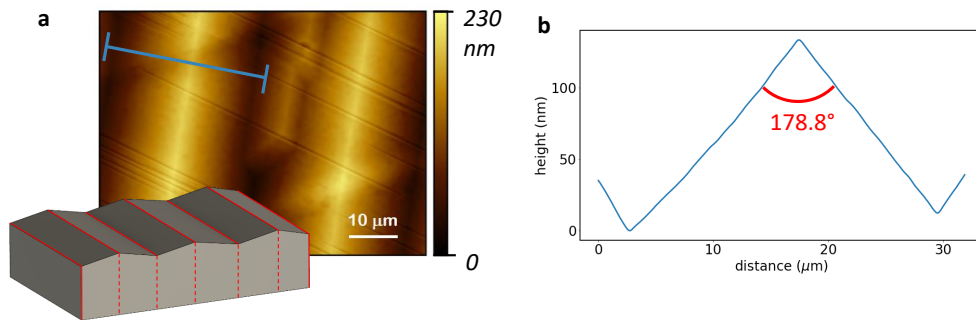


Figure III.1: a. AFM topography image of CaTiO_3 (001) surface, inset schematic of the typical factory roof topography of the surface, and b. height profile along the solid blue line in (a) with a calculated twin angle of 178.8° .

This ferroelastic domain tilt can also be observed in PEEM. Figure III.2a. shows a real space image of two CaTiO_3 domains in PEEM at the Elettra NanoESCA

beamline. Figure III.2b. is a reciprocal space image of the same area. The two spots in III.2b correspond to the bottom of the photoemission parabola for the two domains indicated in red and blue on III.2a. The shift between the spots corresponds to the surface twin angle α_{tilt} between the 2 domains.

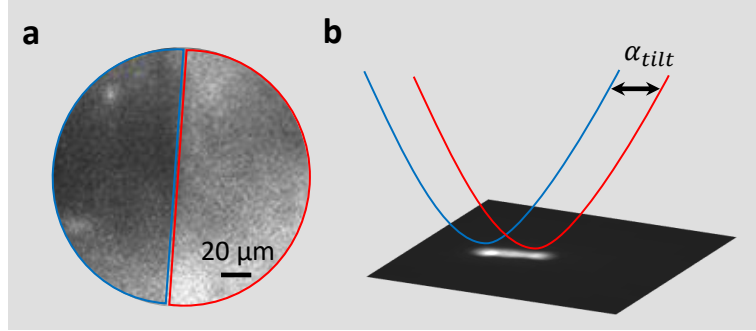


Figure III.2: Real (a) and reciprocal space (b) images of $CaTiO_3$ domains with a tilt angle α_{tilt} . Electrons from the red and blue domains are shown in b. The tilt induces an angular shift in the threshold of the free electron parabola in ARPES, $\alpha_{tilt} = 0.9^\circ$.

Surface ferroelastic angles can be determined in reciprocal space PEEM. The reciprocal space angular shift α_{tilt} between the two parabolas is determined by tilting the sample by a known angle which rigidly shifts the spots. We have for this example an angular distance of $\alpha_{tilt} = 0.9^\circ$ between the spots, i.e. a twin angle of $180 \pm 0.9^\circ$. This twin angle is close to the theoretical twin angle value between S_3 and S_6 domains of table III.1.

However, in reciprocal space, we don't have the spatial resolution offered by real space imagery because the iris aperture of $\approx 10 \mu m$ limits the resolution, we can't determine the twin angle of domains smaller than the iris aperture. Twin angle determination in real space permits a direct determination of all the twin angles of the FoV in the limit of the PEEM spatial resolution of $\approx 50 nm$.

B.2 . Experiment conditions

The sample is a $CaTiO_3$ (001) single crystal from SurfaceNet GmbH. The surface topography is characterized by AFM in contact mode on an area where several ferroelastic domains are present. Figure III.3 shows the AFM amplitude image. Ferroelastic twinning creates a surface topography, visible here. We are interested in the oriented tilt angle of the domains, noted $\alpha_{tilt,i}$ in the figure, from which we can measure the surface twin angle of the domain walls φ . One example between two domains is shown on figure III.3b, $\varphi = \alpha_{tilt,2} - \alpha_{tilt,1}$.

Before introduction into the PEEM vacuum system, the sample was exposed for 5 min to ozone at room temperature to remove the organic contamination. Annealing at $650^\circ C$ in vacuum for 30 min is then sufficient to desorb the oxidized contaminants. It also produces a low concentration of oxygen vacancies, helping to alleviate charging problems during the photoemission process. Furthermore,

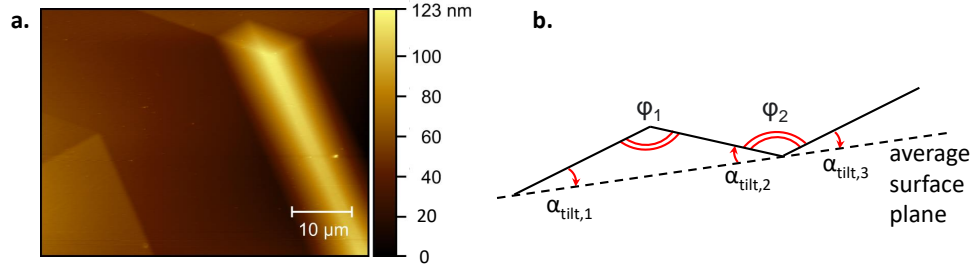


Figure III.3: a. AFM topography image of the analyzed area. A mean plane was subtracted for image clarity, still visible on the second view. b. Schematic showing the ferroelastic twinning at the surface and the domain tilt angles.

in order to avoid charging during photoemission, experiments were carried out at 300°C to improve the evacuation of charges. The experiment was carried out in a ScientaOmicron NanoESCA II with a focused He I source ($h\nu = 21.2$ eV). The pass energy in the double hemispherical analyzer was 50 eV and the entry analyzer slit width was 1 mm so the energy resolution is $\Delta E \approx 0.2$ eV. The spatial resolution is estimated to be $\Delta x \approx 50$ nm [158].

B.3 . Angular sensitivity of the contrast aperture

We use a contrast aperture (CA) of 150 μ m diameter, placed in the back focal plane of the objective lens of the PEEM. Photoelectrons are emitted from the surface with an angular distribution. The ferroelastic twin angle tilts the electron photoemission. The emission is represented in the schematic in figure III.4a. Electrons cross the diffraction plane on the optical axis for normal emission and away from the axis for off-normal emission angles. The CA in the diffraction plane can be moved in the lateral (x) direction to select electrons in a given emission angle range.

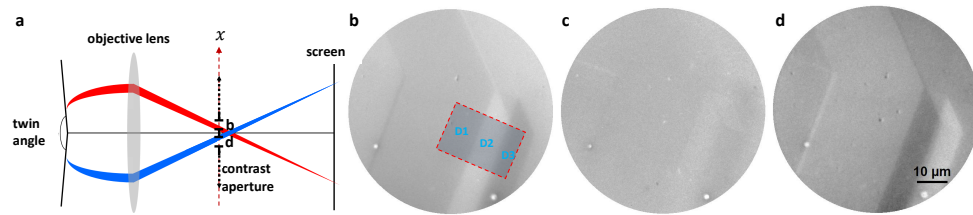


Figure III.4: a. Schematic of the contrast aperture angular selection. PEEM images at $E - E_f = 4.3$ eV. The contrast aperture (CA) is off-centered right b., centered c. and off-centered left d., to improve the contrast between domains. Highlighted domains D_1, D_2, D_3 for the topography analysis are represented on b.

Then, electrons emitted at angles outside the selected area by the CA are cut. This effect can be seen on the PEEM images III.4b-d taken at $E - E_f = 4.3$ eV. The twin walls topography structure means that normal emission from adjacent domains enters the PEEM at different angles with respect to the average surface

normal corresponding to several levels of intensity on the images. The domains contrast in the bottom right of the images (D_2 and D_3) come from domain surfaces with a higher tilt angle than the average domain surface in the FoV, represented by D_1 . Therefore, by off-centering the contrast aperture to the right (fig III.4b) or to the left (fig III.4d), we selectively analyze photoelectrons emitted from the domains on either side of the twin. The average surface plane is assumed to be that of the large central domain D_1 and the PEEM lens optimization has been done in this domain. In III.4b, the emission from the left domain is favored while in III.4d the contrast is inverted.

On the other hand, when the CA is centered on the optical axis, as in Fig III.4c, then the contrast between the twin domains is almost zero. In this configuration, the domains D_2 and D_3 surface normal vectors are symmetrically oriented on either side of the twin wall so the angular selection does not discriminate between them. Higher off-centering of the CA improves dramatically the domain topography contrast in PEEM because of the angular electron selection. However, as we will see, CA off-centering increases the apparent photoemission threshold as measured by the PEEM.

B.4 . Photoemission threshold shift

We have recorded threshold image series for CA positions from -140 to +140 μm with respect to the optical axis. Photoemission threshold image series are acquired as a function of the electron energy with respect to the sample holder Fermi level, in steps of 25 meV. Images are normalized by a flatfield from a known homogeneous area of the sample in order to correct for any detector inhomogeneities (for example defaults on the multichannel plate). The image series at each CA position was analyzed using an automatic procedure by fitting the pixel-by-pixel threshold spectra with an error function, giving photoemission threshold maps shown in figure III.5 (see experimental methods subsection A.3.3 for more details). The non-isochromaticity due to the dispersion in the hemispherical imaging analyzer is also corrected for each threshold image series (details of the procedure in subsection A.3.4).

As it can be seen in figure III.5, the apparent photoemission threshold changes with the aperture position. When the CA is close to the optical axis center, the contrast between ferroelastic domains is low but the measured photoemission threshold of 4.05 eV is a minimum. For modest off-centering, it does not change substantially. When the CA is off-centered far from the optical axis (140 μm here), the contrast between domains is better but the median photoemission threshold over the analyzed area increases with the off-centering. The photoemission threshold shown in figure III.5 symmetrically varies from 4.05 to 4.45 eV between centered and off-centered ($\pm 140\mu\text{m}$) aperture positions. In addition, threshold contrast between D_2 and D_3 is enhanced by 0.2 eV at $\pm 140 \mu\text{m}$.

To quantify the modification of the photoemission threshold with the CA position, we acquired threshold image series using a finer mesh of CA positions for the

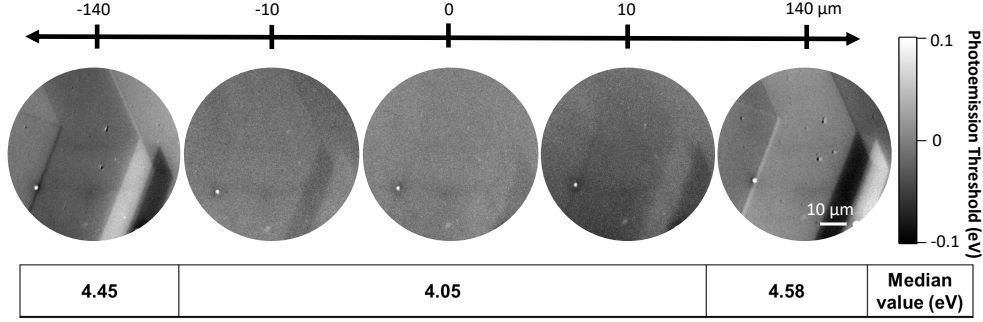


Figure III.5: Photoemission threshold maps at different CA lateral positions from -140 to 140 μm . The middle map at 0 μm is with CA centered on the optical axis. The map's median photoemission threshold values are in the table under the figures, the grey-scale bar is ± 0.1 eV around the median value of each image.

field of view of interest, comprised of 3 ferroelastic domains, represented in figure III.4b. In figure III.6, we plot the evolution of the photoemission threshold of the domains D_1 to D_3 , as a function of the CA lateral position from -230 to $+230$ μm in steps of 10 μm .

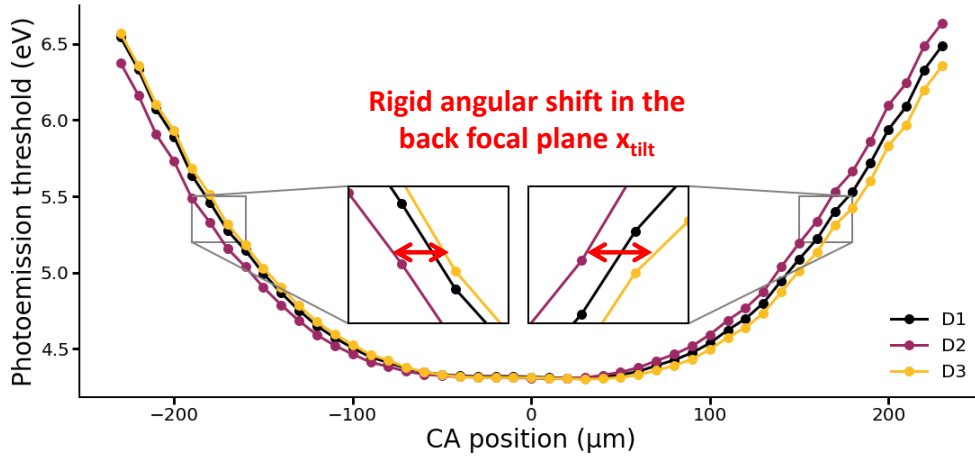


Figure III.6: Photoemission threshold in domains D_1 to D_3 with the contrast aperture off-centered from -230 μm to 230 μm . At 0 μm , the CA is centered on the optical axis.

We can first observe that there is a CA lateral position range around the optical axis where the measured photoemission threshold is stable at 4.05 eV. When the CA is off-centered approximately further than its radius (75 μm), electrons on the optical axis are physically blocked, effectively switching to a dark field mode where only electrons at higher angles on one side of the optical axis are enhanced at the expense of photoelectrons emitted from the opposite slope of the surface twin. Electrons with higher emission angles have lower kinetic energy as measured on the scale of $E - E_F$ making the threshold appear at higher energy, as shown in

figure III.7. Electron emission normal to the sample surface is favored when the CA is centered and electrons emitted at an angle from normal are favored when the CA is off-centered. The extractor field is measured perpendicular to the average sample surface so photoelectrons with higher emission angles have lower kinetic energy ($E_k \approx v_k^2$) as measured on the scale of $E - E_F$ and the threshold will appear at higher energy.

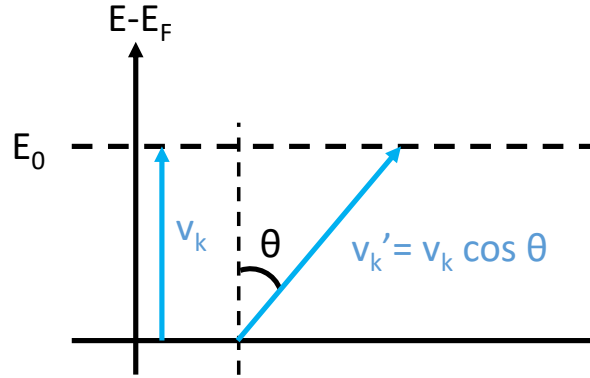


Figure III.7: Schematism of the electron kinetic vector for a normal emission and an emission with an angle θ from the surface normal.

The threshold curves have the same evolution with the CA position, however, they are not centered at the same CA position. Domain D_1 photoemission curve falls in between the D_2 and D_3 curves. D_2 and D_3 have high surface tilt in opposite directions and are rigidly shifted respectively to the left and right from the central position of the CA at 0 μm . D_1 , which has a lower surface tilt shows almost no shift from 0 μm . This is because the global image tilt was aligned with the PEEM optics on D_1 .

In fact, the center of the photoemission threshold curve defines the centered position of the CA in the back focal plane for which the CA is positioned at the PEEM optical axis, normal to the sample surface. When the local surface is tilted (i.e. on a ferroelastic domain), normal emission is also tilted, by an angle α_{tilt} . This surface tilt will off-center the central position of the CA in the back focal plane by a distance x_{tilt} . Therefore, from the shift in the threshold curves, it should be possible to quantify, in the PEEM, the surface topography of the ferroelastic domains.

B.5 . PEEM surface tilt angle

In order to determine the tilt of the domains, we perform a pixel-by-pixel analysis. Threshold curves at each pixel of the FoV are extracted and the objective is to determine x_{tilt} , the shift in the threshold curves, at each pixel of the analyzed area and then to convert this x_{tilt} CA shift in the back focal plane into a surface tilt α_{tilt} in order to reconstruct an angular tilt map of the ferroelastic domains.

B.5.1 . Model

First, to extract an x_{tilt} value at each pixel of the analyzed area, we model the electron path in the PEEM from the sample. The relevant parameters are the electron kinetic energy E_0 , the PEEM column energy E_i , the magnification of the image in the first image plane M , the CA radius r_{ap} , the CA shift in the back focal plane x_{tilt} and the CA lateral position x .

The phase conservation equation of the photoelectrons is written in equation 5. We assume an isotropic emission of electrons from 0° to 90° , i.e. $\alpha_0 = 90^\circ$ and the magnification of the image in the first image plane is given by the ratio between the object size r_0 and the first intermediate image size r_i . The schematic of the electron path emitted with the maximum angle $\alpha_{0,max}$ is shown in figure III.8. The CA is in the back focal plane of the objective lens (in yellow) and can be laterally displaced (red x axis). For a flat surface, the electrons with the highest angle $\alpha_{0,max}$ pass through the contrast aperture in the back focal plane of the objective lens at the border of the aperture, i.e. at a distance $x + r_{ap}$ from the optical axis. For a tilted surface, the optical axis in the back focal plane is shifted by a distance x_{tilt} , and the electrons with an angle $\alpha_{0,max}$ pass through the contrast aperture at a position equal to $(x + r_{ap} + x_{tilt})$.

$$\begin{aligned} \sqrt{E_0} r_0 \sin(\alpha_0) &= \sqrt{E_i} r_i \sin(\alpha_i) \\ M &= \frac{r_i}{r_0} \quad \alpha_0 = 90^\circ \\ \sin(\alpha_i) &= \frac{x + r_{ap} + x_{tilt}}{l} \end{aligned} \quad (5)$$

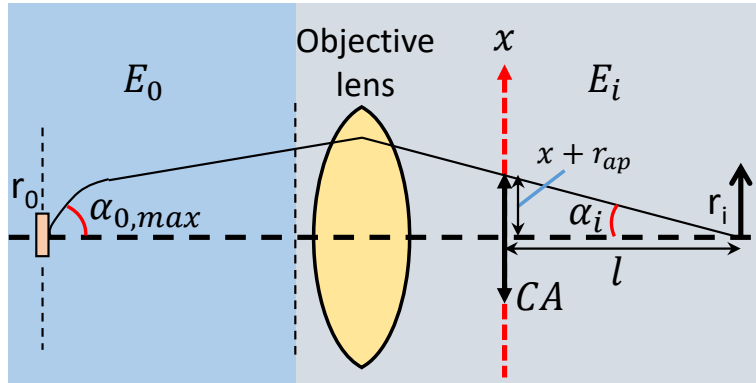


Figure III.8: Maximum emission angle getting through the contrast aperture in our PEEM setup. We off-center the CA in the back focal plane in the x direction to increase the maximum emission angle.

The evolution of the photoelectron kinetic energy at the photoemission threshold E_{Thr} with the CA x position is then given by equation 6. The evolution of the photoemission threshold with the CA lateral position is a parabola with a central

flat range, as observed experimentally. From the PEEM optical setup during the experiment, we have $l = 165\text{mm}$, $M = 35$, and $E_i = 2000\text{eV}$. The function is plotted in figure III.9 in red with $x_{\text{tilt}} = 0$ as if the surface was flat, with the experimental data from a pixel in the domain D_1 which have a tilt close to zero for comparison. We can see that the function evolution with the contrast aperture follows our experimental data. The theoretical law flat range represents the work function of the area, here fixed at 0 eV because we are only interested in x_{tilt} . Experimental data have also the minimum of the photoemission threshold curves (work function) brought down at 0 eV for each pixel.

$$\begin{aligned}
 E_{\text{Thr}} &= \frac{E_i M^2}{l^2} (x + r_{\text{ap}} - x_{\text{tilt}})^2, \text{ for } x \leq -r_{\text{ap}} + x_{\text{tilt}} \\
 E_{\text{Thr}} &= \frac{E_i M^2}{l^2} (x - r_{\text{ap}} - x_{\text{tilt}})^2, \text{ for } x \geq r_{\text{ap}} + x_{\text{tilt}} \\
 E_{\text{Thr}} &= 0, \text{ for } -r_{\text{ap}} + x_{\text{tilt}} \leq x \leq r_{\text{ap}} + x_{\text{tilt}}
 \end{aligned} \tag{6}$$

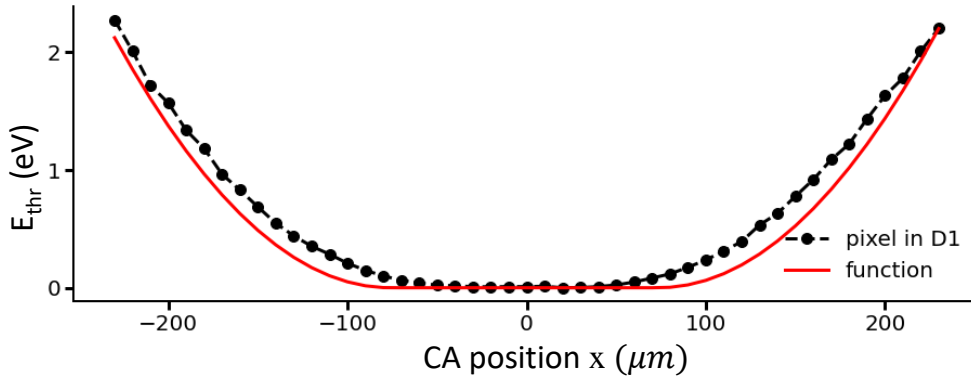


Figure III.9: Theoretical model (red) and experimental data from a pixel in D_1 (black) of the photoemission threshold evolution with the lateral displacement of the contrast aperture from $-230 \mu\text{m}$ to $230 \mu\text{m}$.

B.5.2 . Tilt angle map

From the model, we extract an x_{tilt} at each pixel by fitting the photoemission threshold curves pixel-by-pixel with a least square fit. There are three domains D_1 to D_3 in the selected area.

Then, we convert this x_{tilt} , the CA off-centering from the surface tilt to α_{tilt} the surface tilt angle using a conversion factor. The evolution of the off-centering of the CA in the back focal plane with respect to the surface tilt can be defined theoretically with the hypothesis that the surface topography is a perturbation of the electrons' path above the surface.

As a first approximation, with a linear evolution of α_{tilt} with respect to x_{tilt} , we can use our AFM topography experimental data to deduce the conversion factor.

From the AFM image, we extract the values of the tilt domain plane angles, in table III.2. From the PEEM threshold curves, we extract the mean x_{tilt} for each domain. This gives the conversion factor x_{tilt} to α_{tilt} between domain D_i and D_j : $\frac{\alpha_{D_i} - \alpha_{D_j}}{x_{tilt,D_i} - x_{tilt,D_j}}$, also in table III.2.

Domains	AFM angles (°)	PEEM x_{tilt} (μm)	Conversion factor (°/ μm)
$D_1 - D_2$	$D_1 = -0.359$ $D_2 = -1.006$	-1.230 -8.392	0.090
$D_1 - D_3$	$D_1 = -0.359$ $D_3 = +0.368$	-1.230 +1.962	0.228
$D_2 - D_3$	$D_2 = -1.006$ $D_3 = +0.368$	-8.392 +1.962	0.133

Table III.2: AFM angles and PEEM CA displacements from the surface tilts for each analyzed domain.

The conversion factor calculated with $D_2 - D_3$ would be the most accurate one from our data because it is calculated from domains with the biggest angular difference. $D_1 - D_2$ and $D_1 - D_3$ under-estimate the conversion factor with respect to the twin angle. The angular surface tilt map can then be constructed pixel by pixel from the x_{tilt} values and the conversion factor. The angular maps of the analyzed area deduced from the PEEM x_{tilt} and the AFM conversion factor are given in figure III.10a.

First, we observe a good qualitative agreement between the PEEM and AFM maps. Even if the angular map is constructed with a conversion factor from AFM measurements, and thus the angular PEEM values should correspond to the AFM ones, we can also see that the PEEM analysis correctly discriminates the three main ferroelastic domains on the FoV. Surfaces tilted with a positive or negative angle are correctly revealed by the PEEM analysis and the intermediate domain between D_2 and D_3 , which have the same angle as D_1 from the AFM map, can be distinguished in the PEEM analysis. This domain width is $\approx 1.7 \mu m$. The usual method of imaging in the reciprocal space to deduce surface angles would have been impossible for a domain this small. Real-space imaging to deduce angular maps with the sub-micron resolution is necessary.

Moreover, there is some quantitative agreement between the AFM and PEEM-determined angular maps. The histogram of angular values from the PEEM and AFM data is given in figure III.10b. The overall angular range, as determined by the PEEM threshold measurements is between -1.25° and 0.5° , which fits well with the known twin angles. Notably, D_2 and D_3 which show the extreme tilt angles (-1° and $+0.36^\circ$) are in fairly good correspondence between AFM and PEEM, which is expected from the use of the conversion factor. The main difference between the two angular maps is the tilt angle of D_1 . From the AFM measurement, the tilt angle of D_1 is -0.38° whereas it was found to be -0.15° with the PEEM

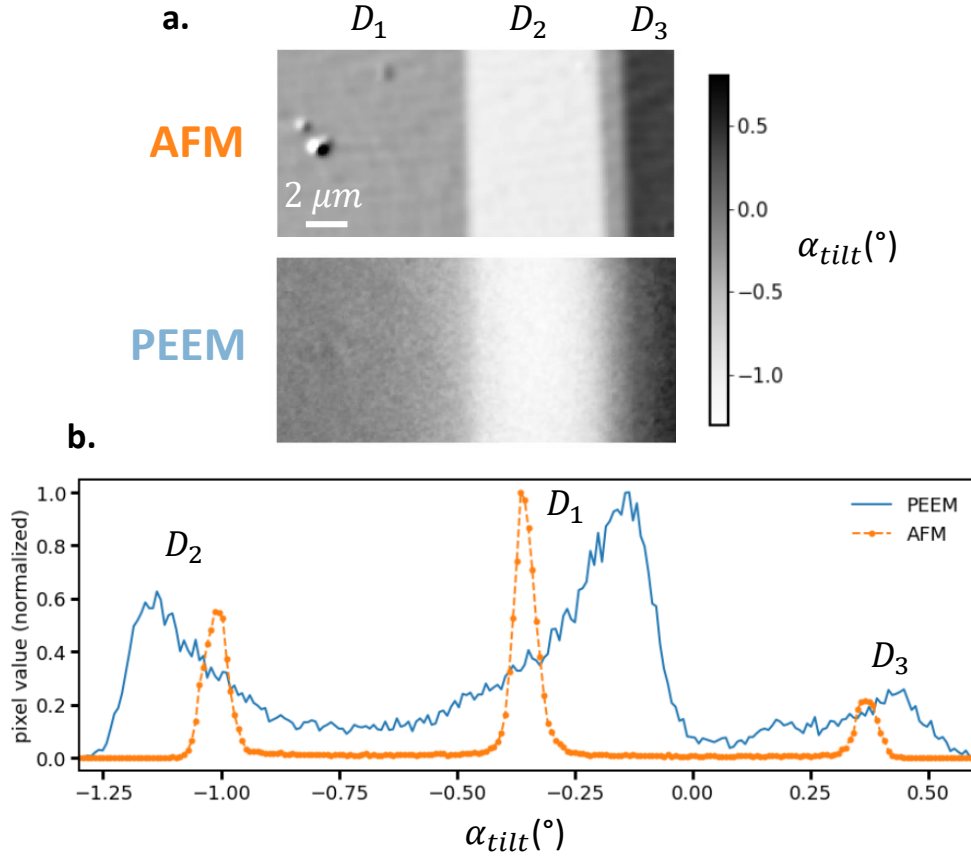


Figure III.10: a. PEEM and AFM angular maps. b. Histogram of the angles extracted from the AFM and PEEM maps.

analysis. This difference could be explained by the PEEM tilt correction effect, which compensates for the sample tilt and D_1 is the biggest domain in the FoV.

The angular spread for each domain is much smaller in AFM compared to the PEEM, typically 0.05° compared to 0.15° - 0.3° . This higher angular spread for the PEEM data is related mainly to the PEEM optics. First the opening angle of $\pm r_{ap}$ means a spread in angles and hence threshold values, absent from the AFM analysis. The PEEM acquires data by parallel imaging at fixed lens parameters. Correlation between position and take-off angle naturally broadens the angular values as measured in PEEM whereas AFM acquires data sequentially, at each data point measuring the same slope.

The standard deviation 2σ ($\approx 95\%$ confidence) map is shown in figure III.11. The intensity at each pixel is two times the standard deviation, giving the pixel-by-pixel error on the fit from our experimental data. We could first observe from the PEEM and AFM angular histograms that the FWHM (Full Width Half Maximum) of the AFM angular peaks were smaller than the PEEM angular peaks, showing a higher standard deviation for PEEM measurements. From the 2σ map, the

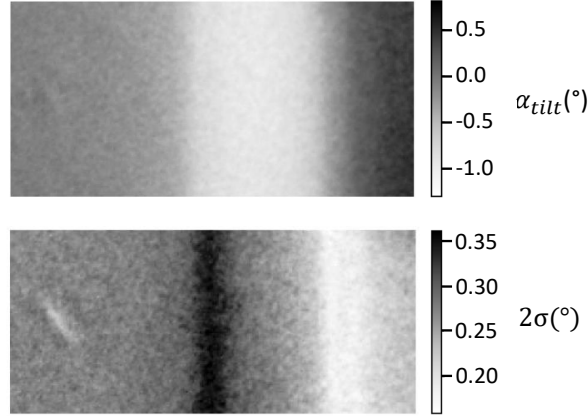


Figure III.11: Map of the 2σ error of the calculated α_{tilt} . The α_{tilt} map is shown again for comparison.

calculated α_{tilt} error is $\pm 0.27^\circ$ in the domains with error extrema of $\pm 0.36^\circ$ and $\pm 0.16^\circ$ around the ridge/valley domain walls. These domain wall areas are transition areas between two different plane tilts where the slope change modifies the local extractor field, therefore, giving rise to a spread of possible values.

B.5.3 . Twin angles

The initial objective was to be able to calculate twin angles directly in the PEEM to have an in-situ identification of the domain walls, moreover, we are also able to determine twin angles in other areas/samples from the method and conversion factor developed in this analysis, as shown in the next section.

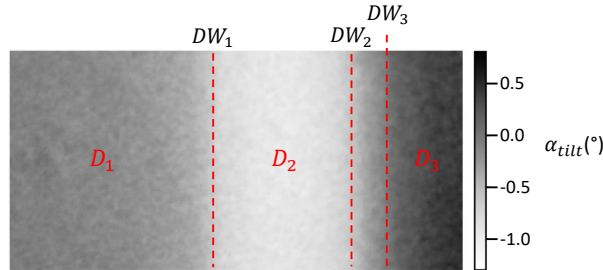


Figure III.12: Position of the domain walls noted DW_i on the analyzed area.

We show in figure III.12 the domain walls on the angular map. The mean tilt angles from the domains, extracted from the PEEM angular map are $D_1 = -0.202^\circ$, $D_2 = -1.151^\circ$, $D_3 = 0.368^\circ$. The intermediate domain between D_2 and D_3 has a tilt angle of -0.422° . We calculate the twin angles of the 3 domain walls from the PEEM measurements. Results are in table III.3 and compared with the theoretically possible twin angles.

The twin angle deduced from the PEEM analysis are in good agreement with the angles measured by AFM. Despite having a bigger standard deviation in the

		Twin angle (°)	
		AFM	PEEM
Measured twin angles	DW_1	179.3	179.1
	DW_2	180.7	180.7
	DW_3	180.7	180.8
Possible W type walls	S_3/S_4	180.9	
	S_3/S_6	180.9	
	S_4/S_5	180.9	
	S_5/S_6	179.1	

Table III.3: Twin angles calculated from the AFM topography and the PEEM measurement, compared with the possible twin angles from the different strain state pairs.

PEEM measurements, this analysis could help to discriminate between different kinds of domain walls directly in the PEEM. We know that DW_1 to DW_3 are W type walls because their surface trace follow a principal orthorhombic axis. Then the possible domain walls have a twin angle of 180° , $180.9^\circ/179.1^\circ$ or $181.3^\circ/178.7^\circ$. Experimental twin angle values can slightly differ from theoretical values. One reason may be that the surface in CTO is polished in the ferroelastic phase (slight miss-orientation from the cubic surface because of the twinning). From the table III.1, we know that we have permissible walls with plane equations $x = \pm y$, (x,y,z) along the pseudocubic axis which have a surface twin angle of $180.9^\circ/179.1^\circ$, the closest to our experimental values from both AFM and PEEM measurements.

Given the consecutive twin angles in this analyzed area, we can propose a possible spontaneous strain configuration. Consecutive angles are $179.1^\circ/180.9^\circ/180.9^\circ$, a possible spontaneous strain ordering which respects the twin angles and the domain walls direction is $S_6/S_3/S_4/S_5$. A sliced schematic of the ferroelastic domains and the proposed spontaneous strain ordering is represented in figure III.13. A schematic highlighting the tensile and shear deformation of the lattice associated with the proposed strain ordering, following the spontaneous strain tensor in 3 is also given.

B.6 . Twin angles of another CTO ferroelastic ordering

If we keep the same PEEM optical configuration, we can analyze the surface topography of other ferroelastic twins, with the same conversion factor determined on the precedent area, without the need to find again the same area in AFM.

We show in figure III.14a an angular map of ferroelastic domain tilts in the same sample in another area. We have again a configuration with three ferroelastic domains named D_4 to D_6 with D_4 and D_6 having a higher tilt in opposite directions. The surface tilt values have a 2σ deviation, reported in figure III.14b, between $\pm 0.15^\circ$ and 0.25° , with again extrema at the transition regions. D_4 have the same tilt than D_3 in the first area. The twin angles calculated from the angular map are reported in table III.4, their surface trace is in the same direction

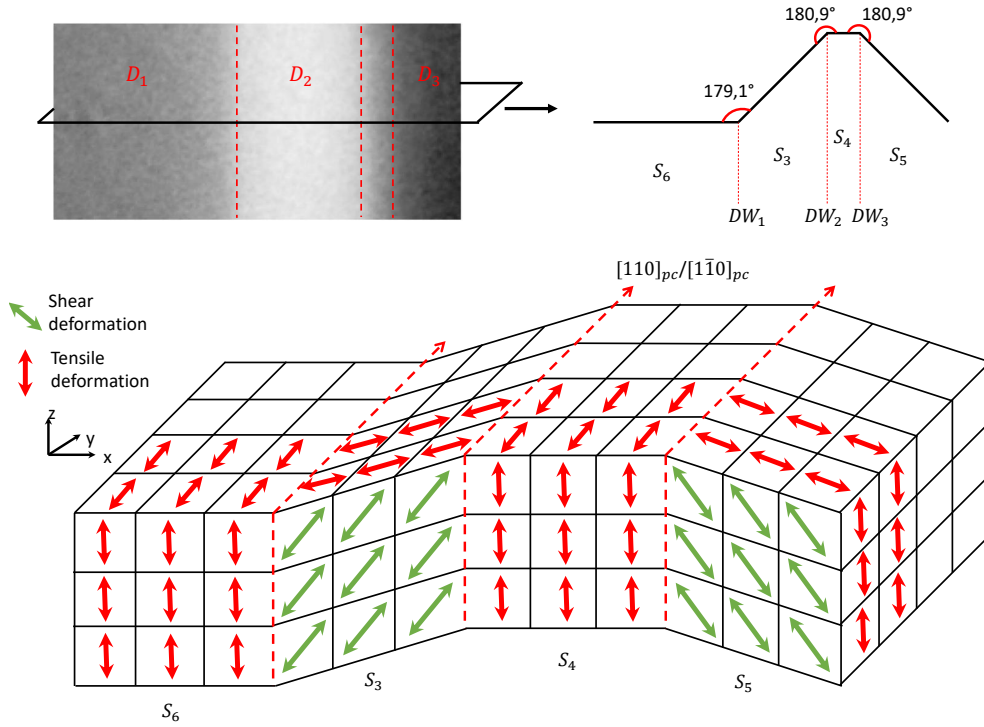


Figure III.13: Schematic of the spontaneous strain configuration in the analyzed area.

as the walls in the former area. If we take into account the standard deviation, these domain walls' twin angles are identical to the ones present in the first area. With only information on the twin angle and the domain wall trace direction at the surface, we can propose two spontaneous strain configurations that would form this ferroelastic domain ordering: $S_5/S_4/S_3$ or $S_5/S_6/S_3$. One way to differentiate between these two possible configurations would be to also measure the strain state in the domains.

		Twin angle (°)
PEEM measured	DW_4	179.1
	DW_5	178.8
Possible theoretical W type walls	S_3/S_4	180.9
	S_3/S_6	180.9
	S_4/S_5	180.9
	S_5/S_6	179.1

Table III.4: Twin angles calculated from the PEEM measurements in the second area.

B.7 . Conclusion

We have used PEEM imaging at the photoemission threshold to study and quantify the physical topography of the $CaTiO_3$ (001) surface with its character-

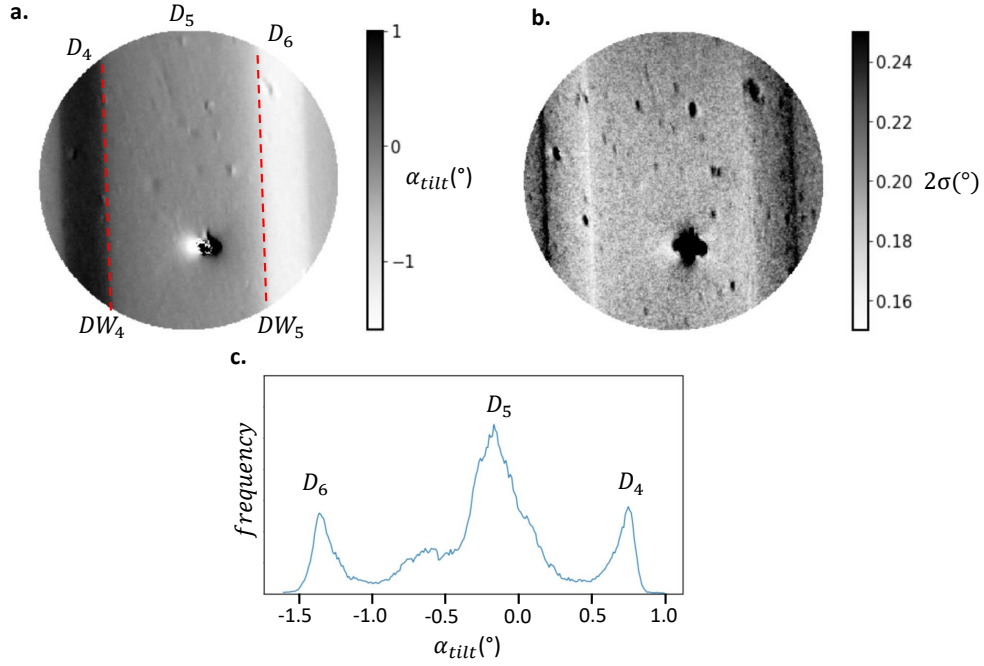


Figure III.14: a. PEEM angular map from another area on the same sample, showing ferroelastic surface topography. b. Map of the 2σ error of the calculated α_{tilt} on the second area. c. Histogram of the angles extracted from the PEEM map.

istic valley/ridge factory roof-like structure and identified the possible twin walls present in the analyzed area.

By off-centering, the contrast aperture from the optical axis, by typically more than the aperture radius, image contrast due to the physical topography is enhanced by collecting only high angular photoelectrons in a near dark field mode. However, electrons emitted at high angles have a lower velocity perpendicular to the average sample surface used to align the PEEM, giving a higher apparent value of the photoemission threshold. Using a simple geometrical approach, relating the take-off angle to the angles inside the PEEM optics, allows quantification of the tilt angle of a domain surface from the measurement of the photoemission threshold.

The results agree well with the independent measurement of the tilt angles using AFM and the calculated twin angles can help to identify the domain order at the $CaTiO_3$ surface from the theoretically possible ferroelastic domain walls. However, because of different equivalent symmetries, some domain walls' twin angles can be formed by different spontaneous strain pairs. Moreover, some possible surface twin angles on the (001) surface are 180° , they don't form a surface topography so these domain walls would be invisible by this technique. Then a complementary in-situ technique to identify the surface strain state would be helpful to identify the ferroelastic domain and domain walls.

C . Ferroelastic domains spontaneous strain observation and quantification by X-ray Linear Dichroism

Ferroelastic materials display domain structures of uniform strain state separated by very narrow twin walls, typically a few nanometers wide, where the spontaneous strain changes sign. The strain breaks the symmetry and in consequence can be probed by X-ray Absorption Spectroscopy in PEEM (XAS-PEEM) at the Ti $L_{2,3}$ edge, in order to study in the future the response of the strain in the domains and the polarity in twin walls to an in-situ applied electric field or mechanical stress.

C.1 . Polarization in X-ray Linear dichroism

In ferroelectric materials, the reduction in symmetry associated with the onset of the ferroelectric order parameter can lead to a pronounced difference at the Ti $L_{3,2}$ absorption edges between spectra measured with the x-ray linear polarization perpendicular and parallel to the deformation. Figure III.15 shows XAS with horizontal and vertical light polarization (respectively red and blue arrows) in an out-of-plane polarized thin film $PbZr_{0.2}Ti_{0.8}O_3$ (PZT) on $SrRuO_3$ [159]. Spectra for the two linear polarizations exhibit four peaks related to the excitation of Ti $2p$ core level into the Ti $3d$ band. $2p$ spin-orbit splits the spectra in $2p_{3/2}(L_3)$ and $2p_{1/2}(L_2)$ structures, which are further split because of the crystal field interaction: t_{2g} (d_{xy} , d_{xz} and d_{yz}) and e_g (d_{z^2} and $d_{x^2-y^2}$) states in the octahedral geometry around the Ti atom.

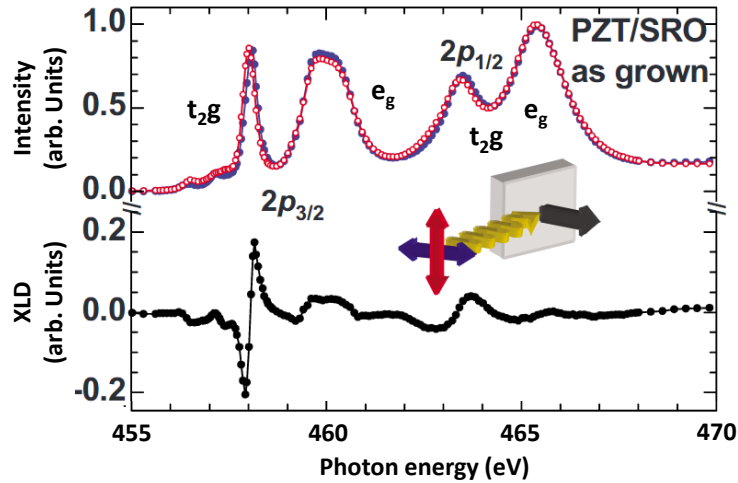


Figure III.15: Experimental Ti $L_{3,2}$ XAS and difference spectra (XLD) of a thin film PZT as grown on SRO, with polarization pointing up from the bottom electrode. From [159].

Polarization in PZT is related to atoms displacements with respect to the oxygen octahedra, in the tetragonal phase. t_{2g} states and also e_g states further

split in the lower tetragonal symmetry, giving a difference between XAS taken with light polarization in- and out-of-plane (vertical and horizontal in the synchrotron reference frame). Figure III.15 of the XLD spectra (difference of the vertical and horizontal polarization) shows that the reduction in symmetry around the Ti^{4+} ions has a pronounced impact on the Ti $L_{3,2}$ absorption edges. Notably, a difference of 20% in the photon energy range of the $2p_{3/2} t_{2g}$ peak was observed, related to the out-of-plane polarization in PZT.

C.2 . XLD contrast in ferroelastic $CaTiO_3$

Here we first develop the same approach to probe the ferroelastic order parameter (spontaneous strain) by XAS-PEEM. The e_g and t_{2g} states are probed at the Ti $L_{3,2}$ edge. The orbitals are represented in figure III.16 and contrarily to s orbitals, their electronic density is directional. The different ferroelastic domain configurations have different spontaneous strain directions and the domain is tilted (twin angle) with respect to the surface. Because of the directionality of the $3d$ orbitals, we can expect different polarized light interactions with the domains depending on their order parameter orientation and a different interaction because of the surface twin angle of the domain walls.

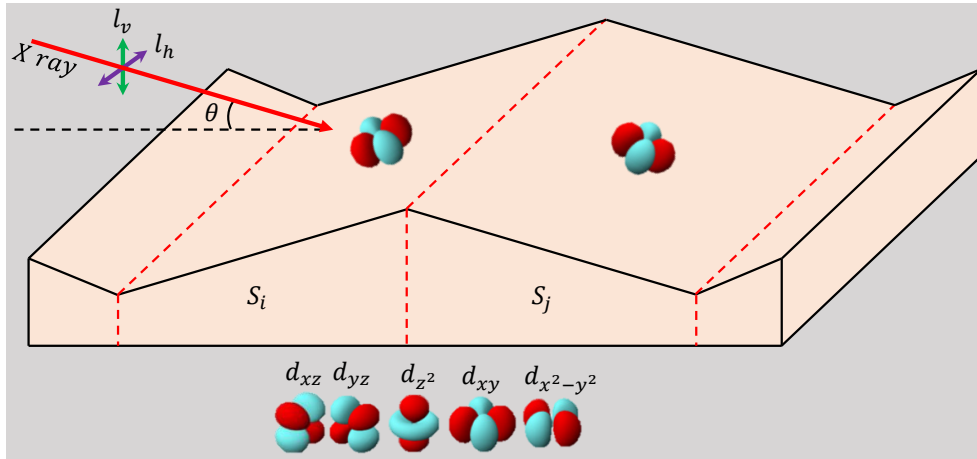


Figure III.16: a. Schematic of the experimental setup. Linearly polarized out-of-plane l_v and in-plane l_h X-ray interact with e_g and t_{2g} orbitals. The X-ray angle with the surface is $\theta=16^\circ$. Ferroelastic domains with different configurations S_i, S_j have different orbital orientations because of the ferroelastic twinning and thus have different interactions with the incident light.

The main advantages of the XAS-PEEM technique are the near-surface probing depth, of $\approx 5nm$ [160, 141], the possibility to image the surface at different energies with an excellent lateral and spectral resolution, and the fact that the observation is non-destructive. These are considerable advantages compared with other strain-sensitive techniques. For example, in Transmission Electron Microscopy (TEM), the strain orientation can be deduced from the atom positions,

with a very good spatial resolution ($\approx \text{\AA}$), however, the technique is destructive and the sample preparation could modify the ferroelastic strain state. Another technique that can probe spontaneous strain is X-Ray Diffraction (XRD) from the lattice parameters measurement. However, the technique can't perform direct imaging of the strain in a single domain, except with nanobeams, for example at ESRF.

C.2.1 . Experimental conditions

The analyzed sample is a CaTiO_3 (001) single crystal from SurfaceNet. The sample borders are along $(100)_{pc}$ and $(010)_{pc}$. Domain walls were identified by LEEM and soft x-ray absorption spectroscopy (XAS) was performed at synchrotron Diamond I06 beamline on an Elmitec LEEM III on the Ti $L_{3,2}$ edge, in total electron yield mode, where we detect all primary photoelectrons and secondary electrons that emerge from the sample surface, independent of their energy. The incident light has two linear polarizations: a vertical polarization which deviates from the normal of the surface by $\theta=16^\circ$ and a horizontal polarization parallel to the surface plane.

The sample surface preparation is straightforward and consists of a short exposure to ozone before insertion into the UHV system, followed by annealing at 650°C in UHV for surface cleaning. The experiment was carried out at 300°C in order to avoid sample charging.

C.2.2 . MEM imaging

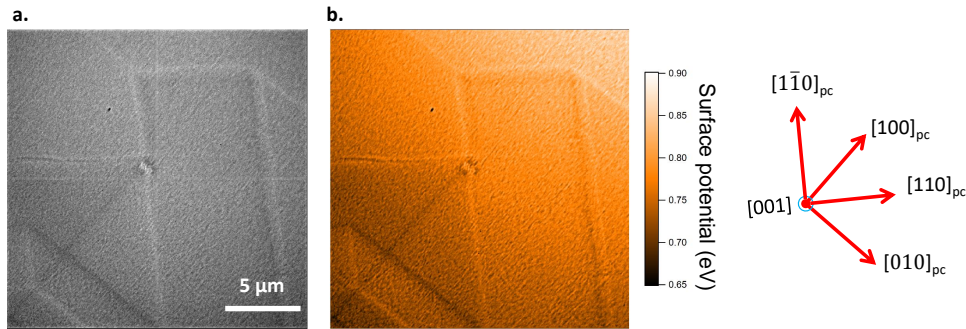


Figure III.17: a. MEM image of the XAS analyzed area. Dark and bright straight lines are domain walls. b. Surface potential map of the analyzed area to identify upward and downward polarized domain walls.

After navigating with LEEM, we focused on an area with several domain wall orientations. Image III.17a is a MEM image showing the analyzed area in XAS. The straight dark and bright lines are domain walls. They have different orientations, so we can expect several twin configurations and deformation directions present. Figure III.17b is a surface potential map of the analyzed area from which we can identify domain walls with upward and downward polarity. Surface potential

map reconstruction is described in the experimental section B.2. The sample pseudocubic axis are 5° off the normal direction, determined by LEED.

The surface topography can be appreciated by off-centering the contrast aperture in the back focal plane of the objective lens to select electrons with a higher take-off angle in four directions, similar to the method in the last section III.B with threshold PEEM. Figure III.18, shows 4 images with the CA off-centered, the contrast is related to the tilt angle of the ferroelastic domains. Different ferroelastic domain angles coexist.

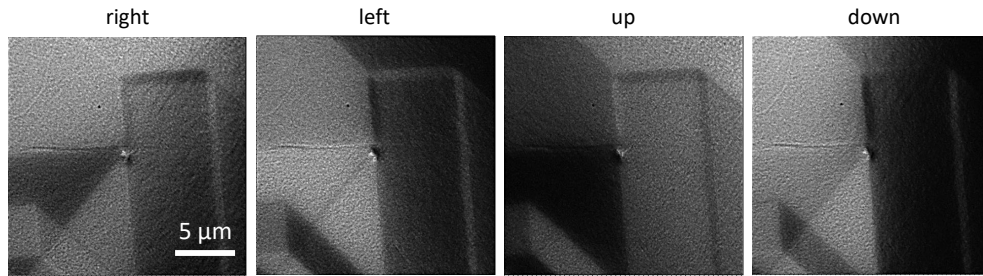


Figure III.18: Surface topography. MEM images of the analyzed area with the contrast aperture off-centered to the right, left, up, and down directions in the back focal plane of the objective lens.

C.2.3 . XAS of the analyzed area

We focused on the $TiL_{2,3}$ absorption edge with horizontally and vertically incident light polarized, at an angle θ of 16° with respect to the surface. Contrast is visible in images for both l_v and l_h polarizations, as shown in figure III.19. It means that the interaction of incident light with Ti 3d orbitals is not equivalent for some domains. From the difference between l_v and l_h images, we can calculate the X-ray Linear Dichroism (XLD), shown in color in figure III.19. We observe XLD contrast between two domains.

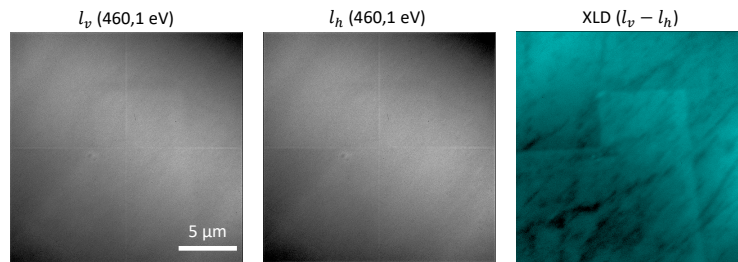


Figure III.19: Linear vertical (l_v) and linear horizontal (l_h) polarized images of the analyzed area at 460.1 eV and the difference image (XLD) between the two polarizations.

To find representative energies with high dichroism, we first looked at the XAS integrated on the whole area for the two polarization, represented in figure III.20a.

The line shape and peak energy positions of Ti L-edge XAS on CTO are in good agreement with bulk stoichiometric $SrTiO_3$ sample [62].

Given the spatial distribution of the $3d$ orbitals (shown in figure III.16a), we can expect a strong dependence of the absorption on the direction of the polarization vector with respect to the crystal axis and, to a lesser extent, the twin angle of each domain configurations. Experimentally, we found that the best contrast between linearly polarized vertical and horizontal images was around the $2p_{3/2}$ e_g peak. XLD images across the first e_g peak are shown in figure III.20b.

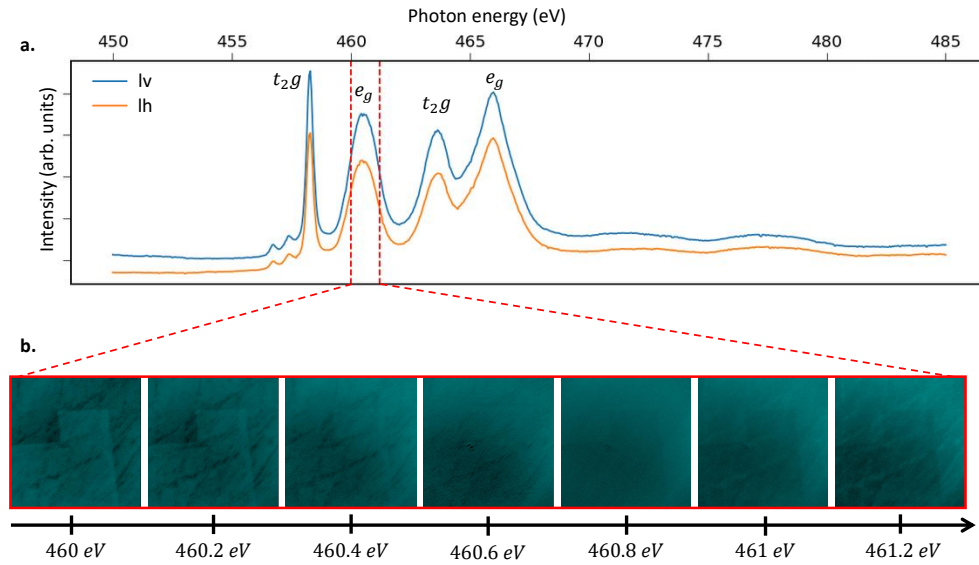


Figure III.20: a. X-ray absorption spectra with linear vertical and horizontal polarizations integrated into the analyzed area. b. XLD ($l_v - l_h$) images through the first e_g peak show a contrast inversion.

We observe a contrast between a central domain and another domain at the top and right side of the image. The domain contrast is inverted between the left side and the right side of the $2p_{3/2}$ e_g peak. Domain walls that separate XLD responsive ferroelastic domains are highlighted on the schematic III.21a with red lines, extracted from the MEM image.

Figure III.21b and c shows XLD images at 460.1 and 461 eV of the analyzed area. The borders of the bright domain at 460.1 eV are along the $[110]_{pc}$ and $[\bar{1}\bar{1}0]_{pc}$ directions, represented with red lines on the schematic III.21a. Other twin walls, represented by dark lines on the schematic, don't show an XLD contrast. For the analysis, we focus on two energies: 460.1 eV and 461 eV. We can accentuate the contrast by the difference image of XLD between 461 eV and 460.1 eV, as shown in image III.21d.

We then rotated the sample around the $[001]$ direction by an angle φ of 45° and 90° . The complete XLD dataset and XLD difference images are shown in figure III.22. On XLD images at 460.1 eV and 461 eV, the contrast between the central

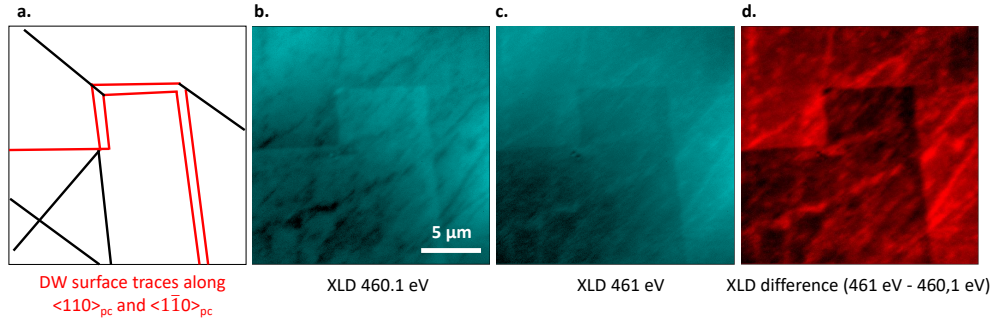


Figure III.21: a. Schematic with the domain wall positions, extracted from the MEM images of the area. XLD images ($l_v - l_h$) of the analyzed area at b. 460.1 eV and c. 461 eV. d. XAS difference between 461 and 460.1 eV.

domain and the surrounding upper and right areas is inverted between $\varphi=0^\circ$ and 90° . No XLD ferroelastic domain contrast is visible at 45° , meaning that the l_v and l_h polarized light interaction with the orbitals are identical. From the 90° contrast inversion, we know that the in-plane domain strain directions are orthogonal. At 450 eV, before the Ti $L_{2,3}$ absorption edge, we also observe XLD, which inverts when rotating the sample by 90° . The origin of this contrast must therefore be different from that observed at the e_g peak. It may possibly be surface dipoles, as already reported [161].

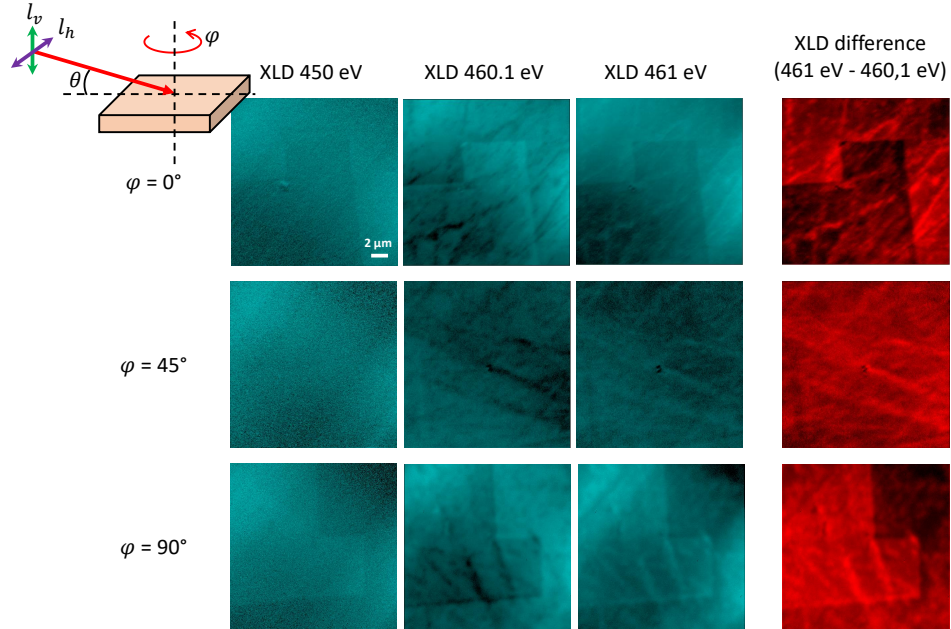


Figure III.22: XLD and XLD difference images of the analyzed area depending on the sample rotation φ around the $[001]$ direction.

C.2.4 . XAS in another area

We observed an XLD contrast only between domains separated by $\langle 110 \rangle_{pc}$ and $\langle 1\bar{1}0 \rangle_{pc}$ domain wall traces with the surface. To confirm this, we looked at another area on the sample with a different domain ordering at the surface, to see if this affirmation is true. We show in figure III.23 XLD and XLD difference images. The azimuthal orientations are the same as in the first area. The ferroelastic domain contrast is only present for domains separated by $\langle 110 \rangle_{pc}$ and $\langle 1\bar{1}0 \rangle_{pc}$ domain wall trace with the surface directions.

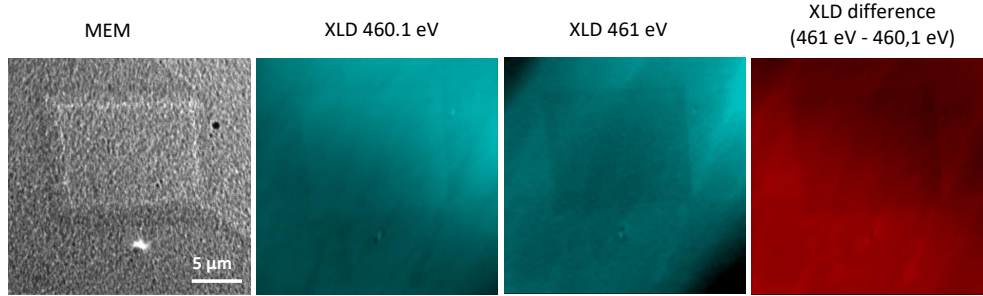


Figure III.23: MEM, XLD, and XLD difference images of another area with a different surface domain ordering.

From the table 1, only the $(S_3 \text{ or } S_5)$ and $(S_4 \text{ or } S_6)$ pair configurations have domain wall traces in the $[110]_{pc}$ and $[1\bar{1}0]_{pc}$ directions. We then calculate the absorption spectra related to these spontaneous strain orientations to determine their XLD intensities.

C.3 . Absorption spectra calculation

In order to identify the domain configurations from the interaction with the incident l_v or l_h polarized light, we have performed simulations of the absorption spectra of all possible domain configurations. The six configurations correspond to six different spontaneous strain orientations which interact differently with the horizontal and vertical polarized light.

We used the FDMNES program [162], which can accurately calculate the absorption spectra of the Ti $L_{2,3}$ edge [163]. It is a relativistic density functional theory (DFT) code used with a Finite Difference Method (FDM) to solve the Schrödinger equation of the 2p to 3d transitions. Using this code, we calculated the absorption spectra with the same incident light orientation and polarizations as the experiment for the six CTO ferroelastic domain configurations S_i . The simulated spectra for the six possible spontaneous strain orientations in CTO are shown in the annexed figure APP1. We show here the simulated spectra for the domain configurations S_4 and S_5 for horizontal and vertical light polarizations and their XLD spectra, which will be enough to understand the ferroelastic ordering on the analyzed area. Peaks associated with the $L_{2,3}$ transitions are present, albeit with low accuracy on the e_g peaks position and their relative intensity compared to the experiment and a better peak position accuracy for t_{2g} peaks.

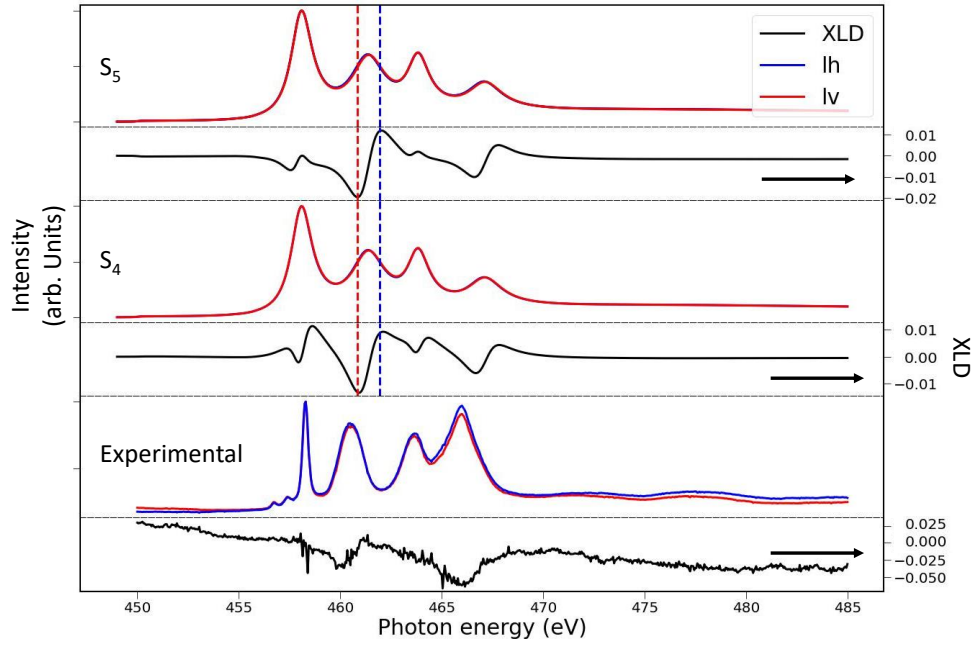


Figure III.24: a. Simulated spectra with the FDMNES program of spontaneous strain orientations S_4 and S_5 , with the same incident light direction and polarization as the experiment and the experimental XAS and XLD averaged on the area. Curves are shifted for clarity. The red and blue vertical dashed lines represent the two sides of the first e_g peak where the absolute XLD signal is the strongest.

We focus on the difference of interaction on the first e_g peak. In the spectra, we can see a difference in orbital interaction for the different strain orientations. We can see here that for both domain configurations, the first e_g l_h peak is shifted to lower energies but not by the same amount. The difference is observable in the XLD spectra where for S_4 the XLD minimum around the first e_g peak is $\approx 1\%$ and $\approx 2\%$ for S_5 . This interaction difference is seen in the experimental XLD images by a contrast difference.

It is also possible to have an opposed contrast between some domain configurations. In the annexed figure APP1, between S_1 and S_3 at the first e_g peak, we observe that for S_1 , the e_g l_v peak is shifted to lower energies with respect to the l_h polarization, and the opposite is seen for S_3 . These differences are highlighted in the XLD spectra ($l_v - l_h$).

In order to directly identify on the experimental images the domain spontaneous orientations, the bar graph in figure III.25 shows the calculated XLD difference intensities between the two energies with the extrema XLD intensity around the first e_g peak ΔXLD for S_3 to S_6 . XLD difference intensities for all domain configurations are in the annexed figure APP2. This calculated XLD difference intensity will then be compared to the intensity in the experimental XLD difference images $\Delta XLD(461 \text{ eV} - 460.1 \text{ eV})$.

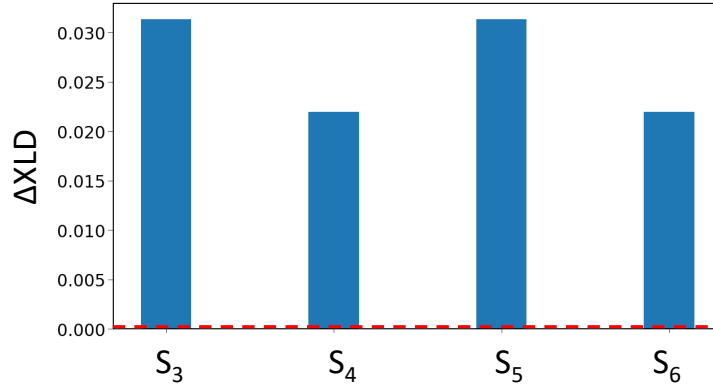


Figure III.25: XLD difference intensity between XLD at the right and left side of the first e_g peak (respectively at the blue and red vertical lines of figure III.24) for S_3 to S_6 configurations.

We can see that the response can discriminate between the configuration pairs: S_3/S_5 , and S_4/S_6 . For example, we can expect an XLD difference contrast between S_4 and S_5 domain configurations and no contrast between S_3 and S_5 . From the contrast, we can identify the domain configuration in the analyzed area, and then, from the strain tensor in each domain configuration, we can be more explicit on the strain ordering.

C.4 . Domain identification

From the simulations of the XLD intensity and possible wall orientations, we can determine the domain configurations present in the analyzed area. We can expect two levels of intensity, a contrast difference is between the (S_3 or S_5) and (S_4 or S_6) configurations where the former will appear darker than the latter.

The XLD difference image of the analyzed area is shown in III.26a and an intensity profile along a central line is given in III.26b. The outer area has a brighter contrast than the inner area. From the intensity simulations, we can identify possible domain configuration pairs that give the observed contrast, highlighted directly in the line profile.

From the table 1, only the (S_3 or S_5) and (S_4 or S_6) configurations have domain wall traces in the $[110]_{pc}$ and $[1\bar{1}0]_{pc}$ directions. From the strain tensors of the domain configurations, we can give an example of the strain relation between the domains, as shown in figure III.27. The walls have an inclination of 90° , a twin angle of $180 \pm 0.9^\circ$ and are along $[110]_{pc}$ and $[1\bar{1}0]_{pc}$ directions. The other red domain walls are in the same orientations and have the same strain configurations.

We can't discriminate between some domain configurations because they interact identically with the incident light in our experiment configuration. For example, there are also diagonal domain walls inside the (S_3 or S_5) area (black diagonal walls in the schematic III.26c), which doesn't show an XLD contrast. From the mechanical compatibility relations in table 1, between S_3 and S_5 (and likewise between S_1

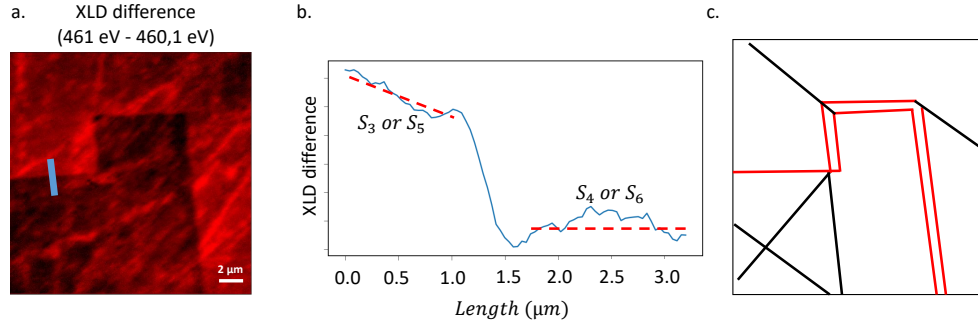


Figure III.26: a. XLD difference image between 461 eV and 460.1 eV with a blue bar representing the intensity difference profile plotted in b. and c. Schematic of the domain wall positions.

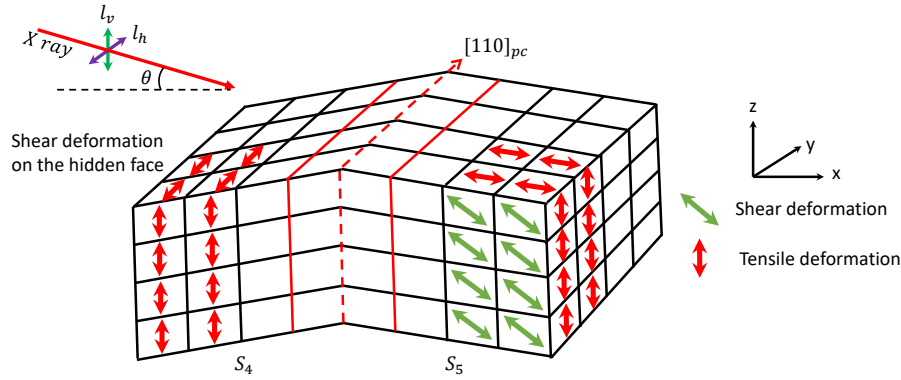


Figure III.27: Schematic of the W type domain wall between the ferroelastic domain configurations S_4 and S_5 , representative of the domain walls between (S_3 or S_5) and (S_4 or S_6).

and S_2 and also between S_4 and S_6), for W type walls, the only possible domain wall orientation is $[100]_{pc}$ and $[010]_{pc}$ (with 90° inclination from the surface), which are the black diagonal walls traces in figure III.26c but they do not give an XLD intensity.

Simulation show that an XLD contrast is possible between (S_1 or S_2) and the other configurations, and the table 1 show that the domain walls formed by this configurations relations would be along the $[100]_{pc}$ and $[010]_{pc}$ directions. We haven't found this strain configuration in our sample. It could be possible to discriminate between all the strain configurations if the sample surface is not along a principal orthorhombic axis, simulations could confirm this.

C.5 . Conclusion

PEEM is a powerful electronic microscopy technique to identify the domain ordering in ferroelastic materials. We are able to calculate the surface twin angle between CTO ferroelastic domains in laboratory PEEM and we can identify the spontaneous strain orientation in the ferroelastic domain separated by specific

domain walls.

We observe an XLD contrast between CTO ferroelastic domains separated by domain walls with identified orientations. Contrast is present because the polarized light interaction with the Ti $3d$ orbitals is not equivalent between the different domains where shear and tensile deformations are not equivalent on either side of a wall. With theoretical calculations, we can identify the spontaneous strain direction on both sides of domain walls which have domains with different XLD intensities.

IV - Surface band gap narrowing in CaTiO_3 domain walls

The modification of the electronic structure at the intersection of the twin walls and sample surface opens up perspectives for engineering and exploiting domain wall functionality. Using electron energy loss spectroscopy in a low energy electron microscopy we have simultaneously revealed the domain wall polarity in ferroelastic CaTiO_3 (001) and band gap narrowing at the intersection between the domain walls and the surface. Moreover, the gap energy varies with the oxygen vacancy concentration, providing a perspective toward tunable band gaps in domain walls.

A . Experimental conditions

The sample is a single crystal CaTiO_3 (001) from SurfaceNet GmbH, polished to $\pm 0.3^\circ$. The sample is first exposed to ozone for 5 minutes at atmospheric pressure and then annealed under UHV at 650°C for 30 min, to remove surface contamination. Surface order and chemistry are then checked with LEED and XPS. The surface contamination level assessed by XPS is low, with a carbon content of about 3% from the survey spectra shown in IV.1a. From the Ti 2p core level spectra shown in IV.1b, there is no peak broadening indicative of Ti reduction at grazing emission. This implies that no additional oxygen vacancies are present at the surface.

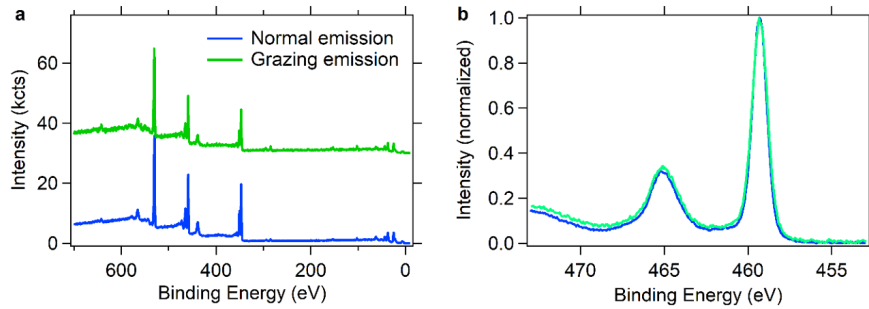


Figure IV.1: a. XPS survey spectra were acquired at normal emission (blue, bulk sensitive) and grazing emission (green, surface sensitive). No significant chemical differences are observable. b. Ti 2p core level spectra at normal (blue) and grazing (green) emission, show no evidence of additional oxygen vacancies at the surface.

The MEM-LEEM and EELS studies were performed with an Elmitec LEEM III. The objective is to identify P_{up} and P_{down} ferroelastic domain walls at the surface of CaTiO_3 and perform EELS measurements on them to extract their band gap energy. The spatial resolution of the LEEM is about 15 nm, greater than

the expected DW width of at most a few nm, however, the stray field originating from the local wall polarization extends much further, providing the mechanism for contrast.

A MEM image of the analyzed area is shown in figure IV.2a, showing dark and bright straight lines corresponding to P_{up} and P_{down} domain wall planes intersections with the surface. The twin walls surface trace on this sample are parallel to $\langle 100 \rangle_o$, $\langle 010 \rangle_o$ or $\langle 110 \rangle_o$ directions. μ -LEED is performed on the MEM image IV.2a, with the LEEM diffraction mode on areas delimited by a field aperture represented by the white circles. LEED patterns in figure IV.2b from the domain D1 and the domain walls W1 and W2 show no spot splitting for D1 and splitting in respectively the horizontal $[100]_o$ and vertical $[010]_o$ directions for W1 and W2. This splitting in different directions is related to the wall twin angle W1 and W2 along $[100]_o$ and $[010]_o$ which shift in the reciprocal space the LEED patterns of their adjacent domains along the same directions. The LEED patterns are consistent with the expected ferroelastic physical topography for twin structures and the (1x1) LEED patterns of the orthorhombic structure.

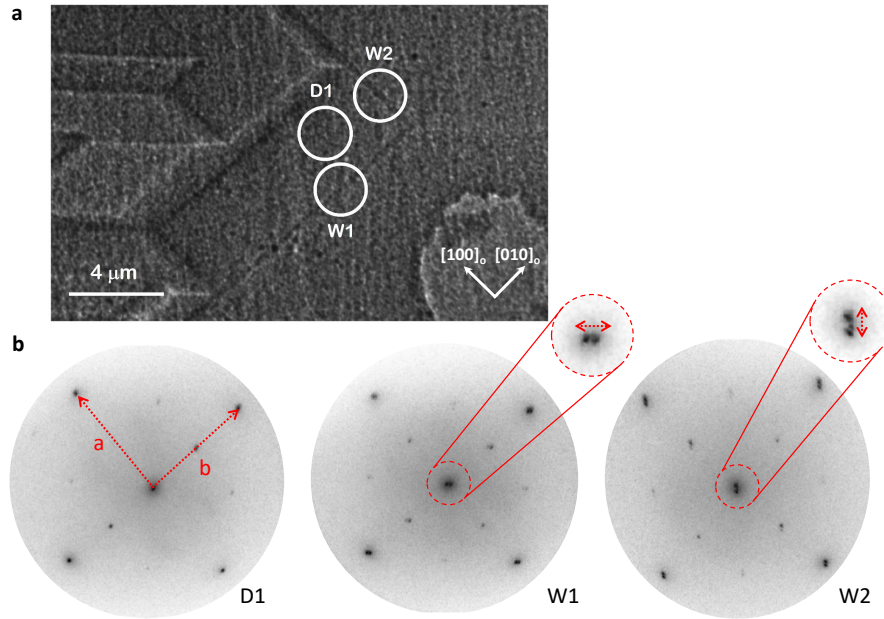


Figure IV.2: μ -LEED analysis at domain walls. a. MEM image acquired at a start voltage of -0.33 eV showing twin walls forming ridges (bright lines) and valleys (dark lines). b. LEED patterns are obtained by positioning a micro-aperture, represented by the white circle in a. For a micro-aperture in the domain D1, single spots are observed whereas, for apertures positioned on domain walls W1 and W2 along $\langle 100 \rangle_o$, $\langle 010 \rangle_o$, spots are split along axes perpendicular to the walls, marked with the double arrows.

B . Domain wall polarity

A large-scale MEM image is shown in figure IV.3a. Bright and dark twin walls trace at the surface along $\langle 100 \rangle_o$, $\langle 010 \rangle_o$ or $\langle 110 \rangle_o$ are visible. The in-plane orthorhombic directions, determined by μ -LEED, are indicated. The bright round patch near the top right of the image is a residue of sample polishing/cleaning but does not interfere with the measurements. The absence of contrast between domains confirms this surface is, like the bulk CTO, non-polar whereas the twin walls show dark and bright contrast with respect to the domains which originate from the domain walls P_{up} and P_{down} polarity and valley and ridge topography (see section II.B for LEEM polar and physical topography origin).

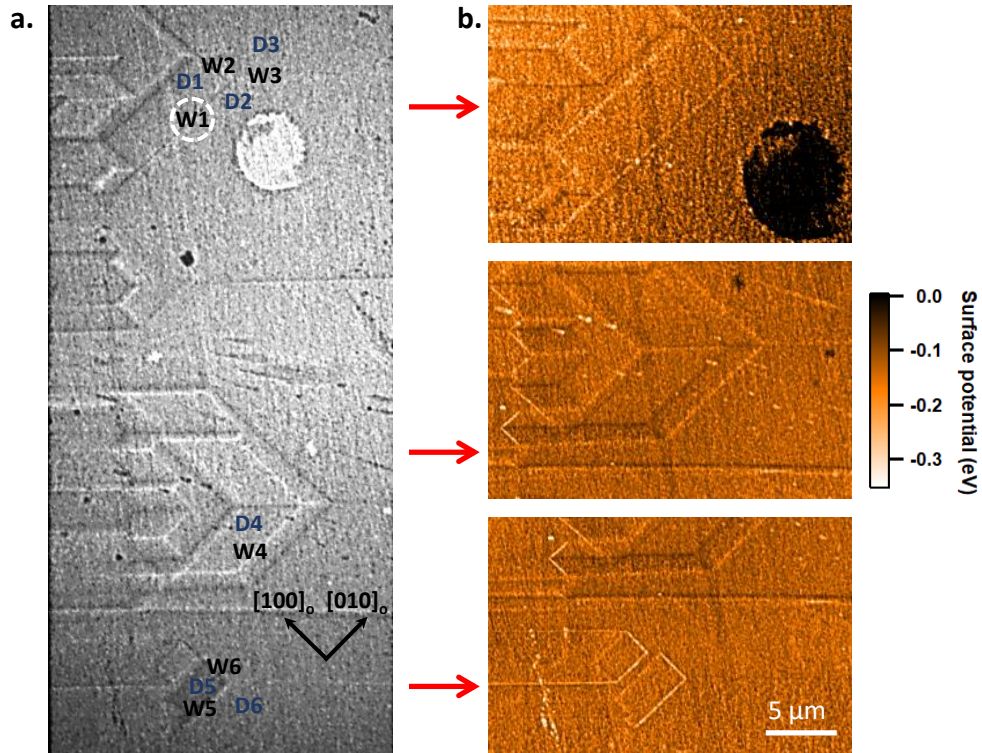


Figure IV.3: a. MEM image of the sample surface. Domain and domain walls for the EELS analysis are noted on the MEM image. b. Surface potential maps acquired in 3 areas of a.

We selected six twin walls, labeled W1 to W6, and associated domains, D1 to D6, on the analyzed area shown in IV.3a for the band gap analysis. The local surface potential was measured by acquiring image series as a function of electron kinetic energy through the MEM-LEEM transition in three areas of the sample surface. Surface potential maps in IV.3b were constructed from the pixel-by-pixel complementary error function fit to the MEM-LEEM transition. A detailed explanation of the MEM-LEEM transition and the surface potential map calculation is in subsection B.2.

The surface potential maps show the signature of polarity in the twin walls.

Domains have a constant surface potential of ≈ -0.13 eV across the three maps. The domain walls W1, W2, W5, and W6 have a lower surface potential than the surrounding domains, from -0.16 eV to -0.26 eV, whereas W3 and W4 have a higher surface potential of ≈ -0.09 eV. The 95% interval of confidence is ± 0.01 eV in the domains and ± 0.02 in the wall. The surface potential differences ΔE_{SP} between the walls and the domains ($\Delta E_{SP} = E_{SP}(W) - E_{SP}(D)$) are represented in figure IV.4a, and given in table IV.2. The twin walls with outward pointing polarity P_{up} have a lower surface potential (positive surface charges) i.e. a negative ΔE_{SP} difference from the domains, whereas twins with inwards pointing polarity P_{down} (negative surface charges) have a higher surface potential than the domains and so a positive ΔE_{SP} difference from the domains. The surface potential modulation is represented in the schematic IV.4b.

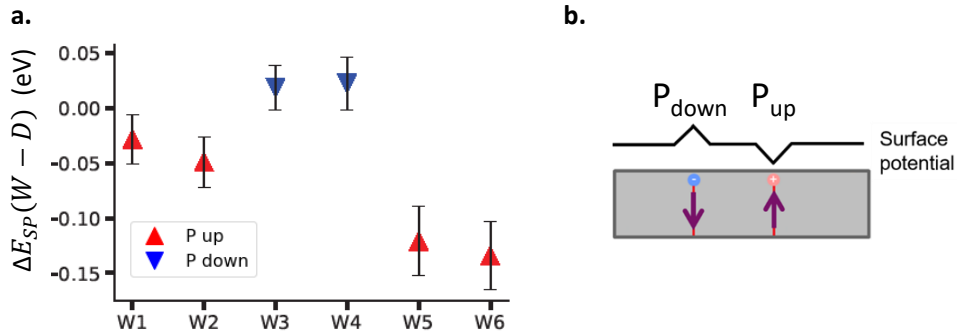


Figure IV.4: a. Surface potential difference ΔE_{SP} between twin walls and the domains. b. Schematic of the surface potential modulation by the polar domain walls.

C . Band gap estimation by EELS

After identifying the polarity at the domain walls, the band gap in domains and DWs are measured using local EELS in the LEEM system. The method is explained in the experimental subsection B.6. Using the LEEM dispersive mode, energy loss spectra were acquired with a primary electron energy of 7 eV from the domain walls and domains labeled in figure IV.3a. The field aperture size used to define the area for the EELS data acquisition is shown by a red circle.

The raw EELS data from W1 is shown in figure IV.5 and plotted as a spectrum from the intensity trace image. The elastic peak is the dominant most intense feature, followed by the secondary electron peak, centered at ≈ 6.5 eV. The position of the inelastic cut-off is at 7 eV, the maximum possible energy loss. The intensity is extracted from the trace image over the yellow rectangle area with an energy scale fixed by having the elastic peak at 0 eV and the maximum loss possible of 7 eV at the cut-off.

The minimum loss of the electrons is the transition from the valence band

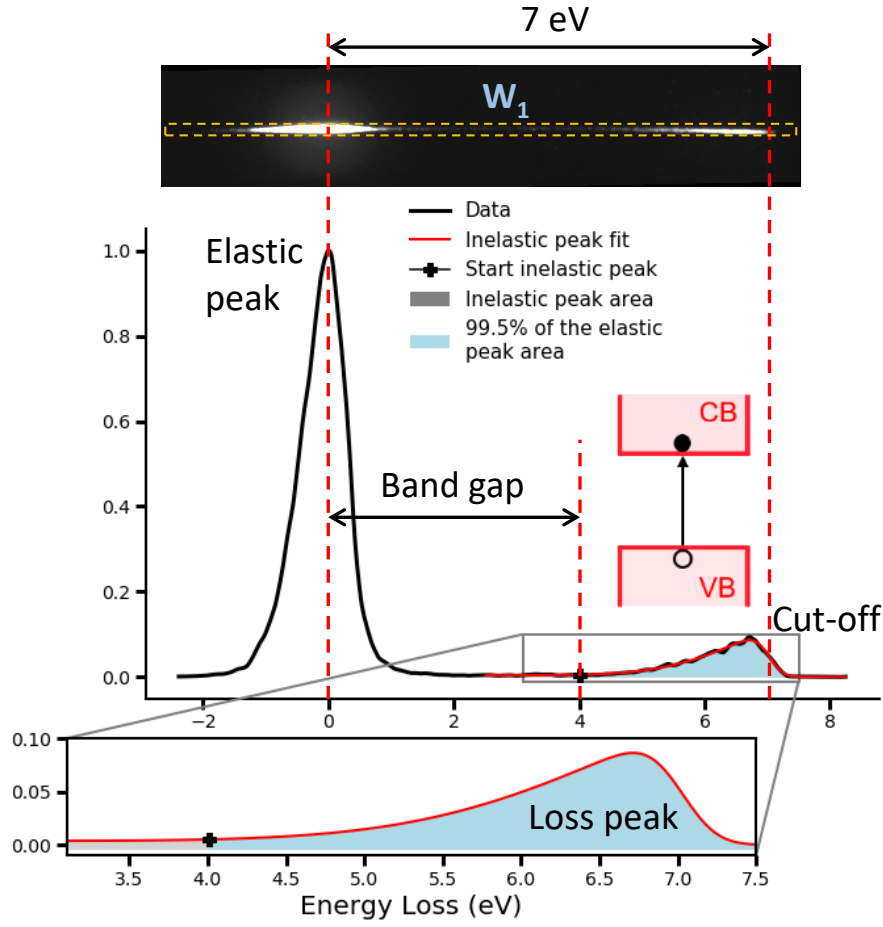


Figure IV.5: Raw EELS data acquired in the dispersive mode of the LEEM from the region of interest including W_1 . In the extracted EELS spectra, the red line shows the fit of the loss peak. The area fill is prolonged for negative intensity values for better visibility of the colors and the transition.

maximum (VBM) to the conduction band minimum (CBM) which corresponds to the band gap energy, as shown in the inset image in the graph. Between the elastic and secondary electron peaks, the intensity falls almost to zero, consistent with the absence of in-gap states. The gap is measured between the maximum of the elastic peak (i.e. at zero energy loss) and the beginning of the loss peak. In order to consistently extract the band gap over the selected domain and domain walls, the loss peak is fitted empirically and the onset of the loss peak is defined as the energy at which the loss becomes significant. More specifically, we took as a criterion for the beginning of the loss peak the energy at which the area under the loss curve represents 0.5% of the complete loss peak area (when the losses become significant). The loss peak is fitted by a function that is a product of a Gaussian, for the start of the peak, and a complementary error function to fit the peak cut-off, detailed in equation 1.

$$a \cdot (e^{-\frac{(x-\mu)^2}{\sigma^2}} + \text{off}) \cdot \text{erfc}(\frac{x-x_0}{\sigma_1\sqrt{2}}) \quad (1)$$

with a the amplitude of the fitting function, μ the center of the gaussian, σ the standard deviation of the gaussian, off the offset of the gaussian which takes into account the non-zero background in the gap region, σ_1 the error function scaling factor and x_0 the offset of the complementary error function, which is at 7 eV. Besides the cut-off position, the other function parameters are fitting parameters for the least square method in order to extract the loss peak shape and then the gap energy for each EELS measurement on domain and domain walls.

The secondary electron or loss peak only emerges for primary electron energies greater than about 4 eV, i.e. greater than the band gap of CTO, as shown by the EELS spectra acquired at 4 eV in figure IV.6. The elastic peak is still clearly visible but there is no longer a distinguishable secondary electron peak since the incident electron energy is less than the band gap, excluding significant electron-electron inelastic losses.

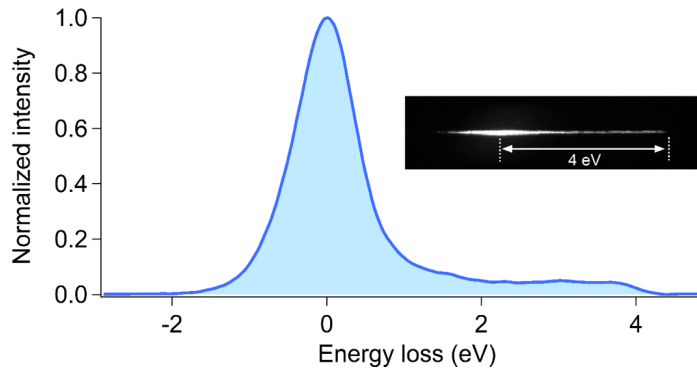


Figure IV.6: EELS spectrum obtained using a 4 eV incident electron energy (start voltage).

The band gap values extracted from the loss spectra are reported in table IV.1. For the error estimation, we give the non-symmetric two-sigma intervals (2 times the standard deviation, $\approx 95\%$ of confidence). The band gap values in the ferroelastic domains are ranging from 3.91 eV to 4.47 eV and from 3.85 eV to 4.16 eV in the domain walls. The 95% interval of confidence on the gap energy values is approximately ± 0.05 eV.

We can first observe that the band gap for the ferroelastic domains is higher than the range for the walls, with some overlapping. The band gap would be expected constant for each domain but we observe here a high variation (from 3.91 eV to 4.47 eV). This variation originates from the LEEM optics aberrations, dependent on the EELS ROI distance from the field of view center, selected by the field aperture. The further from the center, the more deformed the EELS intensity trace. Then, in order to specifically highlight the band gap narrowing in the walls,

	E_g	95% confidence interval
D1	4.24	+ 0.05 - 0.06
D2	4.10	+ 0.06 - 0.05
D3	4.26	+ 0.03 - 0.03
D4	3.91	+ 0.04 - 0.03
D5	4.18	+ 0.05 -0.03
D6	4.47	+ 0.03 - 0.05
W1	4.01	+ 0.05 - 0.06
W2	4.05	+ 0.06 - 0.05
W3	4.16	+ 0.03 - 0.02
W4	3.91	+ 0.04 - 0.03
W5	4.06	+ 0.03 - 0.03
W6	3.85	+ 0.03 - 0.04

Table IV.1: Quantitative results of band gap narrowing of the selected domains and domain walls.

we locally compare the band gap variation between the domain and domain walls. The relevant information is the relative band gap: the band gap difference between a wall and its adjacent domains, ΔE_g , where the aberrations can be considered identical because of the proximity of the field aperture for the EELS measurements. We can then compare the ΔE_g of each wall.

D . Band gap narrowing at the domain walls

In order to observe the band gap difference between each domain and domain wall, we calculate ΔE_g of each wall by taking the difference between the gap energy of the wall and its adjacent domains ($\Delta E_g = E_g(W) - E_g(D)$). These local measurements of the gap difference are reported in [IV.2](#), along with ΔE_{SP} ,

to identify the band gap narrowing and the polarity of each wall.

	Topo- graphy	Polarity	ΔE_g (eV)	ΔE_{SP} (eV)
W1	valley	P_{up}	$-0.16^{+0.10}_{-0.12}$	-0.06 ± 0.02
W2	valley	P_{up}	$-0.20^{+0.10}_{-0.09}$	-0.06 ± 0.02
W3	ridge	P_{down}	$-0.01^{+0.08}_{-0.05}$	$+0.02 \pm 0.02$
W4	ridge	P_{down}	$-0.01^{+0.07}_{-0.06}$	$+0.03 \pm 0.02$
W5	valley	P_{up}	$-0.27^{+0.07}_{-0.07}$	-0.23 ± 0.03
W6	valley	P_{up}	$-0.33^{+0.08}_{-0.08}$	-0.20 ± 0.03

Table IV.2: Quantitative results of band gap narrowing and surface potential shifts (ΔE_g , ΔE_{SP}) of the six domain walls with respect to their adjacent domains, as deduced from the spatially resolved surface EELS measurements.

We then plot in figure IV.7a ΔE_g , the difference between the band gap in the wall and the adjacent domains and ΔE_{SP} , the difference between the surface potential in the wall and the adjacent domains, together with their error bar representing two times the standard deviation. In IV.7b, we plot ΔE_{SP} the difference of the surface potential value between the wall and the adjacent domains. Downward polarized P_{down} domain walls have a positive ΔE_{SP} and upward polarized P_{up} domain walls have a negative ΔE_{SP} . We observe a systematic surface band gap reduction at the domain walls and the reduction depends on the domain wall polarity. The band gap reduction is higher for P_{up} domain walls (0.16-0.33 eV) than for P_{down} domain walls (0.01 eV).

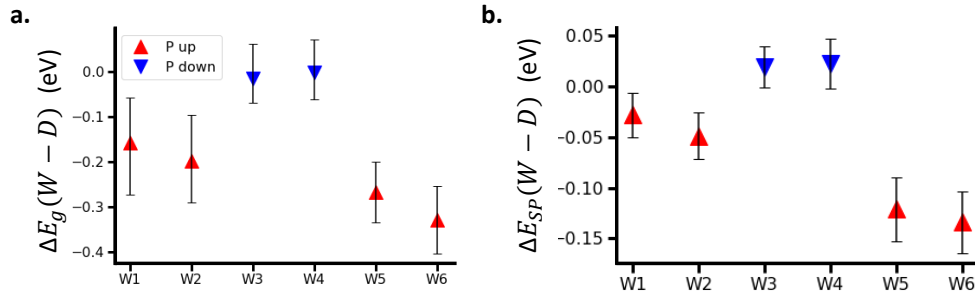


Figure IV.7: Band gap and surface potentials at domain wall/surface intersection. a. Band gap narrowing of the six domain walls with respect to the gap energies measured in their adjacent domains. b. Surface potential shift at each domain wall with respect to that of their adjacent domains, extracted from the surface potential maps in figure IV.2.

The domain wall electronic structure can be altered by both extrinsic and intrinsic mechanisms. Point defects such as oxygen vacancies have lower formation energy at domain walls than in bulk domains [164, 165] and cause intra-band gap

states, which modify the electronic structure. Symmetry breaking in the domain wall can also modify the electronic structure.

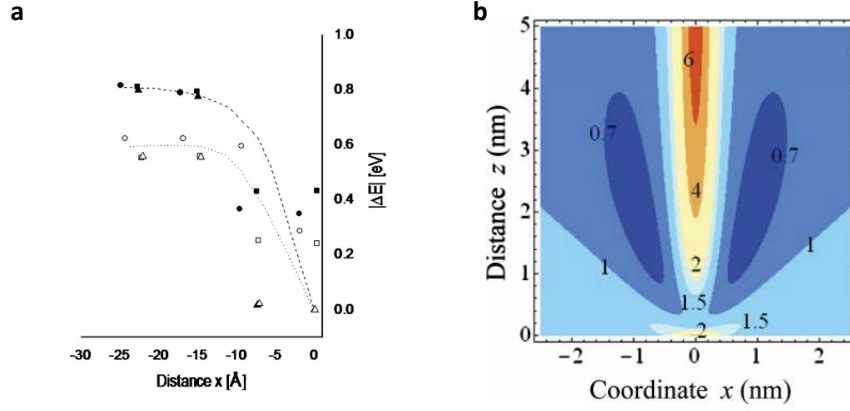


Figure IV.8: a. Relative energies of oxygen vacancies in $CaTiO_3$ with the distance perpendicular to the walls. Circles denote oxygen vacancies bridging titania along [100], squares bridging along [010], and triangles those bridging along [001] [166]. b. Contour maps of the V_O vacancy concentration in the vicinity of the twin-wall/surface junction in $CaTiO_3$. The twin-wall plane is $x=0$ and the surface at $z=0$ [72].

Molecular dynamic calculations of the difference of lattice energies between the presence of vacancies along a ferroelastic [100] twin wall and far from the wall are shown in figure IV.8a [166]. Moreover, the interface between the sample and the surface can have different properties related to surface relaxation. Oxygen vacancy concentration at the intersection between the twin wall and the surface is then also relevant information, as shown in figure IV.8b [72]. We can observe that on the surface, the oxygen vacancy concentration at the domain wall is approximately twice the concentration in the bulk domains (and 6 times more in the bulk domain walls). Theoretical calculations show that, at the surface, it is energetically favorable for oxygen vacancies to concentrate at twin walls rather than in the domains.

The band gap reduction selectivity between P_{up} and P_{down} domain walls directly suggest an extrinsic effect, in addition to the intrinsic wall polarity. Regardless of the polarity direction, domain walls have the same symmetry in the bulk. In the bulk, if the band gap reduction was from an intrinsic effect like the symmetry breaking at the domain wall, the observed reduction should be identical for both polarities, which is not observed here. Moreover, our first principle calculations of the bulk band gap in the domain walls show no band gap reduction due to the symmetry breaking at the domain wall. We can then exclude the intrinsic effect as the cause of the observed selective band gap narrowing.

The valence band of $CaTiO_3$ is dominated by O $2p$ orbital intensity whereas the bottom of the conduction band is mainly of Ti $3d$ character. The free energy

has a minimum for an oxygen vacancy at or near the domain wall and analytical calculations showed that the electron density can be 10-40 times higher at the domain wall intersection with the surface compared to in the bulk twin wall [72].

We suggest that the surface reduction in the gap near the P_{up} domain walls is due to local intra-gap states close to the conduction band, from the oxygen vacancy concentration in the domain walls, as schematized on IV.9. Because of the surface polar discontinuity at the domain wall interface with the surface, the intra-gap states are shifted depending on the wall polarity. Gap states of the P_{up} domain walls which are under the Fermi level, effectively act as shallow traps for electrons. We then observe by EELS that the band gap is lowered in the P_{up} domain walls from this surface effect. The observed band gap narrowing could be under-appreciated by our experimental observation because the spectroscopy measurements are done on an area defined by the field aperture ($\approx 3\mu\text{m}$) where the domain wall contribution represents less than 1% of the area.

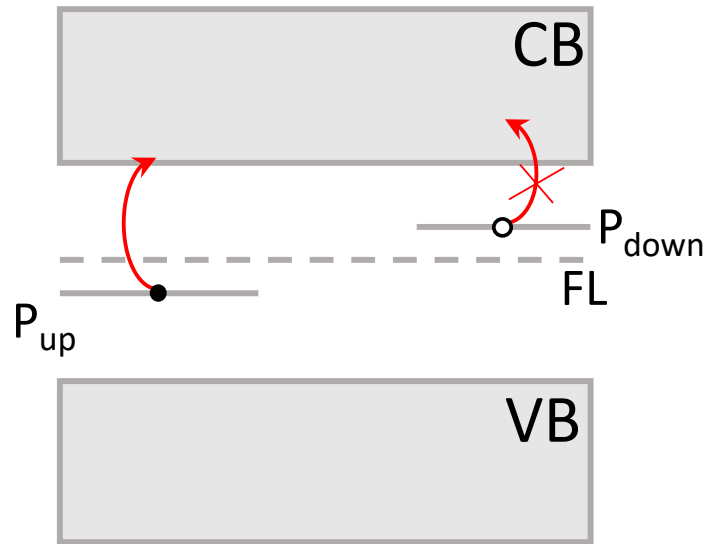


Figure IV.9: Schematic of the shifted intra band gap states by internal field for the P_{up} and P_{down} domain walls from the oxygen vacancies concentration in the wall and possible transitions.

E . Tunable domain wall surface band gap

From the hypothesis of oxygen vacancy concentration narrowing the gap in the P_{up} domain walls, an interesting next step for domain wall engineering is the study of the tunability of the gap energy with the oxygen vacancy concentration in the sample. We can expect to observe a variation of the gap energy with the oxygen vacancy content and maybe a threshold effect after reaching a certain concentration.

First observation of the oxygen vacancy concentration effect on the band gap was performed with a new CaTiO_3 sample. The hypothesis is that a new sample would have very low to no oxygen vacancy and annealing the sample under vacuum is generating oxygen vacancies. We followed the sample color evolution during annealing, which is gradually shifting to black as there are more oxygen vacancies in the sample.

The sample was continuously annealed under vacuum in the LEEM analysis chamber at 600°C and EELS measurements were performed during the annealing. At the end of the experiment, the sample had a strong black color indicating a high oxygen vacancy concentration, the color evolution is represented in the inset of figure IV.10. In the future, we will redo the experiment and measure the Ti valence with time to quantify the surface oxygen concentration. The same process as in the preceding experiment was used to extract the gap energy from the EELS measurements. The gap energy evolution with time annealed at 600°C for a P_{up} , a P_{down} domain wall, and a domain in between is shown in figure IV.10.

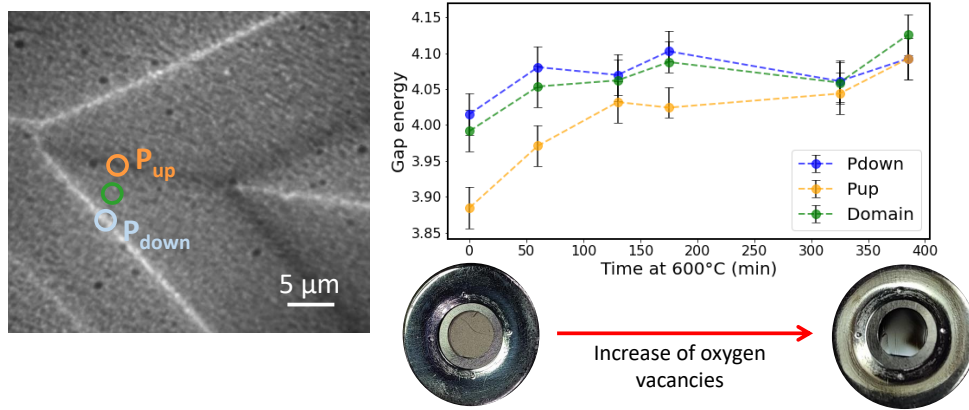


Figure IV.10: MEM image showing the EELS measurement ROI: a P_{up} , a P_{down} and a domain in between. The resulting gap energy is plotted with time at 600°C. The inset below shows the color modification of the CaTiO_3 sample between the beginning and the end of the annealing.

As in the first EELS experiment, we observe that the P_{up} domain wall has a lower gap energy than the ferroelastic domain and the P_{down} wall. The latter is very close to the energy in the domain, so almost no band gap reduction. With the increase of the oxygen vacancies, we observe that the band gap energy of the P_{up} domain wall is increasing until reaching the P_{down} and the domain gap energy value. In the beginning, the sample has a very low oxygen vacancy concentration, the sample is transparent with a light beige color. At the end of the experiment, the sample has a high concentration of oxygen vacancies, the sample is dark, an indication of a high concentration of point defect.

We hypothesize that when annealing, we are creating more oxygen vacancies

over time, which tend to be at some point homogeneously distributed on the surface after the walls are saturated. The material chemistry change by oxygen vacancies, which were first localized in the domain walls for low concentrations of oxygen vacancies, tend to diffuse in the domains. Moreover, electrons tend to be less trapped in the walls with the chemistry change in the domains. We then have the difference in gap energy between P_{up} and P_{down} domain walls reducing over time with the increase of oxygen vacancies concentration. Given our band gap narrowing hypothesis, we would have expected to have the P_{up} gap constant and a reduction of the domain and the P_{down} wall gap with increasing oxygen vacancies.

It could also be possible to perform the opposite experiment where we add oxygen in the chamber to reduce the concentration of oxygen vacancies at the surface. We would expect to see the opposite effect with the gap of P_{up} domain wall remaining constant and the gap of the domain and the P_{down} domain walls increasing back to their values when the sample had low oxygen vacancy concentration.

F . Conclusion

We have measured experimentally a band gap narrowing of 0.01 to 0.33 eV in ferroelastic domain walls at the surface of $CaTiO_3$. Both inwards P_{down} and outwards P_{up} domain wall polarity is observed. The band gap narrows principally in P_{up} domain walls, due to intra-gap state possible transitions by the concentration of oxygen vacancies in the wall. Similarly to many cases in ferroelectric materials, this band gap reduction is ascribed to extrinsic effects such as oxygen vacancies.

The band gap narrowing in the domain wall could be tuned by the oxygen vacancy concentration in the sample. A finer study of the band gap evolution with vacancy concentration is needed to understand the underlying mechanisms. The possible tunability of the $CaTiO_3$ domain wall electronic properties with chemical defects, here oxygen vacancies, opens the perspective for domain wall engineering of the electronic properties.

V - Surface domain wall creep in BaTiO₃

The dynamical domain wall behavior is at the core of ferroelastic/ferroelectric switching. The motion of ferroelectric domain walls is a nonlinear process where continuous propagation often superimposes with sudden jumps called jerks. Such jerks are initiated when walls are pinned and depinned in a stop-and-go mechanism [167]. Many such sudden movements make up an avalanche, which does not depend on the scale of the energies involved, meaning it is scale-invariant [168]. We can describe by power laws the probability to observe an avalanche with a certain energy, as it was first found for earthquake avalanches [95, 169].

We are particularly interested in the creep dynamics of ferroelastic/ferroelectric *BaTiO₃* domain walls at the surface. Domain ordering at the phase transition minimizes the free energy of the system but the room temperature is usually too low for thermally activated movement. Domain reorganization, therefore, takes place by another mechanism and is not, in general, smooth but proceeds rather by an accumulation of jerks [170]. Whereas many experiments have been carried out in the bulk [171, 167], an additional complication arises if one wants to study jerky movement at the surface. Ferroelectric surface order can be quite different from the bulk and crucial in view of device applications.

A . Domain-wall dynamics and avalanches

Jerky movement of domain walls in ferroelastic and ferroelectric domain walls generates a fast strain relaxation, causing acoustic waves (also called crackling noise) in the material, which can be detected by piezoelectric sensors [172]. The signal is statistically analyzed to observe that the accumulation of jerks' energy and amplitude distributions follow a power law. It means that the domain wall movement is scale-invariant and that fast domain wall displacement is possible [51].

Jerk movement can also be analyzed by direct optical microscopy observation. An example of such an analysis is shown in figure V.1 [170]. Two vertical needle domains propagate under external stress. The needle domain movement is smooth and can be described as classic front propagation until it hits a defect (such as a vacancy or a dopant), and is pinned. Increasing stress can depin the needle tip. The total movement is hence a superposition of a smooth movement and a stop-and-go propagation of the needle tip, which generates jerks at any pinning center. The dissipated energy is measured by tracking the distance of the movement x and measuring the kinetic energy as $E_j \approx v^2 \approx (dx/dt)^2$. The jerk energy distribution is represented in figure V.1d and follows a power law $P \approx E^{-\epsilon}$ with an exponent ϵ of 1.8.

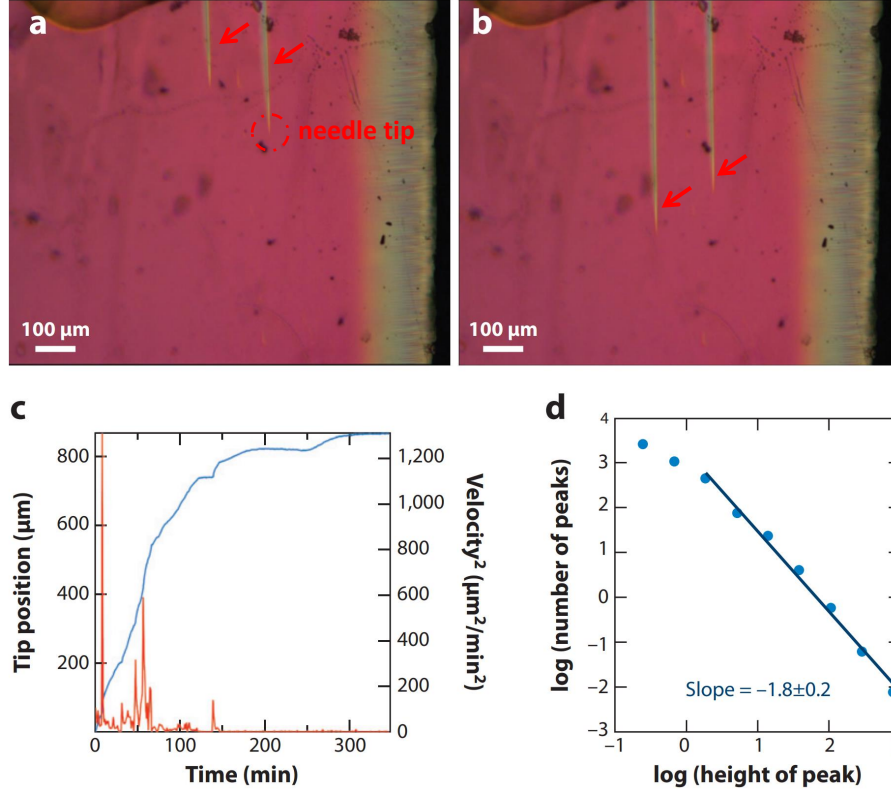


Figure V.1: (a,b) Topology of two large needle domains in ferroelastic $LaAlO_3$, at different times of the experiment, that propagate from one side of the sample surface to the other under stress. (c) Under stress, the needle tip advances (blue curve) with differential changes (red spikes), showing jerks. (d) The jerk statistics follow a power law with an exponent ϵ of 1.8. From [170].

B . Experimental conditions

We have used photoemission electron microscopy in a NanoESCA setup to analyze the jerk of domain walls at the surface of ferroelectric $BaTiO_3$ (001). Images were acquired at the photoemission threshold using a Hg lamp (5.2 eV) and a 39 μm field of view. The spatial resolution is ≈ 50 nm and the overall energy resolution was ≈ 0.2 eV.

The sample is under low mechanical stress (creep scenario) due to the sample mounting in the PEEM sample holder. The creep dynamics of the domain wall were studied over a long time range of ≈ 29 hours (1750 min), with PEEM images acquired at the photoemission threshold at 4.1 eV, every 1 minute. A typical set of images is shown in figure V.2. The sample was heated above the room temperature at 310 ± 0.1 K during the acquisition with a closed loop control on the sample temperature, allowing to record an image sequence of over 29 hours with a minimized image thermal shift.

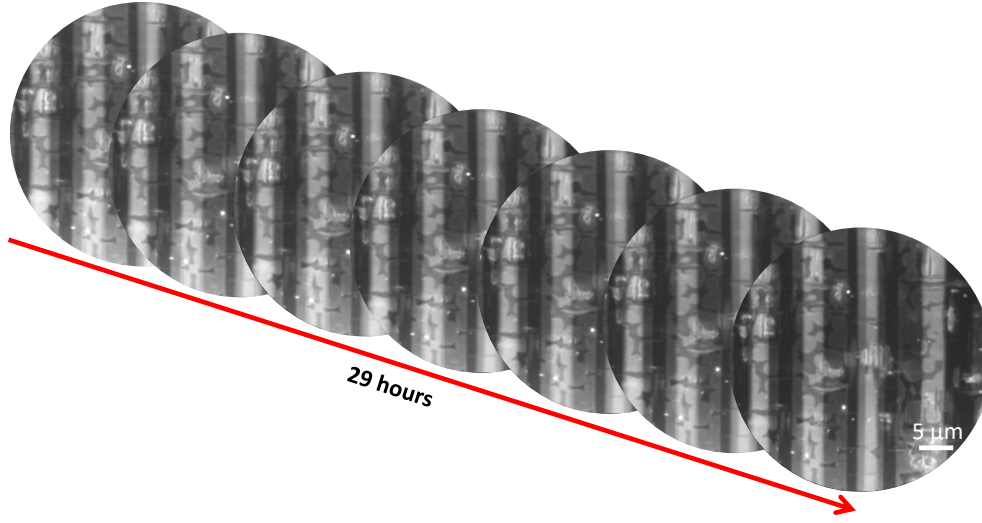


Figure V.2: Creep dataset representation. Threshold PEEM images at the photoemission threshold (4.1 eV), were taken every minute for approximately 29 hours. Field of view $39\ \mu\text{m}$.

At 310K, BaTiO_3 is in its ferroelectric phase. The ferroelectric domain polarity modulates the surface potential and so the photoemission threshold [134]. We can see three levels of intensity (triple contrast) in the PEEM threshold image, representing three polarity states P_{up} , P_{in} , and P_{down} at the surface. The domain walls between an out-of-plane and in-plane polarization are ferroelastic 90° boundaries, and the related domains are the vertical bands on the image. 180° ferroelectric domain walls are between P_{up} and P_{down} domains with curved domain walls shape on the image.

C . Averaged image analysis

We separated the image into five rectangular regions of averaged intensity, parallel to the ferroelastic domain walls, represented in figure V.3a by different colors, to study the creep motion. A small but continuous image thermal drift present during the acquisition over time is corrected. We then compute the PEEM intensity mean value μ for each rectangle Regions Of Interest (ROI), which represents the mean polarization over the ROI. The mean intensities for each ROI are plotted in figure V.3b. We can observe that the mean intensity decreases over time in each ROI, with spikes that correspond to sudden intensity changes related to sudden domain wall movements. We define these peaks as sudden avalanches (a spike can be several jerks) events and compute the jerks amplitude A_j by taking the first derivative of the mean value μ for each region, and the related energies E_j as the amplitude square (1), shown on figure V.3c.

$$\begin{aligned} A_j &= d\mu/dt \\ E_j &= A_j^2 \end{aligned} \quad (1)$$

We observe spikes that correspond to avalanche events with varying energy. There are many small energy jerks with a few higher energy jerks. Compared to having only one region of averaged intensity for the study, the image separation in five regions is to extract more avalanche events (5 times more) to potentially be more sensible to the domain wall jerky movement.

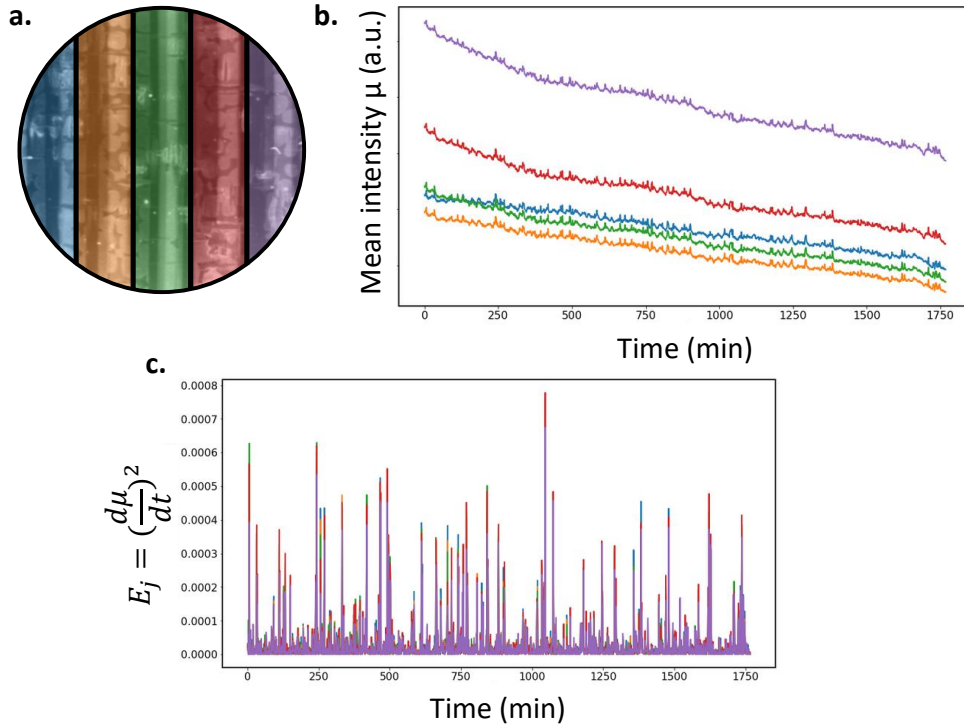


Figure V.3: a. Five rectangle region separation on the analyzed area, parallel to the ferroelastic/ferroelectric domain walls (90° boundaries). b. Mean intensity distribution μ of the 5 regions. c. Calculated jerk energy E_j distribution.

The jerk motion follows a power law distribution with the probability distribution function $PDF(E) \approx E^{-\epsilon}$, where ϵ is the avalanche energy exponent expected at $\frac{4}{3}$ in mean field theory [170] because the creep experiment is at a constant (residual) stress. Some spikes with small energies can originate from the electronic microscope intensity background noise, from a smooth domain wall movement, or from a ferroelectric domain polarization change (we observed that the averaged intensity decreases during the experiment). The spikes originating from non-jerky events would then not follow a power law distribution so an energy cut-off E_0 is introduced in the law. To estimate the power law exponent from the experimental dataset and verify whether it is in agreement with scale-invariant mean-field

models, we use the maximum likelihood method (ML) expressed in equation 2 [173, 93]:

$$\hat{\epsilon} = 1 + N_{E \geq E_0} \cdot \left[\sum_{i=1}^{N_{E \geq E_0}} \ln\left(\frac{E_i}{E_0}\right) \right]^{-1} \quad (2)$$

with $\hat{\epsilon}$ the estimated energy exponent (Maximum Likelihood Exponent MLE), E_0 is the varying energy cut-off, and $N_{E \geq E_0}$ the number of jerks with equal or higher energy than E_0 . Two parameters are estimated from this law: the energy cut-off E_0 which is the lower bound of the power-law behavior in the data and the MLE $\hat{\epsilon}$.

We show in figure V.4a the MLE for the jerk events composed of the sum of all jerks in the five ROI. There is a plateau region in the graph where over an half decade in cut-off energy the maximum likelihood exponent value is identical. The plateau is a clear indication that the data distribution follows at least partially a power law distribution. This plateau stable value is giving us the estimated exponent $\hat{\epsilon} = 2.0$, meaning that the jerky movement of the image is following a power-law distribution with an exponent estimated to be 2.

A more intuitive method to estimate the power law is to look at the jerk energy distribution by plotting the number of the jerk events N as a function of their energy in a log-log plot, shown in figure V.4b. At low energies, real jerk events are mixed with experimental noise, causing a deviation from the linear behavior. At high energies, fewer jerk events are measured so we deviate from the power law because of low sampling statistics. The power law exponent can be deduced by linear regression: $\epsilon = 1.97 \pm 0.16$, close to the predicted MLE.

The creep experiment is under a low residual mechanical strain where the domain walls' jerky movement energy is low. This can be seen by the fact that the plateau region only extends over half a decade, which is low compared to other creep and avalanche motion studies [93, 167]. Moreover, we are interested in the domain wall dynamics but the image division in rectangles is not sufficient to accurately detect small surface jerk relaxations under low creep load. The MLE found with the analysis over the image is higher than the mean-field prediction for an avalanche dynamic. From the MLE analysis, we know that the data at least partially follows a power law but we cannot accurately highlight the domain wall dynamic from the domains.

D . Pixel-by-pixel image analysis

One advantage to study creep domain wall dynamics with PEEM is the good spatial resolution of the measurement (50 nm). Instead of analyzing the data by averaging the intensity over ROI, we can perform a pixel-by-pixel analysis. Now the jerk distribution does not come from an intensity average of a whole region, we separately look at the distribution of jerk energy from each pixel. It would

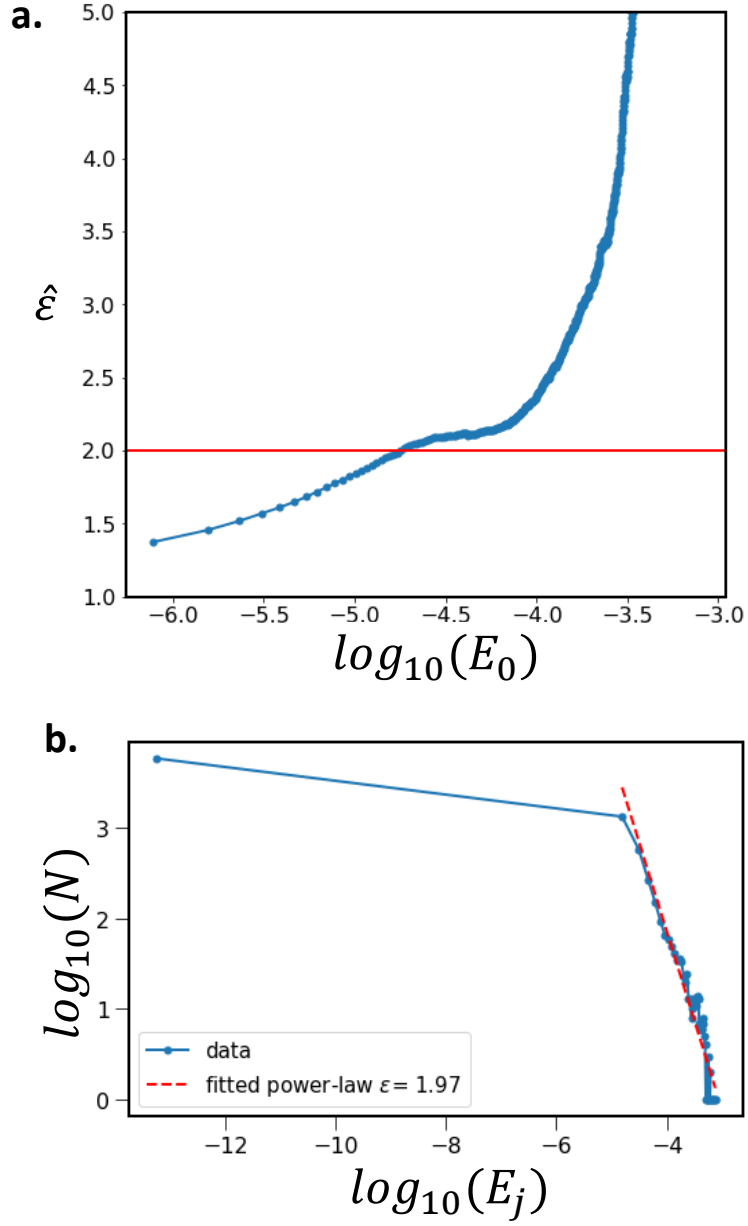


Figure V.4: a. Maximum likelihood estimator (MLE) as a function of the varying cut-off energy E_0 , from avalanche events of the whole image. The plateau is giving the stable estimator value. d. Log-log histogram plot for the jerk events distribution.

be time-consuming ($\approx 10\text{hours}$) to perform the MLE method previously done on five rectangles to every pixel. Moreover, the cut-off E_0 varies across the image so we would have to visually select the start of the plateau region for each pixel to determine the MLE. Instead, we perform a linear regression on the histogram log-log plot of the jerk distribution to deduce a power law exponent ϵ for each pixel ($\approx 15\text{min}$). The power law exponents are then represented on a reconstructed

map, shown in figure V.5a, with a linear regression example on one pixel plotted in figure V.5b. The white repeating small patterns on the image are burnt pixels from the camera which form this pattern after the image thermal drift correction.

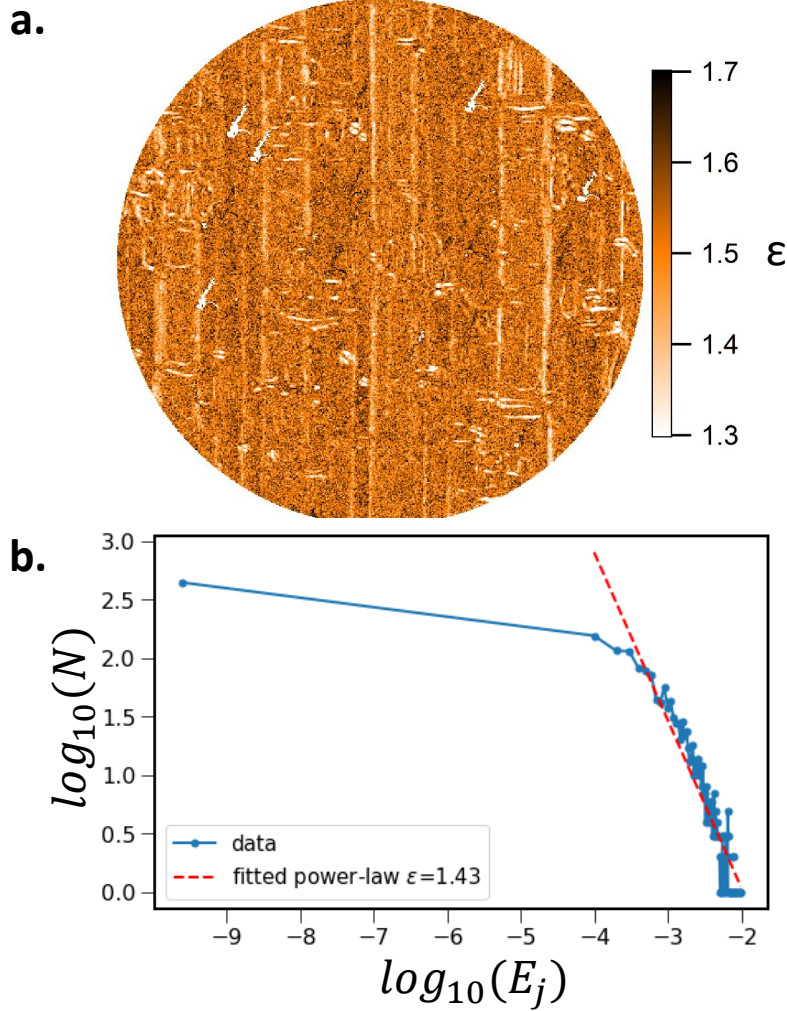


Figure V.5: a. Map of the power law exponents determined by the pixel-by-pixel linear regression method. b. Jerk energy distribution histogram of one pixel of the creep sequence. The linear fit giving the power law exponent ϵ of the pixel is shown.

The map shows a contrast between some domain walls and domains. This difference in power law exponent between domain and domain walls could not be seen with the analysis averaged over the whole image. The lowest values of the power-law exponent are seen in the domain walls, of about 1.37 ± 0.09 , which is close to the MFT value $4/3$. It means that some domain walls in BTO have a scale-independent movement. We can see that the only domain walls with a different contrast are the straight domain walls, which are also ferroelastic and ferroelectric (90° boundaries). We don't observe a different dynamic in purely ferroelectric

domain walls from the bulk. The pixels' power law exponents are quite different from the one calculated over the whole image because the jerk energy distribution for the analysis is now from each pixel.

The total amplitude of the domain walls' avalanche under low creep conditions over the 29 hours corresponds to the width of the regions in figure V.5a where the jerk energy distribution follows a power law with an exponent of 1.37, close to the MFT. The width of these regions is typically between 100 to 500 nm. With the hypothesis that the domain wall jump by one lattice constant at each jerk, we have at minimum recorded 1000 jerks per domain wall over the 29h of accumulation, i.e. a minimum of 1 jerk per 2 minutes.

Figure V.6 represents the standard deviation map of the linear regression analysis. The error is the lowest at the 90° domain walls, suggesting that these domain walls jerk follows more closely a specific power law with an exponent $\epsilon = 1.37 \pm 0.09$ with respect to the rest of the surface. The pixel-by-pixel method enables us to analyze the surface jerks and we can observe a specific dynamic limited to 90° domain walls. The dark repeating patterns on the image are burnt pixels from the camera which form this pattern after the image thermal drift correction.

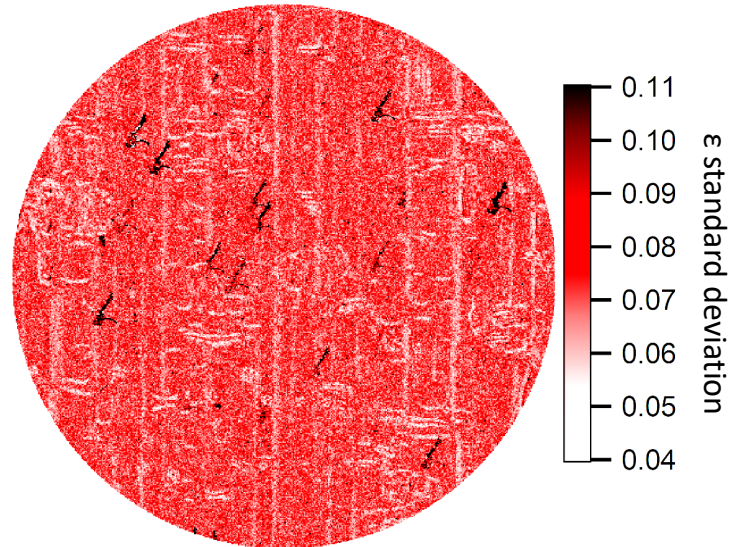


Figure V.6: Standard deviation map of the linear regression on the log-log jerk distribution plot at every pixel.

E . Drift correction and noise

The domain wall movement over the 29 hours is on the scale of very few pixels (500 nm is ≈ 6 pixels) from figure V.5a. One main concern is the effect of image drift correction. A continuous small thermal drift of up to 5 μm in the horizontal

and vertical directions is corrected prior to the analysis. If the drift is not corrected with a sufficient pixel resolution, it could create artifacts that may be confused with jerks (sudden pixel jumps). Similarly, none of the compatible amplitude to the low energy jerks could also modify ϵ .

To verify the effect of the analysis method on noisy and/or badly thermal drift corrected data, we first analyze with the same method a 'noise' sequence consisting of one repeated image of the experimental creep stack with for each image a random shift in both horizontal and vertical direction of ± 1 pixel to mimic a sequence with no jerky movement and a bad thermal drift correction. The power law exponent map is shown in figure V.7a, which is not in the same range as our analysis because there is no high energy jerks and the dynamic behavior between domain and domain walls are inverted with respect to the creep analysis on the experimental data. So the detected avalanches originate from the experimental data.

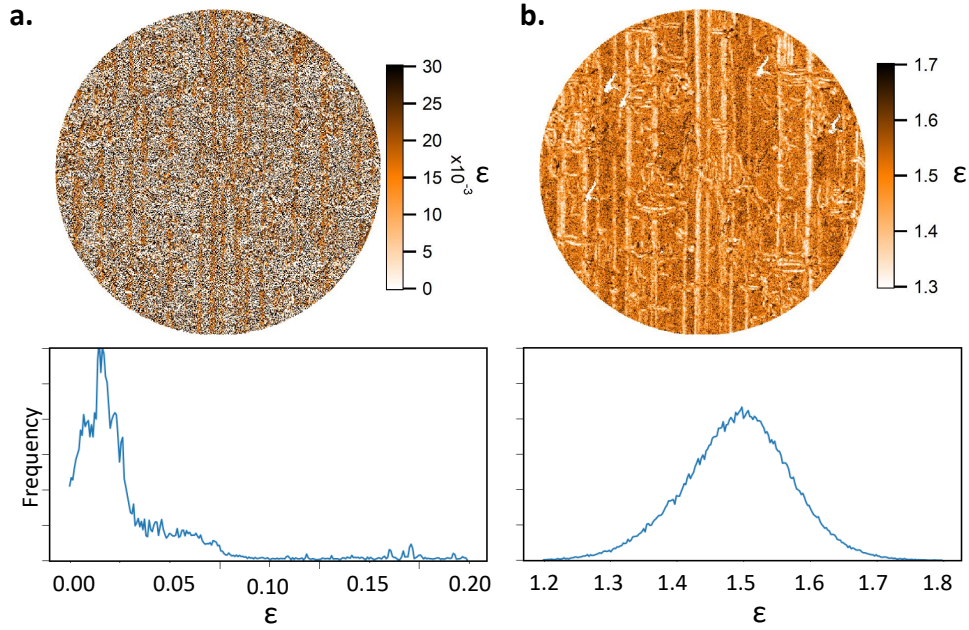


Figure V.7: a. Pixel-by-pixel analysis exponent map from a noise sequence. The initial data sequence consists of one repeated image of the experimental creep stack, repeated as much as the total number of analyzed images, with for each image a random shift in both horizontal and vertical direction of ± 1 pixel. b. Pixel-by-pixel analysis exponent map with the real PEEM acquisition stack and random horizontal and vertical shifts of ± 1 pixel for each image. c. and d. Histogram of the (a. and b.) maps.

We can also perform an analysis with the experimental dataset and add a random pixel shift in both horizontal and vertical direction of ± 1 pixel to see the effect on the power law exponent of a 'bad' thermal drift correction over a sequence with jerk movements. A bad drift correction can create in the data false

sudden jumps which could influence the power law exponent. Here we simulate an exaggerated case where pixels randomly move by ± 1 pixel on each image. The resulting power law exponent map is shown in figure V.7b. We have quantitatively the same results as the creep analysis on the experimental data but the width of the 90° boundaries' total jerk amplitude is increased. If we further increase the random pixel shift, the width would further increase. The drift correction is then not responsible for the observed avalanche behavior of the $BaTiO_3$ domain walls although it could stretch the real jerk amplitude.

F . Discussion and conclusion

We analyzed the $BaTiO_3$ surface domain wall creep by taking advantage of the PEEM spatial resolution to observe domain wall movement over a long time range because of the surface potential modulation from the ferroelectric domain polarizations. The residual stress from the sample mounting provides a driving force for domain wall fluctuating movement over the 29 hours time range. We extracted $BaTiO_3$ domain wall motion from the analysis over 1750 threshold PEEM images with two methods: by averaging the jerk distribution over the whole image and by looking at the jerk distribution pixel-by-pixel.

From the whole image analysis, we determine an energy exponent of approximately 2 from the plateau in the maximum likelihood curves, higher than the predicted mean field theory power law exponent. The approach of slicing the image into five different rectangles to better extract avalanche spikes on the whole image has its limits to extracting a specific dynamic from domain walls with the maximum likelihood analysis. Averaging over ROI with our very small domain wall displacement makes it complicated to extract the jerk power law exponent and we don't use the good spatial resolution of the PEEM.

From the pixel-by-pixel analysis, we determined the power law exponent on each pixel, with values ranging from 1.3 to 1.7 and the lowest values at the domain walls of about 1.37 ± 0.09 , close to the MFT 1.33 value observed for earthquakes, providing striking confirmation of a scale-independent power law dependence of the ferroelastic domain wall jerk motion. From acoustic emission spectroscopy, it was observed in $BaTiO_3$ that electric-field switching of 90° boundaries (ferroelastic/ferroelectric domain walls) generates large strain fields, which emit the measured acoustic phonons during ferroelectric hysteresis measurements. The domain wall jerk motion was following invariant avalanche dynamics and no acoustic waves from the 180° domain wall were detected [90]. This is in agreement with our creep experiment, which highlights from the map of figure V.5 that at the surface, 90° domain walls have a jerky motion.

The domain wall movement can be decomposed into wild events, which correspond to jerks, and mild events (smooth displacement) which do not follow power law distributions [174, 175]. The mild dynamic is not scale invariant and exhibits characteristic energy. The classical nucleation theory of Kolmogorov, Avrami, and Ishibashi (KAI) considers the mild switching process as the phase transformation in infinite media with a constant nucleation rate, and with domain wall velocity as a rate-limiting parameter [81]. The ferroelastic domain wall movement is predominantly wild because of strong strain-induced correlations between domain wall movements. Moreover, the interaction between domain walls and defects such as vacancies causes jerk motion by pinning-depinning mechanisms. Wall-wall and wall-defect interactions induce wild avalanches [176]. Mild and wild fluctuations coexist in domain wall dynamics and could have a potential role in neuromorphic computation [177], where progressing conductive domain walls in electric fields

can, in the case of wild movements, connect defect “reservoirs” similar to synapses (DW) connecting neurons (defects reservoirs) in the brain. The mobile, jerky domain wall can connect or disconnect reservoirs by shifting its position.

Mild and wild domain wall movement coexist in $BaTiO_3$ domain walls [176]. Moreover, domain-like patterns can persist well above the Curie temperature in $BaTiO_3$ [69, 178]. A further extension to the creep analysis is to compare the creep dynamic at different temperatures and different loads closer and above $BaTiO_3$ Curie temperature. We expect to observe a modification from ‘wild’ (at low temperature, far from T_C) to ‘mild’ (closer to T_C) dynamics as a function of the temperature, enabling us to better understand the underlying domain wall dynamic processes [179]. The jerk energy distribution follows a power law for wild dynamics because of the long interaction range of the ferroelastic strain and the collaborative movement of the domain walls and in contrast, the jerk energy probability distribution function for mild dynamics follows an exponential law because of the weak and random movement of the walls [176]. Theoretical calculations showed that in some ferroelastic systems, the energy distribution of jerks follows a power-law noise pattern $P(E) \approx E^{-(\gamma-1)}$ ($\gamma - 1 = 1.3$ to 2) at low temperatures and an exponential distribution (Vogel-Fulcher) $P(E) \approx e^{-(E/E_0)}$ at high temperatures. More complex behavior occurs at the crossover between these two regimes with simulated jerk distributions described by a generalized Poisson distribution $P(E) \approx E^{-(\gamma-1)} \cdot e^{-(E/E_0)^n}$ with $n = 0.4-0.5$ and $\gamma - 1 \approx 0$ [180]. It would mean that the domain wall dynamic is shifting from a more wild to mild regime with temperature.

For a further extension to the creep analysis and mild vs wild domain wall dynamic characterization experiments, a preliminary design and implementation work on a shear stress application PEEM sample holder are presented in the appendix section [Appendix B](#) where different creep loads and sample in-situ heating can be applied to a sample to perform creep analysis in the PEEM. The presented creep results provide a first insight into avalanche motion at the surface of ferroelectric BTO, here ‘at rest’, where the sample has a residual load only from the sample mounting.

VI - Conclusion and perspectives

A . Conclusion

The structural and electronic properties of CaTiO_3 ferroelastic domains and walls were investigated, in addition to the motion mechanism of ferroelastic BaTiO_3 walls, to understand the electromechanical functional properties of the walls.

In the first part of the thesis, we identify the domain ferroelastic ordering in CaTiO_3 with photoemission techniques. We use PEEM at the photoemission threshold to study and quantify the physical topography of the CaTiO_3 (001) surface with its characteristic valley/ridge factory roof-like structure and identify the possible twin walls present in the analyzed area. By off-centering, the contrast aperture from the optical axis, by typically more than the aperture radius, image contrast due to the physical topography is enhanced by collecting only high angular photoelectrons in a near dark field mode. However, electrons emitted at high angles have a lower velocity perpendicular to the average sample surface used to align the PEEM, giving a higher apparent value of the photoemission threshold. Using a simple geometrical approach, relating the take-off angle to the angles inside the PEEM optics, allows quantification of the tilt angle of a domain surface from the measurement of the photoemission threshold. The results agree well with the independent measurement of the tilt angles using atomic force microscopy (AFM). The calculated twin angles can help to identify the domain order at the CaTiO_3 surface from the theoretically possible ferroelastic domain walls. However, because of different equivalent symmetries, some domain walls' twin angles can be formed by different spontaneous strain pairs. Moreover, some possible surface twin angles on the (001) surface are 180° , they don't form a surface topography so these domain walls would be invisible by this technique. Then a complementary in-situ technique to identify the surface strain state would be helpful to identify the ferroelastic domain and domain walls.

Moreover, we also directly identify the ferroelastic spontaneous strain order parameter orientation in ferroelastic domains by X-ray absorption spectroscopy photoemission electron microscopy (XAS-PEEM). The polarized light interaction with the titanium 3d orbitals is not equivalent between ferroelastic domains with different strain orientations. A contrast related to the different spontaneous strain orientations is visible in X-ray linear dichroism (XLD) for some domain wall surface trace orientations. With theoretical calculations, we can identify the spontaneous strain direction on both sides of domain walls which have domains with different XLD intensities.

We are able to calculate the surface twin angle between CTO ferroelastic domains in laboratory PEEM and we can identify the spontaneous strain in the ferroelastic domains in XAS-PEEM. From symmetry considerations, we can then

deduce the ferroelastic strain ordering, i.e. the spontaneous strain orientation. This direct observation of strain and its possible characterization opens perspectives, discussed below, in the study of the response of the strain in the domains and the polarity in twin walls to an in-situ applied electric field.

In the second part of the thesis, we observe and discuss the band gap narrowing at the calcium titanate domain walls. The gap is measured by electron energy loss spectroscopy (EELS) in a low-energy electron microscope (LEEM) in dispersion mode. A field aperture in an image plane is centered on domains and then on domain walls to measure the gap energy between the elastic and the onset of the loss peak. The measured reduction at the domain walls is between 0.01 and 0.33 eV, with a higher band gap reduction for upward polarized than for downward polarized domain walls. The band gap narrowing is suggested to be an extrinsic effect of the interaction between oxygen vacancy defects and the domain walls, generating intra-band states accessible mainly for electrons in upward polarized domain walls. A possible tuning of the band gap energy with the oxygen vacancy concentration is also observed. A finer study of the band gap evolution with vacancy concentration is needed to understand the underlying mechanisms. The possible tunability of the CaTiO_3 domain wall electronic properties with chemical defects, here oxygen vacancies, opens the perspective for domain wall engineering of the electronic properties.

In the last part of the thesis, we investigate the barium titanate ferroelastic domain wall mobility under creep. The dynamical domain wall behavior is at the core of ferroelastic/ferroelectric switching. The motion of ferroelectric domain walls is a nonlinear process where continuous propagation often superimposes with sudden jumps called jerks. We take advantage of the PEEM spatial resolution to observe domain walls over a long time range from the surface potential modulation of the ferroelectric domain polarizations. A residual stress from the sample mounting provides a driving force for domain wall fluctuating movement.

We extracted BaTiO_3 domain wall motion from the analysis over 1750 threshold PEEM images with two methods: by averaging the jerk distribution over the whole image and by looking at the jerk distribution pixel-by-pixel. We determined the power law exponent on each pixel of the analyzed surface, with values ranging from 1.3 to 1.7 and the lowest values at the domain walls of about 1.37 ± 0.09 , close to the MFT 1.33 value observed for earthquakes, providing striking confirmation of a scale-independent power law dependence of the ferroelastic domain wall jerk motion.

With the objective of engineering calcium titanate domain walls, a first discussion of the engineered domain walls in epitaxially grown calcium titanate thin films is presented in [appendix C](#). The epitaxially strained CTO thin films are grown on LaAlO_3 (LAO) by pulsed laser deposition. LAO is also a ferroelastic perovskite at room temperature, with a lattice parameter (3.79 Å) close to that of CTO (3.83 Å), enabling 1% compressive strain. We are able to grow films between 2 and

300 nm thick, showing domain walls at the surface. The twinning of the LAO substrate can couple to and propagate in CTO. Within a single such LAO-induced ferroelastic domain in the CTO, additional twin walls may form, depending on the relaxation of the epitaxial strain with thickness. The relaxation is confirmed by our XRD analysis. Out-of-plane lattice parameters for films of 200 nm and 300 nm are close to that of a 100 nm film, showing that the relaxation is almost complete at 100 nm thickness. The domain wall polarity is observed by LEEM, the walls thermally move at low temperatures, and a first Raman spectroscopy study is performed in order to understand the domain wall ordering in the ferroelastic stack. The possibility of engineering domain walls in thin film samples opens the perspective of an electromechanical control of ferroelastic domain walls in calcium titanate.

B . Perspectives

The electromechanical control of the ferroelastic domain walls in $CaTiO_3$ was hindered by the thickness of the single crystal. The bias voltage needed to move and potentially control the domain wall was high, from the surface size of the walls which are going through the sample. This size lock is resolved with the engineering of CTO thin film samples with domain walls. In order to apply bias across the twin wall, a $La_xSr_{1-x}MnO_3$ (LSMO) bottom electrode is epitaxially grown on the LAO substrate prior to CTO growth. Then, with these samples and the fact that we are able to observe the spontaneous strain in the ferroelastic domains in XAS-PEEM, we could design an experiment to study the response of the strain in the domains and the polarity in twin walls to an in-situ applied electric field, a step forward for domain wall electromechanical control.

This experiment proposal is already accepted in the I-06 beamline at synchrotron Diamond. We plan to use low-energy electron microscopy (LEEM) to locate suitable CTO twin walls. To quantify the polarity of the different twin walls at the film surface, we will use the LEEM contrast between twin walls and surrounding domains. In a previous XAS-PEEM experiment, we observed an XLD contrast between domains separated by specific domain wall orientations, presented in this thesis. The contrast is related to the surface strain state of the domains, which is electromechanically coupled to the polarity in the wall. We plan to observe this XLD contrast on thin film samples and then, we will study the polarity variation when applying an electric field across a twin wall. Although we do not expect a full reversal of the polarization because of the strong coupling between the twin wall polarization and the strain state of the adjacent domains, we do expect variations in the polarity, which should be visible in the $Ti_{2,3}$ pre-edge structure at the domain walls. We should also see an effect on the strain contrast in the ferroelastic domains. This possibility to modify the surface potential at the wall would be a step forward in the design of functional memory devices based on wall motion.

For a further extension to the creep analysis and mild vs wild domain wall dynamic characterization experiments, a preliminary design and implementation work on a shear stress application PEEM sample holder are presented in the appendix section [Appendix C](#) where different creep loads and sample in-situ heating can be applied to a sample to perform creep analysis in the PEEM. The presented creep results provide a first insight into avalanche motion at the surface of ferroelectric BTO, here 'at rest', where the sample has a residual load only from the sample mounting.

Appendices

A . Domain wall orientation table

Pairs	Wall equation	Azimuthal angle/[100]	Inclinaison angle/(001)	Twin angle
S_1/S_2	$x = 0$	90°	90°	180°
	$y = 0$	180°	90°	180°
S_1/S_3	$y = -z$	180°	45°	180°
	$3\epsilon_1 1(y - z) + 2\epsilon_1 2x = 0$	98.8°	98.7°	179.4°
S_1/S_4	$z = x$	90°	135°	180°
	$3\epsilon_1 1(z + x) + 2\epsilon_1 2y = 0$	171.2°	81.3°	180.6°
S_1/S_5	$y = z$	180°	135°	180°
	$3\epsilon_1 1(y + z) + 2\epsilon_1 2x = 0$	98.8°	81.3°	180.6°
S_1/S_6	$z = -x$	90°	45°	180°
	$3\epsilon_1 1(z - x) - 2\epsilon_1 2y = 0$	8.8°	81.3°	180.6°
S_2/S_3	$y = z$	180°	135°	180°
	$3\epsilon_1 1(y + z) - 2\epsilon_1 2x = 0$	98.8°	81.3°	180.6°
S_2/S_4	$z = -x$	90°	45°	180°
	$3\epsilon_1 1(z - x) + 2\epsilon_1 2y = 0$	171.2°	81.3°	180.6°
S_2/S_5	$y = -z$	180°	45°	180°
	$3\epsilon_1 1(y - z) - 2\epsilon_1 2x = 0$	98.8°	98.7°	179.4°
S_2/S_6	$z = x$	90°	135°	180°
	$3\epsilon_1 1(z + x) - 2\epsilon_1 2y = 0$	8.8°	81.3°	180.6°
S_3/S_4	$x = -y$	135°	90°	180.9°
	$3\epsilon_1 1(x - y) - 2\epsilon_1 2z = 0$	45°	167.6°	180°
S_3/S_5	$x = 0$	90°	90°	181.3°
	$z = 0$	-	0°	-
S_3/S_6	$x = y$	45°	90°	180.9°
	$3\epsilon_1 1(x + y) - 2\epsilon_1 2z = 0$	135°	167.6°	180°
S_4/S_5	$x = y$	45°	90°	180.9°
	$3\epsilon_1 1(x + y) + 2\epsilon_1 2z = 0$	135°	12.4°	180°
S_4/S_6	$y = 0$	180°	90°	178.7°
	$z = 0$	-	0°	-
S_5/S_6	$x = -y$	135°	90°	179.1°
	$3\epsilon_1 1(x - y) + 2\epsilon_1 2z = 0$	45°	12.4°	180°

Table 1: Domain walls plane equations, wall angle with respect to (001), and twin angle for each permitted pair of domain walls.

Each domain pair are ordered, i.e. (S_i/S_j) is different from (S_j/S_i) . For

example, three consecutive domains with the consecutive strain state $S_1/S_2/S_1$ will form two walls with opposite P_{up} and P_{down} polarity. So for one possible wall, two supplementary twin angles are possible depending on the wall polarity, but only one is displayed in the table.

B . Simulated XAS spectra

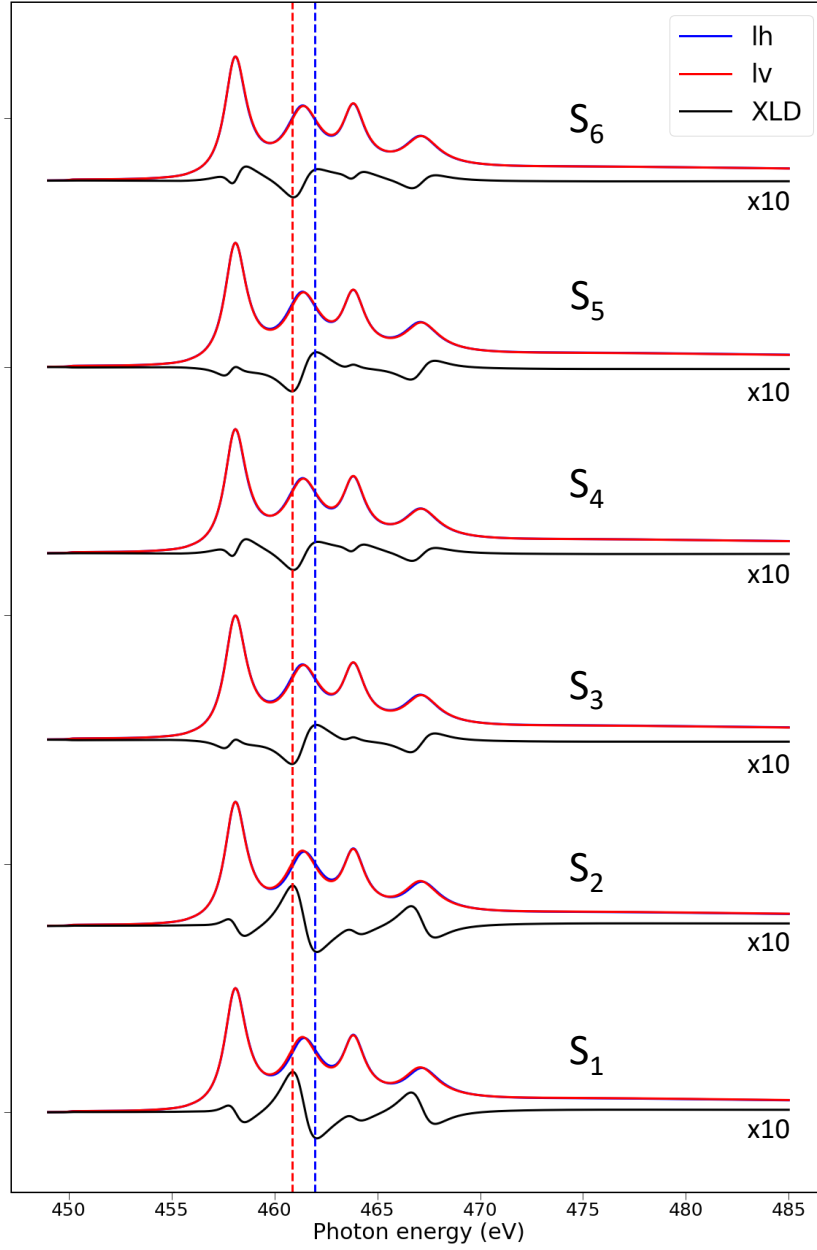


Figure APP1: a. Simulated spectra with the FDMNES program of the six possible ferroelastic domain spontaneous strain orientations, with the same incident light direction and polarization as the experiment. Curves are shifted for clarity. XLD spectra for the 6 strain orientations are also plotted, x10 to enhance the XLD signal visualization. The red and blue vertical dashed lines represent the two sides of the first e_g peak where the absolute XLD signal is the strongest.

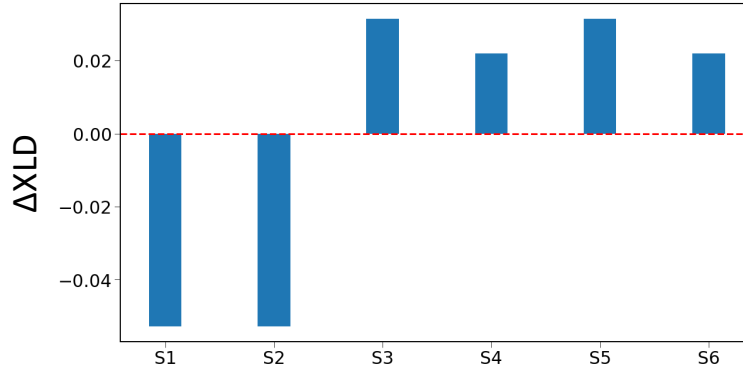


Figure APP2: XLD difference intensity between XLD at the right and left side of the first e_g peak (respectively at the blue and red vertical lines of figure III.24) for all S_i configurations.

C . PEEM shear stress sample holder for creep experiments

An in-situ shear stress application sample holder in the PEEM was designed and implemented during the thesis. It is possible to apply different creep loads and heat the sample. This tailored sample holder will provide a first insight into avalanche motion at the surface of ferroelectric BTO, with varying loads of creep.

C.1 . Shear stress sample holder

The design of a sample holder that can apply stress on a sample in-situ, inside the PEEM UHV environment, must follow strict dimension limitations. The challenge was to fit inside the sample holder 10 mm x 10 mm x 4 mm (length, width, height) a stress system. The holder dimensions are constrained because of the minimal distance between the sample and the extractor inside the PEEM analysis chamber.

Several technical solutions for the integration of a stress system in the sample holder have been put forward because they are feasible in principle while respecting the constraints of the assembly. It is necessary that the proposed solution allows the application of a range of stress that does not break the sample and which is fine enough to access several creep loads to characterize the dynamics of the walls. The samples used have a rectangular parallelepiped shape with a thickness of 500 μm and sides of 5 mm. BaTiO_3 and CaTiO_3 behave like ceramics mechanically: they follow the linear elastic relation $\sigma = E \cdot \epsilon$, with E Young's modulus. They break at a certain stress without passing through a plastic phase. As an order of magnitude, ceramics usually break for 1/100th of deformation i.e. for $\epsilon = 0.01$ at breakage. The bulk Young's modulus of BaTiO_3 is 67 GPa [181] so the breakage would correspond to an applied strain of 670MPa. Usually, samples break for stresses of the order of 300 MPa due to the presence of micro-cracks, points of stress concentrations that lead to its "premature" breakage.

A first design was implemented with four-point stress which applies uniaxial

stress to the sample: the sample is bent by the action of four cylinders, two non-movable on the top and two movable on the bottom surfaces of the sample. A piezoelectric actuator was integrated into the four-point system, inside the sample holder to apply the stress on the two bottom moving points. However, due to the height restriction inside the sample holder, the small integrated actuator could only apply a maximal stress of $\approx 1\text{-}10$ MPa. Moreover, because of the relative Young modulus of the sample and the actuator, half of the deformation was applied to the actuator and not the sample, it was not enough to observe a domain wall displacement.

A second stress application method considered is the shear method, which was proposed by Prof. Ekhard Salje. He found experimentally that shear stress was better than four-point bending for moving domain walls. For integration into the sample holder, the designed system is composed of two "L" shaped pieces, one fixed and one mobile, as shown in the schematic APP3a. The pieces were machined in the lab and the sample holder was reworked and also machined in the lab. The mobile piece is moved by a screw which is rotated by a fine step motor. The sample on top, visible in the image APP3b, is finely glued on the "L" shaped piece steps. A cover, shown in image APP3c, has an opening of 4 mm to observe the sample surface in the PEEM. A specific headless screw with a small thread was designed to move forward and backward the mobile piece.

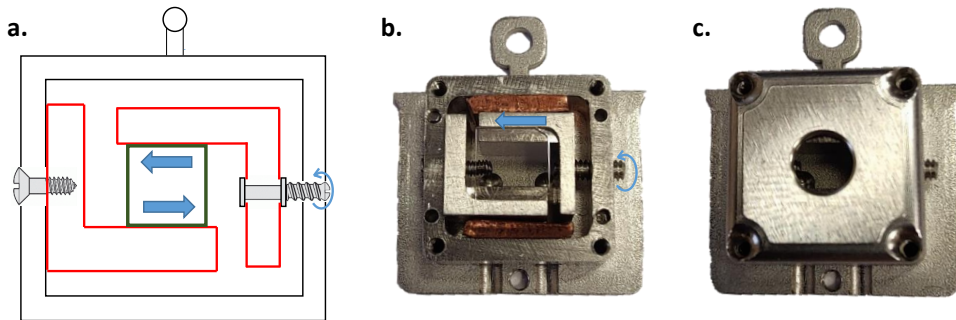


Figure APP3: a. Schematic of the shear stress PEEM sample holder, b. picture of the sample holder without the cap and c. with the cap.

This in-situ shear stress system can reach higher stress values, estimated at 200 MPa at the center for a displacement of $15\text{ }\mu\text{m}$. The stress distribution is not uniform, a gradient is formed from the center to the edges, as shown in figure APP4. We found that, for the same applied stress, domain walls were more easily mobile in the strain system. It could be related to the stress gradient. The PEEM was modified to integrate a UHV step motor, as shown in figure APP5. With this motor, we can apply different creep loads to the sample, and observe the domain wall dynamics over a long time range.

A stepper motor coupled to an epicyclic gear in UHV rotates the screw, to have more precision and extract the strain induced by the rotation of the screw. The

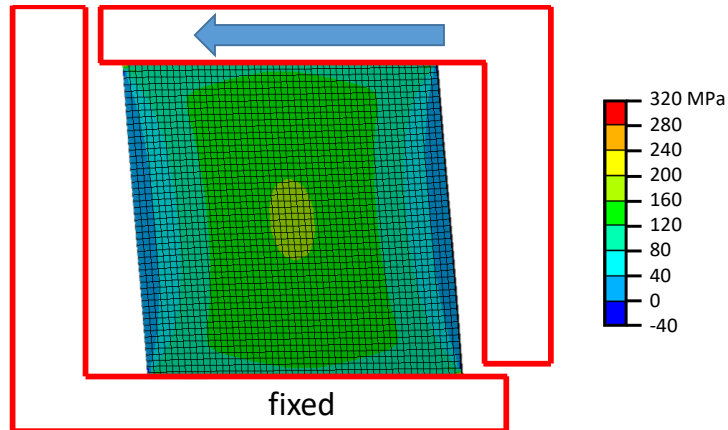


Figure APP4: a. Ansys finite element simulation of the stress distribution from a shear stress application. The upper part of the sample is displaced by 15 μm .

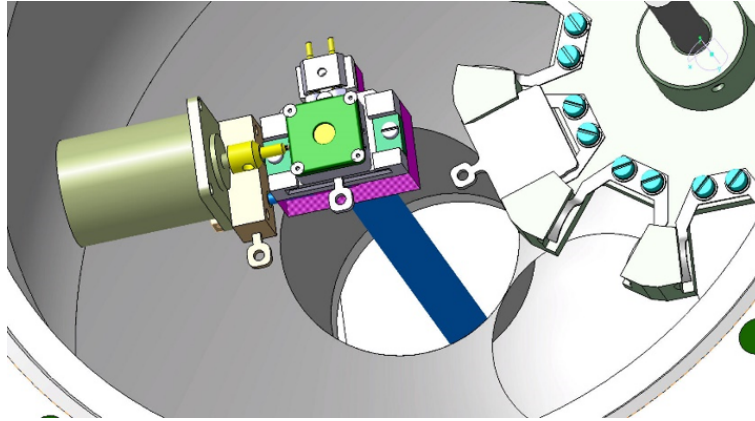


Figure APP5: Modelization of the UHV motor and connections to apply stress on the sample in the PEEM shear stress sample holder.

stepper motor with the reduction has a total of 40 000 steps for a complete rotation but the resolver can only read 170 steps per complete rotation. Moreover, the headless screw is M1,4, with a hexagon socket of 0.7 mm face-to-face and a pitch of 0.3 mm (distance between threads). The pitch gives the screw displacement per motor step. One complete screw rotation is a displacement of 300 μm so the finest reachable step is a shear displacement of ≈ 10 nm, taking into account the mechanical clearances of the motor and the screw, fine steps are ≈ 0.5 μm . Experimentally, BaTiO_3 samples are breaking for a shear displacement of 10-15 μm . It is then possible to analyze a wide range of creep loads in-situ with this system.

C.2 . BaTiO_3 domain wall shear stress test

The assembly tests were first performed under an optical microscope on a test bench to validate the stress application and also to test the fracture limits. In shear

stress, in order to find the applied stress τ , we use $\tau = \gamma \cdot G$, γ the deformation angle, equivalent with $\frac{\Delta l}{l}$, Δl the "L" shaped piece displacement (i.e. the screw displacement) and l the sample length (5mm). G is the shear modulus, 55 GPa for $BaTiO_3$.

We can see some optical microscope images from a stress test of a $BaTiO_3$ sample in figure APP6, extracted from a complete video of domain wall movement with increasing stress. The visible domains are separated by 90° ferroelastic boundaries and we can observe that we are going from a surface globally with one order parameter direction (one domain contrast) to the other direction. The sample broke at ≈ 500 MPa. The domain growth with stress can be quantified and corresponds to the evolution observed in literature [182]. Moreover, some avalanches were directly visible during the experiment.

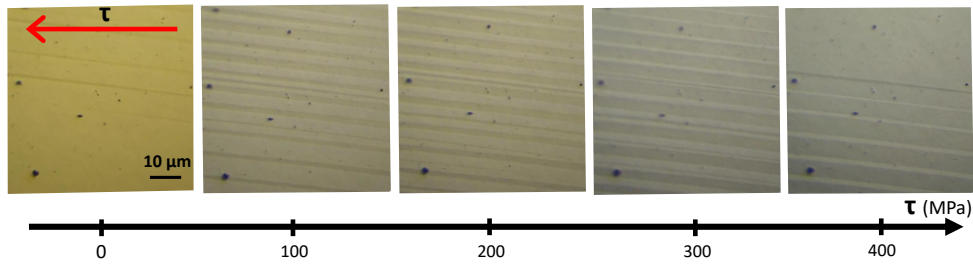


Figure APP6: $BaTiO_3$ domain wall displacement by a shear stress application in the PEEM sample holder. The test is performed outside the PEEM and visualized with an optical microscope.

With this in-situ system, we are able to apply different creep loads to ferroelastic samples and perform a creep analysis on the avalanche motion of the walls at the surface.

D . Domain walls engineering in CaTiO_3 epitaxial thin films

During the thesis, we followed a strain engineering approach by going from CaTiO_3 single monocrystal to thin film in order to study the epitaxial strain effect on the formation and electromechanical dynamics of the twin walls. The thin layer will also potentially reduce the energy needed to interact with the polarity in the domain walls.

D.1 . Epitaxial strain in CaTiO_3 thin films

D.1.1 . Substrate choice

Controlled epitaxial growth enables control of the film's functional properties. Different perovskite substrates are available for the epitaxial growth of CTO, some are represented in the graph APP7 in function of the strain originating from the lattice mismatch between the substrate and the film [183].

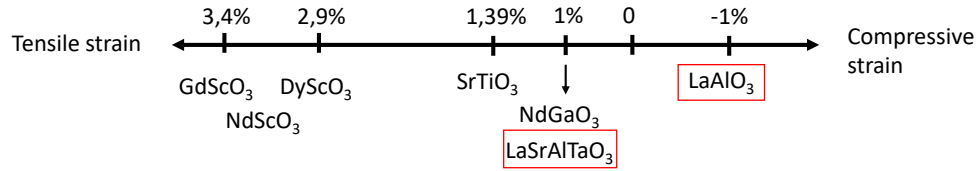


Figure APP7: Potential substrates epitaxial relations with CTO.

The films were deposited on both LaSrAlTaO_3 (LSAT) and LaAlO_3 (LAO) substrate with a LaSrMnO_3 (LSMO) intermediate electrode, generating respectively a tensile for LSAT and compressive for LAO strain of $f = 1\%$ in the CTO film. f is the lattice misfit parameter $f = \frac{a_s - a_e}{a_e}$, with a_e the film lattice parameter and a_s the substrate film parameter. This parameter can be calculated for both a and b directions and averages to $+1\%$ for LSAT and -1% for LAO. Moreover, for both substrates, the epitaxial growth of CTO has a surface plane in the (001) direction. SrTiO_3 would have also been a good substrate candidate but CTO can grow with different epitaxial orientations on the substrate [184].

D.1.2 . CaTiO_3 thin film epitaxial deposition

The epitaxial growth was performed by Pulsed Laser Deposition (PLD) in the C2N (Centre de nanosciences et de nanotechnologies) cleanroom. The method is presented in the experimental chapter. The laser used is a KrF excimer laser of 248 nm wavelength with a fluence of 6.95 J/cm^2 . The repetition rate of the laser can be tuned to change the deposition speed and the energy can be tuned. The CaTiO_3 target used in the PLD is a commercial target from Toshima Manufacturing Co.

The PLD deposition parameters were optimized for the growth of CTO thin films deposited on an LSAT substrate with an LSMO intermediate electrode. Varying parameters are the substrate temperature, laser energy, pulse frequency, and partial pressure of oxygen in the chamber. Films were primarily characterized by XRD to check the orientation and AFM for surface roughness. XPS was used

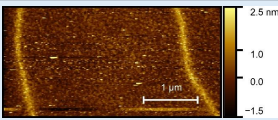
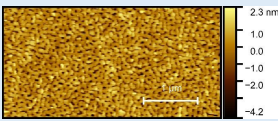
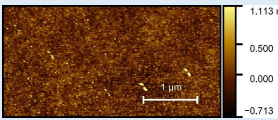
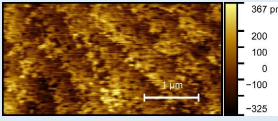
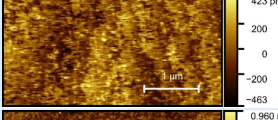
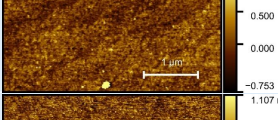
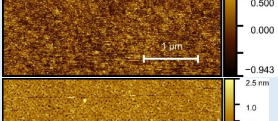
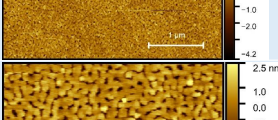
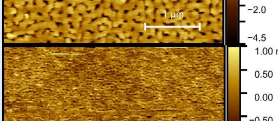
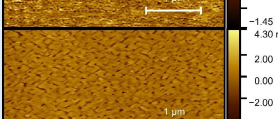
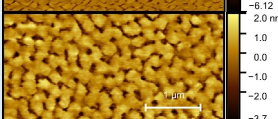
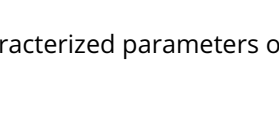
Substrate		Electrode	CTO						
Type	T (°C)	Type	Laser energy (mV)	Pulses	Pulses frequency (Hz)	Thickness (nm)	P (mtorr)	Surface (AFM)	c (Å) from XRD
LSAT	750	LSMO	50	1000	5	42	120		3.81
LSAT	750	LSMO	50	1000	5	42	120		3.82
LSAT	750	LSMO	40	1000	2	42	31		3.82
LSAT	750	LSMO	35	1000	2	42	31		3.81
LSAT	750	-	40	1000	2	42	31		3.81
LSAT	720	LSMO	40	1000	2	42	31		3.81
LSAT	720	LSMO	40	500	2	21	31		3.81
LSAT	750	LSMO	25	1000	2	42	31		3.81
LSAT	750	LSMO	25	1000	2	31	120		3.81
LSAT	750	LSMO	25	1000	2	24	31		3.82
LSAT	800	LSMO	25	1000	2	28	31		3.81
LSAT	800	LSMO	25	1000	2	31	120		3.80

Figure APP8: CTO deposition conditions and characterized parameters on LSAT.

to check the surface stoichiometry. Some of the deposition conditions and AFM surface topography images are shown in the table APP8.

Good deposition parameters for CTO are a laser energy of $3.5 J/cm^2$ (calorimeter 35 mV), a substrate temperature of $750^\circ C$, an oxygen partial pressure of 31 mtorr, and a repetition rate of 2 Hz. A higher substrate temperature and/or partial pressure induces a porous surface and visible cracks at the surface (first AFM image). We can observe the substrate steps on the CTO film with the optimized deposition parameters. For 1000 laser pulses, the measured thickness of the CTO film is 42 nm. For the bottom LSMO electrode, good deposition parameters are a fluence of $6.95 J/cm^2$ (calorimeter 50 mV), substrate temperature of $750^\circ C$, partial pressure of 120 mtorr, and repetition rate of 2 Hz. The electrode thickness is 27 nm.

We have not observed the formation of domain walls in the epitaxially strained CTO thin film on LSAT. The tensile strain could induce a monodomain state. However, for a compressive strain of the film on LAO, we were able to observe domain walls at the surface. Deposition on LAO follows the optimized parameter found on LSAT and the stoichiometry of the film was confirmed by XPS. XRD shows that the film is oriented in the (001) direction. Moreover, the CTO thin film epitaxial strain relaxes with increasing thickness, as shown in figure APP9. CTO (002) peak is shifting to higher 2θ angles, meaning that the out-of-plane lattice parameter is decreasing. We calculated the pseudo-cubic lattice parameter and we can observe that for films of thicknesses higher than 100 nm, the lattice parameter reaches a relaxed value of $\approx 3.825 \text{ \AA}$, close to the single crystal value of 3.82 \AA .

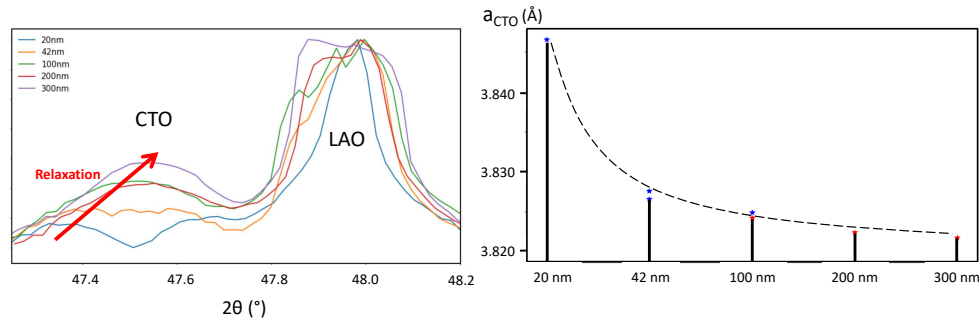


Figure APP9: XRD $\theta - 2\theta$ measurements of LAO/LSMO/CTO thin film samples with different CTO thickness. A relaxation of the CTO film is visible. The calculated out-of-plane CTO pseudo-cubic parameter for different CTO film thicknesses is plotted in the second graph.

Ferroelastic domain walls are visible by optical microscopy on different LAO / LSMO / CTO samples. Figure APP10, show optical microscopy images of 42 nm CTO thin films. The LAO substrate is also ferroelastic at room temperature. Usual single crystal LAO samples have 10-100 μm wide ferroelastic domains, which can be seen by the dark and bright domain contrast on the two optical images on the

right in figure APP10. After the LSMO electrode and CTO thin film deposition, we seem to observe other new domains at the surface of $\approx 2\text{-}10\ \mu\text{m}$.

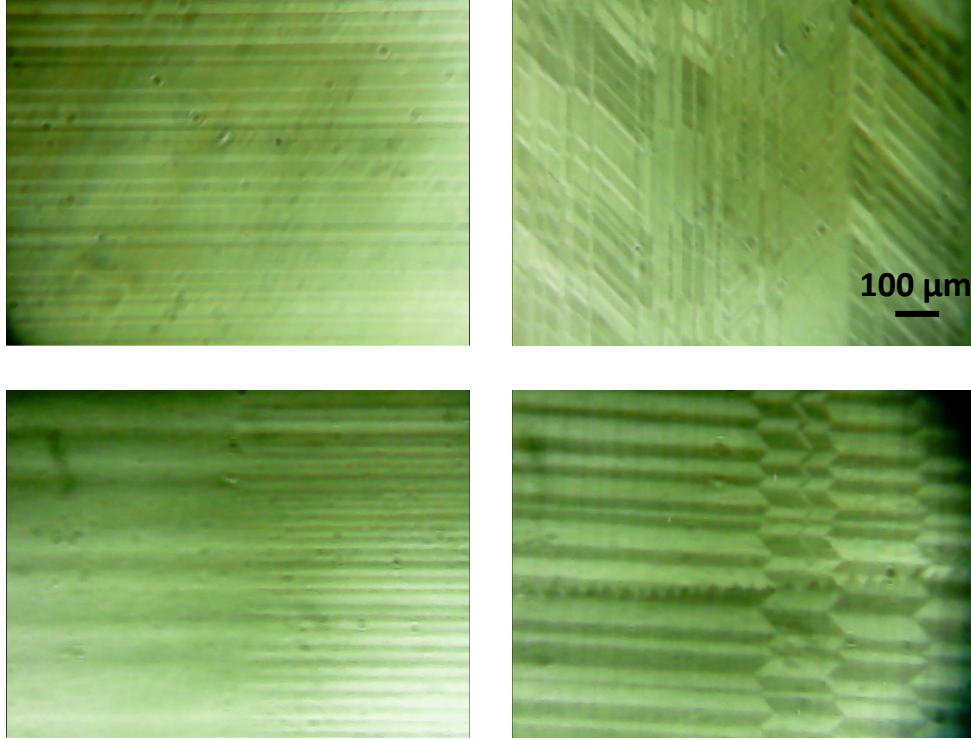


Figure APP10: Microscope images of different 42 nm CTO thin films with visible domain walls.

We observe domain walls at the surface of the CTO thin films but several questions need to be answered. The first question is about the ferroelastic ordering in CTO thin film. Do the domains in CTO only follow the LAO ones or is there in between LAO domain walls a smaller scale CTO ferroelastic ordering? Are the surface domain walls polar and mobile as in single crystal? We started to investigate these questions at the end of the thesis.

D.2 . Domain walls topography in CaTiO_3 thin films

AFM measurements on 42 nm CTO thin films confirm the ferroelastic twinning topography at the surface. Figure APP11 shows topography and amplitude measurement on a 42 nm LAO/LSMO/CTO sample. Domain size is between $2\text{-}10\ \mu\text{m}$ in this analyzed area.

Our ferroelastic ordering hypothesis is described in the figure APP12 schematic. We are expecting that the CTO thin film follows the LAO twinning and other CTO domains can emerge in-between LAO domain walls. The density of domain walls could be influenced by the film thickness, especially between epitaxially strained films (below 100 nm thickness) and relaxed films.

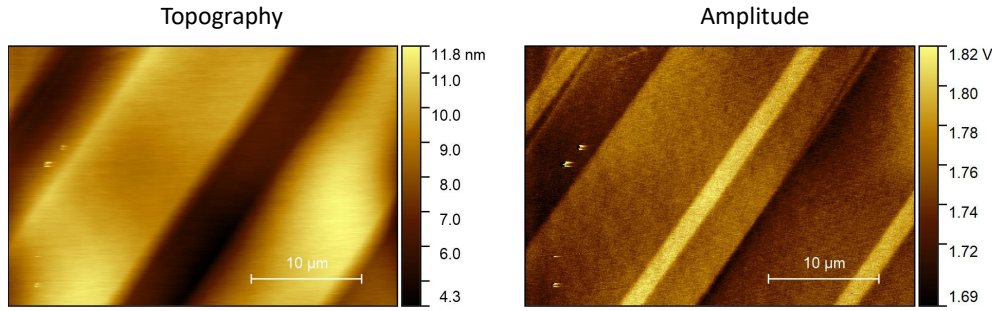


Figure APP11: AFM topography and amplitude of a 42 nm CTO thin film sample with surface topography.

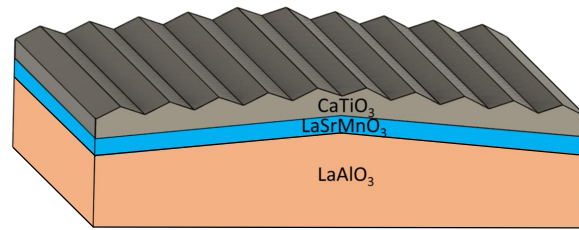


Figure APP12: Schematic of the possible domain ordering continuity between the ferroelectric substrate and the ferroelectric CTO thin film.

D.3 . Domain walls polarity in CaTiO_3 thin films

Bright and dark domain wall traces are visible on CTO thin film surfaces in MEM for different film thicknesses, as shown in figure APP13a. The contrast is a signature of a modulation of the surface potential at the domain walls. For the very thin 2 nm CTO sample, observed ferroelastic domains at the surface have low contrast and the surface has darker lines similar to surface scratches. The MEM contrast is not only from the twin physical topography because we also observe charge/discharge in domain walls with annealing/cooling as we did in single crystals.

Domain walls at the surface can also be thermally displaced. For single crystal domain walls, we usually observe thermal movement for a sample temperature of around 700°C. In 42 nm thin film, we observe domain wall movement starting at 310°C and we show in figure APP13b going from a multiple ferroelastic domain state to a monodomain. Less thermal energy is needed in thin films to move the walls, which was expected. Moreover, the surface domain wall signature in MEM persists above 540°C, the curie temperature of the substrate.

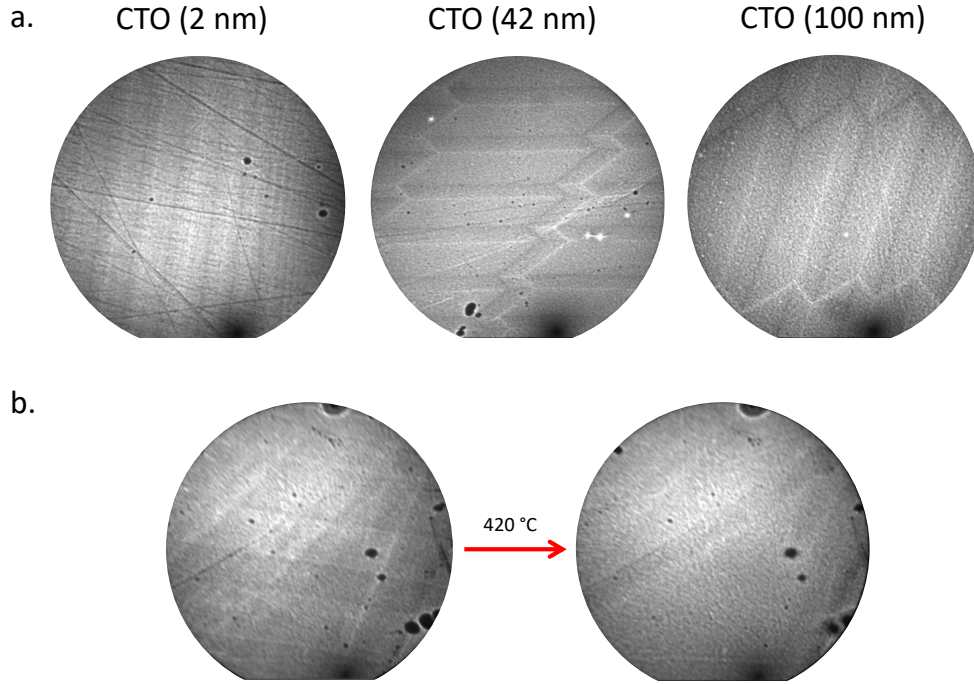


Figure APP13: a. MEM images of the CTO surface for different film thicknesses, with bright and dark lines suggesting ferroelastic domain walls. b. MEM image at room temperature and at 420°C. The MEM images FoV is 70 μm .

D.4 . Vibrational states of $\text{LaAlO}_3/\text{LaSrMnO}_3/\text{CaTiO}_3$

Raman spectroscopy is used to observe the ferroelastic ordering in the thin film stack. We used a polarizer/analyzer setup to analyze the Raman active modes from the film layers and the substrate and a 633 nm laser on first a single crystal CTO sample and a single crystal LAO sample to identify their peaks. Figure APP14a shows the spectra for a CTO single crystal with different configurations of the polarizer/analyzer. HH is linear horizontal polarization for both the polarizer and analyzer and VH is linear vertical for the polarizer and horizontal for the analyzer. There are four possible configurations and, given the crystal symmetry, we also expect an enhanced response if the sample is rotated by 45° . We then worked with a thin film sample at 45° because Raman mode responses have is higher in this sample configuration, notably the HH configuration CTO peak, with the sample at 45° , at 248 cm^{-1} .

We then performed Raman spectroscopy on an LAO/LSMO/CTO stack with a 300 nm CTO thin film rotated at 45° . CTO and LAO peaks are indicated in figure APP14b. We chose a 300 nm CTO thickness because CTO peaks were in the noise for a 42 nm sample and hardly visible for a 100 nm sample. We can first observe that the HV and VH configurations minimize the LAO peaks compared to the CTO peaks, and the HH and VV configurations are only sensitive to the

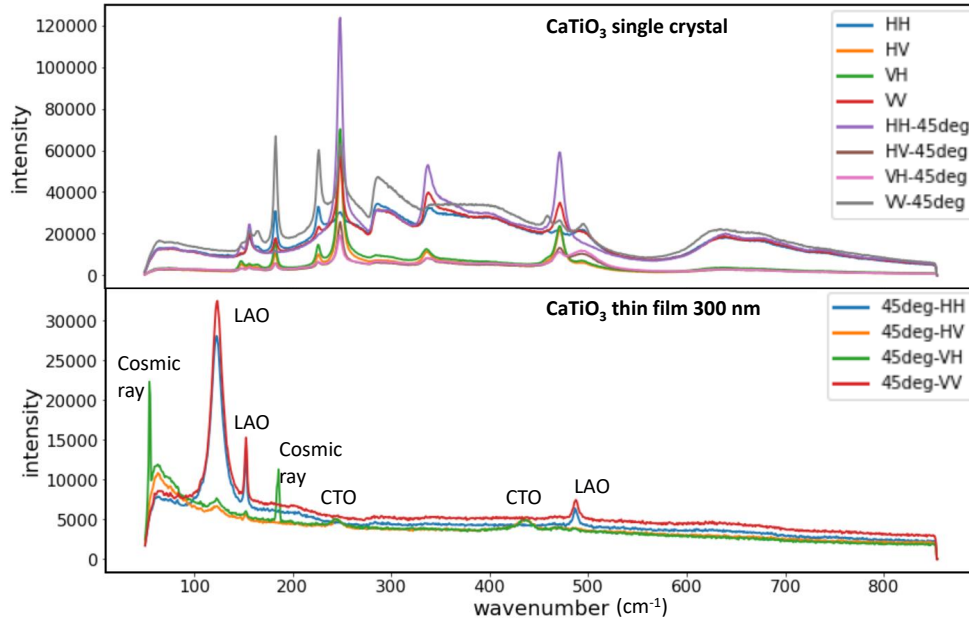


Figure APP14: Raman spectra with different polarizer/analyzer conditions for a CTO single crystal and an LAO/LSMO/CTO 300 nm CTO thin film.

LAO peaks. This difference in interaction is ideal to probe both the substrate's ferroelastic state and the film state. The two sharp spikes in the VH spectra are cosmic rays and not Raman modes.

We then performed pixel-by-pixel acquisition on an area with several domain walls on the 300 nm CTO sample. The area is highlighted by a red rectangle in figure APP16a. Ferroelastic domains are visible by optical microscopy and domain walls around the analyzed area are indicated by black lines. Two pixel-by-pixel acquisitions were performed on the 300 nm CTO sample rotated by 45°, on a 150x100 μm area. The step is 3 μm in the y direction and 0.6 μm in the x direction. The first map is with a HH configuration to be only sensitive to the LAO substrate and the second map is with a VH configuration to have a signal from the CTO thin film.

We used PCA to identify the main change in the spectra across the map. It is a powerful analysis tool to quickly observe variations in the maps and also extract weak signals. It can be used as a basis prior to data analysis. Figure APP15a and b shows the first principal component and coefficient map of the HH pixel-by-pixel acquisition, which accounts for most of the total variance. A second component not shown was related to the microscope focus drift during the measurement. Both components account for $\approx 85\%$ of the total variance. In figure APP15a, we can observe that this first component is sensitive to two LAO peak intensity variations. The map of this component coefficient is in figure APP15b, the coefficient is proportional to the LAO peaks intensity variation across the map. This variation

highlights the LAO domains in the substrate.

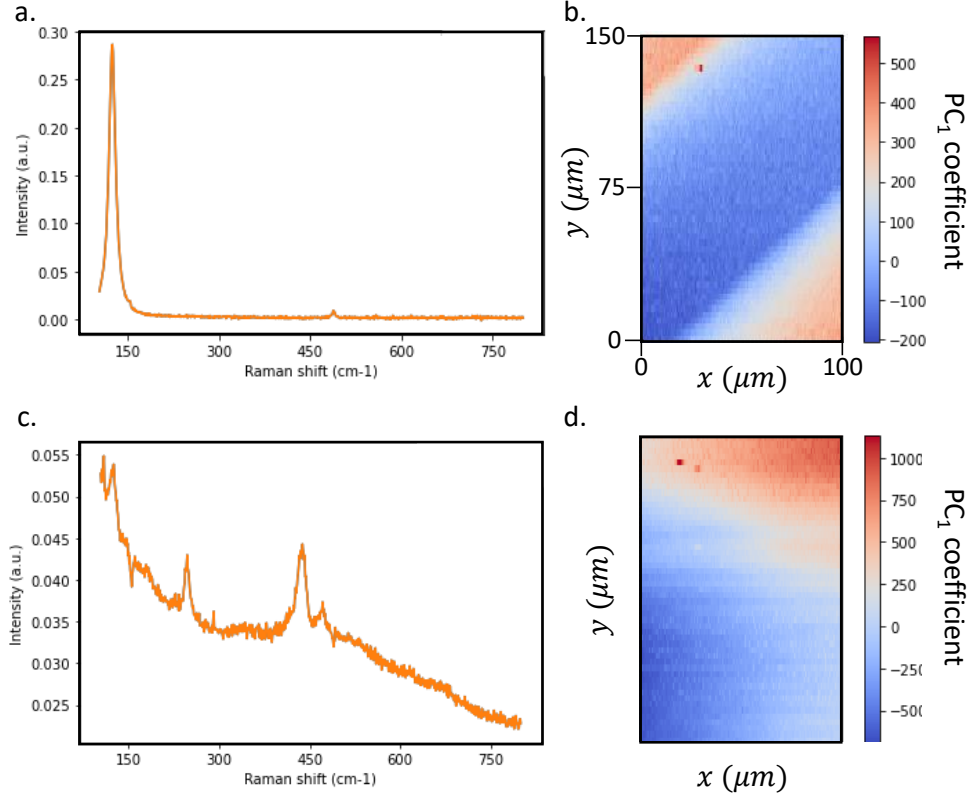


Figure APP15: PCA of Raman cartographies of a 300 nm CTO thin film sample rotated at 45°. a. PC_1 component for an HH acquisition and b. map of the first component coefficient. c. PC_1 component for a VH acquisition and d. map of the component coefficient.

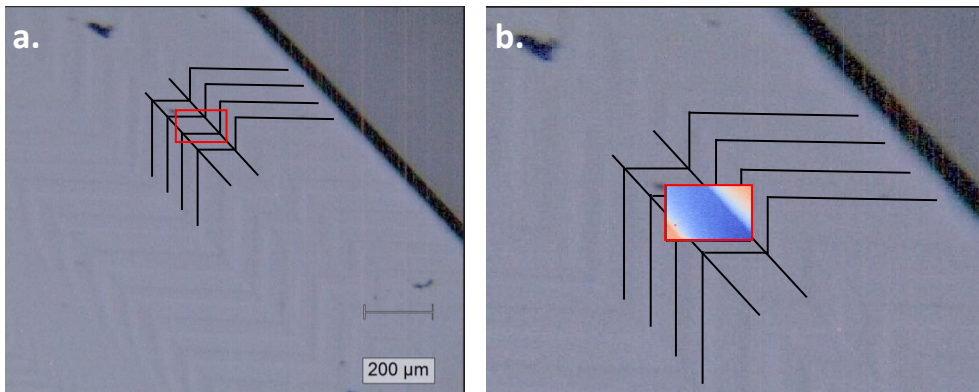


Figure APP16: Optical microscope image of the 300 nm CTO thin film surface with a red rectangle indicating the analyzed 150x100 μm area. Domain walls around the area are highlighted with black lines. b. Superposition of the first PCA component on the HH scan map on the optical image to observe correspondence with the ferroelastic domain wall positions.

Figure APP15c shows the first component of the VH pixel-by-pixel acquisition. This component is related to the intensity variation of both identified CTO peaks but other peaks are visible. A second component not shown is sensitive to the weak LAO peak signal and its map shows the same variation as APP15b. The first component map is shown in figure APP15d and doesn't seem to be related to the surface ferroelastic ordering.

The LAO-sensitive Raman map shows domains that correspond perfectly with microscopy-observed ferroelastic domains, as shown in figure APP16b, for domains with domain walls along the sample border (wider black border on the top right of the image). However, the domain separated by walls in the other directions, along the map x and y directions, are not visible in the LAO map. It could be because these ferroelastic domain walls are CTO-specific and not a repetition of the LAO ferroelastic ordering at the surface.

The more CTO-specific pixel-by-pixel spectra have a lower signal-to-noise ratio than in the LAO map, so observed CTO peaks are weak. This first Raman observation shows that it is possible to observe the ferroelastic ordering in the LAO/LSMO/CTO stack. To improve the signal-to-noise ratio, we will perform Raman spectroscopy on a 500 nm CTO sample. By increasing the thickness we could also observe other CTO peaks in addition to the two peaks observed for the 300 nm sample.

Bibliography

- [1] Alexander K. Tagantsev, L. Eric Cross, and Jan Fousek. *Domains in Ferroic Crystals and Thin Films*. Springer New York, New York, NY, 2010.
- [2] Baoshan Cui, Dong Li, Jijun Yun, Yalu Zuo, Xiaobin Guo, Kai Wu, Xu Zhang, Yupei Wang, Li Xi, and Desheng Xue. Magnetization switching through domain wall motion in Pt/Co/Cr racetracks with the assistance of the accompanying Joule heating effect. *Physical Chemistry Chemical Physics*, 20(15):9904–9909, 2018.
- [3] Kaushik Bhattacharya and Richard D. James. The material is the machine. *Science*, 307(5706):53–54, 2005.
- [4] J. Seidel, L. W. Martin, Q. He, Q. Zhan, Y.-H. Chu, A. Rother, M. E. Hawkrigde, P. Maksymovych, P. Yu, M. Gajek, N. Balke, S. V. Kalinin, S. Gemming, F. Wang, G. Catalan, J. F. Scott, N. A. Spaldin, J. Orenstein, and R. Ramesh. Conduction at domain walls in oxide multiferroics. *Nature Materials*, 8(3):229–234, 3 2009.
- [5] Alison Aird and Ekhard K H Salje. Sheet superconductivity in twin walls: experimental evidence of. *Journal of Physics: Condensed Matter*, 10(22):L377–L380, 6 1998.
- [6] Sandra Van Aert, Stuart Turner, Rémi Delville, Dominique Schryvers, Gustaaf Van Tendeloo, and Ekhard K H Salje. Direct observation of ferrielectricity at ferroelastic domain boundaries in CaTiO₃ by electron microscopy. *Advanced Materials*, 24(4):523–527, 2012.
- [7] Ekhard Salje and Huali Zhang. Domain boundary engineering. *Phase Transitions*, 82(6):452–469, 6 2009.
- [8] G. Catalan, J. Seidel, R. Ramesh, and J. F. Scott. Domain wall nanoelectronics. *Reviews of Modern Physics*, 84(1):119–156, 2012.
- [9] Stuart S. P. Parkin, Masamitsu Hayashi, and Luc Thomas. Magnetic Domain-Wall Racetrack Memory. *Science*, 320(5873):190–194, 4 2008.
- [10] E. K.H. Salje and J. F. Scott. Ferroelectric Bloch-line switching: A paradigm for memory devices? *Applied Physics Letters*, 105(25):1–5, 2014.
- [11] Pankaj Sharma, Theodore S. Moise, Luigi Colombo, and Jan Seidel. Roadmap for Ferroelectric Domain Wall Nanoelectronics. *Advanced Functional Materials*, 32(10):1–16, 2022.

- [12] Karin M. Rabe, Matthew Dawber, Céline Lichtensteiger, Charles H. Ahn, and Jean-Marc Triscone. Modern Physics of Ferroelectrics: Essential Background. In *Physics of Ferroelectrics*, pages 1–30. Springer Berlin Heidelberg, Berlin, Heidelberg.
- [13] P. M. Woodward. Octahedral Tilting in Perovskites. I. Geometrical Considerations. *Acta Crystallographica Section B Structural Science*, 53(1):32–43, 2 1997.
- [14] J. Valasek. Piezo-electric and allied phenomena in Rochelle salt. *Physical Review*, 17(4):475–481, 1921.
- [15] Raffaele Resta. Macroscopic polarization in crystalline dielectrics: the geometric phase approach. *Reviews of Modern Physics*, 66(3):899–915, 7 1994.
- [16] Alexander K. Tagantsev. Size effects in polarization switching in ferroelectric thin films. *Integrated Ferroelectrics*, 16(1-4):237–244, 4 1997.
- [17] R. Resta. Theory of the electric polarization in crystals. *Ferroelectrics*, 136(1):51–55, 11 1992.
- [18] David Vanderbilt and R. D. King-Smith. Electric polarization as a bulk quantity and its relation to surface charge. *Physical Review B*, 48(7):4442–4455, 8 1993.
- [19] Raffaele Resta and David Vanderbilt. Theory of Polarization: A Modern Approach. In *Physics of Ferroelectrics*, pages 31–68. Springer Berlin Heidelberg, Berlin, Heidelberg.
- [20] J. Zak. Berry’s phase for energy bands in solids. *Physical Review Letters*, 62(23):2747–2750, 6 1989.
- [21] Ph. Ghosez, J.-P. Michenaud, and X. Gonze. Dynamical atomic charges: The case of ABO₃ compounds. *Physical Review B*, 58(10):6224–6240, 9 1998.
- [22] Dragan Damjanovic. *The Science of Hysteresis: Hysteresis in Piezoelectric and Ferroelectric Materials*, volume 3. Elsevier edition, 2005.
- [23] A.F. Devonshire. XCVI. Theory of barium titanate. *The London, Edinburgh, and Dublin Philosophical Magazine and Journal of Science*, 40(309):1040–1063, 10 1949.
- [24] M.E. Lines and A.M. Glass. *Principles and Applications of Ferroelectrics and Related Materials*. Oxford edition, 1979.
- [25] H. H. Wieder. Ferroelectric Hysteresis in Barium Titanate Single Crystals. *Journal of Applied Physics*, 26(12):1479–1482, 12 1955.

- [26] I. Krug, N. Barrett, A. Petraru, A. Locatelli, T. O. Montes, M. A. Niño, K. Rahmanizadeh, G. Bihlmayer, and C. M. Schneider. Extrinsic screening of ferroelectric domains in $\text{Pb}(\text{Zr}_{0.48}\text{Ti}_{0.52})\text{O}_3$. *Applied Physics Letters*, 97(22):222903, 11 2010.
- [27] Sergei V. Kalinin and Dawn A. Bonnell. Local potential and polarization screening on ferroelectric surfaces. *Physical Review B*, 63(12):125411, 3 2001.
- [28] M Dawber, P Chandra, P B Littlewood, and J F Scott. Depolarization corrections to the coercive field in thin-film ferroelectrics. *Journal of Physics: Condensed Matter*, 15(24):L393–L398, 6 2003.
- [29] J MIZUSAKI. Nonstoichiometry, diffusion, and electrical properties of perovskite-type oxide electrode materials. *Solid State Ionics*, 52(1-3):79–91, 5 1992.
- [30] N.-H. CHAN, R.K. SHARMA, and D.M. SMYTH. Nonstoichiometry in Undoped BaTiO_3 . *Journal of the American Ceramic Society*, 64(9):556–562, 9 1981.
- [31] Charles Kittel. Theory of the Structure of Ferromagnetic Domains in Films and Small Particles. *Physical Review*, 70(11-12):965–971, 12 1946.
- [32] L. Landau and E. Lifshitz. On the theory of the dispersion of magnetic permeability in ferromagnetic bodies. In *Perspectives in Theoretical Physics*, pages 51–65. Elsevier, 1992.
- [33] Toshito Mitsui and Jiro Furuichi. Domain Structure of Rochelle Salt and KH_2PO_4 . *Physical Review*, 90(2):193–202, 4 1953.
- [34] Donghwa Lee, Rakesh K. Behera, Pingping Wu, Haixuan Xu, Y. L. Li, Susan B. Sinnott, Simon R. Phillpot, L. Q. Chen, and Venkatraman Gopalan. Mixed Bloch-Néel-Ising character of 180° ferroelectric domain walls. *Physical Review B*, 80(6):060102, 8 2009.
- [35] P. Marton, I. Rychetsky, and J. Hlinka. Domain walls of ferroelectric BaTiO_3 within the Ginzburg-Landau-Devonshire phenomenological model. *Physical Review B*, 81(14):144125, 4 2010.
- [36] B Houchmandzadeh, J Lajzerowicz, and E Salje. Order parameter coupling and chirality of domain walls. *Journal of Physics: Condensed Matter*, 3(27):5163–5169, 7 1991.
- [37] Chun-Lin Jia, Shao-Bo Mi, Knut Urban, Ionela Vrejoiu, Marin Alexe, and Dietrich Hesse. Atomic-scale study of electric dipoles near charged and uncharged domain walls in ferroelectric films. *Nature Materials*, 7(1):57–61, 1 2008.

- [38] Tobias Jungk, Ákos Hoffmann, and Elisabeth Soergel. Impact of elasticity on the piezoresponse of adjacent ferroelectric domains investigated by scanning force microscopy. *Journal of Applied Physics*, 102(8):084102, 10 2007.
- [39] H. Chaib, F. Schlaphof, T. Otto, and L. M. Eng. Electrical and Optical Properties in the 180° Ferroelectric Domain Wall of Tetragonal KNbO_3 . *Ferroelectrics*, 291(1):143–155, 1 2003.
- [40] Ekhard K.H. Salje. Ferroelastic Materials. *Annual Review of Materials Research*, 42(1):265–283, 2012.
- [41] E. Salje and G. Hoppmann. Direct observation of ferroelasticity in $\text{Pb}_3(\text{PO}_4)_2$ - $\text{Pb}_3(\text{VO}_4)_2$. *Materials Research Bulletin*, 11(12):1545–1549, 12 1976.
- [42] John F Nye. *Physical Properties of Crystals: Their Representation by Tensors and Matrices*. Oxford University Press, 1957.
- [43] Jean-Claude Tolédano and Pierre Tolédano. Order parameter symmetries and free-energy expansions for purely ferroelastic transitions. *Physical Review B*, 21(3):1139–1172, 2 1980.
- [44] Chun-Lin Jia, Knut W. Urban, Marin Alexe, Dietrich Hesse, and Ionela Vrejoiu. Direct Observation of Continuous Electric Dipole Rotation in Flux-Closure Domains in Ferroelectric $\text{Pb}(\text{Zr,Ti})\text{O}_3$. *Science*, 331(6023):1420–1423, 3 2011.
- [45] K. R. Locherer, J. Chrosch, and E. K. H. Salje. Diffuse X-ray scattering in WO_3 . *Phase Transitions*, 67(1):51–63, 10 1998.
- [46] J. Chrosch and E.K.H. Salje. Thin domain walls in $\text{YBa}_2\text{Cu}_3\text{O}_{7-\delta}$ and their rocking curves an x-ray diffraction study. *Physica C: Superconductivity*, 225(1-2):111–116, 5 1994.
- [47] Stuart A. Hayward, Jutta Chrosch, Ekhard K. H. Salje, and Michael A. Carpenter. Thickness of pericline twin walls in anorthoclase: an X-ray diffraction study. *European Journal of Mineralogy*, 8(6):1301–1310, 1 1997.
- [48] J. Sapriel. Domain-wall orientations in ferroelastics. *Physical Review B*, 12(11):5128–5140, 12 1975.
- [49] Michael A. Carpenter, Ekhard K.H. Salje, and Ann Graeme-Barber. Spontaneous strain as a determinant of thermodynamic properties for phase transitions in minerals. *European Journal of Mineralogy*, 10(4):621–691, 7 1998.
- [50] J. Lajzerowicz and J.J. Niez. Phase transition in a domain wall. *Journal de Physique Lettres*, 40(7):165–169, 1979.

- [51] G. F. Nataf, M. Guennou, J. M. Gregg, D. Meier, J. Hlinka, E. K. H. Salje, and J. Kreisel. Domain-wall engineering and topological defects in ferroelectric and ferroelastic materials. *Nature Reviews Physics*, 2020.
- [52] Ekhard K. H. Salje, Suzhi Li, Massimiliano Stengel, Peter Gumbsch, and Xiangdong Ding. Flexoelectricity and the polarity of complex ferroelastic twin patterns. *Physical Review B*, 94(2):024114, 7 2016.
- [53] V. Janovec, L. Richterová, and J. P[rcirc]ívratská. Polar properties of compatible ferroelastic domain walls. *Ferroelectrics*, 222(1):73–76, 2 1999.
- [54] Dwight D. Viehland and Ekhard K.H. Salje. Domain boundary-dominated systems: adaptive structures and functional twin boundaries. *Advances in Physics*, 63(4):267–326, 7 2014.
- [55] Sergio Conti, Stefan Müller, Arkady Poliakovsky, and Ekhard K H Salje. Coupling of order parameters, chirality, and interfacial structures in multi-ferroic materials. *Journal of Physics: Condensed Matter*, 23(14):142203, 4 2011.
- [56] A. M. Glazer. The classification of tilted octahedra in perovskites. *Acta Crystallographica Section B Structural Crystallography and Crystal Chemistry*, 28(11):3384–3392, 11 1972.
- [57] Liliana Goncalves-Ferreira, Simon A.T. Redfern, Emilio Artacho, and Ekhard K.H. Salje. Ferrielectric twin walls in CaTiO₃. *Physical Review Letters*, 101(9):1–4, 2008.
- [58] P. Zubko, G. Catalan, A. Buckley, P. R.L. Welche, and J. F. Scott. Strain-gradient-induced polarization in SrTiO₃ single Crystals. *Physical Review Letters*, 99(16):99–102, 2007.
- [59] Simon A T Redfern. High-temperature structural phase transitions in perovskite CaTiO₃. *Journal of Physics: Condensed Matter*, 8(43):8267–8275, 10 1996.
- [60] W. T. Lee, E. K. H. Salje, L. Goncalves-Ferreira, M. Daraktchiev, and U. Bismayer. Intrinsic activation energy for twin-wall motion in the ferroelastic perovskite CaTiO₃. *Physical Review B*, 73(21):214110, 6 2006.
- [61] Roushown Ali and Masatomo Yashima. Space group and crystal structure of the Perovskite CaTiO₃ from 296 to 1720 K. *Journal of Solid State Chemistry*, 178(9):2867–2872, 9 2005.
- [62] Yanwei Cao, Se Young Park, Xiaoran Liu, D. Choudhury, S. Middey, D. Meyers, M. Kareev, P. Shafer, E. Arenholz, and J. Chakhalian. Orbital configuration in CaTiO₃ films on NdGaO₃. *Applied Physics Letters*, 109(15):152905, 10 2016.

- [63] G. F. Nataf, M. Guennou, J. Kreisel, P. Hicher, R. Haumont, O. Aktas, E. K. H. Salje, L. Tortech, C. Mathieu, D. Martinotti, and N. Barrett. Control of surface potential at polar domain walls in a nonpolar oxide. *Physical Review Materials*, 1(7):074410, 2017.
- [64] W. Zhong, R. D. King-Smith, and David Vanderbilt. Giant LO-TO splittings in perovskite ferroelectrics. *Physical Review Letters*, 72(22):3618–3621, 5 1994.
- [65] H. Yokota, H. Usami, R. Haumont, P. Hicher, J. Kaneshiro, E. K.H. Salje, and Y. Uesu. Direct evidence of polar nature of ferroelastic twin boundaries in CaTiO₃ obtained by second harmonic generation microscope. *Physical Review B - Condensed Matter and Materials Physics*, 89(14):1–9, 2014.
- [66] G. H. Kwei, A. C. Lawson, S. J. L. Billinge, and S. W. Cheong. Structures of the ferroelectric phases of barium titanate. *The Journal of Physical Chemistry*, 97(10):2368–2377, 3 1993.
- [67] N. T. Tsou, P. R. Potnis, and J. E. Huber. Classification of laminate domain patterns in ferroelectrics. *Physical Review B*, 83(18):184120, 5 2011.
- [68] A. Höfer, M. Fechner, K. Duncker, M. Hölzer, I. Mertig, and W. Widdra. Persistence of Surface Domain Structures for a Bulk Ferroelectric above T_C. *Physical Review Letters*, 108(8):087602, 2 2012.
- [69] C. Mathieu, C. Lubin, G. Le Doueff, M. Cattelan, P. Gemeiner, B. Dkhil, E. K.H. Salje, and N. Barrett. Surface Proximity Effect, Imprint Memory of Ferroelectric Twins, and Tweed in the Paraelectric Phase of BaTiO₃. *Scientific Reports*, 8(1), 12 2018.
- [70] B Houchmandzadeh, J Lajzerowicz, and E Salje. Relaxations near surfaces and interfaces for first-, second- and third-neighbour interactions: theory and applications to polytypism. *Journal of Physics: Condensed Matter*, 4(49):9779–9794, 12 1992.
- [71] D. A. Allwood, G. Xiong, C. C. Faulkner, D. Atkinson, D. Petit, and R. P. Cowburn. Magnetic Domain-Wall Logic. *Science*, 309(5741):1688–1692, 9 2005.
- [72] Eugene A. Eliseev, Anna N. Morozovska, Yijia Gu, Albina Y. Borisevich, Long Qing Chen, Venkatraman Gopalan, and Sergei V. Kalinin. Conductivity of twin-domain-wall/surface junctions in ferroelastics: Interplay of deformation potential, octahedral rotations, improper ferroelectricity, and flexoelectric coupling. *Physical Review B - Condensed Matter and Materials Physics*, 86(8):1–10, 2012.

- [73] C.-H. Yang, J. Seidel, S. Y. Kim, P. B. Rossen, P. Yu, M. Gajek, Y. H. Chu, L. W. Martin, M. B. Holcomb, Q. He, P. Maksymovych, N. Balke, S. V. Kalinin, A. P. Baddorf, S. R. Basu, M. L. Scullin, and R. Ramesh. Electric modulation of conduction in multiferroic Ca-doped BiFeO₃ films. *Nature Materials*, 8(6):485–493, 6 2009.
- [74] T. Choi, Y. Horibe, H. T. Yi, Y. J. Choi, Weida Wu, and S.-W. Cheong. Insulating interlocked ferroelectric and structural antiphase domain walls in multiferroic YMnO₃. *Nature Materials*, 9(3):253–258, 3 2010.
- [75] A. Aird and E.K.H. Salje. Enhanced reactivity of domain walls in with sodium. *The European Physical Journal B*, 15(2):205–210, 5 2000.
- [76] J. Seidel, P. Maksymovych, Y. Batra, A. Katan, S.-Y. Yang, Q. He, A. P. Baddorf, S. V. Kalinin, C.-H. Yang, J.-C. Yang, Y.-H. Chu, E. K. H. Salje, H. Wormeester, M. Salmeron, and R. Ramesh. Domain Wall Conductivity in La-Doped BiFeO₃. *Physical Review Letters*, 105(19):197603, 11 2010.
- [77] Jan Seidel, Guneeta Singh-Bhalla, Qing He, Seung-Yeul Yang, Ying-Hao Chu, and Ramamoorthy Ramesh. Domain wall functionality in BiFeO₃. *Phase Transitions*, 86(1):53–66, 1 2013.
- [78] S. Farokhipoor and B. Noheda. Conduction through 71° Domain Walls in BiFeO₃ Thin Films. *Physical Review Letters*, 107(12):127601, 9 2011.
- [79] Axel Lubk, S. Gemming, and N. A. Spaldin. First-principles study of ferroelectric domain walls in multiferroic bismuth ferrite. *Physical Review B - Condensed Matter and Materials Physics*, 80(10):1–8, 2009.
- [80] Jill Guyonnet, Iaroslav Gaponenko, Stefano Gariglio, and Patrycja Paruch. Conduction at Domain Walls in Insulating Pb(Zr_{0.2}Ti_{0.8})O₃ Thin Films. *Advanced Materials*, 23(45):5377–5382, 12 2011.
- [81] A. Gruverman, D. Wu, and J. F. Scott. Piezoresponse Force Microscopy Studies of Switching Behavior of Ferroelectric Capacitors on a 100-ns Time Scale. *Physical Review Letters*, 100(9):097601, 3 2008.
- [82] James F. Scott. Switching of Ferroelectrics Without Domains. *Advanced Materials*, 22(46):5315–5317, 12 2010.
- [83] Er-Jia Guo, Robert Roth, Andreas Herklotz, Dietrich Hesse, and Kathrin Dörr. Ferroelectric 180° Domain Wall Motion Controlled by Biaxial Strain. *Advanced Materials*, 27(9):1615–1618, 3 2015.
- [84] Shi Liu, Ilya Grinberg, and Andrew M. Rappe. Intrinsic ferroelectric switching from first principles. *Nature*, 534(7607):360–363, 6 2016.

- [85] Alexei Grigoriev, Dal-Hyun Do, Dong Min Kim, Chang-Beom Eom, Bernhard Adams, Eric M. Dufresne, and Paul G. Evans. Nanosecond Domain Wall Dynamics in Ferroelectric Pb(Zr,Ti)O₃ Thin Films. *Physical Review Letters*, 96(18):187601, 5 2006.
- [86] E. A. Eliseev, A. N. Morozovska, G. S. Svechnikov, E. L. Rumyantsev, E. I. Shishkin, V. Y. Shur, and S. V. Kalinin. Screening and retardation effects on 180°-domain wall motion in ferroelectrics: Wall velocity and nonlinear dynamics due to polarization-screening charge interactions. *Physical Review B*, 78(24):245409, 12 2008.
- [87] Vladimir Ya. Shur. Kinetics of ferroelectric domains: Application of general approach to LiNbO₃ and LiTaO₃. In *Frontiers of Ferroelectricity*, pages 199–210. Springer US, Boston, MA.
- [88] G F Nataf and M Guennou. Optical studies of ferroelectric and ferroelastic domain walls. *Journal of Physics: Condensed Matter*, 32(18):183001, 5 2020.
- [89] D. Meier, J. Seidel, M Gregg, and R Ramesh. *Domain Walls: From Fundamental Properties to Nanotechnology Concepts*. Oxford univ. press edition, 2020.
- [90] E. K.H. Salje, D. Xue, X. Ding, K. A. Dahmen, and J. F. Scott. Ferroelectric switching and scale invariant avalanches in BaTiO₃. *Physical Review Materials*, 3(1):1–8, 2019.
- [91] E. K.H. Salje, X. Ding, Z. Zhao, T. Lookman, and A. Saxena. Thermally activated avalanches: Jamming and the progression of needle domains. *Physical Review B - Condensed Matter and Materials Physics*, 83(10):1–8, 2011.
- [92] Richard J. Harrison and Ekhard K. H. Salje. The noise of the needle: Avalanches of a single progressing needle domain in LaAlO₃. *Applied Physics Letters*, 97(2):021907, 7 2010.
- [93] Blai Casals, Sebastiaan Van Dijken, Gervasi Herranz, and Ekhard K.H. Salje. Electric-field-induced avalanches and glassiness of mobile ferroelastic twin domains in cryogenic SrTiO₃. *Physical Review Research*, 1(3):1–6, 2019.
- [94] James P. Sethna, Karin A. Dahmen, and Christopher R. Myers. Crackling noise. *Nature*, 410(6825):242–250, 3 2001.
- [95] K. Wadati. On the Frequency Distribution of Earthquakes. *Journal of the Meteorological Society of Japan. Ser. II*, 10(10):559–568, 1932.
- [96] Daniel Bonamy. Intermittency and roughening in the failure of brittle heterogeneous materials. *Journal of Physics D: Applied Physics*, 42(21):214014, 11 2009.

- [97] Z. Zhao, X. Ding, J. Sun, and E. K.H. Salje. Thermal and athermal crackling noise in ferroelastic nanostructures. *Journal of Physics Condensed Matter*, 26(14), 2014.
- [98] H. Hertz. Ueber einen Einfluss des ultravioletten Lichtes auf die electrische Entladung. *Annalen der Physik und Chemie*, 267(8):983–1000, 1887.
- [99] A. Einstein. On a heuristic viewpoint concerning the production and transformation of light. *Annalen der Physik*, 17:132–148, 1905.
- [100] Carl Nordling, Evelyn Sokolowski, and Kai Siegbahn. Precision Method for Obtaining Absolute Values of Atomic Binding Energies. *Physical Review*, 105(5):1676–1677, 3 1957.
- [101] R. Courths and S. Hüfner. Photoemission experiments on copper. *Physics Reports*, 112(2):53–171, 10 1984.
- [102] P H Citrin and G K Wertheim. Photoemission from surface-atom core levels, surface densities of states, and metal-atom clusters: A unified picture. *Physical review B*, 27(6):3176–3200, 1982.
- [103] I Adawi. Theory of the Surface Photoelectric Effect for One and Two Photons*. *Physical review*, 134(3A):788, 1964.
- [104] J B Pendry. Theory of photoemission. *Surface Science*, 57:679–705, 1976.
- [105] J. Cooper and R. N. Zare. Angular distribution of photoelectrons, 1968.
- [106] J J Yeh and I Lindau. Atomic subshell photoionization cross sections and asymetry parameters: $1 < Z < 103$. Technical report, 1985.
- [107] Aleksander Jablonski. Database of correction parameters for the elastic scattering effects in XPS. *Surface and Interface Analysis*, 23(1):29–37, 1995.
- [108] <https://vuo.elettra.eu/services/elements/WebElements.html>.
- [109] C R Brundle. Elucidation of surface structure and bonding by photoelectron spectroscopy. *Surface Science*, 48:99–136, 1975.
- [110] C. R. Brundle. The application of electron spectroscopy to surface studies. In *J Vac Sci Technol*, volume 11, pages 212–224, 1974.
- [111] G.A. Somorjai. *Chemistry in two dimensions: surfaces*. Cornell University Press, 1981.
- [112] Stefan Hüfner. *Photoelectron Spectroscopy*. Advanced Texts in Physics. Springer Berlin Heidelberg, Berlin, Heidelberg, springer edition, 7 2003.

- [113] C S Fadley, R J Baird, W Siekhaus, T Novakov, and S A L Bergstrom. Surface analysis and angular distributions in x-ray photoelectron spectroscopy. *Journal of Electron Spectroscopy and Related Phenomena*, 4:93–137, 1974.
- [114] Jurgen Thieme, Gunter Schmahl, Dietbert Rudolph, and Eberhard Umbach. *X-Ray Microscopy and Spectromicroscopy: Status Report from the Fifth International Conference, Wurzburg*. Springer science edition, 8 1996.
- [115] S Gunther, B Kaulich, L Gregoratti, and M Kiskinova. Photoelectron microscopy and applications in surface and materials science. Technical report, 2002.
- [116] Claus M Schneider and Gerd Schonhense. Investigating surface magnetism by means of photoexcitation electron emission microscopy. *Reports on Progress in Physics*, 65(12):1785–1839, 12 2002.
- [117] M. Escher, N. Weber, M. Merkel, C. Ziethen, P. Bernhard, G. Schönhense, S. Schmidt, F. Forster, F. Reinert, B. Krömker, and D. Funnemann. NanoESCA: A novel energy filter for imaging x-ray photoemission spectroscopy. *Journal of Physics Condensed Matter*, 17(16), 4 2005.
- [118] C. M. Schneider, C. Wiemann, M. Patt, V. Feyer, L. Plucinski, I. P. Krug, M. Escher, N. Weber, M. Merkel, O. Renault, and N. Barrett. Expanding the view into complex material systems: From micro-ARPES to nanoscale HAXPES. *Journal of Electron Spectroscopy and Related Phenomena*, 185(10):330–339, 10 2012.
- [119] A. Locatelli and E. Bauer. Recent advances in chemical and magnetic imaging of surfaces and interfaces by XPEEM. *Journal of Physics Condensed Matter*, 20(9), 3 2008.
- [120] R. M. Tromp, Y. Fujikawa, J. B. Hannon, A. W. Ellis, A. Berghaus, and O. Schaff. A simple energy filter for low energy electron microscopy/photoelectron emission microscopy instruments. *Journal of Physics Condensed Matter*, 21(31), 2009.
- [121] R.M. Tromp, J.B. Hannon, A.W. Ellis, W. Wan, A. Berghaus, and O. Schaff. A new aberration-corrected, energy-filtered LEEM/PEEM instrument. I. Principles and design. *Ultramicroscopy*, 110(7):852–861, 6 2010.
- [122] A. Howie and U. Valdre. *Surface and Interface Characterization by Electron Optical Methods*. Springer US, Boston, MA, 1989.
- [123] Lee H. Veneklasen. The continuing development of low-energy electron microscopy for characterizing surfaces. *Review of Scientific Instruments*, 63(12):5513–5532, 12 1992.

- [124] E Brüche. Elektronenmikroskopische Abbildung mit lichtelektrischen Elektronen. *Ans dem Forschungs-Institut der AEG.*, pages 448–450, 1933.
- [125] A Recknagel. Theorie des elektrischen Elektronenmikroskops für Selbststrahler. Technical report.
- [126] Gertrude F Rempfer, Karen K Nadakavukaren, and O Hayes Griffith. Topographical effects in emission spectroscopy. *Ultramicroscopy*, 5:437–448, 1980.
- [127] Ernst Bauer. A brief history of PEEM. *Journal of Electron Spectroscopy and Related Phenomena*, 185(10):314–322, 10 2012.
- [128] GÜNTER. *History of Electron Microscopy in Switzerland*. Birkhäuser edition, 2012.
- [129] M. Escher, K. Winkler, O. Renault, and N. Barrett. Applications of high lateral and energy resolution imaging XPS with a double hemispherical analyser based spectromicroscope. *Journal of Electron Spectroscopy and Related Phenomena*, 178-179(C):303–316, 5 2010.
- [130] B.P. Tonner. Energy-filtered imaging with electrostatic optics for photoelectron microscopy. *Nuclear Instruments and Methods in Physics Research Section A: Accelerators, Spectrometers, Detectors and Associated Equipment*, 291(1-2):60–66, 5 1990.
- [131] B. Krömker, M. Escher, D. Funnemann, D. Hartung, H. Engelhard, and J. Kirschner. Development of a momentum microscope for time resolved band structure imaging. *Review of Scientific Instruments*, 79(5):053702, 5 2008.
- [132] O. Renault, N. Barrett, A. Bailly, L.F. Zagonel, D. Mariolle, J.C. Cezar, N.B. Brookes, K. Winkler, B. Krömker, and D. Funnemann. Energy-filtered XPEEM with NanoESCA using synchrotron and laboratory X-ray sources: Principles and first demonstrated results. *Surface Science*, 601(20):4727–4732, 10 2007.
- [133] Olivier Renault, Renaud Brochier, Paul-Henri Haumesser, Nick Barrett, B. Krömker, and D. Funnemann. Energy-filtered PEEM imaging of polycrystalline Cu surfaces with work function contrast and high lateral resolution. *e-Journal of Surface Science and Nanotechnology*, 4:431–434, 2006.
- [134] N. Barrett, J. E. Rault, J. L. Wang, C. Mathieu, A. Locatelli, T. O. Montes, M. A. Niño, S. Fusil, M. Bibes, A. Barthélémy, D. Sando, W. Ren, S. Prosandeev, L. Bellaiche, B. Vilquin, A. Petraru, I. P. Krug, and C. M. Schneider. Full field electron spectromicroscopy applied to ferroelectric materials. *Journal of Applied Physics*, 113(18), 2013.

- [135] N. Barrett, D. M. Gottlob, C. Mathieu, C. Lubin, J. Passicousset, O. Renault, and E. Martinez. Operando x-ray photoelectron emission microscopy for studying forward and reverse biased silicon p-n junctions. *Review of Scientific Instruments*, 87(5):053703, 5 2016.
- [136] G. Xiong, R. Shao, T.C. Droubay, A.G. Joly, K.M. Beck, S.A. Chambers, and W.P. Hess. Photoemission Electron Microscopy of TiO₂ Anatase Films Embedded with Rutile Nanocrystals. *Advanced Functional Materials*, 17(13):2133–2138, 9 2007.
- [137] Olivier Copie, Nicolas Chevalier, Gwenael Le Rhun, Cindy L. Rountree, Dominique Martinotti, Sara Gonzalez, Claire Mathieu, Olivier Renault, and Nicholas Barrett. Adsorbate Screening of Surface Charge of Microscopic Ferroelectric Domains in Sol-Gel PbZr_{0.2}Ti_{0.8}O₃ Thin Films. *ACS Applied Materials and Interfaces*, 9(34):29311–29317, 2017.
- [138] K. Takeuchi, A. Suda, and S. Ushioda. Local variation of the work function of Cu(111) surface deduced from the low energy photoemission spectra. *Surface Science*, 489(1-3):100–106, 8 2001.
- [139] O. Renault, R. Brochier, A. Roule, P. H. Haumesser, B. Krömker, and D. Funnemann. Work-function imaging of oriented copper grains by photoemission. In *Surface and Interface Analysis*, volume 38, pages 375–377, 4 2006.
- [140] F. De La Peña, N. Barrett, L. F. Zagonel, M. Walls, and O. Renault. Full field chemical imaging of buried native sub-oxide layers on doped silicon patterns. *Surface Science*, 604(19-20):1628–1636, 9 2010.
- [141] Bradley H Frazer, Benjamin Gilbert, Brandon R Sonderegger, and Gelsomina De Stasio. The probing depth of total electron yield in the sub-keV range: TEY-XAS and X-PEEM. *Surface Science*, 537(1-3):161–167, 7 2003.
- [142] Paolo Carra, B. T. Thole, Massimo Altarelli, and Xindong Wang. X-ray circular dichroism and local magnetic fields. *Physical Review Letters*, 70(5):694–697, 2 1993.
- [143] Ingo P. Krug, Hatice Doganay, Florian Nickel, Daniel M. Gottlob, Claus M. Schneider, Alessio Morelli, Daniele Preziosi, Ionela Lindfors-Vrejoiu, Robert Laskowski, and Nick Barrett. Interface-mediated ferroelectric patterning and Mn valency in nano-structured PbTiO₃/La_{0.7}Sr_{0.3}MnO₃. *Journal of Applied Physics*, 120(9):0–7, 2016.
- [144] V.K. Zworykin. On electron optics. *Journal of the Franklin Institute*, 215(5):535–555, 5 1933.

- [145] W. Teliëps and E. Bauer. An analytical reflection and emission UHV surface electron microscope. *Ultramicroscopy*, 17(1):57–65, 1985.
- [146] E. Bauer. *Surface microscopy with low energy electrons*, volume 23. Springer, 2014.
- [147] G. F. Nataf, P. Grysan, M. Guennou, J. Kreisel, D. Martinotti, C. L. Rountree, C. Mathieu, and N. Barrett. Low energy electron imaging of domains and domain walls in magnesium-doped lithium niobate. Technical report, 2016.
- [148] N. Barrett, J. Rault, I. Krug, B. Vilquin, G. Niu, B. Gautier, D. Albertini, P. Lecoeur, and O. Renault. Influence of the ferroelectric polarization on the electronic structure of BaTiO₃ thin films. *Surface and Interface Analysis*, 42(12-13):1690–1694, 2010.
- [149] S. A. Nepijko and N. N. Sedov. Aspects of Mirror Electron Microscopy. *Advances in Imaging and Electron Physics*, 102(C):273–323, 1997.
- [150] S A Nepijko, N N Sedov, G Scho, and È Nhense. Peculiarities of imaging one- and two-dimensional structures using an electron microscope in the mirror operation mode. Technical report, 2001.
- [151] S A Nepijko, N N Sedov, O Schmidt, G Scho È Nhense, X Bao, and W Huang. Imaging of three-dimensional objects in emission electron microscopy. Technical report, 2001.
- [152] Alejandro Ojeda-G-P, Max Döbeli, and Thomas Lippert. Influence of Plume Properties on Thin Film Composition in Pulsed Laser Deposition. *Advanced Materials Interfaces*, 5(18):1701062, 9 2018.
- [153] Mariola O. Ramirez, Tom T.A. Lummen, Irene Carrasco, Eftihia Barnes, Ulrich Aschauer, Dagmara Stefanska, Arnab Sen Gupta, Carmen De Las Heras, Hirofumi Akamatsu, Martin Holt, Pablo Molina, Andrew Barnes, Ryan C. Haislmaier, Przemysław J. Deren, Carlos Prieto, Luisa E. Bausá, Nicola A. Spaldin, and Venkatraman Gopalan. Emergent room temperature polar phase in CaTiO₃ nanoparticles and single crystals. *APL Materials*, 7(1), 2019.
- [154] G. F. Nataf, N. Barrett, J. Kreisel, and M. Guennou. Raman signatures of ferroic domain walls captured by principal component analysis. *Journal of Physics Condensed Matter*, 30(3), 1 2018.
- [155] Hervé Abdi and Lynne J. Williams. Principal component analysis, 7 2010.
- [156] Michael A. Carpenter, Ana I. Becerro, and Friedrich Seifert. Strain analysis of phase transitions in (Ca,Sr)TiO₃ perovskites. *American Mineralogist*, 86(3):348–363, 3 2001.

- [157] C. Mathieu, N. Barrett, J. Rault, Y. Y. Mi, B. Zhang, W. A. de Heer, C. Berger, E. H. Conrad, and O. Renault. Microscopic correlation between chemical and electronic states in epitaxial graphene on SiC (000-1). *Physical Review B*, 83(23):235436, 6 2011.
- [158] Maylis Lavayssière, Matthias Escher, Olivier Renault, Denis Mariolle, and Nicholas Barrett. Electrical and physical topography in energy-filtered photo-electron emission microscopy of two-dimensional silicon pn junctions. *Journal of Electron Spectroscopy and Related Phenomena*, 186(1):30–38, 2013.
- [159] E. Arenholz, G. Van Der Laan, A. Fraile-Rodríguez, P. Yu, Q. He, and R. Ramesh. Probing ferroelectricity in $\text{PbZr}_{0.2}\text{Ti}_{0.8}\text{O}_3$ with polarized soft x rays. *Physical Review B - Condensed Matter and Materials Physics*, 82(14):1–4, 2010.
- [160] A. Ruosi, C. Raisch, A. Verna, R. Werner, B. A. Davidson, J. Fujii, R. Kleiner, and D. Koelle. Electron sampling depth and saturation effects in perovskite films investigated by soft x-ray absorption spectroscopy. *Physical Review B*, 90(12):125120, 9 2014.
- [161] Z. Zhao, N. Barrett, Q. Wu, D. Martinotti, L. Torteche, R. Haumont, M. Pellen, and E. K.H. Salje. Interaction of low-energy electrons with surface polarity near ferroelastic domain boundaries. *Physical Review Materials*, 3(4):1–12, 2019.
- [162] O Bunău and Y Joly. Self-consistent aspects of x-ray absorption calculations. *Journal of Physics: Condensed Matter*, 21(34):345501, 8 2009.
- [163] Oana Bunău and Yves Joly. Time-dependent density functional theory applied to x-ray absorption spectroscopy. *Physical Review B*, 85(15):155121, 4 2012.
- [164] Lixin He and David Vanderbilt. First-principles study of oxygen-vacancy pinning of domain walls in PbTiO_3 . *Physical Review B - Condensed Matter and Materials Physics*, 68(13):1341031–1341037, 2003.
- [165] Xiaomei He, Suzhi Li, Xiangdong Ding, Jun Sun, Sverre M. Selbach, and Ekhard K.H. Salje. The interaction between vacancies and twin walls, junctions, and kinks, and their mechanical properties in ferroelastic materials. *Acta Materialia*, 178:26–35, 2019.
- [166] Liliana Goncalves-Ferreira, Simon A T Redfern, Emilio Artacho, Ekhard Salje, and William T. Lee. Trapping of oxygen vacancies in the twin walls of perovskite. *Physical Review B - Condensed Matter and Materials Physics*, 81(2):1–7, 2010.

- [167] Blai Casals, Guillaume F. Nataf, David Pesquera, and Ekhard K. H. Salje. Avalanches from charged domain wall motion in BaTiO₃ during ferroelectric switching. *APL Materials*, 8(1):011105, 1 2020.
- [168] Blai Casals, Guillaume F. Nataf, and Ekhard K.H. Salje. Avalanche criticality during ferroelectric/ferroelastic switching. *Nature Communications*, 12(1):1–7, 2021.
- [169] Tokuji Utsu. Representation and Analysis of the Earthquake Size Distribution: A Historical Review and Some New Approaches. In *Seismicity Patterns, their Statistical Significance and Physical Meaning*, pages 509–535. Birkhäuser Basel, Basel, 1999.
- [170] Ekhard K.H. Salje and Karin A. Dahmen. Crackling Noise in Disordered Materials. *Annual Review of Condensed Matter Physics*, 5(1):233–254, 3 2014.
- [171] Philippe Tückmantel, Iaroslav Gaponenko, Nirvana Caballero, Joshua C. Agar, Lane W. Martin, Thierry Giamarchi, and Patrycja Paruch. Local Probe Comparison of Ferroelectric Switching Event Statistics in the Creep and Depinning Regimes in Pb(Zr_{0.2}Ti_{0.8})O₃ Thin Films. *Physical Review Letters*, 126(11):117601, 3 2021.
- [172] Ekhard K. H. Salje, Hanlong Liu, Linsen Jin, Deyi Jiang, Yang Xiao, and Xiang Jiang. Intermittent flow under constant forcing: Acoustic emission from creep avalanches. *Applied Physics Letters*, 112(5):054101, 1 2018.
- [173] Aaron Clauset, Cosma Rohilla Shalizi, and M. E.J. Newman. Power-law distributions in empirical data. *SIAM Review*, 51(4):661–703, 2009.
- [174] J. Weiss, W. Ben Rhouma, T. Richeton, S. Dechanel, F. Louchet, and L. Truskinovsky. From Mild to Wild Fluctuations in Crystal Plasticity. *Physical Review Letters*, 114(10):105504, 3 2015.
- [175] Yang Yang, Suzhi Li, Xiangdong Ding, Jun Sun, Jerome Weiss, and Ekhard K.H. Salje. Twisting of pre-twinned α -Fe nanowires: from mild to wild avalanche dynamics. *Acta Materialia*, 195:50–58, 8 2020.
- [176] Yang Yang, Libo Zhang, Suzhi Li, Xiangdong Ding, Jun Sun, Jerome Weiss, and Ekhard K. H. Salje. Mild fluctuations in ferroelastic domain switching. *Physical Review B*, 104(21):214103, 12 2021.
- [177] Ekhard K. H. Salje. Mild and wild ferroelectrics and their potential role in neuromorphic computation. *APL Materials*, 9(1):010903, 1 2021.
- [178] N. Barrett, J. Dionot, D. Martinotti, E. K.H. Salje, and C. Mathieu. Evidence for a surface anomaly during the cubic-tetragonal phase transition in BaTiO₃(001). *Applied Physics Letters*, 113(2):1–5, 2018.

- [179] Libo Zhang, Suzhi Li, Xiangdong Ding, Jun Sun, and Ekhard K. H. Salje. Statistical analysis of emission, interaction and annihilation of phonons by kink motion in ferroelastic materials. *Applied Physics Letters*, 116(10):102902, 3 2020.
- [180] X. Ding, T. Lookman, Z. Zhao, A. Saxena, J. Sun, and E. K. H. Salje. Dynamically strained ferroelastics: Statistical behavior in elastic and plastic regimes. *Physical Review B*, 87(9):094109, 3 2013.
- [181] Liang Qiao and Xiaofang Bi. Evaluation of magnetoelectric coupling in a BaTiO₃–Ni composite ferroic film by impedance spectroscopy. *Applied Physics Letters*, 92(21):214101, 5 2008.
- [182] J. Muñoz-Saldaña, G.A. Schneider, and L.M. Eng. Stress induced movement of ferroelastic domain walls in BaTiO₃ single crystals evaluated by scanning force microscopy. *Surface Science*, 480(1-2):L402–L410, 5 2001.
- [183] Darrell G. Schlom, Long Qing Chen, Xiaoqing Pan, Andreas Schmehl, and Mark A. Zurbuchen. A thin film approach to engineering functionality into oxides. *Journal of the American Ceramic Society*, 91(8):2429–2454, 2008.
- [184] Gwladys Steciuk, Adrian David, Václav Petříček, Lukáš Palatinus, Bernard Mercey, Wilfrid Prellier, Alain Pautrat, and Philippe Boullay. Precession electron diffraction tomography on twinned crystals: application to CaTiO₃ thin films. *Journal of Applied Crystallography*, 52(3):626–636, 2019.

VII - French summary

Un matériau ferroélastique forme des domaines avec une même direction de déformation spontanée, renversable en appliquant une contrainte macroscopique sur l'échantillon, afin de réduire l'énergie libre du matériau. Les parois de domaines sont des régions de transition entre des domaines de paramètres d'ordre uniforme, qu'il s'agisse de magnétisation, de polarisation électrique ou de déformation mécanique. Leur formation est un compromis entre le coût énergétique de la paroi et le gain associé à la formation du domaine. Leur structure, leur symétrie et même leur chimie peuvent différer de celles des domaines parents adjacents, ce qui donne lieu à des propriétés physiques uniques. En tant que tels, ils ont le potentiel pour devenir un nouveau paradigme pour la nanoélectronique où la paroi est l'élément actif du dispositif et offre des perspectives en termes de densité d'information, de (multi-)fonctionnalité et de faible consommation d'énergie. Nous étudions dans cette thèse les propriétés structurales et électroniques des parois ferroélastiques de la céramique $CaTiO_3$ afin de les contrôler électro-mécaniquement.

Les parois de domaine sont des interfaces qui peuvent influencer la structure du domaine. Par exemple, jusqu'à 40% (33%) du coefficient piézoélectrique d_{33} dans $BaTiO_3$ ($PbZrTiO_3$) proviendrait du mouvement des parois. Il est alors devenu intéressant de comprendre et de concevoir des matériaux avec des parois de domaines spécifiques pour améliorer les propriétés du matériau. De plus, les parois de domaine sont également des interfaces distinctes du matériau avec des propriétés uniques. Des propriétés spécifiques peuvent exister aux parois de domaine, comprenant de la conductivité, supraconductivité et polarité. À partir de ces propriétés intéressantes, un sujet de recherche connexe a été baptisé "ingénierie des parois de domaine" ou "nanoélectronique des parois de domaine", où les parois de domaine offrent des possibilités intéressantes pour porter l'information que le matériau en lui-même et potentiellement servir dans un dispositif de mémoire en raison de leur haute densité du fait de la faible épaisseur de paroi, de leurs propriétés fonctionnelles et de leur contrôle.

Dans cette optique, nous avons étudié de manière approfondie le $CaTiO_3$, un matériau ferroélastique pérovskite, qui possède des parois de domaine polaires orientés vers le haut (P_{up}) et vers le bas (P_{down}). L'origine de la polarité aux parois provient de l'un des angles d'inclinaison des octaèdres d'oxygène qui passe à zéro, ce qui permet l'émergence de la polarité par le décentrage du cation Ti. Cette propriété pourrait être contrôlée électromécaniquement, ajoutant une fonctionnalité au système. Le caractère polaire des parois a un potentiel pour les dispositifs de mémoire.

La présentation du manuscrit est la suivante : Dans le Chapitre I, la physique derrière les domaines ferroélectriques et ferroélastiques et les parois de domaines est présentée, ainsi que les matériaux étudiés $CaTiO_3$ et $BaTiO_3$. L'accent est mis

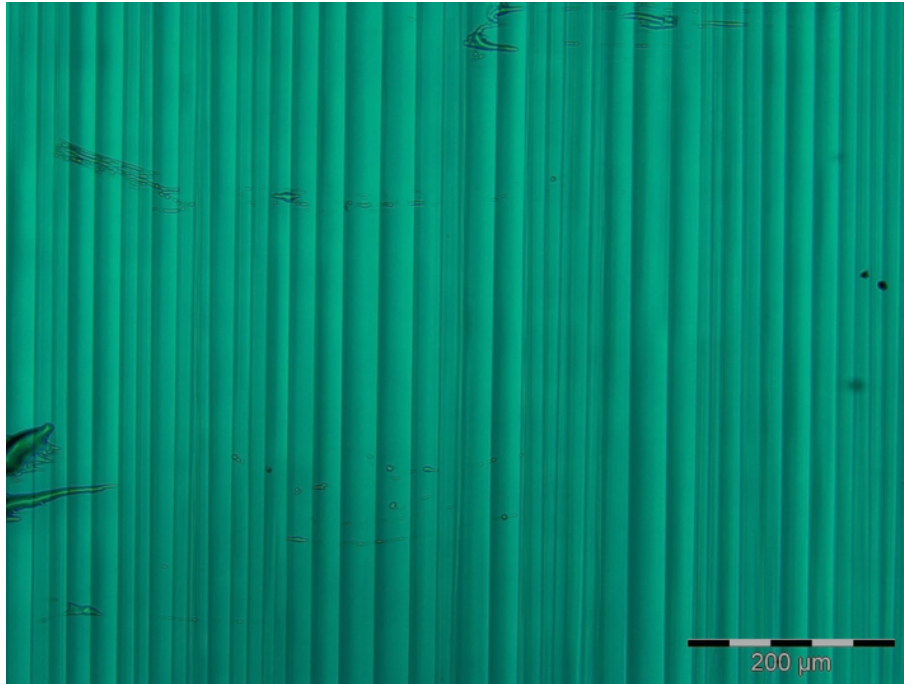


Figure VII.1: Image optique d'un cristal de CaTiO_3 . Les domaines parallèles sont visibles par biréfringence.

sur les propriétés fonctionnelles et l'ingénierie des parois de domaine. Les méthodes expérimentales utilisées pour l'observation des parois de domaine sont expliquées dans le Chapitre II. Dans le chapitre III, nous étudions l'ordre ferroélastique de la surface du CaTiO_3 à l'aide de techniques de photoémission. Nous décrivons d'abord les orientations de déformation possibles dans les parois du domaine à partir de la rupture de symétrie à la transition ferroïque, puis nous quantifions les angles de parois in-situ par microscopie électronique à photoémission (PEEM). Enfin, nous observons la déformation ferroélastique à la surface par spectroscopie d'absorption des rayons X (XAS) dans un PEEM. A partir de la détermination de l'angle entre parois et de l'observation de la déformation spontanée dans les domaines, nous sommes en mesure de décrire l'ordonnancement ferroélastique à la surface. Dans le chapitre IV, nous rapportons la mesure du potentiel de surface et de la bande interdite des parois de domaine à la surface de CaTiO_3 (001). Le contraste du potentiel de surface montre la présence de parois avec une polarité pointant vers le haut (P_{up}) ou vers le bas (P_{down}). La spectroscopie de perte d'énergie d'électrons (EELS) sur des parois permet de mesurer la bande interdite. Dans le chapitre V, on étudie le saut de paroi de domaine de surface dans les parois de domaine ferroélastiques de BaTiO_3 sous fluage.

Dans le chapitre I, nous présentons les propriétés ferroélectriques et ferroélastiques des matériaux et l'organisation en domaines composé d'une même direction de paramètre d'ordre. Les parois à l'interface entre domaines dont des objets

2D intéressants du fait de propriétés uniques qui n'existent pas dans les domaines adjacents. On retrouve par exemple des parois conductrices dans certains ferroélastiques comme le $BiFeO_3$ et superconductrices dans WO_3 . On se concentre dans la thèse sur les domaines et parois dans les céramiques ferroélectriques $BaTiO_3$ et ferroélastique $CaTiO_3$. Les propriétés physiques et électrique de ces matériaux et plus localement des parois sont alors analysés par des techniques expérimentales appropriés.

Les techniques expérimentales utilisés et certaines méthodes d'analyse associés sont présentés dans le chapitre II. L'imagerie par microscopie de photoémission d'électrons (PEEM) est utilisé pour l'étude de la topographie physique des surfaces de matériaux ferroélastiques comme $CaTiO_3$ et pour analyser quantitativement les angles de macle. Il s'agit d'une technique de microscopie électronique non-destructive sous ultra haut vide, avec une résolution spatiale d'environ 50 nm. Cette technique de microscopie est aussi utilisé pour observer la polarisation dans les domaines ferroélectriques afin de détecter le mouvement rapide des parois ferroélastiques dans le $BaTiO_3$. La spectroscopie d'absorption des rayons X dans un microscope d'électrons en photoémission (XAS-PEEM) est utilisé pour observer la déformation spontanée dans les domaines ferroélastiques de $CaTiO_3$ par différence d'interaction entre les polarisations transverses orthogonales de la lumière incidente. Enfin, la microscopie électronique à basse énergie (LEEM) est utilisé pour observer le potentiel de surface des matériaux ferroélastiques et caractériser la polarité aux parois. En mode dispersif, la spectroscopie des pertes d'énergie électronique permet de mesurer localement la bande interdite.

Le chapitre III est consacré à l'observation et quantification in-situ de l'ordre ferroélastique dans le titanate de calcium par des techniques de microscopie à photoémission. Nous utilisons l'imagerie par microscopie de photoémission d'électrons (PEEM), au seuil de photoémission, pour étudier la topographie physique de la surface ferroélastique avec sa structure caractéristique en forme de toit d'usine de type vallée/crête et pour quantifier les angles de macle. Par des considérations de symétrie, à partir des angles de macle, on peut déduire les directions des déformations ferroélastiques dans les domaines. Les résultats concordent avec la mesure indépendante des angles par microscopie à force atomique (AFM). Avec cette méthode, il serait possible de mesurer avec précision la topographie physique sur n'importe quelle surface ferroélastique et de quantifier les états de contrainte dans les domaines jacents.

De plus, nous identifions directement l'orientation du paramètres d'ordre ferroélastique dans les domaines, la déformation spontanée, par la spectroscopie d'absorption des rayons X dans un microscope d'électrons en photoémission (XAS-PEEM). La grandeur de l'interaction de la lumière polarisée avec les orbitales 3d du titane dans le titanate de calcium dépend de l'orientation de la déformation des domaines. Ainsi, un contraste correspondant aux différents états de déformation spontanée est visible par dichroïsme linéaire des rayons X (XLD), qui est

la différence entre les images avec des polarisations de la lumière transverse orthogonales. La détermination in-situ des angles de topographie physique et de l'orientation de la déformation par PEEM ouvre des perspectives pour une analyse complète de la réponse électromécanique des parois ferroélastiques.

Ensuite, dans le chapitre IV, nous avons étudié un rétrécissement de la bande interdite au niveau des parois de domaine dans le titanate de calcium. La bande interdite est mesurée par spectroscopie des pertes d'énergie électronique (EELS) dans un microscope électronique à basse énergie (LEEM) en mode dispersif. Un diaphragme dans un plan image est centré sur les domaines ou sur les parois. Dans chaque cas nous mesurons l'écart en énergie entre le pic élastique et le début du pic des pertes. Le rétrécissement aux parois est compris entre 0.01 et 0.33 eV, avec une réduction plus importante pour les parois de domaine polarisées vers le haut que pour celles polarisées vers le bas. Le rétrécissement de la bande interdite est suggéré comme un effet extrinsèque de l'interaction entre les lacunes d'oxygène et les parois, générant des états dans la bande interdite. Une modulation du rétrécissement de la bande interdite en fonction de la concentration des lacunes d'oxygène est également observée.

Dans la dernière partie, nous étudions la mobilité des parois de domaine ferroélastiques du titanate de baryum sous l'effet d'un fluage. Le mouvement des parois ferroélastiques de domaine ferroélectrique est un processus non linéaire où la propagation continue des parois se superpose souvent à des sauts soudains. L'accumulation de plusieurs sauts forme une avalanche. Nous profitons de la résolution spatiale du PEEM pour observer les parois de domaines sur une longue plage de temps en s'aidant de la modulation de la polarisation des domaines ferroélectriques. Nous avons constaté que la distribution en énergie du mouvement brusque des parois ferroélastiques suit une loi de puissance avec un exposant de 1.37, ce qui confirme la dépendance du mouvement d'avalanches indépendante de l'échelle.

En annexe, une première discussion sur les parois de domaine créées dans des films minces de titanate de calcium obtenus par croissance épitaxiale est présentée en annexe. Les films minces de CTO déformés épitaxialement sont déposés sur $LaAlO_3$ (LAO) par dépôt laser pulsé (PLD). Le LAO est également un ferroélastique pérovskite à température ambiante, avec un paramètre de maille (3,79 Å) proche de celui du CTO (3,83 Å), permettant une déformation compressive de 1%. Nous sommes capables de faire croître des films de 2 à 300 nm d'épaisseur, présentant des parois de domaine à la surface. Les macles du substrat LAO peuvent se propager dans le CTO. Au sein d'un seul domaine ferroélastique induit par le LAO dans le CTO, d'autres parois peuvent se former, en fonction de la relaxation de la déformation épitaxiale avec l'épaisseur. Cette relaxation est confirmée par notre analyse XRD. Le paramètre de maille hors plan pour les films de 200 nm et 300 nm sont proches de ceux d'un film de 100 nm, ce qui montre que la relaxation est presque complète à 100 nm d'épaisseur. La polarité des parois de

domaine dans ces couches minces est observée par LEEM, les parois se déplacent thermiquement à une basse température de 250°C et une première étude par spectroscopie Raman est réalisée afin de comprendre l'ordonnement des parois de domaine dans l'empilement ferroélastique. La possibilité d'ingénierie des parois de domaine dans des échantillons de films minces ouvre la perspective d'un contrôle électromécanique des parois de domaine ferroélastiques dans le titanate de calcium.